ENABLING TECHNOLOGIES FOR AUTONOMOUS LANDING WITH ROBOTIC LANDING GEAR

A Dissertation
Presented to
The Academic Faculty

By

Benjamin León

In Partial Fulfillment
of the Requirements for the Degree
Doctor of Philosophy in the
School of Aerospace Engineering

Georgia Institute of Technology

May 2020

Copyright © Benjamin León 2020

ENABLING TECHNOLOGIES FOR AUTONOMOUS LANDING WITH ROBOTIC LANDING GEAR

Approved by:

Dr. Claudio V. Di Leo, Advisor
School of Aerospace Engineering
Georgia Institute of Technology

Dr. Julián J. Rimoli
School of Aerospace Engineering
Georgia Institute of Technology

Dr. Jonathan Rogers
School of Aerospace Engineering
Georgia Institute of Technology

Dr. William Singhose
School of Mechanical Engineering
Georgia Institute of Technology

Dr. Ashish Bagai
buGiAero, LLC

Date Approved: March 25, 2020

An ounce of practice is generally worth more than a ton of theory.

E. F. Schumacher

To my loving and supportive parents, Enrique and Jean.

ACKNOWLEDGEMENTS

I would like to thank my labmates at the Center for Advanced Machine Mobility and the Multiphysics Mechanics of Materials Lab for their eagerness to discuss ideas and concepts, and shared a common passion for aerospace engineering. Specifically, I would like to thank Seth Burdette, Dooroo Kim, Kyle Solomon, and Jake Wachlin. You helped foster an insightful and productive lab environment.

I would like to thank my advisor, Dr. Di Leo, for his support and guidance throughout the past few years. I greatly appreciate your insight and drive to ever improve hardware, software, and technical report quality. I would also like to thank Dr. Costello for his creative insight and advice on multiple occasions throughout the past five years. Your guidance was invaluable early in my graduate education and in my professional development.

The experimental work presented here had sponsorship from the Defense Advanced Research Projects Agency (DARPA) Tactical Technology Office (TTO) and The Boeing Company's Mesa Phantomworks and S-100 teams. I would like to thank DARPA, and in particular, Timothy Chung, Ryan Hofmeister, Natalie Van Osch, Matthew Tallent, and Michael Ol for providing valuable comments and guidance. I would like to thank the Boeing Mesa team, and in particular, Ray Lopez, Steve Low, Roy Bergman, and Bill Brady for their assistance with technology integration and ground/flight testing of these enabling technologies.

TABLE OF CONTENTS

LIST OF TABLES

LIST OF FIGURES

NOMENCLATURE

Acronyms

AACUS Autonomous aerial cargo/utility system

ACTH Access time history

AHRS Attitude and heading reference system

BD Body

CAD Computer aided design

CFRP Carbon-fiber reinforced polymer

CG Center of gravity

CNC Computer numerical control

COTS Consumer-off-the-shelf

CRC Cyclic-redundancy checksum

DAQ Data acquisition

DC Direct current

DoF Degree(s) of freedom

DVE Degraded visual environment

FBD Free-body diagram

FEA Finite element analysis

FEM Finite element model

GUI Graphic user interface

IMU Inertial measurement unit

LiDAR Light detection and ranging

LSE Least-squares estimator

MEMS Micro-electromechanical system

PBC Parking brake control

PCB Printed circuit board

PD Proportional-derivative

PID Proportional-integral-derivative

POSE Position and orientation state estimate

RADAR Radio detection and ranging

RF Radio frequency

RK4 Fourth-order, Runge-Kutta

RLG Robotic landing gear

RPM Revolutions per minute

RTV Room temperature vulcanizing

SLS Standard linear solid

SMP Ship motion program

SS Sea State

STH Ship time history

UAV Unmanned air vehicle

VTOL Vertical takeoff and landing

Subscripts

$0, e$ Initial engineered cavity property

$0, s$ Initial off-the-shelf sensor cavity property

$asym$ Asymmetric

D differential

DB Deadband

i Counting index

k Discrete interval counting index

L Left

lat Lateral

$long$ Longitudinal

max Maximum

min Mininum

R Right

sym Symmetric

Symbols

α	Low-pass filter parameter or angular acceleration
β	Spool rotation angle
ΔF	Difference in applied force
Δ	Ground clearance from the ground to the fuselage
δ	Spring displacement or small change in value
$\dot{\delta}$	Time rate of change of spring displacement
$\dot{\gamma}$	Time rate of change of ground slope
$\dot{e}$	Time rate of change of error
η	Rotor plane angle
γ	Ground slope
$\hat{\theta}$	Estimate of leg angle
μ	Friction coefficient
ω	Angular rate
ϕ	Fuselage roll angle
σ	Standard deviation of uncertainty
τ	First-order system time constant
θ	Leg angle
$\tilde{P}$	Normalized pressure
ζ	Damping ratio
A	Sinusoid amplitude

B_1 Distance from the crank-fuselage pin to the ground

B_2 Distance from the crank-fuselage pin to the bottom of the fuselage

B_3 Distance between two crank-fuselage mounting points

B_4 Distance between two foot contact points

c Damping coefficient

e Error scalar

F Applied force

f Frequency

$H,\ [H]$ Translation force or Jacobian matrix

I Identity matrix

J Mass moment of inertia

K Gain scalar or matrix

k Spring stiffness

L_1 Crank length

L_2 Vertical distance between the crank-leg and follower-leg joints

L_3 Vertical distance between the follower-leg joint and foot

L_4 Horizontal distance between the crank-leg joint and the foot's tip

M Applied moment

n Motor speed

P Pressure or covariance matrix

p Fuselage roll rate

Q Generalized force term

q Fuselage pitch rate, generalized coordinate, or quaternions

R Correlation coefficient or motor winding resistance

T Thrust, temperature, or kinetic energy

u, v, w Aircraft standard body frame velocities

V Axial force, volume, applied voltage, or potential energy

W weight

x, y Position coordinates or state/measurement scalars

z Vertical height between the left and right foot contact points or vertical height above the inertial origin

SUMMARY

Runways or prepared landing sites are not always available for vertical take-off and landing (VTOL) aircraft, such as rotorcraft. Unprepared or moving surfaces encompass situations that result in the rotorcraft coming to rest outside of its roll and pitch specifications. Furthermore, some prepared, moving landing sites, such as maritime ship decks, present different challenges to manned and unmanned rotorcraft because of the landing surface dynamics. Research and development into robotic landing gear (RLG) for rotorcraft provides a tool for these aircraft to land on completely unprepared and dynamic surfaces. They do so by articulating the landing gear until it conforms to the surface beneath the aircraft.

Theoretical studies and limited flight tests of RLG for rotorcraft showed that, given ideal feedback, RLG reduces fuselage impact loads, reduces pilot effort, and drastically increases the envelope of landable surfaces. First generation experimental RLG were able to land on static landing surfaces only, such as hillsides and rigid obstacles. These first generation systems incurred a substantial weight increase compared to rigid gear. Further theoretical exploration into RLG showed the usefulness for dynamic surface landings through simulation. However, no experimental development efforts of technologies that enable such landings have been presented to date.

This dissertation develops necessary contributions in three of the required technology areas for autonomous rotorcraft landings on static and moving landing surfaces using RLG. Namely, these technologies include a crashworthy, novel topology; a low-force, large-deformation force sensor for ground contact sensing; and a discrete, real-time, sensor-fused RLG controller. These technologies are transformative from previous RLG research because of their ability to increase autonomy, reliability, and applicability for fielded VTOL systems. Each technology is developed generally from first principles and applied to a RLG design on a commercial airframe. For each

technology, design tools are expanded upon to aid future designs without the need for extensive experimental verification. Simulations conducted using said tools are then used to improve each technologies design for the specific application, and lab experiments are conducted to show their practicality. Finally, a series of ground and flight tests on the commercial airframe bolster this dissertation aimed at developing autonomous, robust, and practical RLG.

CHAPTER 1
INTRODUCTION AND RELEVANT BACKGROUND

Throughout their history, rotorcraft have proven to be a vital tool for accessing landscapes that traditional fixed-wing aircraft are unable to reach due to their smaller landing zone footprint. Generally, rotary-wing aircraft landing zones fall into two primary categories, static and dynamic. Runways are often unavailable for fielded rotorcraft to land on, so pilots or autopilot systems must face the complexity of landing on an uneven, albeit static, terrain. Rotorcraft specifically have limitations on acceptable static slopes ranging from 6° to 10°, depending on their mission requirements and design [1]. The complexity, workload, and risks increase for landings on mobile surfaces, such as maritime ship decks, because of the periodic, coupled landing surface dynamics [2, 3]. Further complications arise when the rotorcraft operates in degraded visual environments (DVEs), where the pilot or camera systems cannot see the landing surface. The primary risk to rotorcraft landing on sloped or dynamic surfaces and in DVEs is dynamic rollover [1]. Dynamic rollover occurs when the rotorcraft rotates about a gear's contact point(s) without the ability to control the roll rate. Generally, the aircraft impacts the ground on its side or worse, completely rolls over. The risk for dynamic rollover cause operators and designers to limit mission objectives in some cases. These limits inherently stem from the use of rigid or passive, shock-absorbing landing gear because they cannot conform to the landing surface and maintain the fuselage at a safe orientation. Robotic, or articulating, landing gear (RLG) were developed as a potential solution to these challenges.

Robotic legs, used in a number of ground applications for quadrupedal and bipedal locomotion, allow a system to maneuver through irregular and rugged terrains [4–7]. Because of their usefulness on rugged terrains, robotic legs have been a topic of focus

on VTOL vehicles. Modern research and development into RLG for rotorcraft was introduced by Manivannan et al. [8]. Their concept and theoretical design provided a replacement to skid gear that enables rotorcraft landings on static sloped or obstacle-laden surfaces. The single physical sloped landing limitation of the concept was rotor tip ground impact. This meant that, independent of pilot skill level, the rotorcraft could land on a sloped surface; immensely expanding the usable static landing zones. Their work showed the theoretical capability increase of such a concept at a time when needs for this technology in autonomous VTOL systems are emerging.

Urban air mobility represents the largest sector with emergent needs for applied RLG. Urban air mobility encompasses any commercial cargo and passenger transport in densely populated areas [9–11]. Al Haddad et al. [12] developed acceptance models of robotic/autonomous urban air mobility systems and found that safety, reliability, and trust in the systems that make an aircraft safe and reliable are critical factors to the adoption of these VTOL systems. RLG have the ability to reduce load on the airframe and passengers during a hard impact landing, mitigate ground resonance, and reduce pilot or flight controller workload [8, 13]. Both of these factors improve the safety and reliability of the system during landing, making urban air mobility market a VTOL aircraft sector that would benefit from active landing gear.

Military cargo transport and persistent intelligence, surveillance, and reconnaissance (ISR) rotary wing aircraft present a sector of early adopters with needs for RLG. Recent solicitations from the Army look at the development and trade studies for RLG on Class IV UAS because current missions requirements for persistent ISR cannot be reasonably met using rigid landing gear [14]. In addition to the military, first responders are a market of early adopters with needs for RLG. Use of manned or unmanned rotorcraft during an emergency response after a significant natural disaster or in a remote location is limited by the landscape. Often, responders cannot land their rotorcraft to recover injured persons or deliver supplies because the land-

scape has many obstructions present. Both of these examples include users that must complete their mission regardless of the terrain. Operationally viable systems for cargo transport, such as the Autonomous Aerial Cargo/Utility System (AACUS) [15] that was designed to identify a landing zone and avoid obstacles, do not have systems capable of landing on highly sloped or dynamic surfaces. Furthermore, in harsh environments or in emergency landings there may not be time to conduct landing zone recognition. RLG has the potential to mitigate risk to a rotary wing aircraft when there is terrain uncertainty. These examples support that VTOL aircraft have near-term requirements that a practical, robust RLG with autonomous landing capabilities would meet. The subsequent background review analyzes the state of the art with regard to applied RLG research, and it outlines technologies gaps that must be addressed to enable RLG use for autonomous landings in these emerging sectors.

1.1 Relevant Background

Five engineering disciplines are required to complete an autonomous landing with RLG. Figure 1.1 illustrates these disciplines. These include mechanical design and structures, dynamics and controls, embedded systems (namely sensing and actuation), robust flight software, and landing zone detection. This section details the relevant work in specific areas that have engineering technology gaps for RLG. Topology and mechanical design is the first subject matter reviewed, followed by sensors and landing zone detection, and the section concludes with a review of control and flight software literature.

1.1.1 Topology and Mechanical Design

In application-specific design, RLG mechanical design concepts have few, proven capabilities. Each of the subsequent robotic or articulating landing gear concepts are illustrated in Figure 1.2. Baker et al. [16] (top left image) designed a passive, adap-

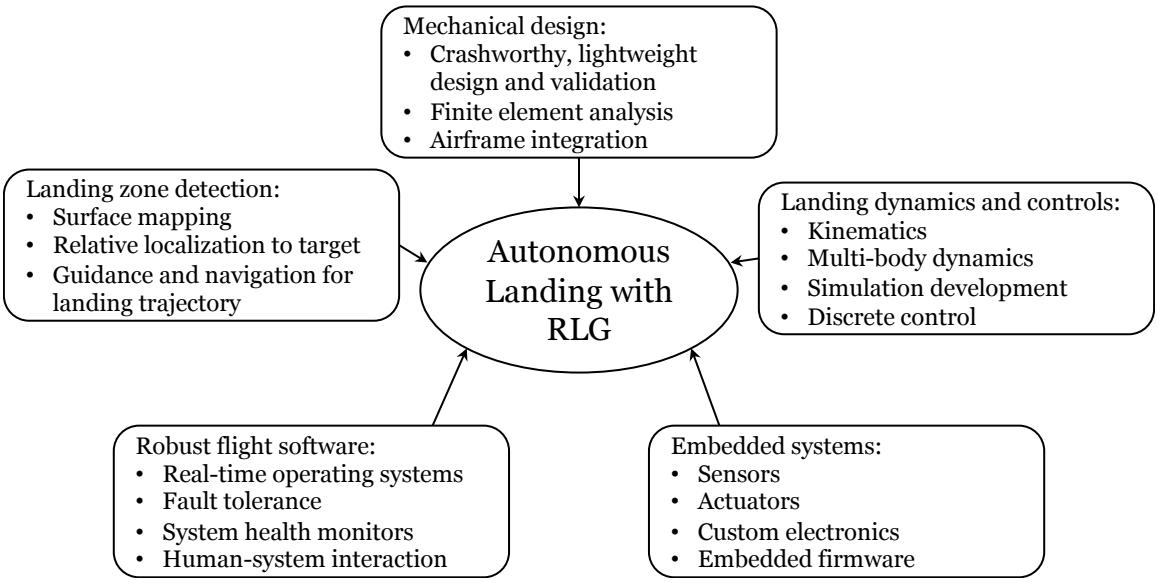

Figure 1.1: Disciplines required for autonomous landings with RLG.

tive landing gear which has a direct, extensible design for active control when using variable length gas dampers. Huang et al. [17] showed that a spacecraft with active landing legs could successfully absorb impact loads and level the body on slopes up to 35° using variable length gas dampers. They verified the concept's range of motion using a 20 kg octocopter, but did not validate their theoretical impact absorption through experimentation. Wachlin [18] designed a spacecraft landing gear for the Europa lander and completed simulations for actuator force requirements and approach orientation and velocity. He did so with a multi-jointed, active landing gear. Stolz et al. from ETH Zurich [19] developed an active landing gear to extend the landing range of a rotorcraft that weighed 78 kg. Their RLG design used a four-bar linkage mechanism driven by a linear ball screw. They completed tests on a small-scale helicopter, and the gear permitted landing on previously restricted surfaces such as the steps depicted in Figure 1.2.

An experimental flight vehicle based on Manivannan's work demonstrated, in a limited fashion, the viability and capability of RLG for rotorcraft [20]. Figure 1.3 illustrates the remotely piloted Rotor Buzz aircraft with an experimental, four-legged

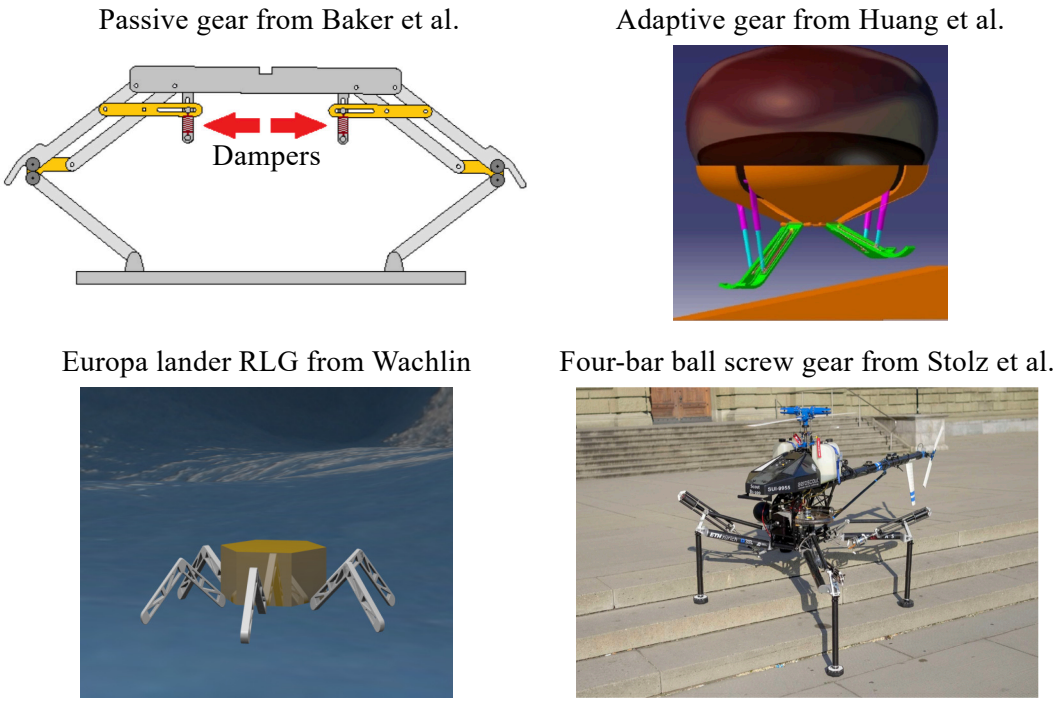

Figure 1.2: Visual summary of other active landing gear mechanical designs adapted into a single format from [16–19]

RLG design. This RLG conducted autonomous feedback and control of each leg, while it was up to the pilot to find the landing surface, align the aircraft, and then land the aircraft. The Rotor Buzz RLG design was a retrofit implementation, replacing the

Figure 1.3: Rotor Buzz helicopter with a flight tested experimental robotic landing gear concept

existing landing gear with minimal direct integration into the airframe. This meant the legs were designed, manufactured, and tested as an individual unit, then strapped onto the helicopter. Figure 1.4 shows the complete design as a separate unit from

the helicopter. Included in the avionics enclosure of the system are the control and communication electronics, a battery, and an inertial measurement unit (IMU). Each joint includes an angle encoder, and the bottom of each foot has a contact sensor. This set of sensors, actuators, and battery allowed for the operation of the system independent of the Rotor Buzz helicopter.

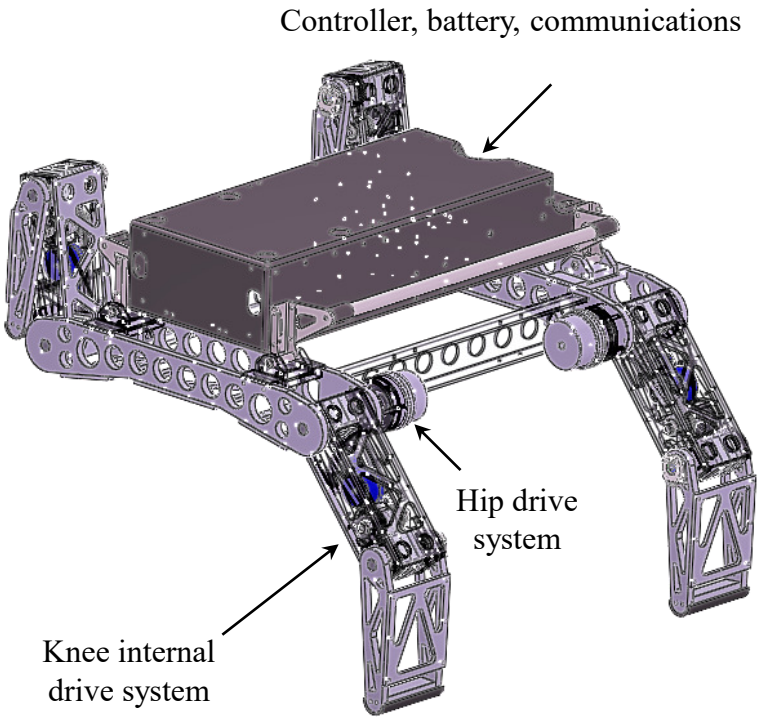

Figure 1.4: Rotor Buzz RLG CAD Model ISO View

Figure 1.5 shows the cross-sectional view of each leg on this design. Each joint uses a motor, brake, and gearbox sized for the loads expected in that joint. Since each leg has two joints, there are eight total motors, gearboxes, and brakes across the four legs. This design provides 170° of leg rotation from the highest point (restricted by the fuselage) and the lowest point which points directly down from the helicopter. The result of such a large range of motion is that the limiting factor for achievable slopes is the rotor plane at approximately 30°. The use of a two-jointed, four-legged landing topology provided a large range of motion and capability for unprepared landing sites

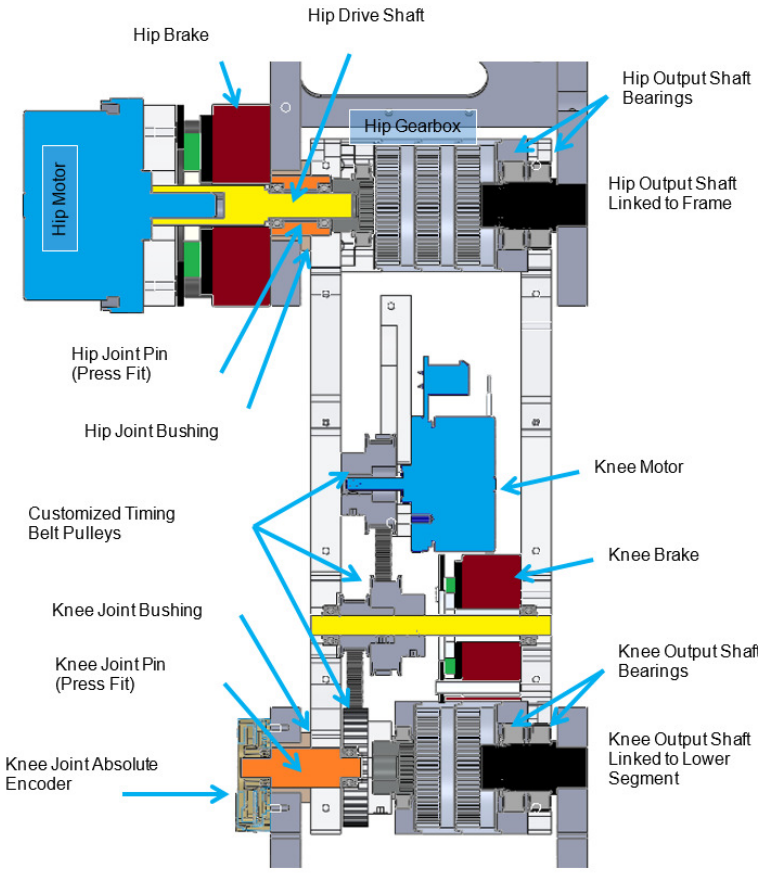

Figure 1.5: Cross section view of Rotor Buzz RLG leg assembly

but came at a *significant weight increase*. Eight total actuation assemblies, and their associated structure, drove the landing gear weight from 2.2 kg (5 lb) to 21 kg (46 lb). None of the relevant RLG concepts have been designed *and* verified for hard landing impact mitigation. Furthermore, they have not been optimized with respect to weight. This leaves a noticeable technology gap for a crashworthy, lightweight RLG topology and mechanical design.

1.1.2 Sensing

The Rotor Buzz RLG employed resistive film force sensors on each foot, providing feedback for leg control. Resistive film force sensors estimate force based on the change in resistance caused by deformation in the film [21–24]. During a landing,

each foot would measure force and feed that data back into a force-feedback control logic that conforms each leg under load until all legs make contact. Once all legs measure contact, the landing gear locks into position. This design showed the practical integration of the RLG concept, but with limitations. Specifically, the sensors required calibration prior to each flight, and they were unable to withstand sustained usage. Furthermore, these sensors offered no redundancy against failure. Once a film sustained damage, all sensing capabilities were lost, and the the legs were unable to conform to the surface. Figure 1.6 shows permanent damage to the resistive film sensors from limited laboratory usage. The extensive damage to these sensors under

Figure 1.6: Damaged experimental RLG resistive film force sensors

mild operating conditions made them impractical for fielded aircraft use. Since contact feedback is a critical part of the RLG control, a fielded RLG requires a robust, reliable contact sensor.

Contact sensing

Three types of contact sensors have been realized to date for robotics: binary, proximity, and force sensors. Binary contact sensors have been used primarily in surface

"search" and "unexpected collision" detection roles of slow moving robotic manipulators, but they have not provided the necessary feedback for fast, guided manipulator motion operations [25]. The primary reason for this limitation is the oscillatory or bouncing nature of the robotic manipulator that results from a binary contact sensor on fast moving arms.

Proximity sensors act as ground contact sensors through measurements of distance to the surface until contact is achieved. One example of proximity sensors is the experimental octocopter platform for adaptive landing gear designed by Huang et al. [17]. Their gear had optical proximity sensors integrated into each leg to predeform each leg prior to contact. These sensors have nonlinear measurement behavior, increasing their complexity. Additionally, they were unable to detect the force on each leg. So if any leg made contact early, then it would retract until the leg was no longer in contact. In a rotorcraft landing scenario, this presents an opportunity for inadvertent bouncing or punching of the leg on the desired landing surface. Another example of proximity sensor use is from Goger et al. [26], where they designed two proximity-detection sensors for haptic grippers and one for robotic skin. Their design used conductive electrodes and a small custom circuit to detect proximity to an object within 40 mm. This type of sensor has such a close proximity that it effectively acts as a binary on/off. This risks inadvertent and undesired leg bouncing or "punching" of the landing surface during nominal landing scenarios where a rotorcraft lands faster than a robotic manipulator. For this reason, proximity sensors are not an ideal fit for RLG ground contact sensing feedback.

Haptic robotic systems often require contact measurements in the form of force magnitude, and sometimes direction, between an articulating extremity and a contact surface in order to generate controlled motion of the extremity [27–30]. Force sensors on these systems take on a variety of form factors that can rely on optics [31–33], wave propagation through materials [34], capacitance [35, 36], and strain [37]. Ideal

sensors for RLG must be sensitive and accurate at low forces, on the order of $\leq 10N$, so they are capable of accurately detecting contact on uneven or sharp terrains. They also must be robust enough to survive hard landings with maximum loads on the order of thousands of newtons [13, 38]. Additionally, landing gear for rotorcraft require harsh environment durability, robustness, low complexity, and the ability to withstand unforeseen impacts on a regular basis. As a direct result, force sensors for RLG must have the same durability as the landing gear. Further review into relevant force sensor research provided four primary contenders: resistive film sensors (already discussed), load cells, elastomer encased magnets, and elastomer or elastomer composite encapsulated pressure sensors.

Load cells are potential candidates for contact force sensors, and they have been investigated in the literature [27, 29, 39–46]. However, the use of load cells for ground contact sensing has some significant drawbacks. First, load cells rated to withstand the entire weight of an aircraft, in addition to any impact loads, do not have sufficient sensitivity at the small loads required for RLG functionality. Second, load cells generally suffer from inertial effects where vibrations or dynamic motion of the load cell produce force readings which can be misinterpreted as actual contact [47–49]. Additionally, load cells can add significant weight when compared to the sensors developed in this work. Although some load cells have built-in accelerometers to compensate for this effect in the direction of loading, it is difficult to ensure that inertial loads will not lead to ground contact errors in a rotorcraft where vibrations occur at various magnitudes and directions. Finally, load cells specially designed for contact sensing scenarios carry a high cost. Buehler et al. [5] described a custom load cell force sensing approach for the Big Dog robot that cost on the order of hundreds of dollars per foot.

A sensor developed by Liu et al. [50] estimates contact force based on magnetic field changes. This sensor relies on the magnetic field changes caused by a magnet em-

bedded in a deformable structure to estimate contact force and stick-slip interactions. Similarly, Ananthanarayanan et al. [51] developed a sensor that uses magnets embedded in an elastomer along with a suitable magnetic field detector to measure changes in the deformation of the elastomer and subsequently estimate forces. This system enables the tailoring of sensor properties from elastomer material properties, magnet strength, and magnet placement. The mapping between force and measurement data is difficult to predict prior to sensor construction; therefore, sensor performance relies on training data in order to be effective. However, any force sensor that relies on magnetic field changes does not have a straightforward design path for use on a rotorcraft. Specifically, a sensor which requires accurate measurement of a magnetic field on a rotorcraft with large, mobile, metal components as well as interactions with unprepared surfaces, including metallic surfaces such as ship decks, eliminated this sensor design from further consideration for this application.

Another promising ground contact sensing technique reviewed is based on barometric pressure sensors cast in a variety of compliant materials such as elastomers. Here, contact forces deform an elastomer, which produces a pressure change on a barometric pressure sensor embedded in the elastomer. With suitable calibration, the barometric pressure change can be converted to an accurate contact force measurement. Chuah and Kim [52] developed a fiberglass and elastomer composite structure on a series of pressure sensors as a ground contact foot sensor. Zillich and Feiten [53] used a foam core and rubber exterior as the interface between the contact surface and pressure sensor. Tenzer et al. [54] presented similar methods that require rubber directly cast onto barometric pressure sensors in an array. Although successful, all of the aforementioned investigations involve direct casting of rubber onto the sensor which fundamentally limits the achievable sensing characteristics. Further, these previous works relied solely on experimental calibration of the sensor (or sensor array) to determine its force sensing characteristics. The direct casting of rubber onto the

pressure sensor limits the force sensitivity and also raises concerns for sensor damage. By exposing the barometric sensor directly to the encapsulating elastomer — in particularly, by exposing the port where pressure changes are measured — it is possible to damage the MEMS electronics used within the sensor to measure pressure changes.

Table 1.1 summarizes the positive and negative attributes of sensors reviewed in this section as relevant to RLG contact sensing. Limitations in these sensors, as outlined in the table, identify a technology gap in regard to contact force sensing for RLG. A new sensor is necessary that has excellent analytic predictions, high sensitivity at low forces, and protection from high loads.

Table 1.1: Summary of ground contact sensors

Type	Sensor	Pros	Cons
Binary	Mechanical switch	Simplest design	Undesired bouncing/punching with closed loop control
Proximity	Infrared	Conform legs before contact	Binary feedback once in contact
	Conductive electrodes		
Force	Resistive film	Simple design and integration	Recalibrate often, not robust
	Load cell	COTS	Cost, sensitivity
	Elastomer cast magnet array	Tailored sensitivity	EMI interference, poor analytic predictions
	Elastomer cast on a pressure sensor	Simple design	Poor analytic predictions, poor sensitivity

Landing zone mapping and recognition

Landing zone identification and mapping sensors, which are well understood and readily available, will be required to conduct autonomous landings using RLG in the

future. Because of this, they are often recommended as a replacement to contact sensors. Another reason for this recommendation is the idea that landing zone mapping sensors enable the RLG to conform *prior* to landing. Advanced VTOL aircraft incorporate LiDAR as one example of surface mapping and autonomous landing zone recognition. They do so to aid pilots and flight software operating in degraded visual environments. Such systems provide a point cloud of objects detected by laser reflections. The point cloud is then input into identification algorithms that search for suitable landing zones [55]. An example of this is AACUS [15], which has a forward-facing LiDAR system. The detriment of these systems is their inability to determine what the landing surface is made of. This class of system requires some type of force or contact feedback signal to determine if the aircraft is landing on a solid or flexible, spongy surface. This is important as the landscape may change during landing if the surface is flexible and spongy. In combination with force sensors, LiDAR could be used to determine solid landing sites. Additionally, LiDAR-based mapping systems require hover time to create a point map of the landing surface. RLG must be available and ready to react to dynamic landing surfaces and at a moment's notice in emergency situations. In these situations, the aircraft may not have enough hover time to detect and identify the landing surface slope. For these reasons, LiDAR mapping technologies are not suitable as a sole replacement to ground contact sensors for RLG.

Synthetic aperture RADAR is another potential method of mapping landing surfaces. This concept requires the VTOL aircraft to fly around the landing zone so a map of surface objects and slope may be generated [56]. This is not practical for ship deck landings where the surface slope changes in real time. Similar to the LiDAR mapping sensors, RADAR is not a suitable replacement to RLG contact force sensing. LiDAR and RADAR mapping sensors may be well suited as a complement to ground contact sensors for autonomous landings in the future; however, there is a clear gap

in the available technologies for a robust, reliable foot-force sensor.

1.1.3 State Estimation and Control

Training simulations, sensor suites, and flight controllers have all been developed to reduce workload and maximize safety margins associated with rotorcraft landings on static and dynamic surfaces. Reber and Bernard developed a game-based learning, high-fidelity training simulation that removed the need for highly skilled instructor oversight [57]. Their research showed that trainees of their program operated with improved safety margins during normal and extreme helicopter operations on maritime vessels over a control group. This shows the importance of human factors and training. Xu et al. [58] and Saripalli et al. [59] approached the problem through a combination of sensor suites and control algorithm development to implement computer vision driven landing guidance. Using a reference object of known size, shape, and orientation on the landing surface, they showed basic results that IR and color spectrum imagery can be used to land on a moving platform. This body of research did not consider or attempt to verify operational capability during rough slopes or high Sea State conditions, limiting their practicality in the most challenging conditions. In terms of applied unmanned aircraft research, the aforementioned AACUS [15] represents the publicly released state of the art. Aurora's LiDAR ground mapping kit allows the aircraft to avoid obstacles and choose what it believes is a safe location to land. It has fundamental sensing limitations as described in 1.1.2. Numerous other researchers have approached the landing and approach problem through unique deep reinforcement learning [60], nature inspired controllers [61], or optimal control techniques to path plan and land on a moving platforms [62–64]. These research topics showed increases autonomy and personnel workload reduction during approach and landing. However, they do not focus on dynamic rollover prevention or botched landing impact mitigation during the landing event by maintaining a safe and stable

fuselage orientation. RLG address each of these concerns.

RLG is a unique field with respect to the control and state estimation requirements. The uniqueness of RLG exists because it is a research area situated between locomotive-legged robots and statically mounted robotic arms. Locomotive-legged robots have needs for complete position and orientation state estimation (POSE) and control using fused sensor feedback [65–67]. Sensors typically incorporated on legged robots include rangefinders (ultrasonic [68], laser [69], and infrared [70]), IMUs [71], and angle encoders.

Statically mounted robotic arms implement joint angle measurements with respect to their mounting base and some sensor interaction with the world at the end effector. Observers (state estimators) have been designed specifically for this use case [72]. RLG may seem more similar to robotic arms than locomotive-legged robots, but a complete and robust RLG system requires some aircraft position and orietation state estimates (POSE). Namely, aircraft roll and pitch are critical orientation estimates required by RLG that are neglected if RLG state estimation and control considerations focus on the hardware as a robotic arm with a fixed base. There could be a future of locomotive-legged robotic aircraft [73], but the practicality of such systems on weight-constrained airframes is limited [74]. Therefore, RLG generally requires reduced POSE compared to locomotive robots, but more sensor data and fusion than statically-mounted robotic arms in order to handle the challenges associated with high slope and dynamic landing surfaces.

Few researchers have considered the problem of control methods of RLG outside of the controllers flown on the Rotor Buzz and the design by Stolz. The research similar to the Rotor Buzz RLG system [8, 19] implemented contact feedback control using binary contact or proximity detection sensors. None of them used fuselage-orientation and foot-force feedback. The primary assumptions of the Rotor Buzz and similar works are 1) that the closed loop contact control will react faster than the

aircraft descends and 2) the relative descent rate between the aircraft and landing surface is constant. Both are idealizations of the problem that do not extend to real-world applications. The first assumption suggests that the legs will not cause a significant perturbation to the aircraft's roll or pitch throughout the landing. This assumption is acceptable for low descent rates while landing on static surfaces with *ideal* force sensors or orientation feedback, and high update rate control because the closed loop system will react faster than the aircraft descends. This is not a valid assumption during emergency, higher-speed landings, or on helicopters with unique landing gear configurations. The second assumption is true for static landing surfaces, but cannot be true for landings on dynamic platforms. Orientation and position of the landing surface results in variable velocity between the aircraft and landing surface. For this reason, the second assumption used on force feedback controlled landing gear is not valid for dynamic platform landings. The lack of closed loop roll and/or pitch feedback is a limitation of contact feedback RLG controllers. Kim and Costello [75] expanded on the original RLG research with a theoretical study on virtual model control for four-legged RLG landings on naval ship decks. Their simulations found that such a controller in conjunction with a four-legged, two-jointed system will absorb and conform to ship decks in rough seas up to Sea State 6. The virtual model controller presents multiple challenges on the practical application side, though. This stems from limited computational resources available on today's microcontrollers. No relevant literature was found where such a controller was implemented at high update rates on a consumer-grade micro-processor. This background review into possible state observers and controllers illustrates that, at present, an ideal solution for practical, robust, autonomous RLG operation on static and dynamic landing surfaces does not exist. Therefore, a technical gap exists in terms of sensor-fused state observation, real-time control with multiple fused sensor inputs from contact sensors and aircraft orientation channels.

1.2 Contributions of the Dissertation

The objective of this thesis is to generate technologies that will enable autonomous landings using RLG integrated on rotorcraft in the near future. The literature review illuminates technology gaps in the areas of mechanical and structural design; force sensing; and sensor-fused RLG state estimation, system health monitoring, and control. Figure 1.7 depicts technologies related to RLG and their approximate timeline of development. Previous technologies that drove progress for RLG were as recent as

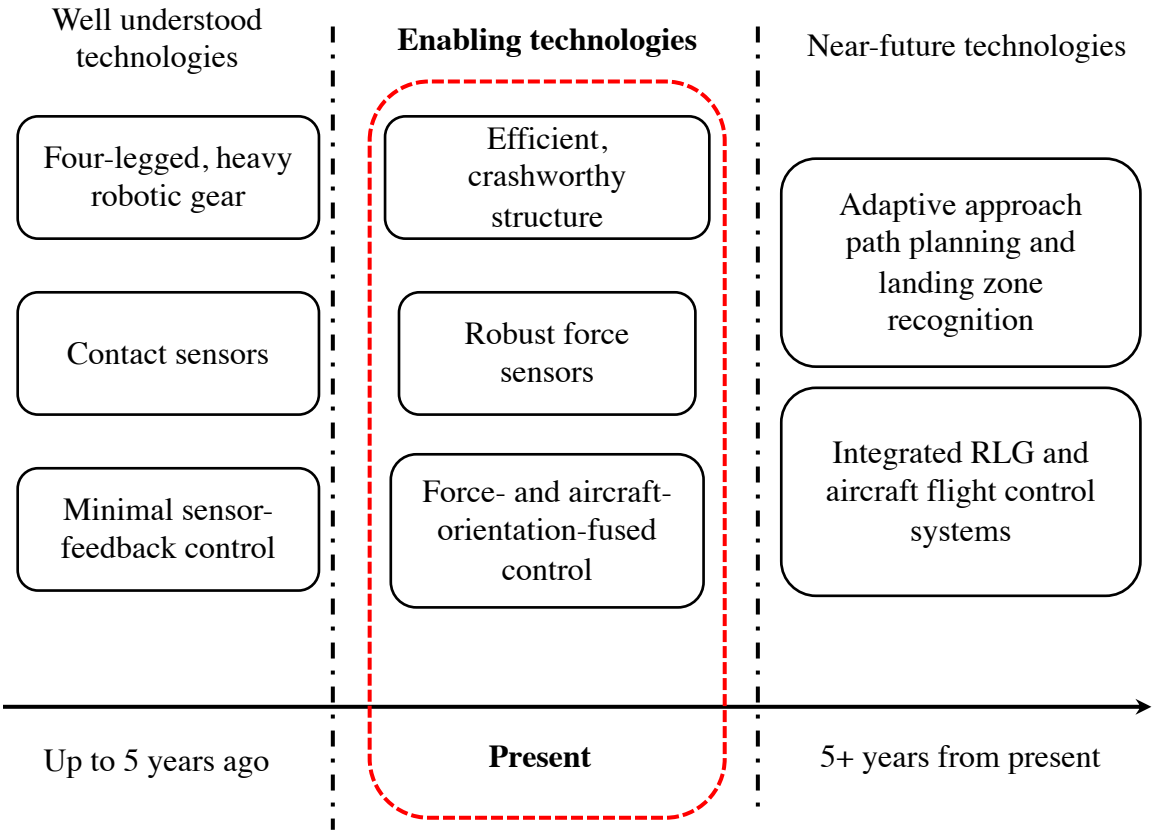

Figure 1.7: Diagram of technologies related to RLG development in the past, present, and 5+ years in the future.

five years ago based on the available literature. Looking to the future, technologies such as complete integration between RLG and aircraft flight systems are years away from proven usability. This dissertation presents three enabling technologies (boxed

in red) and complementary experimental tests on a commercial rotorcraft airframe. The presented technologies and experiments will show real-world practicality that support a path to future RLG technologies for autonomous landings. These technologies are transformative from previous RLG research because of their ability to increase autonomy, reliability, and applicability for rotorcraft RLG systems. The subsequent development and demonstration efforts summarize the specific contributions realized by this dissertation:

1. **Crashworthy, Cable-Driven, Four-Bar Linkage RLG:** Development of a novel RLG topology, structural design for crashworthiness, and actuation methodology.

2. **Low-Force, Large-Deformation Force Sensor:** Invention of a robust force sensor with high sensitivity at low applied force and the ability to withstand large impact forces during repeated landings.

3. **Discrete, Real-Time RLG Control:** Design of a robust, sensor-fused RLG controller that conforms the legs to static or dynamic surface without prior knowledge of the surface.

1.3 Dissertation Outline

This dissertation is composed of seven additional chapters which are described below:

- **Chapter 2: Four-Bar Linkage Mechanism RLG.** This chapter details composite, four-bar linkage mechanisms as a crashworthy, lightweight RLG structure. Various actuation methods and the design's kinematic range of motion under physical constraints are reviewed. The cable-driven design is detailed as the most viable RLG variant, and it is studied in more detail. An experimental airframe and full-scale test bed for the application of this new RLG structure

are presented as well. Lastly, a crashworthy design is iteratively constructed for flight-worthy operation.

- **Chapter 3: Low-Force, Large-Deformation Force Sensor.** This chapter details the invention of a novel force sensor made from an elastomer-encapsulated pressure sensor. A computer-aided-design procedure is outlined and a sensor is designed specifically for RLG purposes. Additional applications of the sensor are provided as well.

- **Chapter 4: Discrete, Real-Time, Sensor-Fused RLG Control.** In this chapter, a new RLG controller that fuses force feedback and aircraft orientation feedback is presented. A baseline force feedback controller is presented and used as a comparison in simulation and experiments of later chapters. This chapter also describes robust flight software components which integrate into the controller. Namely, these are hardware and software health monitors.

- **Chapter 5: Dynamic Simulation Tools.** Overviews of two simulation tools used as part of this work are described in this chapter. First, A set of subsystem physics models used throughout both simulation tools are detailed. Next, a landing surface simulator used to input surface motion data into the previous simulation tools is presented. The first dynamics simulator, which is used as a rapid design iteration tool, is based on planar Lagrange unconstrained equations of motion of a RLG system with a cable-driven, four-bar linkage RLG. The second is a multibody dynamics simulation that uses feedback linearization to stabilize joint constraints and resolve joint forces and moments between connected rigid bodies.

- **Chapter 6: Design and Integration with the S-100 Rotorcraft.** This chapter outlines the specific steps taken to integrate the cable-driven, four-bar mechanism, force sensor, and sensor-fused RLG control into the S-100 Cam-

copter commercial airframe. Sensors and state estimation algorithm implementations are presented. Dynamic rollover risk for the airframe is examined through Monte Carlo simulations. Finally, simulation iteration procedures for the design of the mechanical drivetrain are summarized.

- **Chapter 7: Simulation and Experiment Results.** The aim of this dissertation is to develop enabling technologies for real-world systems, so this chapter provides experimental test results of each technology. Since experiments cannot fully test the landing envelope and beyond, additional simulations are provided to cover the entire operational envelope.

- **Chapter 8: Conclusions and Future Work.** This chapter summarizes the conclusions of the dissertation and suggests future work based on the lessons learned throughout this research.

CHAPTER 2
FOUR-BAR LINKAGE MECHANISM ROBOTIC LANDING GEAR

The RLG in this dissertation makes use of a four-bar linkage mechanism as the landing gear structure. This chapter 1) outlines multiple four-bar link actuation strategies and the justification for the use of a cable-driven mechanism, 2) details the design of a RLG making use of two, four-bar mechanisms connected by a single cable, 3) examines the associated kinematics and potential performance of the landing gear in conforming to sloped grounds, 4) studies the expected loads on each component of the mechanism for static loading cases, and 5) presents the final design iteration used to generate a crashworthy structure. Contents of this chapter have been peer reviewed and published in [38, 76].

2.1 Actuation Strategies

Four possible actuation strategies were considered on four-bar linkage mechanisms as illustrated in Figure 2.1. Configuration 1 is a cable-driven actuation scheme with a passive spring-like element. This spring element is used to drive upward motion of the leg, thus retracting the leg toward the fuselage. A cable routing through the lower-left corner and terminating at the upper-right corner of the four-bar mechanism is used to counter the movement of the spring and lower the four-bar mechanism. Configuration 1 is not limited to the use of a torsional spring but can be thought of as any design in which the legs are retracted toward the fuselage by a passive spring-like element.

Configuration 2 is an extension of Configuration 1 with an added shock-absorbing component. The purpose of the shock absorber is to reduce high-impact loads and provide redundancy against cable failure. If the cable fails in this configuration, then the landing gear may still be load carrying through the shock absorber. Configuration

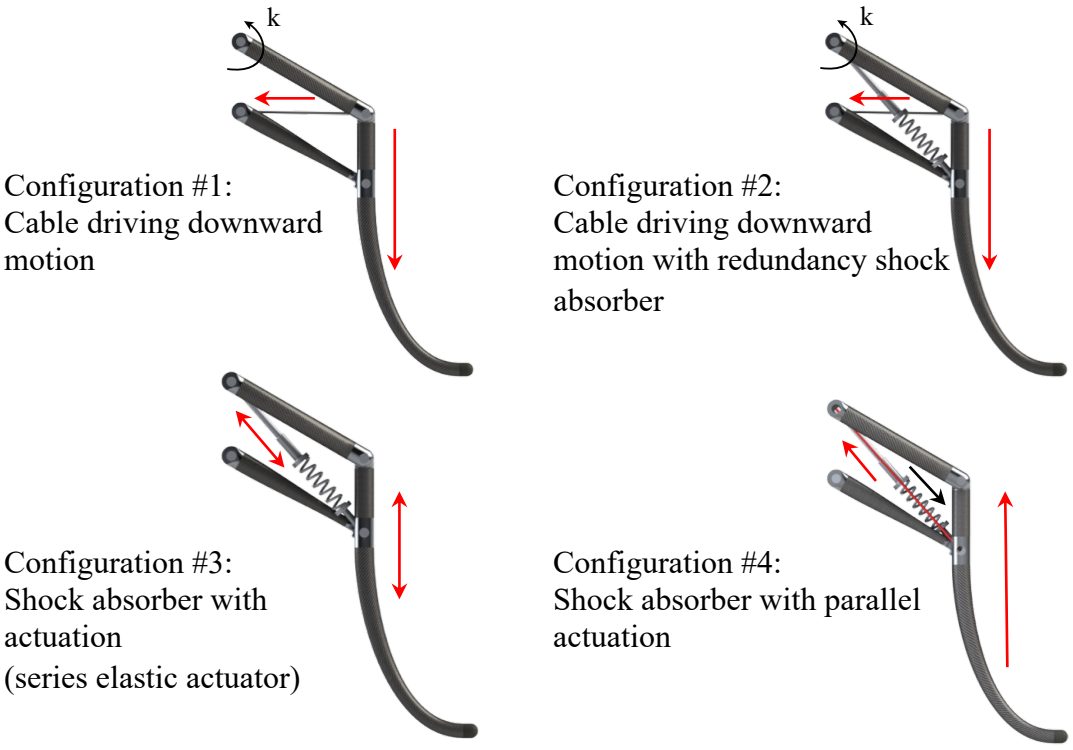

Figure 2.1: Four-bar linkage actuation configurations. Red arrows denote the direction of actuated motion. Black arrows denote the direction of passive motion.

3 uses a shock absorber with actuation, known as a series elastic actuator, along one diagonal to drive motion of the legs in either direction. This configuration is simple in that motion in both directions is controlled by a single actuator (i.e. no need for separate cable and spring element). However, one major drawback is that there is no clear way to couple the motion of two legs. Therefore, Configuration 3 will suffer from an inability to transfer and share loads from one leg to another. Finally, Configuration 4 is a cable-driven concept in which the cable is used to retract the legs upward into the fuselage while the passive element (spring/damper) is used to push the legs toward the ground; without cable tension, the legs will move to their fully lowered position.

The first characteristic used to compare these configurations is the maximum load applied to the structural components and the actuator. Figure 2.2 shows the static free-body diagram (FBD) for all configurations used to compute the structural and

actuation loads. In order to compare each concept, baseline dimensions and applied

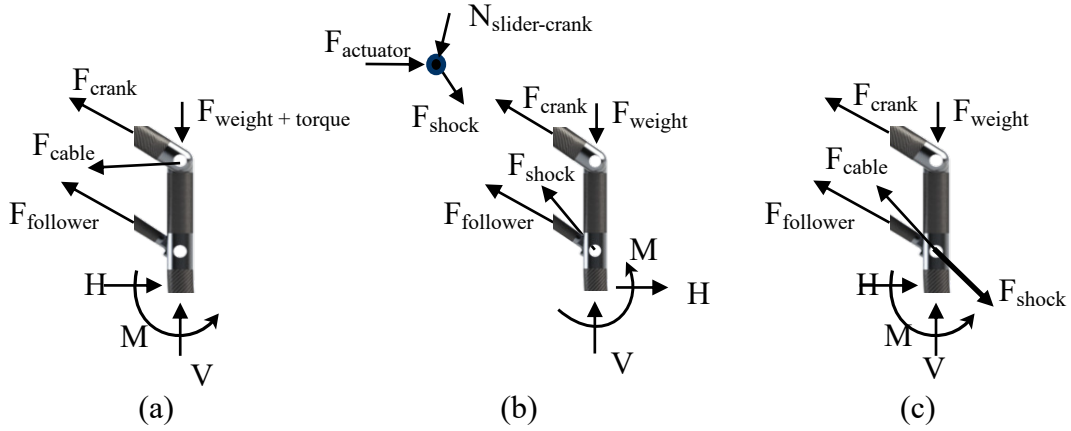

Figure 2.2: Static free body diagrams for (a) Configurations 1 and 2, (b) Configuration 3, and (c) Configuration 4.

loads were defined. For clarity, Figure 2.3 shows a schematic of the landing gear in 2.3(a) the *neutral* configuration, and 2.3(b) on a *sloped* configuration at a particular ground angle γ. All important dimensions are labeled and variable names can be found in the nomenclature description. Note the four-bar component names: crank, leg, and follower. These names will be used throughout this dissertation. The author

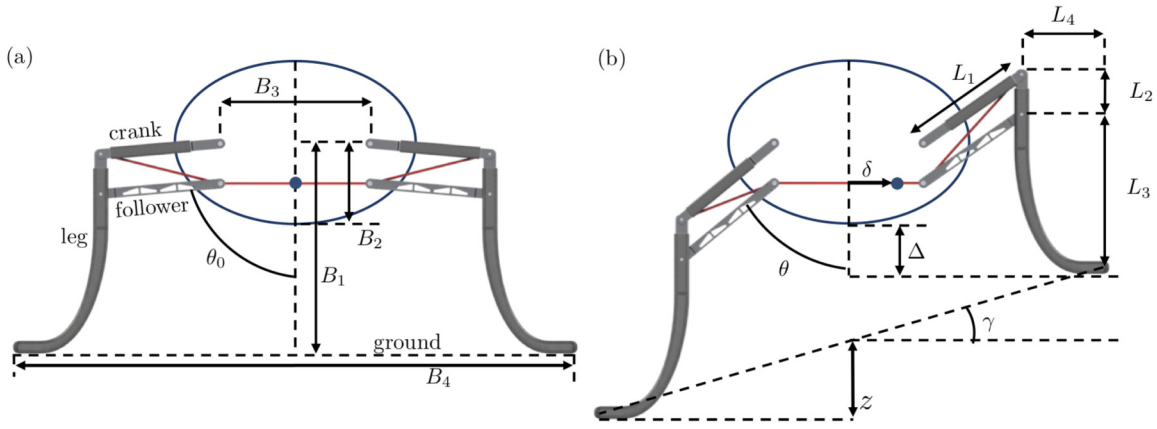

Figure 2.3: Schematic of the two legs. In (a), the *neutral* configuration and (b) the sloped configuration. In (b), the center of the cable has displaced an amount δ from the centerline causing a resulting ground angle, γ

assumes that the RLG foot may see vertical, V, and horizontal, H, forces, where the

horizontal forces would arrive from frictional loads due to contact with the ground. A representative vertical load, V, of 1962 N (400 lb) was chosen as the baseline for comparison. For the horizontal load, it is assumed that the friction load of the legs is $H = 0.3V$. Table 2.1 lists the physical dimensions used to compare each configuration. Also, if a configuration uses a shock absorber for impact purposes only, then that shock absorber has an assumed compression stroke of ≈5 cm (2 in).

Table 2.1: Four-bar linkage geometric baseline parameters

Parameter	Value
L_1	12" (0.305m)
L_2	4" (0.102m)
L_3	10" (0.254m)
L_4	4" (0.1016m)
B_3	15.5" (0.394m)
θ	[45° 130°]

Using all of the aforementioned information, the maximum static structural loads experienced by each configuration were computed. They are listed in Table 2.2. As

Table 2.2: Maximum loads computed for each four-bar linkage actuation configuration.

Configuration	Crank (lb, N)	Follower (lb, N)	Actuator/Cable (lb, N)
1	-1200, -5337	500, 2224	260, 1156
2	-1000, -4448	350, 1556	170, 756
3	-850, -3780	1300, 5782	-400, -1779
4	<-100, 444	1000, 4448	1000, 4448

previously stated, Configurations 1 and 2 have the same structural design, and it is assumed that the shock absorber does not apply any load unless there is a high velocity impact and the cable fails. However, in order to allow for the shock absorber to compress, the author limited the range of motion of a leg to a max ground angle of

18° in this study, this reduces the loads possibly seen in the static configurations since the range of motion of the leg is limited. This explains the load differences between Configurations 1 and 2 in Table 2.2.

Configuration 3 has a lower maximum load on the crank, but the reduced compressive load transfers to the follower and actuator. As expected, since Configuration 3 uses a series elastic actuator rather than a cable, the series elastic actuator is in compression. The range of motion for this concept would also have a similar restriction in order to allow the shock absorber to compress effectively during a hard landing.

Configuration 4 is attractive and considered because it provides the most redundancy. In the event of a cable failure, this RLG configuration will revert back to a traditional shock absorbing landing gear. Configuration 4 is essentially a traditional landing gear with a spring/damper. The motion is achieved by a cable which contracts the spring/damper moving the legs to a new configuration. During this motion, however, the cable is required to compress the spring/damper which is sized to carry the loads of the full helicopter frame. As shown in Table 2.2, this results in large actuator/cable loads for this configuration.

Multiple factors drove the final decision as to which configuration to implement. Configurations 1, 2, and 4 may each use a single cable connected through the fuselage, sharing load across the left/right leg assemblies. This allows the design to use a single, fuselage-housed actuator to drive both legs. Further, the force required to actuate is computed as the difference in forces seen by each cable.

Configuration 3 does not have this capability, so there must be independent actuators driving each leg. It was therefore not considered further as it did not provide sufficient structural benefits to outweigh this deficiency. Configuration 4 requires the largest actuation force due to the parallel shock absorber. This configuration has the most redundancy, but was not considered further due to its large actuation forces. Finally, Configuration 2 requires additional hardware to include a redundant

shock absorber that would result in a large weight increase. The weight penalty was seen as significant enough to exclude this configuration from further consideration. Therefore, the final actuation method chosen was Configuration 1.

2.2 Design

The chosen configuration for the cable-driven, four-bar link mechanism used in the remainder of this dissertation is schematically shown in Figure 2.4. It consists of a spring driving upwards motion of the legs, and a cable driving downwards motion of the legs. The schematic shows an extension spring spanning the top-left to bottom-right diagonal of the four-bar linkage which, when extended, would cause a retraction force making the legs move upwards. When the cable retracts (i.e. shortened), by pulling a length of it into the fuselage, the leg is driven downwards. It is important to note about this configuration that loads due to impact or landing with the ground are carried by the cable, rather than the spring. There are a number of possible ways to actuate a cable-driven, four-bar mechanism, including reversing the positioning of the passive element and the cable such that cable retraction induces an upward motion. Further, as will be explored in later designs of this work, one may also use a compression spring in parallel with the cable, connecting the lower-left and upper-right corner, to drive the upward motion of the system.

This type of mechanism has some unique advantages for the design of actuated robotic legs. The four-bar nature of the design reduces each mechanism to a single degree of freedom (DoF) system, which is denoted by θ in Figure 2.3. In turn, this reduces the number of drivetrain components required to actuate each leg. The cable-driven design allows the actuators to be placed within the fuselage, rather than at joints external to the body, which in turn minimizes the weight of the structural components. These benefits apply to a single-leg mechanism as described in Figure 2.4; however, there are some additional advantages when considering two, linked-leg mech-

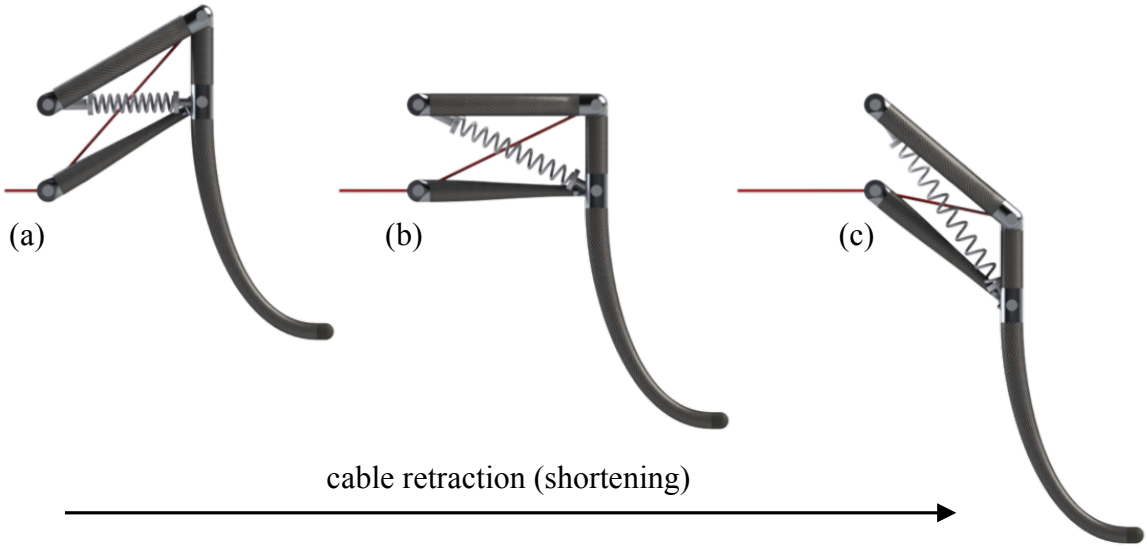

Figure 2.4: Example spring and cable configuration of a cable-driven, four-bar linkage mechanism.

anisms.

Figure 2.5 illustrates two, four-bar linkages joined on a single fuselage (denoted by the blue circle), with *a single cable connecting the two mechanisms*. Sharing a single cable between the two-leg mechanisms has some unique actuation as well as structural benefits. From an actuation perspective, by coupling the cable of the two legs, it is now possible to couple the motion of the two legs. Consider, as shown in Figure 2.5(b), a system with two legs wherein the cables connect on a center spool denoted by a blue dot. The system achieves symmetric leg motion — where both legs move together either upwards or downwards — by changing the overall length of the cable, see Figure 2.5(b) to (a) and vice-versa. This can be achieved, for example, by shortening the overall length of the cable by wrapping it around a spool. The mechanism achieves differential leg motion — where one leg moves up and the other moves down — by changing the "center" of the cable without changing its overall length, see Figure 2.5(b) to (c) and vice-versa. For example, this is achievable by translation of the spool within the fuselage.

The two-leg design with a shared cable provides some unique benefits in terms of

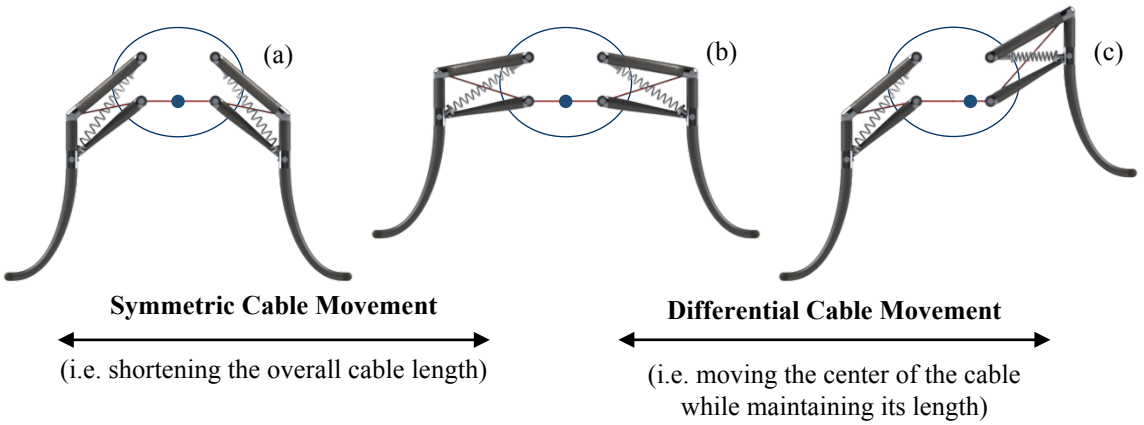

Figure 2.5: Schematic illustrating a two-leg, shared-cable system using cable-driven, four-bar linkage mechanisms.

actuation and the forces required for actuation. One may use a different type/size actuator for the symmetric leg movement (i.e. shortening/lengthening the cable) and for the differential leg movement (i.e. motion of the spool). This is particularly interesting in the design of RLG since one might be more interested in a rapid differential leg movement, to conform with a sloped ground upon landing, but have more lenient requirements for symmetric leg movement. With this particular design one can optimize for these two types of movements independently. Of course, one can still achieve movement of a single leg while the other is stationary through a combined motion of the symmetric and differential degrees of freedom.

The final benefit of this design is the failsafe condition. The cable may snap during a crash, absorbing a large amount of energy, or by accident from mid-air impacts. If any event severs the cable, then the passive, spring force retracts each leg to the full-up position. At this full-up position, a mechanical stop comprised of the gas spring and interference between the crank-leg and follower-leg joints maintains the mininum intended ground clearance, Δ. The remaining landing loads must be absorbed by this mechanical stop. This design ensures the aircraft maintains a safe ground clearance and rotor clearance from the landing surface.

An experimental prototype realizing the aforementioned structure and actuation

strategy was developed to explore the four-bar linkage configuration. This prototype had two functions. First, to show the feasibility of the four-bar linkage actuation method. Second, to test possible control logic and sensors for future integration into a 100-180 kg (220-400 lb) rotorcraft. A schematic of the prototype actuation system is shown in Figure 2.6(a), while the prototype platform, highlighting the symmetric motion drive system and the differential motion system, is shown in Figure 2.6(b).

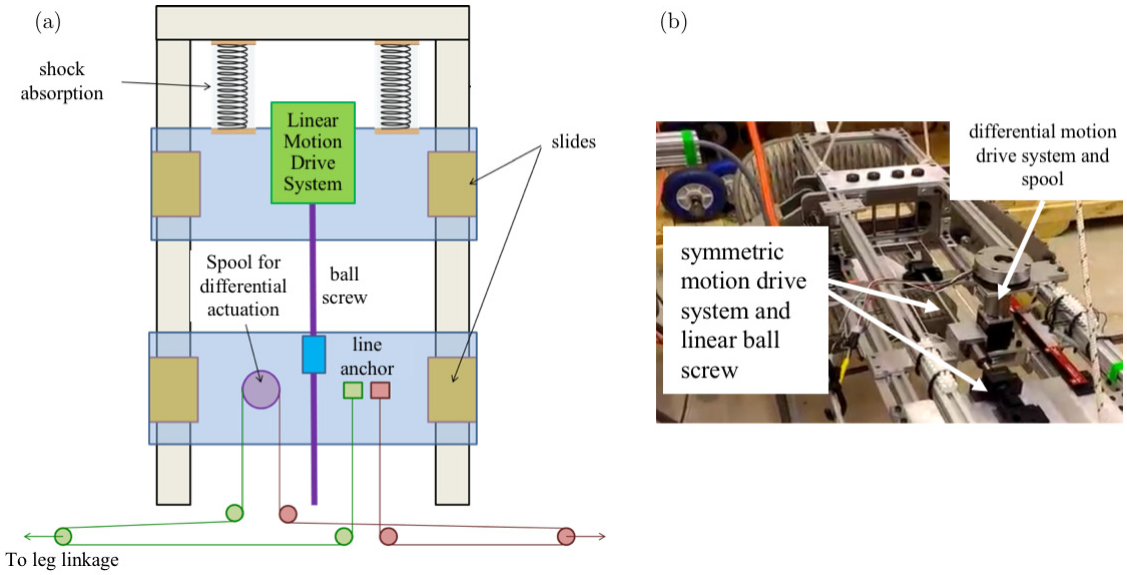

Figure 2.6: (a) Schematic of the cable-driven, four-bar linkage prototype drive system. (b) Photograph of the prototype's two drive systems.

In this design, the differential motion is achieved by rotating a spool. The spool is mounted on a moving carriage from where cables route to both legs and then route back and terminate on the carriage. While the platform is stationary, motion of the spool results in lengthening of the cable for one leg and shortening the cable for the other leg, which in turn results in differential leg motion. The carriage carrying the spool is mounted on linear slides and actuated through a linear ball screw. With the spool stationary, motion of the carriage results in both cables being lengthened or shortened in unison, thus resulting in a symmetric leg motion. In this particular design, the platform housing the drive system for the linear motion ball screw was also

mounted on slides and grounded to the prototype through shock absorbing elements. This has the added benefit that impact loads on the system are mitigated through a shock absorbing mechanism housed inside the fuselage. Lastly, this prototype uses tension springs in an orientation that pulls the legs upward (i.e. retracts toward the fuselage).

Figures 2.7(a) to (b) shows symmetric leg motion achieved through the linear actuator where the carriage containing the cable spool moves, effectively lengthening or shortening the driving cable for both legs in unison. Figures 2.7(b) to (c) illustrate the differential motion achieved by rotation of the cable spool. While these figures show symmetric and differential motion separately, the system is capable of a combination of symmetric and asymmetric motion simultaneously.

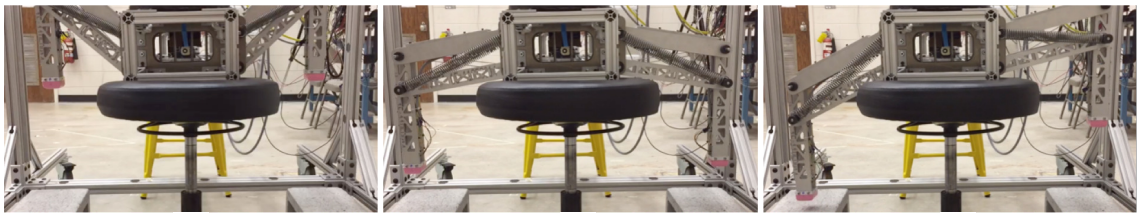

(a) (b) (c)

Figure 2.7: (a) to (b) Contain images showing symmetric leg motion driven by linear actuation. (b) to (c) Show images of differential leg motion driven by rotary actuation.

The prototype also provides a test bed to test all sensors, actuators, cable routing methods, and control algorithms that are necessary for future integration into a desired rotorcraft airframe. There are AMT203 rotary angle encoders at each crank-frame joint, on the linear ball screw, and on the spool joint of the prototype. Additionally, there is a Zettlex linear distance encoder attached to the linear ball screw. These encoders provide the feedback necessary to drive both legs to a known symmetric and asymmetric leg angle defined by

$$\theta_{sym} = \frac{\theta_L + \theta_R}{2}, \quad \text{and} \quad \theta_{asym} = \frac{\theta_L - \theta_R}{2}. \tag{2.1}$$

A 100 W brushless direct current (DC) motor connected to a Power-Off electromagnetic brake and gearbox drive each degree of freedom.

Figures 2.8(a) and (b) show performance plots of the leg-angle feedback control using a proportional-integral-derivative (PID) controller on both control channels. In this article, the left and right leg angles are defined in Figures 2.3(a) and (b), wherein these angles are measured between a vertical line and the crank or follower components of the four-bar mechanism. The prototype designed here uses an 80° symmetric neutral angle leg angle, θ_0, with a maximum angle of 133° and a minimum of 45° due to physical impact of the four-bar linkage on itself. This range of motion allows this prototype to conform to a sloped ground with an angle of up to 28°. The asymmetric motion achieves a maximum rate of $27°/s$ while the symmetric channel achieves $53°/s$. These promising results showed that a cable-driven, four-bar linkage is a viable RLG

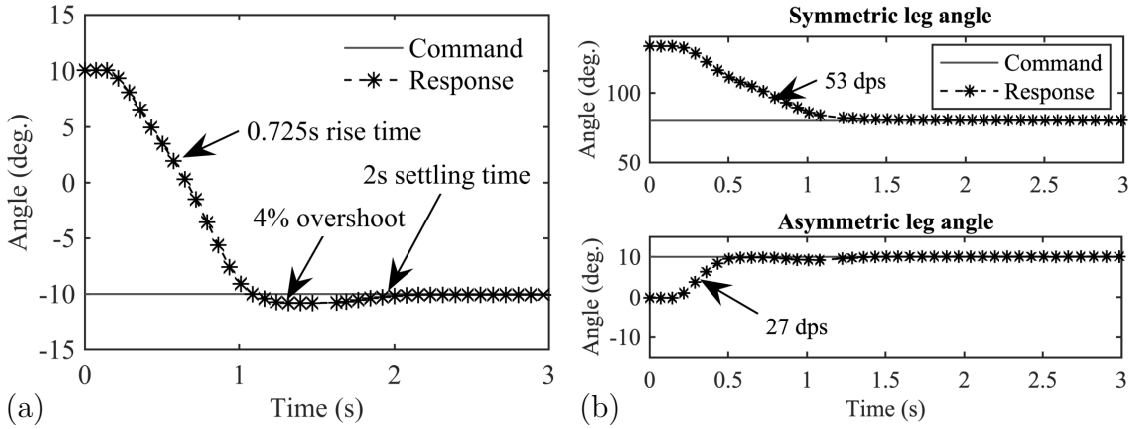

Figure 2.8: Angle measurements of the small-scale prototype RLG system for (a) PID asymmetric leg control response given a step input, and (b) simultaneous symmetric and asymmetric PID leg control responses given step inputs.

configuration to reduce the number of actuators and actuator weights compared to two-jointed leg designs. The number of actuators reduces from four to two per pair of legs. These actuators can be easily positioned within the body/fuselage of interest and reduce the size and weight of the leg components. In addition, actuation components can be shielded from foreign objects and debris. Finally, this design can achieve a

similar range of motion to that achieved by the two-joint configurations of traditional robotic arms or legs.

The next section presents a kinematics study of this configuration in detail to understand how sizing of the system affects its performance with the particular goal of conforming to a sloped ground. Under normal sloped surface landings, rotorcraft approach with their roll axis parallel to the slope and complete the landing one skid/leg at at time [1]. This negates the need for symmetric motion in the majority of landings. Hence, there are weight and volumetric savings from the implementation of asymmetric motion only. Therefore, the remainder of this dissertation restricts the design to *a RLG system with a single DOF that results in an asymmetric motion of the landing gear.* That is, the gear will have only one DOF which results in one leg retracting and the other leg extending by moving the cable connecting the two cable-driven, four-bar link mechanisms without changing its length.

2.2.1 Kinematics

Kinematic trade-studies of the system help to understand how the geometry of the system will affect the ability of the landing gear to conform to sloped ground. Previously, Figure 2.3 showed a schematic of the landing gear in (a) the *neutral* configuration, and (b) on a sloped angle. All important dimensions are labeled and variable names can be found in the nomenclature description. This study and subsequent sections *focus only on the differential leg movement* induced by a motion of the center of the cable as shown schematically going from Figure 2.3(a) to (b). It is important to note that designs considered here have the distance of the mounting points for the four-bar linkage to the ground, B_1 and B_2 in Figure 2.3(a), as fixed values. Hence, variation of the the neutral leg angle θ_0, and the dimensions L_1 and L_2, are not independent of the final vertical dimension L_3.

In this study, there are three possible parameters which can limit the motion of

the system:

$$\begin{aligned} &\text{either leg reaches a maximum leg angle, } \theta = \theta_{\max}, \\ &\text{either leg reaches a minimum leg angle, } \theta = \theta_{\min}, \\ &\text{the fuselage ground clearance reaches a minimum value, } \Delta = \Delta_{\min}. \end{aligned} \tag{2.2}$$

The neutral configuration, defined by the leg angle θ_0, see Figure 2.3(a), plays an important role in the kinematics of the system and which of the three limiting conditions given in Equation (2.2) is reached first. This behavior is illustrated in Figure 2.9 where three neutral angles are considered as (a) $\theta_0 = 70°$, (b) $\theta_0 = 85°$, and (c) $\theta_0 = 100°$. Note that in each case, as mentioned in the previous paragraph, the distance from the fuselage to the ground in the neutral configuration is fixed. Hence, for each design having a different θ_0, there exists a different value of L_3, the height of the leg. In all of the results shown in this section, the study relies on the following parameters:

$$\begin{aligned} &\theta_{\max} = 135°, \quad \theta_{\min} = 45°, \quad \Delta_{\min} = 5\,\text{in } (0.127\,\text{m}), \\ &L_1 = 12\,\text{in } (0.305\,\text{m}), \quad L_2 = 4\,\text{in } (0.102\,\text{m}), \quad L_4 = 4\,\text{in } (0.102\,\text{m}), \\ &B_1 = 21\,\text{in } (0.533\,\text{m}), \quad B_2 = 8\,\text{in } (0.204\,\text{m}), \quad B_3 = 15\,\text{in } (0.381\,\text{m}). \end{aligned} \tag{2.3}$$

For each design shown in Figures 2.9(a), (b), and (c) the movement of the legs is generated by a displacement of the center of the cable by an amount δ until one of the three limiting conditions in (2.2) is reached. Figure 2.9(g) shows the ground angle, γ, as a function of the differential movement of the center of the cable, δ, for the three designs studied. For the case of $\theta_0 = 70°$, the system first reaches the limit whereby the left leg reaches the minimum allowable angle $\theta = \theta_{\min}$, Figure 2.9(d). This occurs at a ground angle of $\gamma \approx 12°$. For the case of $\theta_0 = 85°$, neither leg reaches the envelope of allowable leg angles; however, the upward moving leg reaches the minimum allowed clearance from the fuselage $\Delta = \Delta_{\min}$, Figure 2.9(e), and this

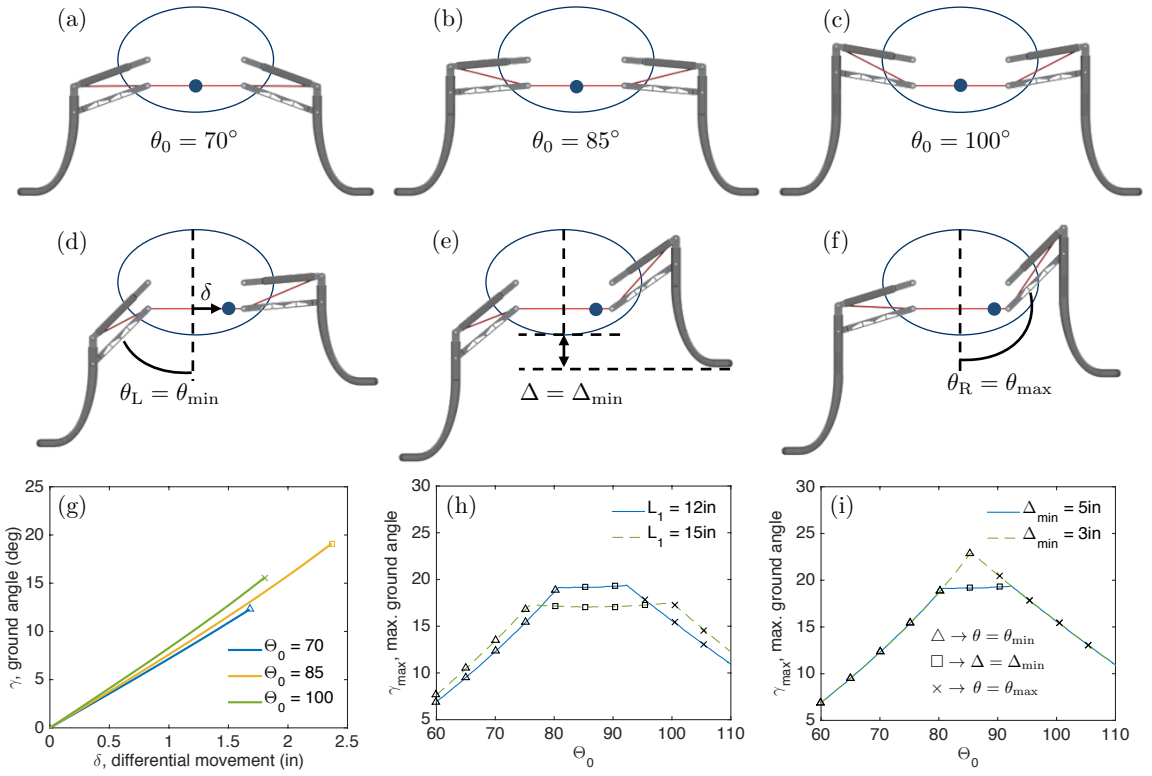

Figure 2.9: Kinematics of the two leg system. (a)-(c) Shows a design with varying neutral angle θ_0 and (d)-(e) show the corresponding mechanisms limiting motion. (g) shows ground angle γ as a function of the displacement, δ, of the cable. (h) and (i) show the maximum achievable ground angle, γ_{max}, as a function of neutral leg angle, θ_0, for varying L_1 and Δ_{min}.

occurs at a ground angle of $\gamma \approx 19°$. Finally, for the case of $\theta_0 = 100°$ the right leg reaches the maximum allowable angle $\theta = \theta_{max}$, Figure 2.9(f), at a ground angle of $\gamma \approx 15°$. These results highlight the importance of choosing a geometry, in particular a neutral angle θ_0 and the leg dimension L_2, to optimize the maximum possible ground angle, γ_{max}, which a particular geometry can achieve under the restrictions given in Equation (2.2). Other quantities such as B_1, B_2, B_3, and L_2 are also important and can affect the maximum achievable ground angle, γ_{max}. The quantities related to the vehicle geometry, B_1, B_2, and B_3, are usually fixed and treated as such in this study. Similarly, the quantity L_2 is limited to a narrow range so as to fit within the envelope of the fuselage; therefore, no design studies involving variations of L_2 are shown.

Figure 2.9 (h) shows the maximum achievable ground angle, $\gamma_{\max}$, as a function of the neutral leg angle, θ_0, for designs with $L_1 = 12\,\text{in}$ (solid blue line) and $L_2 = 15\,\text{in}$ (dashed green line). In each line, the marker denotes the limiting condition with the $\triangle$ marker denoting $\theta = \theta_{\min}$; the square marker denoting $\Delta = \Delta_{\min}$, and the $\times$ marker denoting $\theta = \theta_{\max}$. For both lines ($L_1 = 12\,\text{in}$ or $L_1 = 15\,\text{in}$), at low values of θ_0 the system is limited by $\theta = \theta_{\min}$ and $\gamma_{\max}$ increases with θ_0. At some point as θ_0 increases, the system becomes limited by $\Delta = \Delta_{\min}$ and $\gamma_{\max}$ plateaus, where changes in θ_0 have no significant effect on $\gamma_{\max}$. Finally, at a large enough θ_0 the system becomes limited by $\theta = \theta_{\max}$, and at this point, $\gamma_{\max}$ begins to decrease with increasing values of θ_0.

The author notes that in Figure 2.9(h) that the maximum value of $\gamma_{\max}$ as a function of θ_0 occurs in the plateau where the system is limited by $\Delta = \Delta_{\min}$ and that the lower leg length of $L_1 = 12\,\text{in}$ improves the maximum achievable ground angle. This suggests that the minimum clearance to the fuselage $\Delta_{\min}$ is also an important parameter in determining $\gamma_{\max}$. To illustrate this, Figure 2.9(i) shows $\gamma_{\max}$ as a function of θ_0 for a design with $\Delta_{\min} = 5\,\text{in}$ (solid blue line) and for a design with $\Delta_{\min} = 3\,\text{in}$ (dashed green line), both for $L_1 = 12\,\text{in}$. As shown, decreasing $\Delta_{\min}$ makes the plateau disappear entirely, and the maximum achievable ground angle increases from $\gamma_{\max} \approx 19^\circ$ to $\gamma_{\max} \approx 23^\circ$. Finally, it is noteworthy from Figure 2.9(g) that it only takes a small displacement of the center of the cable, on the order of 2.5 in to generate the leg movement required for the landing gear to conform to a ground slope of $\gamma \approx 19^\circ$.

2.2.2 Static Loads

The two-leg mechanism presented also has some unique benefits in terms of how loads are distributed across the structure and onto the actuator. Presented here is a simple static analysis based on static force balances across the structure. Consider the FBD

on the geometry shown in Figure 2.10(a), where the weight, W, of the vehicle is balanced by two vertical loads V_1 and V_2 which are computed from a sum of force and moments about the center of the fuselage. The moment arms for V_1 and V_2 with respect to the center of the fuselage vary slightly as γ changes, and this is accounted for in all calculations. Also shown in Figures 2.10(a) and (b) is a torque, T, presumed to be acting on the upper attachment point of the four-bar link of either leg. This torque accounts for the spring-like elastic element required to drive the legs upward (see Figure 2.4). T does not enter into the FBD of Figure 2.10(a) but is included there for clarity. T is computed from the FBD shown in Figure 2.10(b) at a leg angle of $\theta = 90^\circ$ and is meant to balance the weight of the three main components at $3.5\,g$ where g is the Earth's gravitational acceleration. The torque is presumed strong enough such that $3.5\,g$ vertical maneuver would not result in downward movement of the legs.

With V_1, V_2, and T determined from the FBDs shown in Figures 2.10(a) and (b), use the FBD shown in Figure 2.10(c) to determine the force on the crank F_{crank}, the force on the cable F_{cable} and the force on the follower F_{follower} for any given leg angle θ (or for a corresponding ground angle, γ). Note that in Figure 2.10(c) the effect of T and the weight of the components (at $1\,g$) is accounted for through a simple vertical load acting as shown. In Figure 2.10(c), the moment $M = L_4 \cdot V$ and the horizontal contact force H can be added to account for potential horizontal contact forces due to lateral landing velocities or frictional forces.

All of the results shown in this section use the following parameters along with the parameters shown in Equation (2.3):

$$
\begin{aligned}
&m = 400\,\text{lb}\ (181\ \text{kg}),\\
&m_{\text{crank}} = 3.3\,\text{lb}\ (1.5\ \text{kg}),\quad m_{\text{follower}} = 1.1\,\text{lb}\ (0.5\ \text{kg}),\quad m_{\text{leg}} = 5.5\,\text{lb}\ (2.5\ \text{kg}),\\
&g = 32.17\,\text{ft/s}^2\ (9.81\ \text{m/s}^2),\quad \theta_0 = 80^\circ,\quad L_1 = 12\,\text{in}\ (0.305\ \text{m}).
\end{aligned}
\tag{2.4}
$$

First, consider the case where there are no lateral contact forces ($H = 0$) for both the left and right legs. These results are shown in Figures 2.10(d) through (f). Figure 2.10(d) and (e) show the loads on the cable, crank, and follower for the left and right legs respectively both as a function of γ. Note that the cable is always in tension and carries loads on the order of 800 lb (3560 N). In the two-leg, cable-driven, four-bar linkage design, the force experienced by the central actuator is the difference in loads seen by the right and left leg cables as defined by Equation (2.5). Figure 2.10(f) shows the force that would be required by a single actuator to maintain

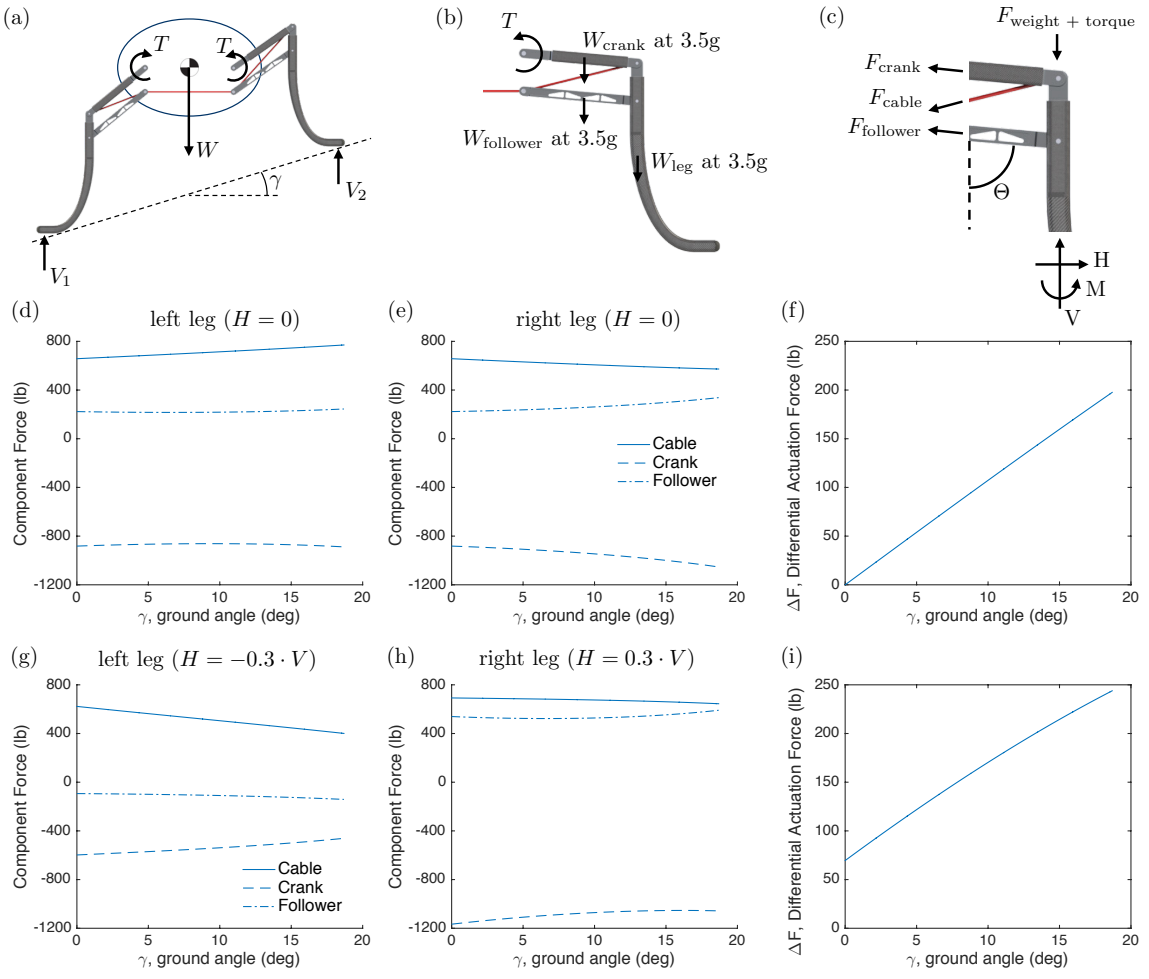

Figure 2.10: (a) through (c) Show FBDs used to determine in (a) V_1 and V_2, in (b) T, and in (c) F_{crank}, F_{cable}, and F_{follower}. (d) through (f) Show results for $H = 0$ for both legs and (g) through (f) show results for $H = -0.3$ for the left leg and $H = 0.3V$ for the right leg.

the current position of the legs. This is referred to as the differential actuation force, and it is computed as

$$\Delta F = F_{\text{cable}}^{\text{right}} - F_{\text{cable}}^{\text{left}}. \tag{2.5}$$

As shown in Figure 2.10(f), the differential actuation force is significantly lower than the loads seen independently by either cable and in this particular analysis ranges from zero to 250 lb (1110 N). In contrast, for a design with independent actuators controlling the length of the cable for a given leg, those actuators would have to be sized to hold the full cable loads which are approximately 800 lb (3560 N). In fact, when the vehicle is sitting on level ground, it is clear that there is no net load on the actuator since the force from the left and right leg cables cancel each other out.

Second, consider the case where there are lateral contact forces on both the left and right legs. In particular for the left leg, $H = -0.3 \cdot V$ (with the horizontal force pushing into the fuselage), and for the right leg $H = 0.3 \cdot V$ (with the horizontal force pushing away from the fuselage). This mimics frictional forces at an angle of roughly 16°. The resulting loads on the cable, crank, and follower are shown in Figure 2.10(g) for the left leg and (h) for the right leg. Note, from a comparison between Figure 2.10(d) and (g), the horizontal forces change the loads for the crank and follower of the left leg. The follower is now in compression (whereas it had been in tension before), and the load on the crank is lower. The loads on the cable are of similar magnitude as before; however, there is now a larger difference between the cable loads experienced by the left and right leg due to horizontal contact forces. This manifests itself clearly in Figure 2.10(i), which shows the differential actuation force ΔF. In contrast to Figure 2.10(f), ΔF is non-zero even at $\gamma = 0$, and it is generally higher.

In addition to the horizontal forces experienced by the feet due to friction from landing on a sloped surface, there is the potential for loads to arise due to horizontal motion of the legs even on a flat surface. The legs are not constrained to only move

vertically, and during motion of the four-bar link mechanism, they laterally translate horizontally up to 2 in. During this motion, the legs undergo lateral translation (and possibly sliding) and apply lateral loads on the fuselage. These forces are presumed small during landing on an obstacle or sloped terrain as little motion occurs once both legs are in contact, but this assumption cannot be made when the RLG is operated with both legs on the ground such as during rotorcraft leveling fuselage roll on ship decks. If the full weight of the aircraft is on the legs and they undergo motion, then the aircraft sees net lateral loads at the crank and follower mount points as presented in Figure 2.11. This is computed as the net lateral component of force applied to the fuselage from the left and right cranks and followers due to frictional sliding of the feet. The maximum value of this net lateral load is 40 lb (177 N), illustrating that the use of the cable-driven, four-bar mechanism inherently applies a small but non-negligible lateral load to the airframe. Therefore, the fuselage mount points and structure must be able to withstand these lateral loads and any dynamic motions that may ensue, such as sliding or yawing.

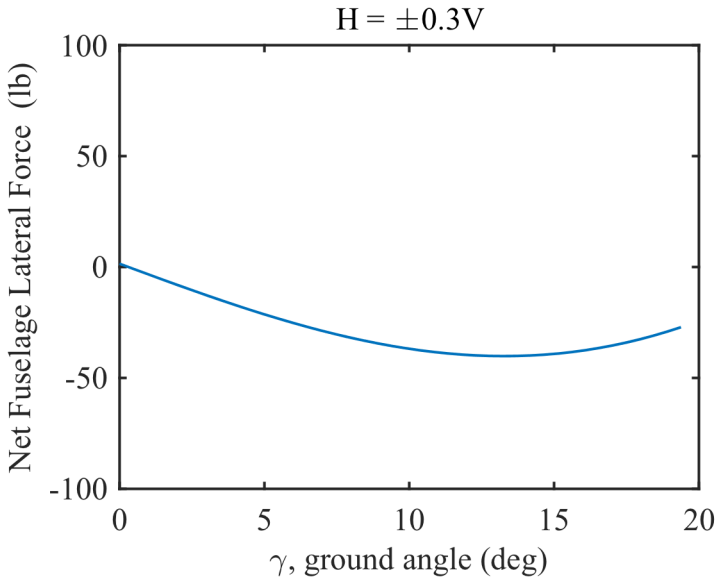

Figure 2.11: A plot of lateral forces on the fuselage inherent from the cable-driven, four-bar linkage mechanism with $H = 0.3V$ for the right leg and $H = -0.3V$ for the left leg.

2.3 Crashworthiness

One of the key novelties of this work is the development of a workflow which enables the rapid design, manufacture, and drop tests of RLG systems based on the cable-driven, four-bar mechanisms with the desire to verify crashworthiness. A particular benefit of this workflow for RLG is the decoupling of rigid body dynamic simulations (Step 2 in Figure 2.12) and structural finite element analysis (Step 3 in Figure 2.12). Since RLG are inherently active, the multibody dynamic simulations, in addition to being used in this particular workflow for generating landing loads, also serves two additional functions. First, they are used to iterate over a number of RLG designs to arrive at the basic topology. Second, they can be used to simulate active landings where the gear conforms to the landing surface. In these active landing scenarios, the simulation tool provides feedback both on performance of the control law as well as on the requirements for the actuators. This will be discussed in more detail in Chapters 5 and 6.

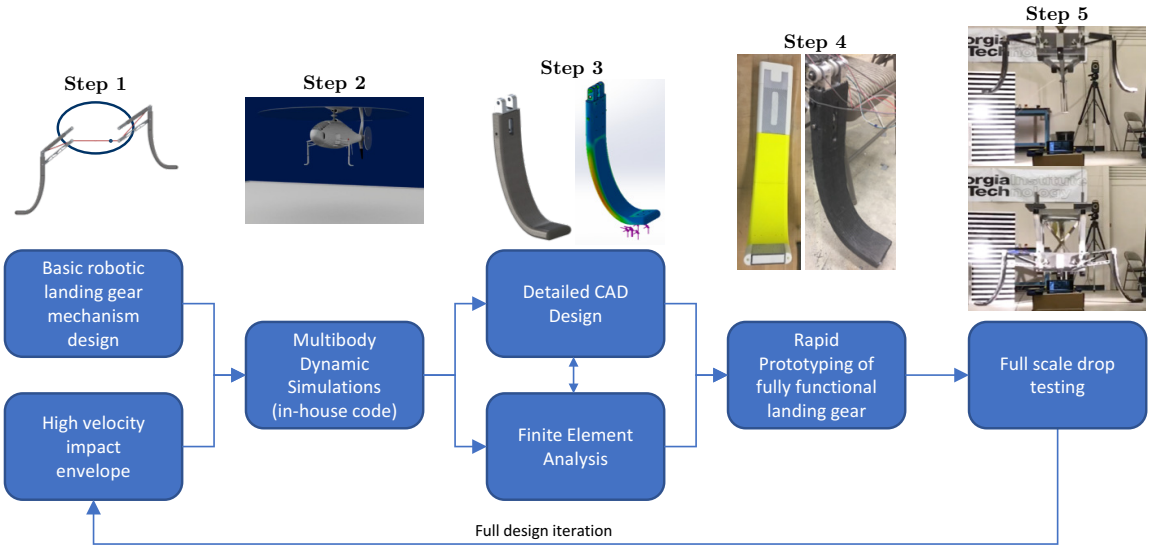

Figure 2.12: Design, manufacturing, and testing workflow for the rapid development of RLG.

This workflow is designed with a survivability target, as measured by drop testing,

as one of the main performance parameters to achieve. The target drop test parameters were an impact velocity of 5 m/s with a drop weight in the range of 370 to 440 lb (168 to 200 kg). As detailed in this section, a frame was built onto which the RLG system is attached and drop tested. A successful drop test is characterized as a drop test in which *the frame does not impact the ground*; however, damage is allowed — and designed for — in the RLG structure.

This section begins by summarizing the design, manufacturing, and testing workflow which is shown schematically in Figure 2.12 and consists of the following five steps:

Step 1. A design iteration begins with the basic geometry of the RLG mechanism as discussed in detail in Section 2.2 as well as an envelope of high velocity impact conditions which the system will be subjected to. The impact conditions considered in this dissertation are: i) 5 m/s impact velocity with level fuselage, ii) 5 m/s impact velocity with 5° pitch, and iii) 5 m/s impact velocity with 5° pitch and 5° roll. These are similar in style, but more lenient than MIL-STD-1290A for human-rated rotorcraft impact survivability.

Step 2. The geometry and impact conditions are fed into a multibody dynamic simulation tool which simulates the impact condition and produces the resultant forces on each of the system components. A brief description of this simulation process is given in Sect. 2.3.1 below.

Step 3. The forces produced by the dynamic simulations are then imported and appropriately smeared onto a detailed finite element model of each of the system components. For example, Figure 2.12 shows a finite element calculation for the leg component with loads predicted by the multibody dynamic simulation tool. Within Step 3, iterations between the detailed CAD design and its corresponding finite element analysis occur until the design converges on the desired

structural behavior under the loads produces from Step 2.

Step 4. Based on the detailed CAD design from the previous step, manufacture of a fully-functional RLG system proceeds. This step involves traditional manufacturing processes, such as subtractive metal machining, as well as a series of rapid additive manufacturing (3D printing) processes aimed at minimizing the time required to produce a system for testing.

Step 5. In the final step, the manufactured robotic landing system is drop tested on a full-scale drop test platform which can achieve the desired impact conditions outlined in Step 1. Details of the experimental drop test setup are given in Sect. 2.3.2. Based on the observed outcomes of the experimental drop test, design modifications are suggested which are then fed back into the workflow outlined here for a new design iteration. If the design modification involves a change to the geometry, then the workflow starts again at Step 1. However, if the geometry is unchanged and the design modification involves a change to the detailed mechanical design, the workflow for the new design iteration returns to Step 3.

The author would like to highlight that using the workflow described above, a full design iteration — from a new basic geometry to full-scale drop testing — may be performed in approximately *two weeks*.

2.3.1 Simulations Tool Interactions

The rigid body dynamics simulation tool used as part of the design workflow is presented with more detail in Chapter 5. For this section, it suffices to summarize the process as follows: the rotorcraft and landing gear system are modeled as a connected set of N rigid bodies with M connection joints. Each rigid body is first treated as an isolated body with its own six degrees of freedom. The constraint forces and mo-

ments, arising from the M connection joints, are treated as externally applied forces and moments to each body undergoing structural design.

As shown in Figure 2.13, for each of the impact scenarios of interest, a multibody dynamic simulation of the impact was performed. This produces, for each of the rigid

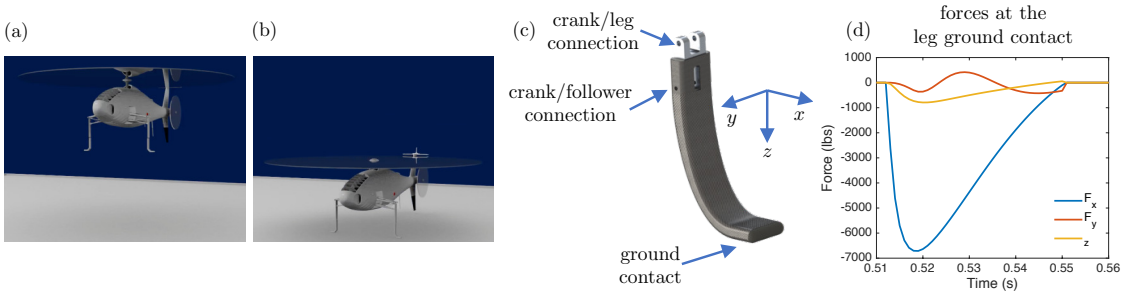

Figure 2.13: Example process for producing loads from the multibody dynamic simulations. A particular simulated event as shown in (a) and (b) produces loads at a given component connection as illustrated through (c) and (d).

bodies in the system, a set of forces and moments for each of the connections of a body. For example, Figure 2.13(c) shows the leg which has three points at which forces and moments can be applied: the crank/leg connection, the crank/follower connection, and the ground contact. For each of these points, there is a time history of forces and/or moments generated due to the impact, with the ground contact forces for this example shown in Figure 2.13(d). These time histories for each of the components of the robotic landing system are then transferred to a finite element simulation used for the detailed structural sizing of each component. Although Figure 2.13(a) through (d) shows the simulation rendered on a detailed geometry for illustration purposes, the only information the simulation uses for each rigid body is the location of the connection points and its mass and moment of inertia properties. There is no accounting for the detailed geometry in the rigid body dynamic simulation step of the design process.

Once the multibody simulations are completed, Step 3 proceeds where iteration between CAD design and FEA analysis occurs to arrive at the mechanical design of

a RLG sized to survive the required impacts. This process is fairly standard and the commercially available software packages Solidworks for CAD design and Abaqus for FEA analysis were used. Since this process is recognized as standard (a similar process was used by Manivannan et al. [8]); detailed results are not presented here.

2.3.2 Experimental Drop Test Setup

The final step in the design, manufacturing, and testing workflow outlined in Figure 2.12 is the full-scale drop testing. To perform full-size drop tests, the author designed and manufactured a drop test rig shown in CAD in Figure 2.14(a). The structure is designed to mimic the weight and CG of a rotorcraft in the approximately 400 lb (180 kg) category, and it is manufactured from steel tubing and has an empty weight of 180 lb (82 kg). As shown in Figure 2.14(c), there are four, forward-facing mounting holes for the two sets of cable-driven, four-bar link leg mechanisms, a platform in the forward top surface where weights can be added to vary the overall drop weight and center of gravity (CG) of the rig, and a rear mounting hole for a tail leg. Figure 2.14(b) shows a front view of the drop test rig with the robotic landing system loaded to 440 lb (200 kg). Although the weight and weight distribution of a potential UAV in this general size and weight category may be matched using this test frame, the structural frame of a UAV where a RLG system is mounted would be significantly less stiff than the steel frame utilized here. As such, the loads experienced by the RLG in these experiments are likely to be higher than those experienced in actual flight testing; therefore, this experiment provides a conservative estimate of the survivability of a given design.

The drop test rig is suspended by three cables, red arrows in Figure 2.14(a), the length which is variable to maintain the fuselage at the desired pitch and roll angle. To facilitate this, each cable has a turnbuckle for fine adjustments. The cables terminate on a three-ring release mechanism is attached to a pulley suspended from a gantry.

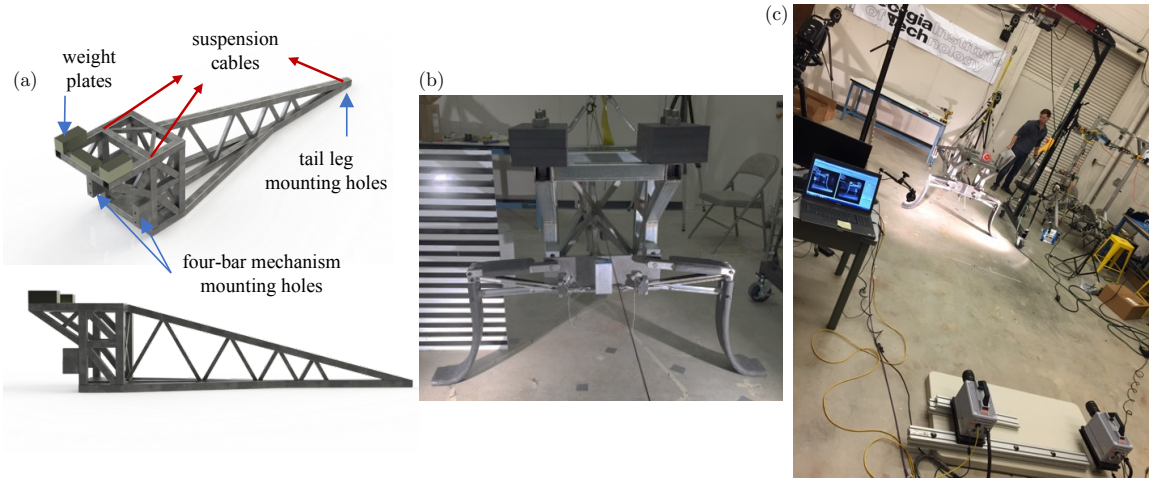

Figure 2.14: Experimental drop test setup. (a) Shows the CAD design of the steel drop test frame. (b) Shows the drop test frame with cable-driven leg system installed. (c) Illustrates the experimental setup with two, high-speed cameras.

In this configuration, the drop test rig can be suspended in the air at a height of up to 50 inches, see Figure 2.14(c).

Each drop test was instrumented with two, high-speed cameras as shown in Figure 2.14(c). Each camera was set to record at 2000 frames per second and aimed at one set of the two robotic landing legs. For some drop tests, the crank component was instrumented with strain gauges as shown in Figure 2.15 and recorded data at 2000 Hz with a Vishay 7000 data acquisition module. Shunt calibration was used, and the strain gauges were zeroed when the drop test rig was suspended prior to drop testing. The metallic arm connecting the crank to the interface plate was instrumented with three strain gauges aligned in the direction of the crank. Two gauges were placed on the top and bottom surfaces of the crank and a third was placed on the side, see Figure 2.15(a). It's assumed that during impact the crank is under a state of compression and bending (about the $z-$axis) as shown in Figure 2.15(c). Under this assumption, the strains at the three gauges can be converted onto a reaction force and moment that would be experienced by the crank at the crank/drop test rig connection through

the simple relations

$$F_x = E_{\text{Al}} \left(\frac{\epsilon_{\text{top}} + \epsilon_{\text{bottom}}}{2} \right) A,$$
$$M_z = E_{\text{Al}} \left(\epsilon_{\text{side}} - \frac{\epsilon_{\text{top}} + \epsilon_{\text{bottom}}}{2} \right) \frac{2I_{zz}}{h}, \tag{2.6}$$

where E_{Al} is the Young's modulus of 7075 aluminum, A is the cross-sectional area, I_{zz} is the moment of inertia, and h is the thickness. These measurements are particularly useful as the experimental values of F_x and M_x, as calculated through (2.6), may be directly compared to the values predicted from the multibody dynamic simulation discussed above. Such comparison will be shown in Section 2.3.3.

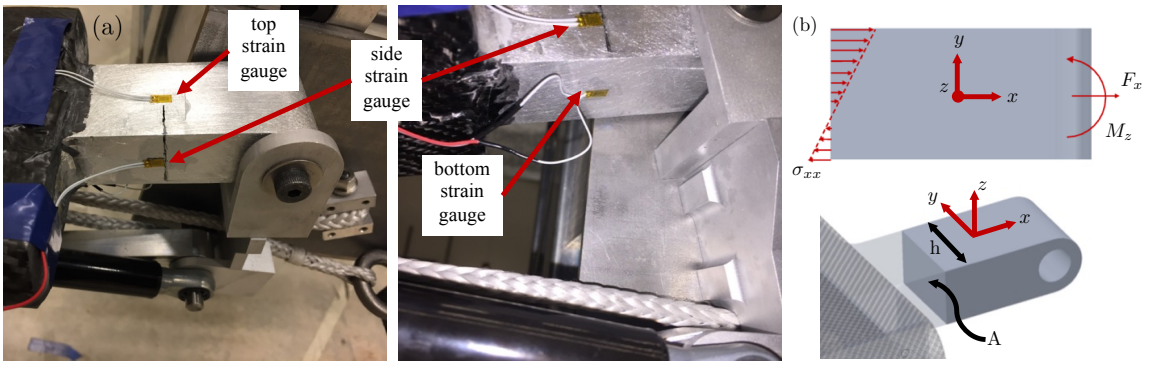

Figure 2.15: (a) Views of the top, side, and bottom strain gauges mounted on the crank arm near the crank/frame connection. (b) Illustrates the assumed state of stress in the crank arm which maps contact force F_x and bending moment M_z to the measured strains.

2.3.3 Final Design Iteration

This section presents the final design iteration that met the impact survivability requirements. It was the fourth iteration of the workflow illustrated in Figure 2.12. The three previous iterations and their drop test results may be found in Appendix A.

The final design iteration is shown in Figure 2.16. The crank and leg are manufactured using a rapid manufacturing method that may be found in [38]. This process used ABS printed core sections that connect metal hardpoints. Then, carbon-fiber

reinforced polymers (CFRP) undergo a wet layup and heat-cure procedure on the combine ABS-metal structure. The different layers of the leg are visible in Figure 2.17, where the white components are ABS, silver components are aluminum, and black components are CFRP.

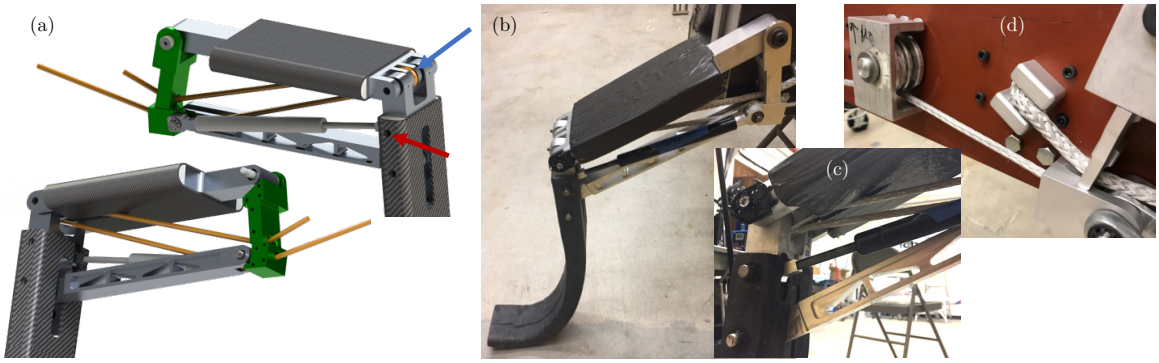

Figure 2.16: Final design iteration CAD and physical implementation. (a) shows the CAD model, (b) shows the right leg assembly view from the front, (c) shows the right leg assembly where the cable routing is visible, and (d) shows the internal cable routing within the "fuselage."

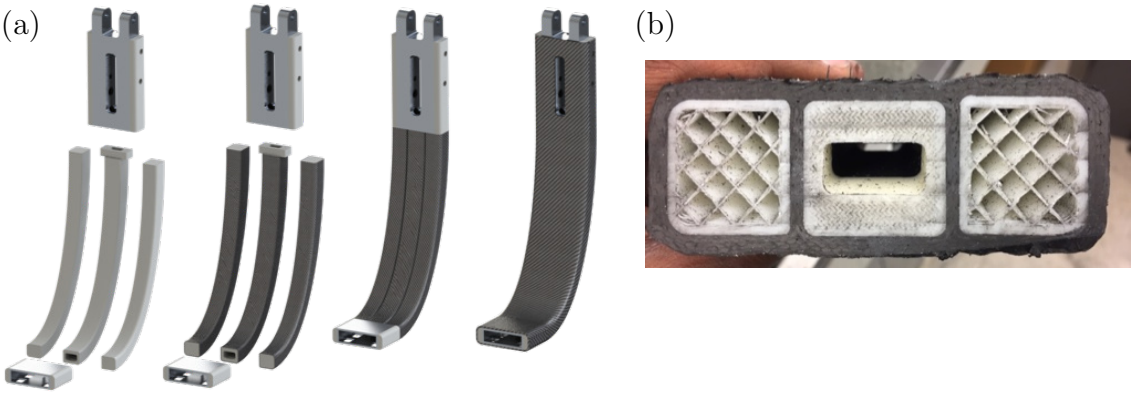

Figure 2.17: Specialized leg design of the final iteration, where multiple ABS cores in (a) are used to manufacture the CFRP leg resulting in the ribbed cross-section shown in (b).

A gas spring is used in this design to provide the retraction force required by the chosen cable-driven configuration. The cable is a 6 mm diameter heat-treated dyneema rope (also known as high modulus polyethylene) that is designed specifically to be stronger than steel cables, and have an extended lifespan in marine environments

compared to metal cables. It has a rated tensile strength of 55,000 N (12,385 lb), and the cable is also coated to mitigate UV degradation [77, 78]. This cable was chosen for its smaller diameter for the same tensile strength compared to metal cables, and its current widespread use in maritime environments. It feeds from the spool to each half of the design through smooth guides on the green plate to the crank-leg joint where it doubles back into the fuselage to a shock absorber. The design of the leg was specialized in this iteration based on previous design iteration failures. This specialization includes CFRP ribs running the full length of the leg connecting two metal hard points. In the new design, shown in Figure 2.17(a), the manufacturing process uses three internal ABS cores, each of which is covered with its own carbon fiber sleeve before being assembled into an internal core which is then covered with additional, larger diameter CFRP sleeves. This results in a cross section as shown in Figure 2.17(b), which has significant impact strength. Such a unique design has minimal financial and time cost, and it would not be possible without the use of 3D-printed ABS tooling.

Multiple drop tests were conducted with this design iteration to verify crashworthiness. The first drop test was performed at a weight of 370 lb (168 kg) and a drop height of 50 in (1.27 m). This equates to an impact velocity of roughly 5 m/s, and an impact energy of roughly 2000 J which is the target drop weight and velocity. As shown in Figure 2.18, the RLG incurs damage but the drop test *is successful* because the fuselage never touches ground and the minimum ground clearance is sustained.

As shown in Figure 2.18(c), the system incurs damage on the cables for both leg assemblies simultaneously at crank/leg pin joints. This causes the legs to move to their fully retracted fail-safe position, where the gear is still load bearing. The second drop test was performed at the same weight and drop height conditions — 370 lb (168 kg) and 50 in (1.27 m) — however, the fuselage was suspended with a 5° pitch and a 5° roll (in this case the height is measured from the higher of the two legs). This

condition is worse than the level condition as the fuselage will pivot, first about the tail leg and then about the right leg, inducing higher velocities on the left leg which impacts last.

Figure 2.19 (a) shows the moment when the tail makes first contact, highlighting both the pitch and roll angles, (b) the moment when the right leg makes first contact, and (c) the moment when the left leg makes first contact. Figure 2.19(d) shows the maximum deflection incurred by the robotic landing system before any damage. Figure 2.19(e) shows the gear sustain damage. In this particular test, it takes the form of delamination of the metal hard point of the crank at crank/leg interface, causing the metal hard point to be compressed into the crank. Once the hard point is compressed into the crank, the leg comes into contact with the CFRP of the crank resulting in no further damage. Again, although the RLG sustained damage, this is a *successful* drop test as the frame did not impact the ground; the vehicle carrying the RLG would not have incurred any damage.

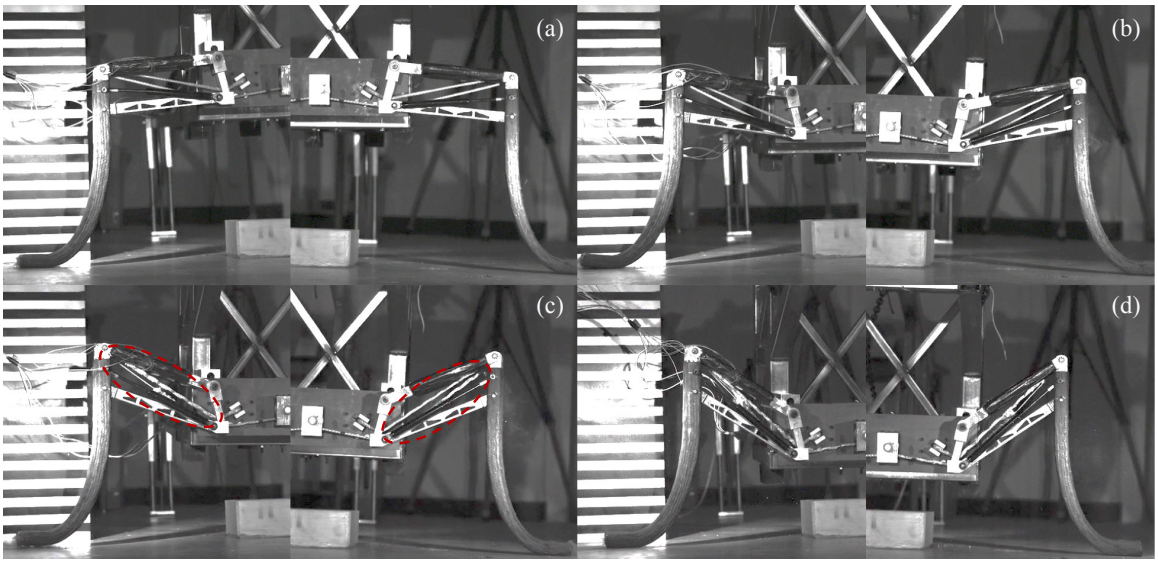

Figure 2.18: Final design iteration drop test at 50 in (1.27 m) and 370 lb (168 kg) ($\approx$ impact velocity of 5 m/s and impact energy of 2000 J). (a) Shows the moment moment of first contact. (b) Shows the point of maximum loading. (c) Shows failure of the right and left leg cable at the crank/leg joint. (d) Shows the legs in their fully retracted position.

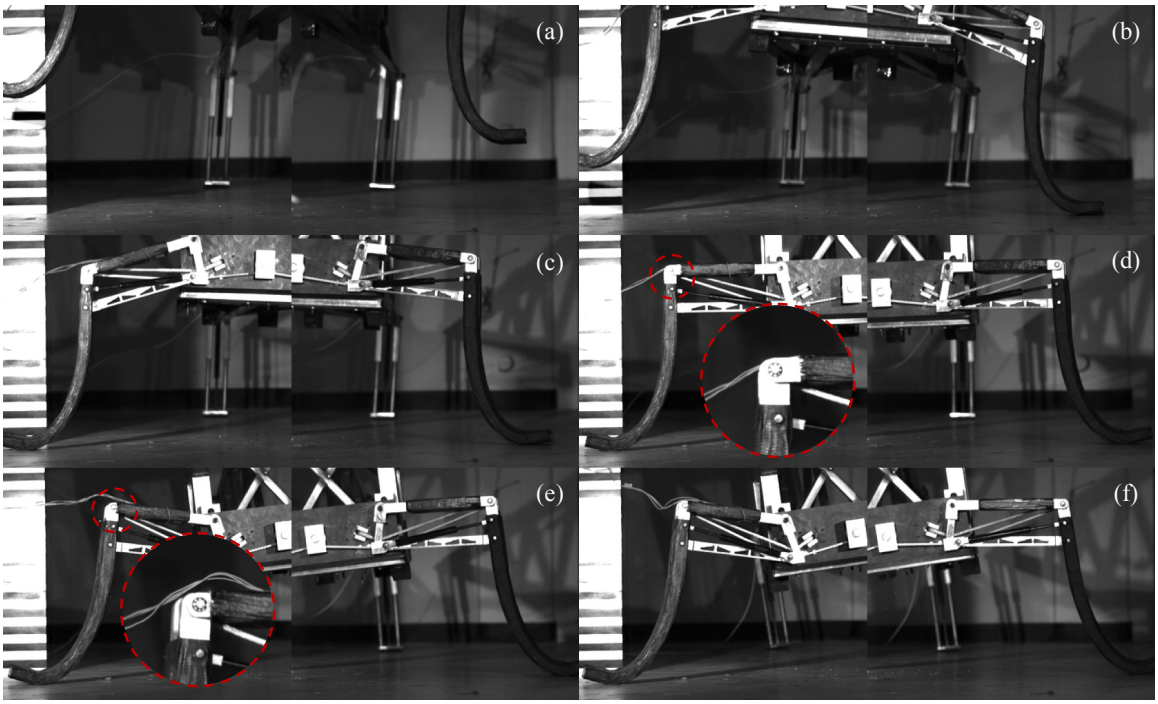

Figure 2.19: Fourth design iteration drop test at 50 in (1.27 m) and 370 lb (168 kg) with 5° pitch and 5° roll. Sequence of images show the crank sustaining damage and retraction of the RLG to its fail-safe, fully-retracted position.

Experimentally measured loads and comparison to simulated results

This section presents the experimentally measured loads at the crank/drop test rig connection as recorded through the strain gauges and analysis described in Section 2.3.2. Load measurements presented are for the drop tests shown in Figures 2.18-2.19. The particular component of force being measured and simulated is the F_x component as described in Figure 2.15(b). The experimentally measured loads are compared to simulated crank/drop test rig interface loads as computed using the multibody dynamic simulation introduced in Section 2.3.1.

The comparison is presented to validate the portion of the workflow making use of the dynamic multibody simulation loads in the subsequent finite element modeling used for sizing components. The results are shown in Figure 2.20 wherein both cases, the orange line is the experimentally measured load at the crank/drop test joint, and the blue line is its simulated counterpart. Overall, there is good agreement between

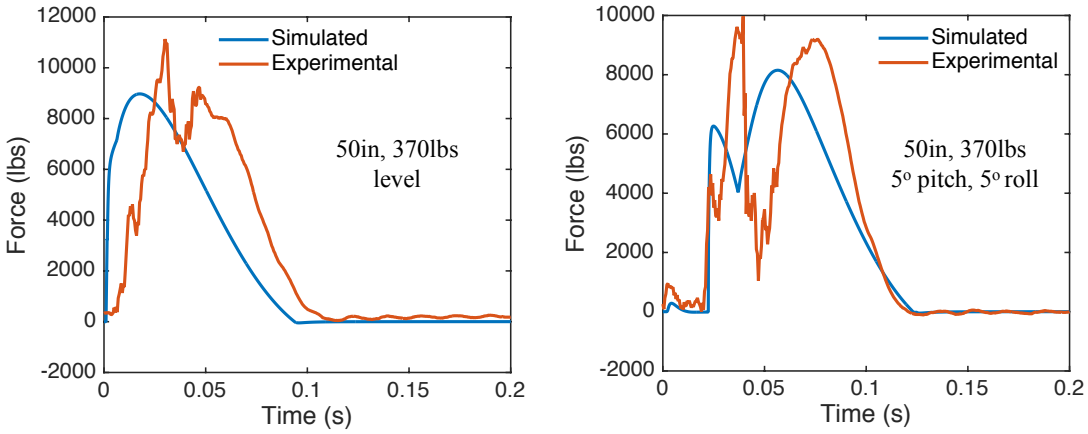

Figure 2.20: Experimentally measured and simulated F_x component of the force at the crank/drop test rig interface joint (see Figure 2.15 for force orientation).

the simulated and experimentally measured force, particularly in the magnitude of forces experienced in all cases. For the final design iteration drop at 5° pitch and 5° roll, the simulation also recovers the double-peak nature of the impact force which arises from the slanted impact and bounce. The experimental data for some of the drop tests has a significant amount of noise, even though the sampling rate is sufficient at 2000 Hz for the impact duration times measured and estimated here. It is possible that there could have been some adhesion issues or delamination between the strain gauges and crank, but the overall agreement in force magnitude and impulse between simulation and experimental systems indicates the simulation tool is valid for future design iterations without experimentation.

CHAPTER 3
LOW-FORCE, LARGE-DEFORMATION FORCE SENSOR

The relevant literature presented in Chapter 1 showed that a multitude of force sensing options exist. Each of the presented sensors were unable to meet the needs specific to RLG, though. Resistive films sensors were simple, but unable to withstand repeated use without calibration or replacement. Load cells are widely used in robotics, but they are expensive, not sensitive enough in the low force range when designed to withstand impact, and they require inertial compensation. Pressure sensors with over-molded elastomers were the most promising candidates; however, they did not offer enough sensitivity when designed to withstand the full weight of the rotorcraft upon impact. These findings led to the novel force sensor engineered in this chapter. This force sensor is an elastomer-encapsulated pressure sensor with an engineered air cavity that provides tunable sensitivity a low forces, while avoiding damage to the pressure sensor under high loads because it deforms into a structural housing. A key novelty of this sensor is the ability to rapidly design it through finite element analysis (FEA) for custom applications. This chapter presents the sensor concept, FEA-enabled design, experimental validation of the design tools, and applications for RLG and sensing arrays. Contents of this contribution have been peer reviewed and published by León et al. [79].

3.1 Sensor Concept

The force sensor contributed is illustrated conceptually in Figure 3.1. The concept consists of a MEMS absolute barometric pressure sensor, an engineered elastomer adhered to that MEMS pressure sensor, and a protective structural housing. The engineered elastomer has a cavity designed into the structure that creates an air pocket

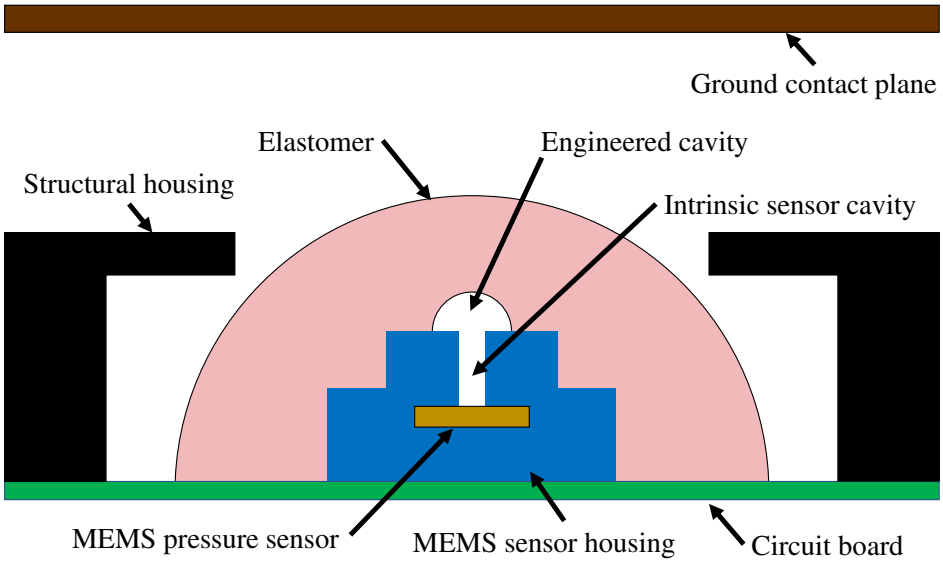

Figure 3.1: Force sensor design concept.

between the elastomer and pressure sensor. By design, if the elastomer undergoes deformation by the ground contact surface/plane, the air cavity deforms reducing the total cavity volume and increasing the pressure within the cavity. Therefore, by controlling the mechanical behavior of the elastomer (i.e. its geometry and mechanical properties), as well as the air cavity geometry, it is possible to fine tune the transducer characteristics of the sensor. Further, the sensor is designed such that a portion of the elastomer protrudes from a structural housing. Under load, from ground contact for example, the elastomer will deform until the loading surface contacts the structural housing at which point the housing itself will take up the load. This design allows the force sensor to have high sensitivity at small loads, when the elastomer is being deformed, while still being able to withstand very large loads where the structural housing acts as the load-bearing structure. The use of an elastomer-based sensor — which incurs large deformation at small loads — enables this manner of design where the sensor is shielded from large loads by deforming into a structural housing.

The air cavity interfacing the elastomer and MEMS pressure sensor is composed of two volumes. The first volume is defined by the engineered elastomer, and it is

denoted as the engineered cavity, $V_{0,\mathrm{e}}$. The second volume is inherent to the particular MEMS sensor chosen, and it is referred to here as the intrinsic sensor volume, $V_{0,\mathrm{s}}$. The intrinsic sensor volume is a measurable feature of any commercial sensor while the engineered cavity is a controllable geometric feature. During practical operation, the elastomer structure, and therefore the engineered air cavity, deforms under load. This generates an increase in air pressure until the engineered volume is completely filled and the pressure remains constant.

The sensor has initial pressure and volume, P_0 and $V_0 = V_{0,\mathrm{e}} + V_{0,\mathrm{s}}$, and deformed pressure and volume, P_d and $V_d = V_{\mathrm{e}} + V_{0,\mathrm{s}}$, wherein writing V_d, it is assumed that during deformation only the engineered air cavity volume V_{e} changes. The pressure changes may be related to the volume changes to find the normalized pressure, $\tilde{P} = P_d/P_0$, through

$$\tilde{P} = \frac{P_d}{P_0} = \frac{V_0}{V_d} = \frac{V_{0,\mathrm{e}} + V_{0,\mathrm{s}}}{V_{\mathrm{e}} + V_{0,\mathrm{s}}}, \tag{3.1}$$

where, for simplicity, the air is treated as an ideal gas at a constant temperature. In the case of a completely collapsed engineered air cavity, that is $V_{\mathrm{e}} = 0$, (3.1) reduces to the theoretical maximum normalized pressure, $\tilde{P}_{max}$, as

$$\tilde{P}_{max} = \frac{P_{d,\mathrm{max}}}{P_0} = 1 + \frac{V_{0,\mathrm{e}}}{V_{0,\mathrm{s}}}. \tag{3.2}$$

This relation assumes that, under peak loading, the elastomer will not penetrate the intrinsic sensor air cavity such that $V_{0,\mathrm{s}}$ remains unchanged.

Equation (3.2) serves as a simple but useful design guideline as it may be used to compute the maximum allowable engineered volume to prevent sensor damage from occurring due to overpressure. That is, for a given sensor with a maximum operating pressure (and known sensor volume $V_{0,\mathrm{s}}$), one may engineer the elastomer such that the MEMS maximum operating pressure is never exceeded. This behavior will be demonstrated experimentally in Section 3.2. The sensitivity of the force sensor — its

contact force versus measured pressure characteristics — requires understanding of the mechanical behavior of the elastomer itself and is discussed in the next section.

3.2 Numerical Modeling and Experimental Characterization

This section presents a finite element model (FEM) of the sensor to explore the role of elastomer dome geometry and material properties on sensor performance. In parallel, various sensors were manufactured and experimentally characterized to validate new numerical tools and provide additional insight. The goal of exploring each property is to generate a qualitative and quantitative set of design-performance rules which in turn enable the rapid design of a force sensor with a required sensitivity and saturation pressure. As a proof of concept, the design-performance rules developed in this section will be applied in Section 3.3 toward the design and field testing of a sensor for RLG of rotorcraft with mass up to 200 kg.

3.2.1 Numerical Modeling

The commercial finite element package Abaqus [80] was used to develop a model of the elastomer-encapsulated sensor. For simplicity, the model assumes radial symmetry about the axis shown in Figure 3.2. In the model, an analytical rigid surface, initially set above the elastomer as called out in Figure 3.2, is prescribed a constant velocity and used to indent/deform the mesh by a prescribed amount. The reaction force on the analytical surface is computed and can be compared to an experimentally applied force. The elastomer material is modeled as an isotropic, hyperelastic material with a Neo-Hookean strain energy potential [80, 81]. As such, the model does not incorporate any viscous (rate-dependent) mechanisms and will inherently not describe any hysteretic behavior. The MEMS sensor and its accompanying intrinsic air volume are modeled through the rigid elements shown in Figure 3.2. With respect to the nodes denoted in Figure 3.2, the nodes along the line AB have zero radial displacement in

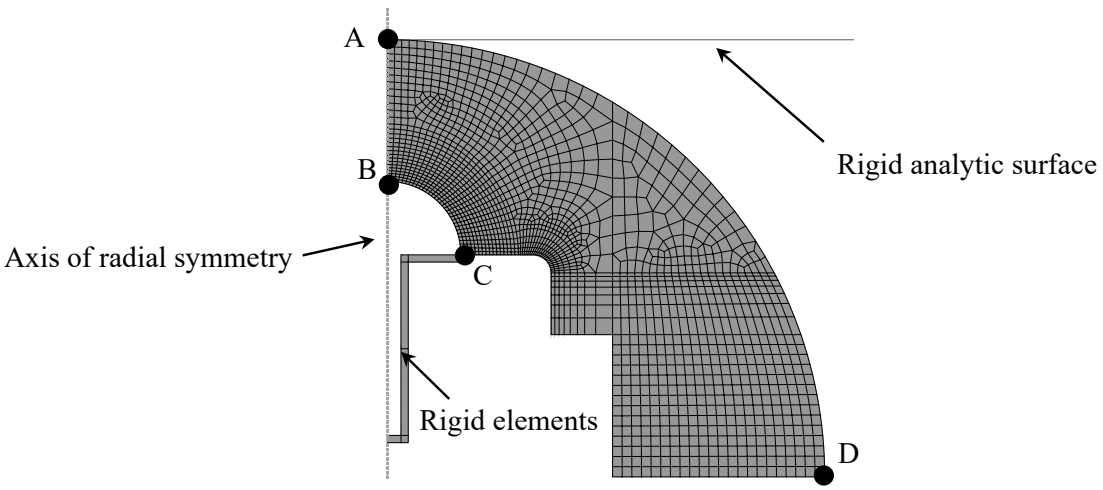

Figure 3.2: Simulation domain and finite element mesh for the behavior of the elastomer-encapsulated force sensor with engineered air cavity.

the horizontal (radial) direction. The nodes along BC, which represent the inside of the engineered air cavity, are free to deform onto the rigid elements shown. The denoted rigid elements act as the contact surface of the sensor housing. The nodes along the edge between points C and D are fixed, modeling perfect adhesion between the elastomer, MEMS sensor, and PCB. Finally, the nodes along the edge between points A and D are prescribed a contact condition with the rigid, analytic indenter surface. At each contact surface — either between the indenter and the elastomer, or the elastomer and the MEMS sensor — there is an isotropic friction coefficient. As a baseline, this coefficient is set to 0.5 for all simulations unless otherwise noted. Results from this numerical model will be presented in Section 3.2.4.

Table 3.1 summarizes the geometric and material properties varied in the numerical model to analyze their effect on sensor performance. Due to the finite element model's inviscid material assumption, the author did not simulate or analyze loading rate as it would have no effect. Hysteretic behavior will be experimentally analyzed in a subsequent section. The elastomer material properties considered are limited to a select set of silicone products manufactured by Smooth-On since these are readily

Table 3.1: List of properties varied in numerical finite element modeling of sensor performance.

Geometric	**Material**
Engineered Volume	Indenter/Polymer Friction
Elastomer Shape	Sensor/Polymer Friction
Adhered Surface Area	Shore Hardness

available and easy to manufacture for experimental comparison. The Shore A hardness provided by the manufacturer [82] was converted using ASTM D2240 [83] and the experimental work of Joyce et al. [84] to a ground state shear modulus. This shear modulus may be input to the constitutive model in the FEM. The Poisson ratio for silicone elastomers was assumed to be $\nu = 0.45$ based on experimental data presented by O'Hara [85], which is in agreement with the near incompressible behavior of elastomeric materials. Specifically used in this work for the elastomeric structure, were Mold Max 10 (MM10), which has a Shore 10A hardness and corresponding shear modulus of $G_0 \approx 0.136\,\text{MPa}$ and bulk modulus of $K \approx 1.311\,\text{MPa}$, as well as Mold Max 20 (MM20), which has a Shore 20A hardness and corresponding shear modulus of $G_0 \approx 0.228\,\text{MPa}$ and bulk modulus of $K \approx 5.63\,\text{MPa}$. These material properties fully define the Neo-Hookean constitutive model used to characterize the elastomeric materials in the FEM.

3.2.2 Experimental Setup

All experiments make use of Honeywell TruStability MEMS Pressure Sensors with a measurable pressure range between 0 and 202 kPa and I2C digital communication [86]. The internal volume of air within the sensor is $V_{0,\text{s}} \approx 75\,\text{mm}^3$ with a standard deviation of $0.57\,\text{mm}^3$ based on measurements from four sensors. In order to perform repeatable and automated experiments, the author developed a characterization setup

using a CNC mill, which allowed for repeatable, accurate, and automated experimentation. As shown in Figure 3.3, a Transducer Techniques DSM-50 load cell [87] was mounted on the cross-head of the CNC mill. This load cell has a threaded attachment point such that various kinds of fixtures may be used to indent the pressure sensor as depicted in Figure 3.3. The cross-head provides vertical displacement accuracy up to 0.0127 mm and a consistent indentation speed of 0.85 mm/s while the load cell and signal conditioner output a 12-bit force measurement up to 225 N. This is sufficient

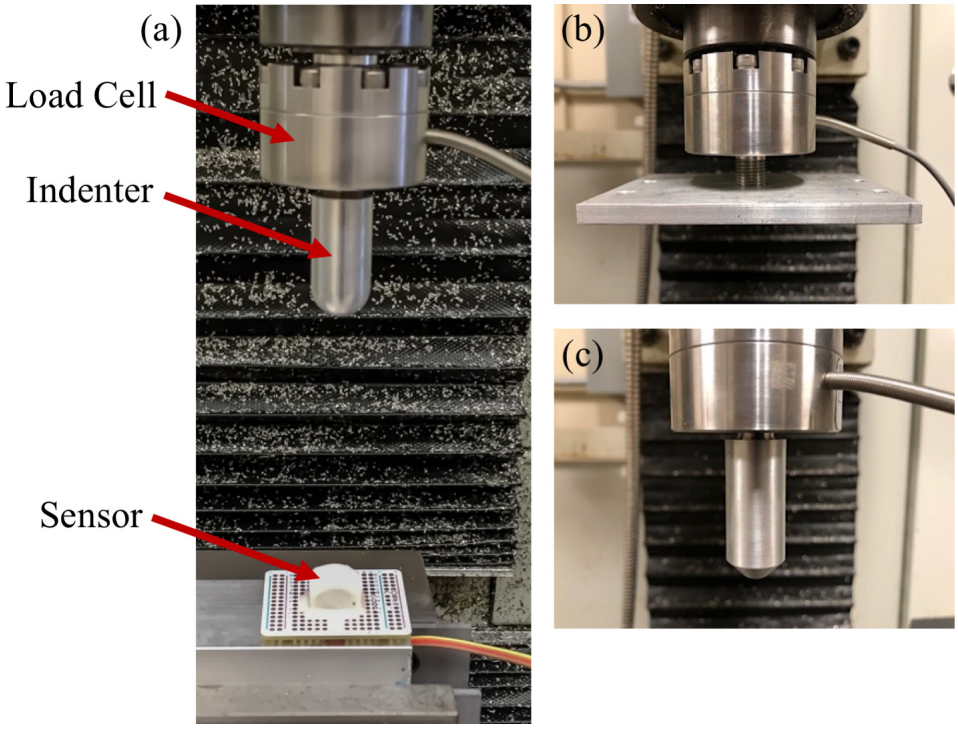

Figure 3.3: Experimental sensor characterization setup where (a) shows the load cell mounted on a Tormach PCNC 1100 Mill with a 19.05 mm radius indenter and the sensor beneath the indenter. (b) Shows the system mounted with a flat plate, and (c) shows it with a 6.35 mm radius indenter.

for quasi-static, force-pressure response of the sensor. An aluminum vice was used to mount the force sensor to the base of the CNC mill to minimize any deformations other than those of the elastomer dome during indentation. The force from the load cell and pressure from the force sensor were captured using a National Instruments DAQ board [88] synchronously recorded at ≈30 Hz.

An array of experiments were conducted using the variables and values listed in Table 3.2. These variables represent the set of physical (geometric), material, or loading properties which can be quantitatively compare to the numerical simulations and which are expected to govern the behavior of these sensors. In experimental characterization, the effect of friction between the indenter and the ground force sensor was not considered since it is difficult to repeatably characterize. However, this property will be explored numerically. A baseline force sensor is defined, before

Table 3.2: Properties varied in experimental characterization of sensor performance.

Variable	**Tested values**
Engineered Volume (mm^3)	17.5; 65
Indenter shape	6.35 & 19.05 mm radius domes; flat plate
Elastomer structure	25.4 mm diameter dome; 25.4 mm side length cube
Elastomer material	Mold Max 10; Mold Max 20

presenting the numerical and experimental results in Section 3.2.4. From this baseline sensor, the effect of varying sensor properties on its performance can be quantified and compared. The baseline force sensor — shown in Figure 3.4 adhered on a Honeywell MEMS pressure sensor — is made from Mold Max 10 (MM10), has a $V_{0,e} = 17.5\,mm^3$ engineered air cavity volume and a 25.4 mm diameter elastomer dome adhered to the pressure sensor. The $V_{0,e} = 17.5\,mm^3$ engineered volume and measured $V_{0,s} = 75\,mm^3$ sensor internal volume yield a theoretical $\tilde{P}$ of 1.23, well within the specification of the pressure sensor ($\tilde{P} \approx 2.0$). The baseline experiment is characterized by a flat plate (see Figure 3.3(b)) compressing the sensor at a displacement rate of 0.85 mm/s. This loading rate represents a quasi-static loading condition.

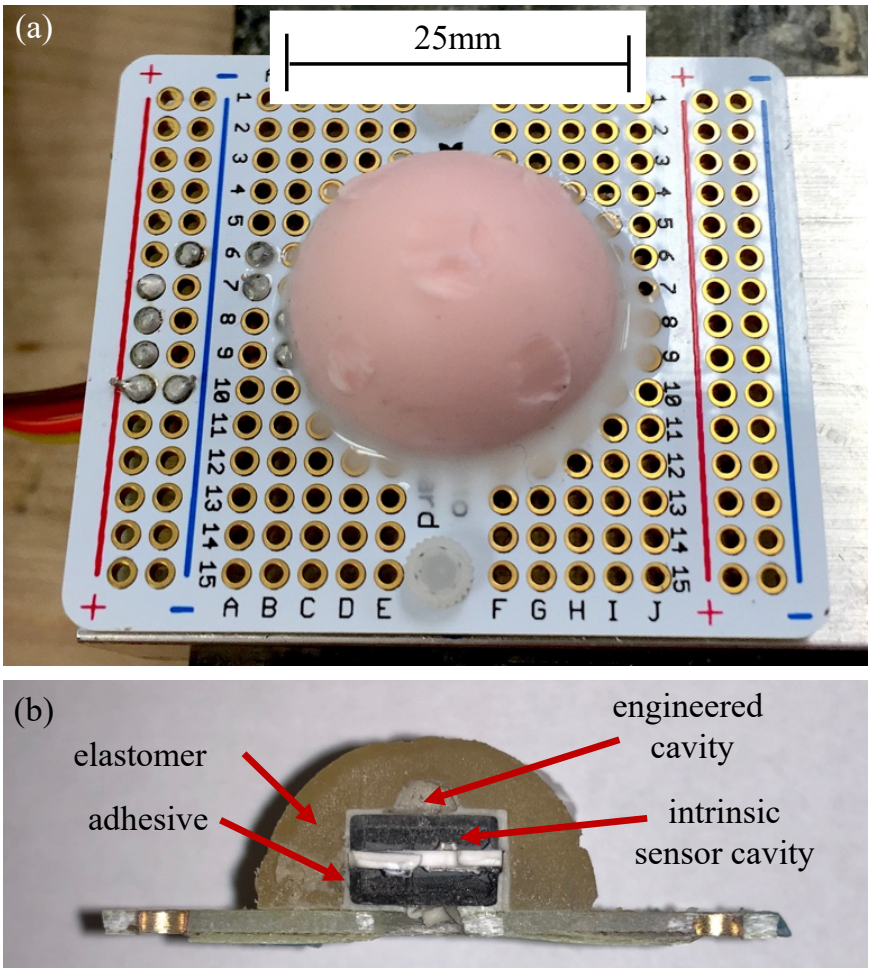

Figure 3.4: (a) Baseline sensor on an experimental PCB. (b) Baseline sensor cut view showing internal air cavities and dome structure. Note that the roughness shown in (b) is due to the waterjet cutting process used to expose the inside of the sensor.

3.2.3 Sensor Manufacturing

The force sensors are manufactured in a three-step process. First, the elastomer structure is cast in a rigid mold separate of the pressure sensor to ensure the desired engineered cavity geometry. This is different from previous designs where the polymer is cast directly onto the pressure sensor [52]. This casting process requires millimeter scale manufacturing techniques. This is a substantial reduction in complexity and cost compared to sensors requiring micrometer scale manufacturing (see Choong et al. [89]). The two-part mold used to create round and/or rectangular prism elastomer

structures is shown in Figure 3.5, where there is an example of a completed sensor with a square-prismatic elastomer. Prior to casting, the silicone elastomer is mixed and degassed in a vacuum chamber for five minutes. Then, a handheld pressure feed system is used to push the elastomer into the mold through a nozzle (see Figure 3.5). Excess air and liquid elastomer escapes through release vents. This ensures that the cured elastomer structure will have minimal voids or other imperfections that can result from a pour-over method at such a small scale. It is important to note that the process described here is amenable to large scale manufacturing where domes can be mass produced through injection molding.

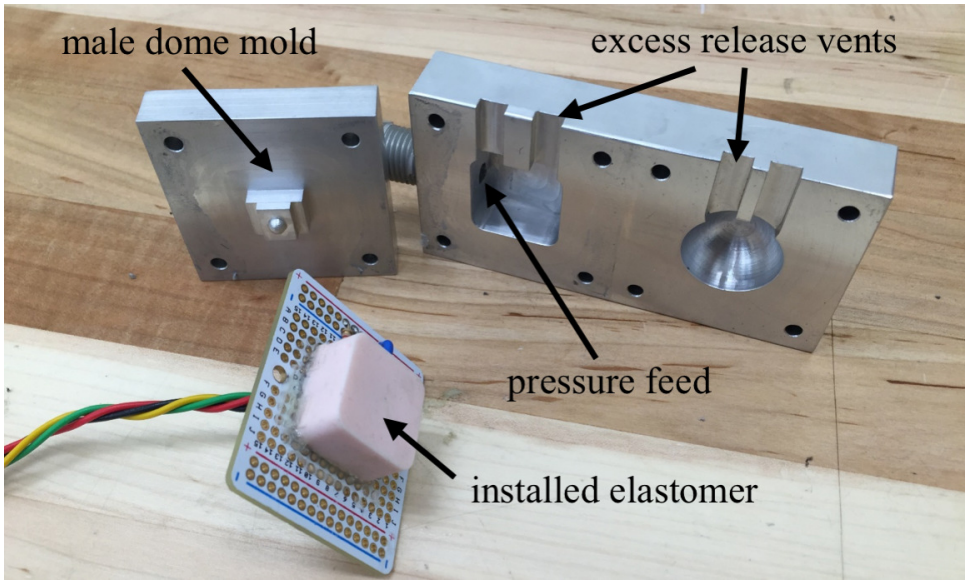

Figure 3.5: Image of two-part-mold components used to manufacture the elastomer dome.

Once cast, the elastomer dome is adhered to the pressure sensor and electronics board using two adhesives. The first adhesive is a primer and cyanoacrylate combination. This combination is applied at the interface between the MEMS pressure sensor and the elastomer near the engineered cavity (near reference point C in Figure 3.2). This adhesive yields a stiff bond. However, it does not fill any possible gaps and hence does not provide a perfect air-tight seal. For this, an industrial grade silicone RTV sealant is applied near the base of the sensor at the interface of the elastomer, the

MEMS pressure sensor, and the circuit board. The temperature-stable silicon adhesive that is resistant to various chemicals covers the remaining surface between points C and D in Figure 3.2. In combination, these adhesives provide a secure, air-tight, and robust bond between the elastomer and the pressure sensor.

3.2.4 Analytic and Experimental Results

This section presents and compares the numerical predictions and experimental results of the force sensor's response. Figure 3.6 shows a representative simulation result where contours of vertical displacement are shown for the baseline force sensor design. Beyond providing quantitative data, these numerical simulations give qualita-

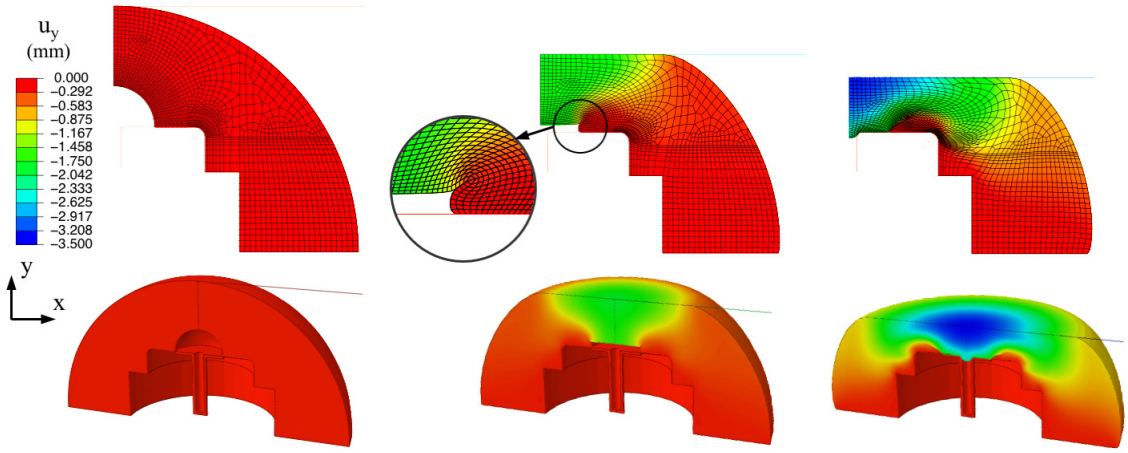

Figure 3.6: Finite element results showing contours of vertical displacement, u_y, for the baseline sensor design. The bottom row shows the simulation domain revolved 180° with the FEA mesh hidden. The top-middle inset highlights the manner in which the elastomer folds over itself during collapse of the engineered air cavity.

tive insight into the elastomer deformation process that reduces the engineered-cavity volume and increases pressure. As seen in Figure 3.6, as the sensor deforms, the elastomer begins to fold onto itself until the original volume of the engineered cavity fills with elastomer. Finally, once the air cavity completely collapses, a minimal amount of elastomer presses into the sensor cavity. This agrees well with the design assumption from Section 3.1. There, it was assumed that the maximum measured pressure of

the sensor will be due to a complete collapse of the engineered volume, $V_{0,e}$, without changes to the volume of air, $V_{0,s}$, within the sensor.

Baseline sensor response & results with varying indenter shape

The first comparison for this section is between the numerically predicted and experimentally measured behavior of the baseline sensor described in Section 3.2.2. The results of this comparison are shown in Figure 3.7(a). Note that the results henceforth are presented as a normalized pressure ratio, $\tilde{P}$, versus the applied force during loading and unloading of each considered sensor. The applied force is either measured experimentally through the load cell or numerically through the reaction force on the rigid analytical surface. All experimental measurement uncertainties are shown as shaded regions around the provided data. With respect to measurement uncertainty, there are two sources. First, there is uncertainty of 515 Pa from the chosen MEMS pressure sensor's accuracy. After normalization by the unloaded pressure sensor measurement, this nominally represents an uncertainty of ± 0.00509. Next, there is uncertainty from the load cell. Based on the specification for the given load cell, there is a ± 0.778 N uncertainty in measurements. These two uncertainties are used to formulate the shaded region around all experimental data. The horizontal line in Figure 3.7(a) shows the theoretical $\tilde{P}_{\max}$ of the baseline sensor for comparison to numeric and experimental results. The experimental data in Figure 3.7(a) (points) shows a nearly linear relation between $\tilde{P}$ and the applied force until the response saturates. The nominal experimental sensitivity of the sensor between $\tilde{P}$ and applied force is approximately 0.00833 1/N with $R^2 = 0.991$ within the linear region of the response. This is computed using a standard linear regression of the experimental or numerical data, given the start and end points of the linear response. The linear response is defined from zero load to 75% of the saturation pressure. The experimental data has a $\tilde{P}_{\max} = 1.228$, within 0.4% of the analytic prediction using (3.2). The FEA

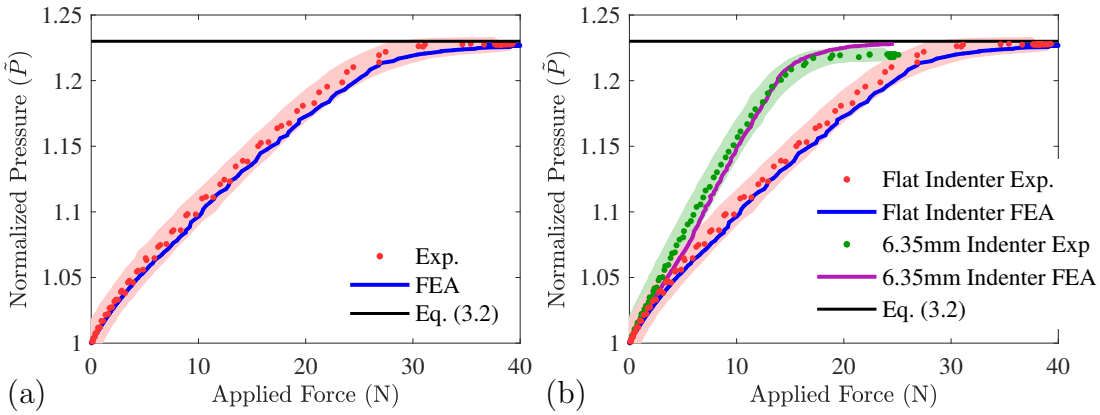

Figure 3.7: Numerically predicted and experimentally measured pressure ratio $\tilde{P} = P_d/P_0$ versus applied force showing the (a) baseline sensor design and (b) role of using flat plate (baseline) versus 6.25 mm radius indenter.

numerical prediction in Figure 3.7(a) (solid line) is in good quantitative agreement with the experimentally measured response and has a $\tilde{P}_{\max} = 1.233$. It is crucial to note that this prediction is performed with **no fitting parameters**. The FEA predicts a sensor sensitivity of 0.00809 1/N with $R^2 = 0.994$. This result represents a 2.9% difference between the experimental and finite element sensitivity response results.

Having established a good quantitative agreement between the numerically predicted and experimentally measured sensor response, the author investigated the role that the indenter (surface area contacting the sensor) has on its performance. Figure 3.7(b) shows the sensor response, both numerical and experimental, for the baseline using a flat plate to deform the sensor and for an indenter with a tip radius of 6.35 mm (see Figure 3.3). First, note that the numerically predicted response closely matches the experimentally measured response again, which adds confidence that the numerical tool developed can be used to design the force sensor for a given set of target sensor characteristics. As shown in Figure 3.7(b), the change from a flat plate to a domed indenter changes the sensitivity of the sensor where using the indenter yields a higher $\tilde{P}$ measurement at lower applied forces. This makes intuitive sense as the localized deformation caused by the indenter results in the engineered air cavity

collapsing at lower forces. Another way of thinking about this is that the indenter is engages less elastomer material (and hence requiring less force) in the process of collapsing the air cavity. For the 6.35 mm radius indenter, the nominal experimental sensitivity of the sensor is 0.0149 1/N (1.4% error from the FEA prediction) with $R^2 = 0.998$ and a $\tilde{P}_{\max}$ of 1.215 (1.5% error from the analytic prediction). Importantly, $\tilde{P}_{\max}$ is essentially unchanged by the use of either a flat plate or an indenter to deform the force sensor. This is attributed to the fact that the $\tilde{P}_{\max}$, as discussed in Section 3.1, should be a function only of the geometry of the engineered volume.

Some discrepancies between the numerically-predicted and experimental-measured results in Figure 3.7 are expected for various reasons, but the author emphasizes again that the FEA model has no fitting parameters. Most variation is attributed to the fact that material properties assigned in the FEA model are taken from manufacturer reported Shore A hardness values, and they are not taken from direct measurements of as-cast materials. Furthermore, geometric variations in the manufacturing process will also lead to some discrepancies between the numerical and experimental results. Still, as shown in Figure 3.7, the numerical model developed is shown capable of quantitatively predicting sensor performance well within 5% of the real-world performance.

Results with varying engineered volume & varying elastomer geometry

Next, the effect of varying two critical geometric features on sensor performance was explored. Namely, this included variation of the engineered cavity volume, $V_{0,\mathrm{e}}$, and variation of the exterior elastomer structure shape while maintaining $V_{0,\mathrm{e}}$ constant. The engineered cavity volume was varied from the baseline of $V_{0,\mathrm{e}} = 17.5\,\mathrm{mm}^3$ to $V_{0,\mathrm{e}} = 65\,\mathrm{mm}^3$. Figure 3.8(a) shows the results where increasing engineered volume resulted in an increase in the experimentally measured $\tilde{P}_{\max}$ from the baseline sensor value of 1.228, to a value of 1.837. This change is captured by (3.2), shown as

horizontal lines in Figure 3.8(a). This predicts the change in volume to raise the $\tilde{P}_{\max}$ from 1.233 to 1.866. This further confirms that, under these loading characteristics, the air within the engineered volume behaves as an ideal gas and that $\tilde{P}_{\max}$ is governed by the collapse of the engineered volume. Again, the numerical FEA predictions, solid lines in Figure 3.8(a), provide a good, quantitative prediction of the experimental results. Given the increase in $\tilde{P}_{\max}$ due to the increased $V_{0,e}$, the experimental sensor sensitivity is now 0.0269 1/N with $R^2 = 0.989$. It is important to note that changing the engineered volume results in an increased $\tilde{P}_{\max}$ while maintaining the applied force required to reach $\tilde{P}_{\max}$ mostly constant. As such, it is an important design tool in controlling the sensitivity of the sensor. The experimental sensor's response with increased engineered volume (see Figure 3.8(a)) has three times the sensitivity as the baseline sensor with a smaller engineered volume. In essence, increasing $\tilde{P}_{\max}$ while maintaining the applied force at which this maximum is reached better utilizes the full range of the MEMS pressure sensor.

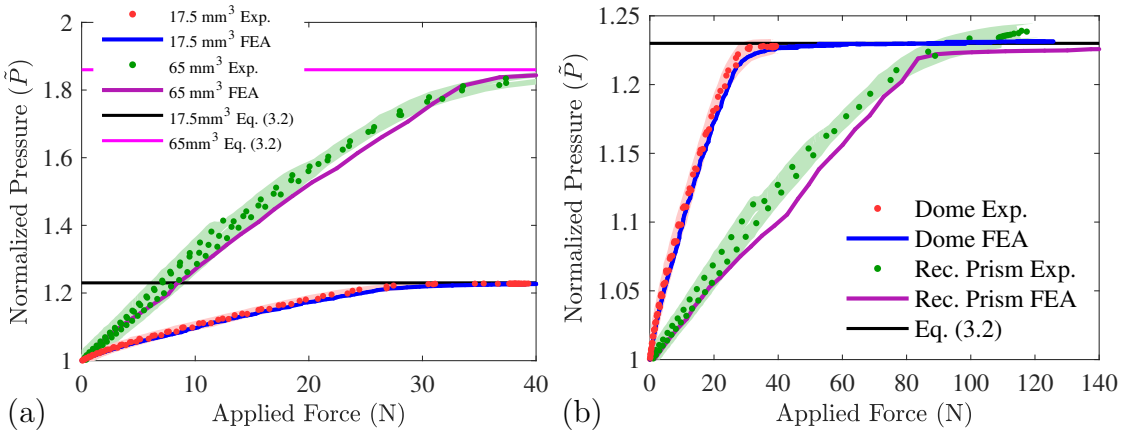

Figure 3.8: Numerically predicted and experimentally measured pressure ratio $\tilde{P} = P_d/P_0$ versus applied force showing the (a) role of varying the engineered air cavity volume between $V_{0,e} = 17.5\,\text{mm}^3$ (baseline) and $V_{0,e} = 65\,\text{mm}^3$; (b) role of varying the elastomer structure at constant engineered volume between a dome structure (baseline) and a rectangular prism

The next comparison focused on the overall geometry of the elastomer while maintaining the engineered volume constant. This study compares the baseline sensor

which has a domed shaped elastomer (see Figure 3.4) to a rectangular prism shaped sensor (see Figure 3.5). The dimensions of both are provided in Table 3.2. Figure 3.8(b) shows the numerical predictions and experimental results for this comparisons. Here, $\tilde{P}_{\max}$ remains unchanged, while the force required to reach saturation is significantly increased for the prismatic dome. Similar to the effect of changing from an indenter to a flat plate, varying the geometry from a dome to a rectangular prism requires more elastomeric material to be engaged in the process leading to the deformation and collapse of the engineered volume. As such, more force is required to reach $\tilde{P}_{\max}$ for the rectangular-prism elastomer. This translates to a reduced sensitivity. The rectangular-prismatic elastomer sensor has an experimentally measured sensitivity of $0.00284\,1/\mathrm{N}$ with $R^2 = 0.996$. This represents approximately a three-times reduction from the baseline sensor. Finally, it is clear that consistent agreement between the numerically predicted and experimentally measured data exists. The FEM mimics the rectangular prism through a cylindrical prism with equal surface area where contact occurs in order to use an axisymmetric model.

To summarize this section: 1) changes in the engineered volume geometry can be used to tailor $\tilde{P}_{\max}$ with minimal changes to the required force to reach this pressure ratio and 2) changes to the elastomer structure may be used to tailor the applied force required to reach $\tilde{P}_{\max}$ with no impact on the maximum itself. In combination then — and as will be demonstrated in Section 3.3 — these geometric properties may be used to yield targeted sensor characteristics in a straight forward fashion.

Results with varying material properties & varying contact friction

Figure 3.9(a) presents a comparison between the baseline sensor manufactured with MM10, having Shore 10A hardness and an approximate shear modulus of $G \approx 0.136\,\mathrm{MPa}$, with a sensor manufactured with MM20, having Shore 20A hardness and an approximate shear modulus of $G \approx 0.228\,\mathrm{MPA}$. As expected, the sensor with

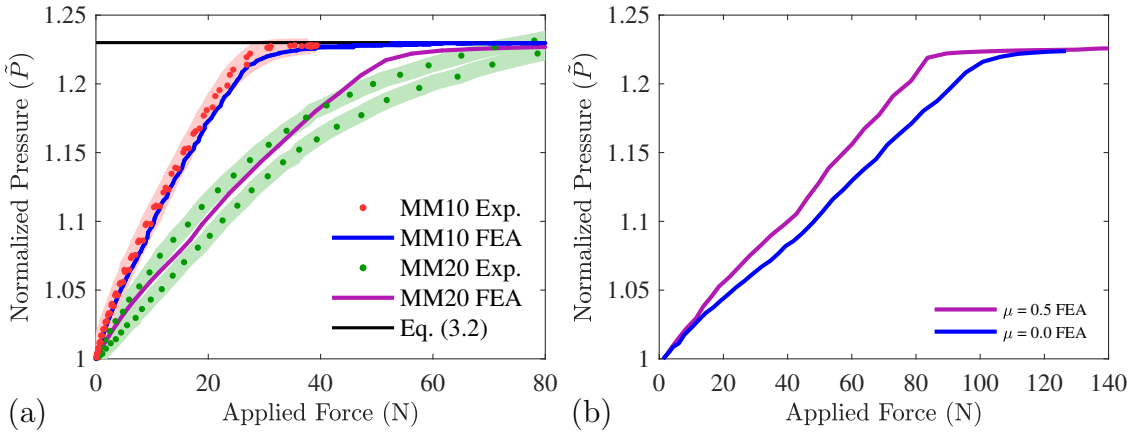

Figure 3.9: Numerically predicted and experimentally measured pressure ratio $\tilde{P} = P_d/P_0$ versus applied force showing the (a) role of varying the elastomer material properties between MM10 (baseline) and MM20; and (b) role of surface friction at the interface of the indenter/elastomer and of the elastomer/pressure sensor.

higher stiffness (higher shear modulus) requires more force to reach $\tilde{P}_{\max}$. This results in a sensitivity change from 0.00833 1/N of the baseline MM10 sensor to 0.00442 1/N with $R^2 = 0.992$ for the MM20 sensor; a 47% decrease in sensitivity. As expected, $\tilde{P}_{\max}$ remains unchanged by the change in material properties. Similar to a change in the overall elastomer structure, variation of the elastomer material properties tailors the amount of applied force that is required to reach $\tilde{P}_{\max}$. This makes sense as the stiffness of the elastomer structure is dependent on both its geometry and its material properties. Finally, it's noteworthy that there is overall consistent agreement between the numerically predicted and experimentally measured data.

The frictional properties between the force sensor and the surface being used to deform the sensor potentially could be important. An experimental effort was not undertaken to quantify this effect, as tailoring and measuring interfacial frictional properties is challenging and beyond the scope of this work. However, a numerical analysis was performed to investigate the effects of this property. Figure 3.9(b) shows numerically predicted sensor response for two varying cases of the friction, μ, between the flat surface and the elastomer. It is important to note here that a prismatic-rectangular sensor geometry is used to maximize the elastomer surface in contact

with the flat plate, maximizing the possible effects of surface friction. Consider a simulation with $\mu = 0.5$, and a simulation which is frictionless ($\mu = 0.0$). As shown in Figure 3.9(b), increasing the friction coefficient between the elastomer and the flat plate leads to a reduction in the amount of applied force required to reach $\tilde{P}_{\max}$. In this particular case, decreasing friction results in an increase in the required force to reach $\tilde{P}_{\max}$. This phenomena is rationalized by looking at the deformation as shown in Figure 3.10, which shows contours of vertical displacement at the same force level of $F = 85\,\mathrm{N}$. When $\mu > 0$, the elastomer surface will "stick" to the plate which in turn results in a smaller contact surface between the two. This results in a lower applied force necessary to reach $\tilde{P}_{\max}$, and this is in agreement with previous results when comparing a domed elastomer structure to a rectangular prismatic structure. The variation in friction from $\mu = 0.5$ to $\mu = 0.0$ is significant, and the author notes that, in application, variations in friction would be much smaller.

Results with varying loading rate, sensor hysteresis

Experiments were conducted with varying loading rate to construct a basic experimental understanding of possible loading-rate dependence and hysteresis behavior. For these experiments, an Instron E3000 dynamic load frame was used with an inertially-compensated load cell. The sensor was loaded at 0.85, 5, 15, and 25 mm/s. Figure 3.11 illustrates the hysteresis response of a sensor at these rates. The data presented here is the average response during loading and unloading over five cycles. Note that the sensor used here is a variation of the designs summarized in this section; manufactured with MM20 elastomer and with a bubble volume of 52 mm^3.

As shown in Figure 3.11, the sensor exhibits loading rate dependence and a subsequent hysteresis. The author notes that this behavior arises mainly due to the rate-dependent (viscoelastic) behavior of the elastomer. During loading, a viscoelastic elastomer has a higher effective stiffness. This in turn leads to the loading path

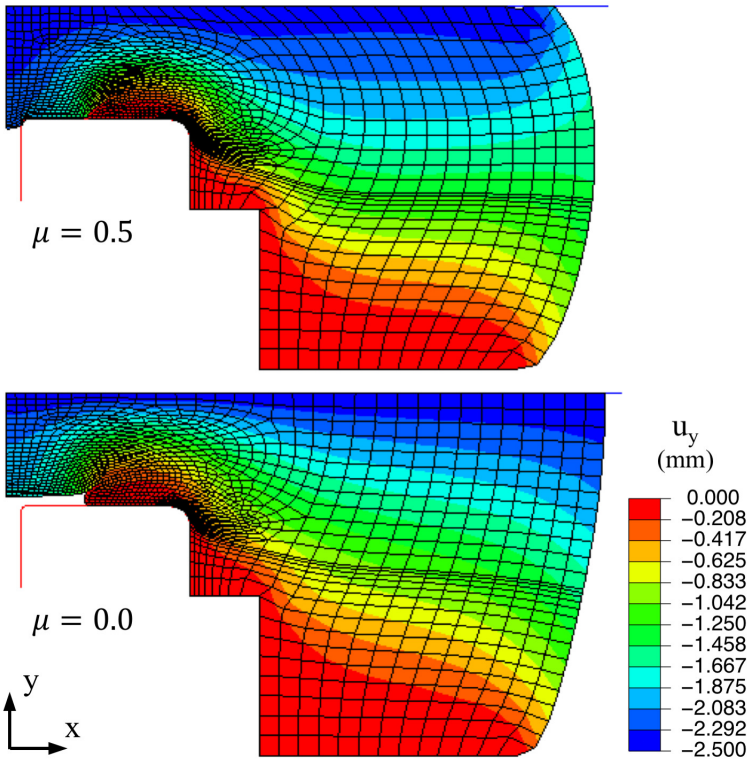

Figure 3.10: Finite element results showing contours of vertical displacement, u_y, with varying friction between the flat analytical surface and the elastomer. Results for $\mu = 0.5$ (top) and $\mu = 0$ (bottom) are shown at the same applied force of 85 N.

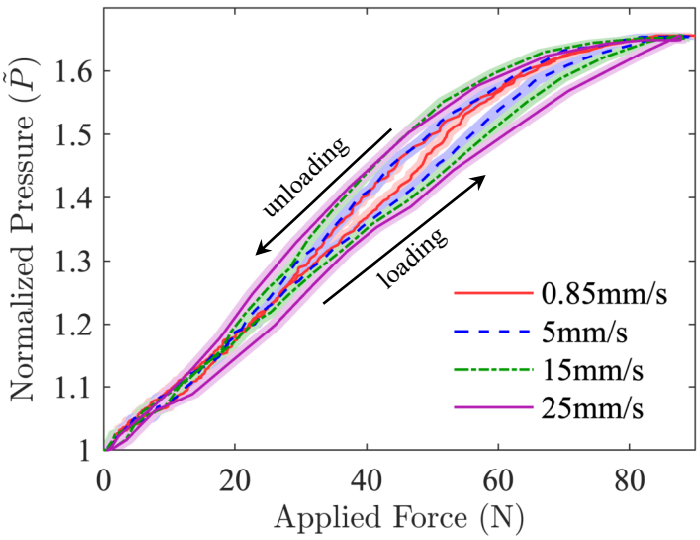

Figure 3.11: Loading rate dependent response of the force sensor and resulting hysteresis behavior.

shown in Figure 3.11 where there is a higher normalized pressure at a given force. At the peak load, the elastomer's effective stiffness returns to the quasi-static value, and the measured force decreases. The time it takes for the sensor to do this is called the relaxation time, and for this particular silicone material, it is experimentally measured to be 0.3-0.5 s. During unloading, the viscoelastic elastomer has a lower effective stiffness, which in turn leads to higher normalized pressures at a given applied force. The rate dependent behavior shown in Figure 3.11, although important, does not hinder any of the practical applications demonstrated later in this chapter. A detailed simulation model and analysis of this hysteresis behavior is left for future work.

3.2.5 Summary of Design Parameters and Their Role on Sensor Performance

The results from the previous sections may be summarized into three design rules to achieve target sensor characteristics (see Figure 3.12). First, as shown in Figure 3.12(a), an increase in the amount of elastomer deformed, mainly by increasing the area of the elastomer engaged in the deformation process, results in an increase in the applied force required to reach $\tilde{P}_{\max}$. This reduces sensitivity. Second, as shown in Figure 3.12(b), increasing the stiffness of the elastomer also results in an

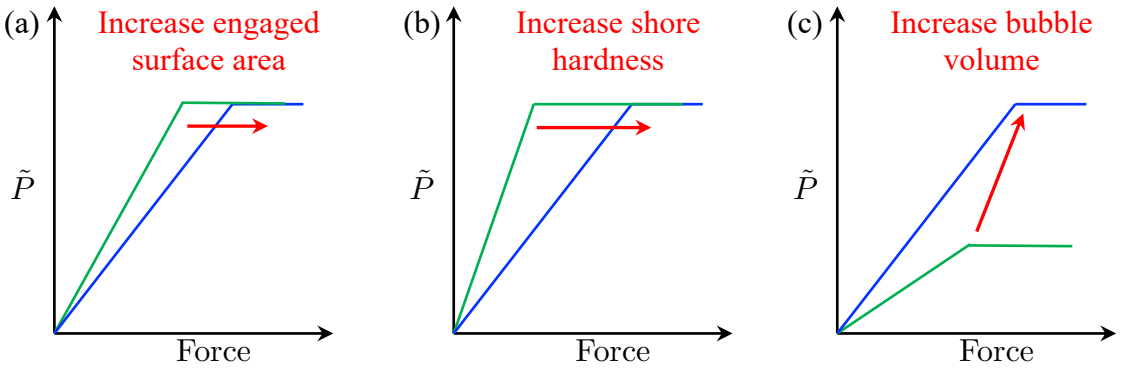

Figure 3.12: Generalized sensor response characteristics from (a) increasing elastomer surface engagement, (b) increasing shore hardness, or (c) increasing engineered volume.

increase in the applied force required to reach $\tilde{P}_{\max}$. In combination, the effects shown in Figures 3.12(a) and (b) are both related to increasing the overall stiffness of the elastomer structure either through its geometry or its material properties. Neither of these changes noticeably change $\tilde{P}_{\max}$. Finally, as depicted in Figure 3.12(c), increasing the volume of the engineered cavity within the elastomer results in an increase in $\tilde{P}_{\max}$ with little to no change in the applied force required to reach said $\tilde{P}_{\max}$. This trend is explained and predicted through ideal gas behavior as described through Equation (3.2). Equation (3.2) can quickly determine the desired air cavity required to achieve a given target maximum pressure sensor. In addition to these design rules, the author reiterates that the force sensor's response is linear until saturation independent of the geometric design, unlike some aforementioned sensors with similar force ranges such as the engineered surface by Helseth [90]. Furthermore, this sensor has a clear, simple path for design from (3.2) for the engineered volume geometry and the basic FEM for tunable force sensitivity.

In concert, these guidelines are simple, yet powerful, design rules. These rules enable the rapid design, manufacture, and deployment of a force sensor with desired transducer characteristics. Section 3.3 will demonstrate the use of these guidelines in a requirement-driven sensor design, and Section 3.4 will conclude this chapter with demonstrated applications of these sensors.

3.3 Sensor Design for Given Target Characteristics

This section demonstrates a use of the design guidelines and numerical model developed in Section 3.2 toward the development of a sensor with target characteristics. This task serves as a brief case study on the use of these novel force sensors in robotics, and in particular, on RLG for rotorcraft. The primary driver for the requirements is a set of RLG designed for rotorcraft up to 200 kg. From the onset, the author chose to use Honeywell MEMS absolute pressure sensors described in Section 3.2.2, which can

measure a maximum absolute pressure of 202 kPa. Since these force sensors are manufactured at ambient conditions and near sea level, the reference pressure is assumed to be $P_0 \approx 101\,\text{kPa}$. The sensors are rated so the maximum normalized pressure should be below $\tilde{P}_{\max} = 2$ as to avoid damaging the MEMS device. An engineered cavity volume of $V_{0,\text{e}} = 65\,\text{mm}^3$, which yields $\tilde{P}_{\max} = 1.86$, utilizes a large range of the sensor's capability without approaching its maximum, which could result in damage.

Additionally, the sensor's design assumes contact against a flat indenter (plate) located between the sensor and any external forces on the RLG. Integration of this force sensor with a flat indenter (plate) transforms point, or nonuniform, forces applied to the flat plate into planar forces on the sensor. This improves the predictability of the sensor response since it provides a consistent contact surface.

The RLG system under consideration requires repeatable, linear force measurements up to 45 N on each leg for feedback control. This decision is based on roll controllability of the rotorcraft. Based on previous experience with RLG flight test research, foot forces within 2-5% of maximum takeoff weight induce a rolling moment on the aircraft that is controllable by a pilot or stability augmentation system. Therefore, on a 200 kg rotorcraft, 45 N is well within the safe region of allowable foot forces at 2.2% of maximum takeoff weight. In order to have a linear response region up 45 N, the sensor will need the saturation force to be between 48 and 58 N based trends observed in Section 3.2. Another restriction for this particular application, which was not imposed previously, is on the physical size of this sensor. The cable-driven, four-bar linkage RLG of Chapter 2 cannot house multiple sensors inside each foot unless the overall width is less than 18 mm. These two requirements provide guidance for material properties and establish a form factor limit.

A few iterations on the overall elastomer structure were completed to arrive at the design shown in Figure 3.13, wherein (a) shows the results of the FEA simulation used during targeted design, (b) compares the numerically predicted and experimentally

measured sensor behavior, and (c) illustrates the manufactured sensor. Note how in order to fit within the necessary physical space, these sensors have a rectangular base (see Figure 3.13(c)) but a dome-like top and flat surface to yield the desired sensor response. The overall geometry, and the flat section at the top in particular, was designed using the FEM described earlier to produce the desired $\tilde{P}_{\max}$ at an applied load of 56 N. The final material chosen was MM10 silicone rubber. All iterations were completed in the numerical model by varying the material properties and the geometry to achieve the target performance to arrive at the design shown here.

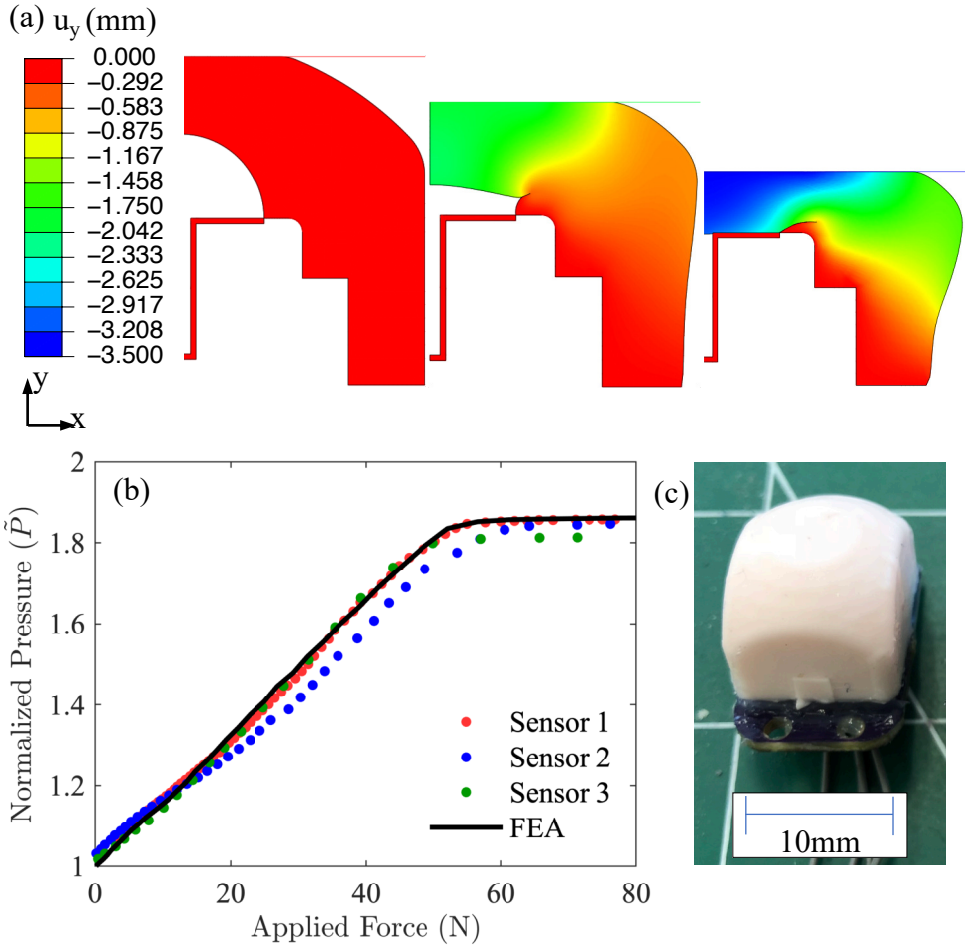

Figure 3.13: (a) FEA output images showing contours of vertical displacement for the target sensor design. (b) Numerically predicted and experimentally measured pressure ratio $\tilde{P} = P_d/P_0$ versus applied force. (c) Manufactured sensor mounted on PCB.

Figure 3.13(b) shows the FEA prediction and experimental responses of three sensors of this new design. It's important to emphasize that the numerical predictions shown here were performed entirely before sensor manufacturing and testing. No *experimental* iterations were performed to arrive at this particular sensor design. Each of the sensors achieves the target $\tilde{P}_{\max}$ within 3% at an applied force of approximately 56 N. The three example sensor responses shown have an average sensitivity of 0.0156 1/N with $R^2 = 0.993$.

Frequency response experiments were completed on this sensor design using displacement sine waves generated by an Instron E3000 ranging from 0.01 to 40 Hz. Figure 3.14 shows amplitude and phase angle response data from two sensors. The

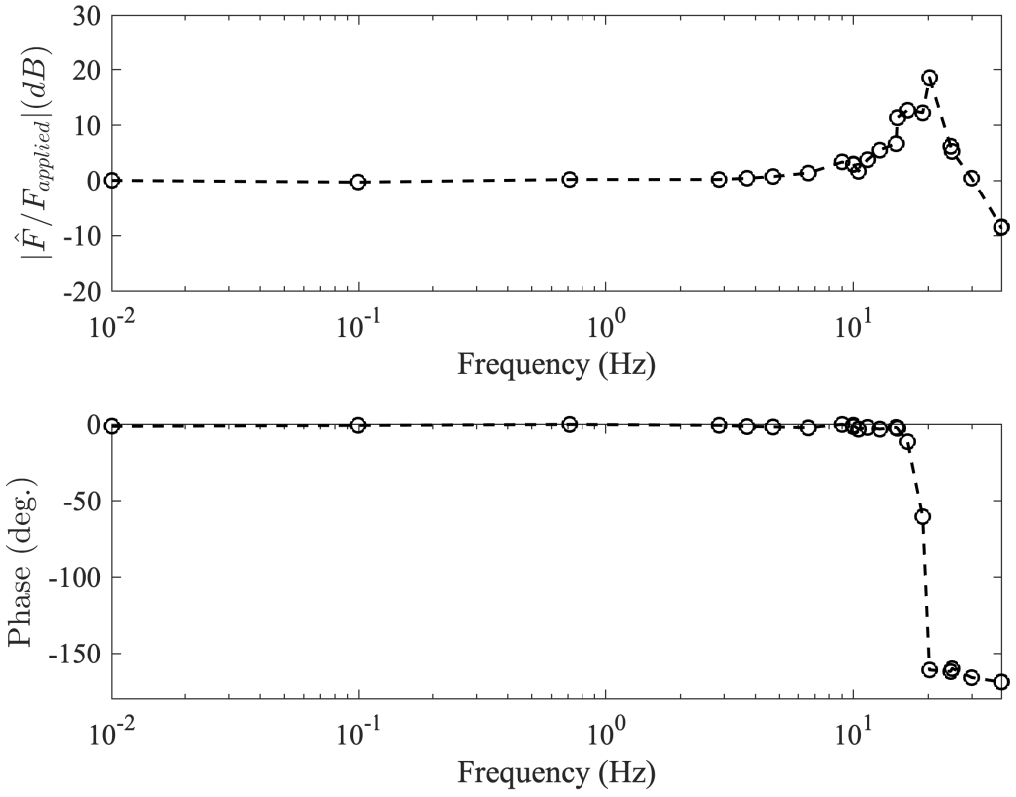

Figure 3.14: Amplitude and phase angle of the elastomer-encapsulated force sensor when loaded from 0.01 to 40 Hz using displacement sine waves.

sensors track the measured force and frequency of the Instron within a phase angle

of between 0 and -5° up to 5 Hz, where the transmittance of the sensor's measured $\tilde{P}$ leads to force estimates larger than the amplitude of the sine wave. At 20 Hz, the phase shift rapidly approaches ≈-160°, and the measured force from the sensor diminishes. This is consistent other findings in the literature for silicone elastomer dampers, where the elastomer's damping behavior has a resonant frequency near 20 Hz [91]. The author emphasizes that these tests were conducted *after* the experimental tests of Chapters 4 through 7, so the implications of potential resonant frequency around 20 Hz were not considered during sensor integration on an experimental RLG. With regard to potential vibration modes in the test fixture, the Instron E3000 has a theoretical resonant frequency at 19 Hz, but experiments could not verify a resonant frequency below 100 Hz [92]. The FR4 printed circuit boards with fixed/clamped boundary conditions (similar to those used in this experiment) have resonant frequencies in the hundreds of Hz [93]. The last source of error considered is the piezoresistive, silicon pressure sensor. These sensors generally have resonant frequencies in the kHz spectrum [94]. Therefore, the behavior measured is believed to be a result of the viscoelastic material behavior of the silicone.

3.4 Applications

This section presents various applications of the novel force sensors. First, this section presents results of force-feedback control on a small-scale RLG platform using a single force sensor designed in Section 3.3. Next, an array of force sensors is characterized with the potential for real-time force estimation and localization using a least-squares estimator on a trained measurement model.

3.4.1 Single Sensor Force Feedback Control

This section begins by presenting a basic application of a single force sensor in a feedback control framework for RLG. Unlike the design shown in Figure 3.1, the

sensor is shielded by a rubber enclosure which does not bottom out on a structural housing, and all load will be carried by the force sensor at all times. Figure 3.15(a) shows the single sensor used for this test with Figure 3.15(b) illustrating the sensor mounted on a RLG prototype covered by the elastomer shield. The specific RLG

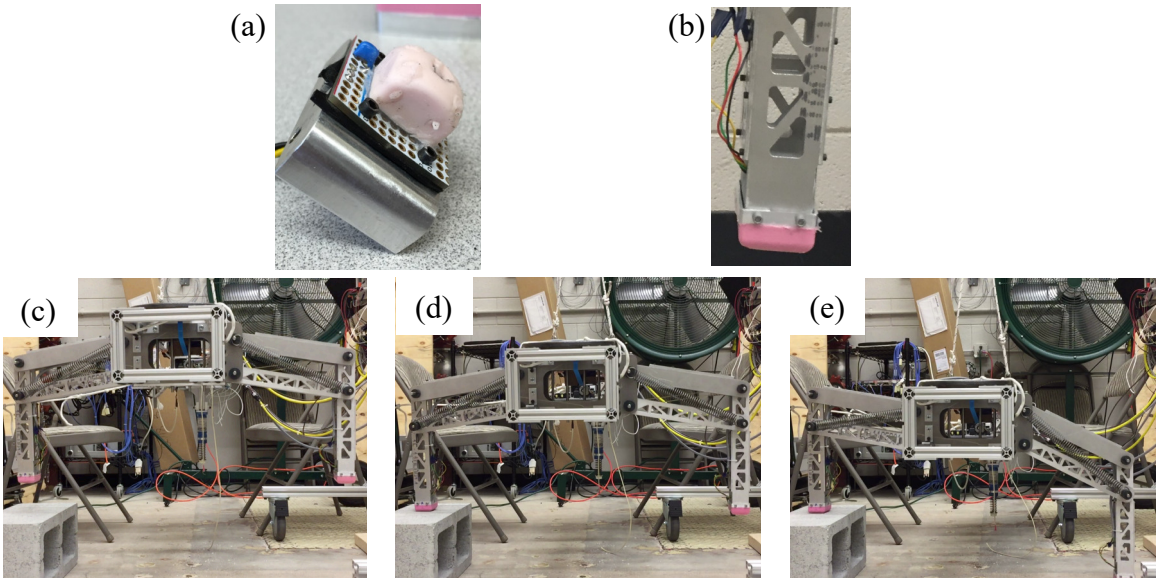

Figure 3.15: Single-sensor RLG concept for ground testing. (a) Image showing a sinngle elastomer-encapsulated sensor with (b) its polymeric shield. (c) through (e) Show force feedback control of a prototype RLG with (c) showing the suspended prototype, (d) the instance of first contact, and (e) the prototype with both robotic feet on the ground.

prototype, based on a cable-driven, four-bar linkage concept, is the same as introduced in Chapter 2. The controller used is designed to minimize the force on each foot until both feet pass a force threshold set by the author. It is important to note that the force measurement is a direct inversion of the force-pressure sensitivity provided in Section 3.3.

Figures 3.15(c) through (d) show the stages of an experiment where the force feedback provided by the force sensors allows the prototype to conform its legs onto an 8 in obstacle. The corresponding real-time force measurements on both the left and right foot are shown in Figure 3.16. In Figure 3.15(c), the frame is lowered by a gantry onto the floor, and the sensors read a nominal load of 0 N. This corresponds

to the first phase of the results shown in Figure 3.16. Feedback control of the left leg begins as the left foot (front view) makes contact and the force increases above the user-defined threshold of 1 N, see Figure 3.15(b), and continues while only one foot contacts the ground. As shown in Figure 3.16, during feedback control, the force measurement from the ground force sensor is used to maintain a roughly constant $3 - 4$ N of contact force on the left leg. Once both legs are in contact, the landing gear locks and both force sensors max out momentarily. Note that in phase three of the landing in Figure 3.16, the gantry was immediately lifted after both legs made contact to prevent sensor damage, hence the reduction in force observed.

As demonstrated, a single force sensor can be used for fine force feedback control of robotics legs. However, the performance of the system can be significantly improved with the use of multiple sensors in an array. Multiple sensors increase the contact area which can be critical when landing on sloped terrains. Furthermore, multiple sensors add redundancy where the malfunction of a single sensor does not disable the robotic leg. Such a multi-sensor array is discussed next.

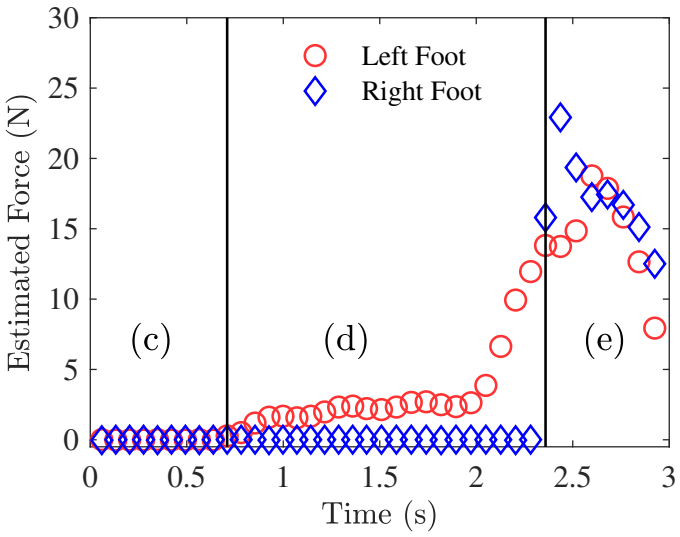

Figure 3.16: Example of force feedback measurements through three phases of an experiment on a RLG prototype. The three phases of landing (descent, force feedback control, landing) correspond to images in Figure 3.15(c) through (e).

3.4.2 Sensor Array Force Feedback and Localization

The basic design proposed in the previous section can be extended to accommodate multiple sensors in an array. An array with known sensor locations may also be used to determine the location of force contact with respect to the array. Figure 3.17(a) presents an exploded CAD model of an experimentally-realized force sensor array where three sensors mount onto a single PCB. This design is mounted inside a structural housing and covered with an elastomer shield with an embedded force distribution plate. In line with the concept proposed in Figure 3.1, this design incorporates a structural housing such that the force plate bottoms out on the structural housing and high loads are not be transferred onto the sensor array. The remainder of this section focuses on the array's calibration via indentation, as shown in Figure 3.17(b), and real-time estimation of the applied force magnitude and location relative to the sensors.

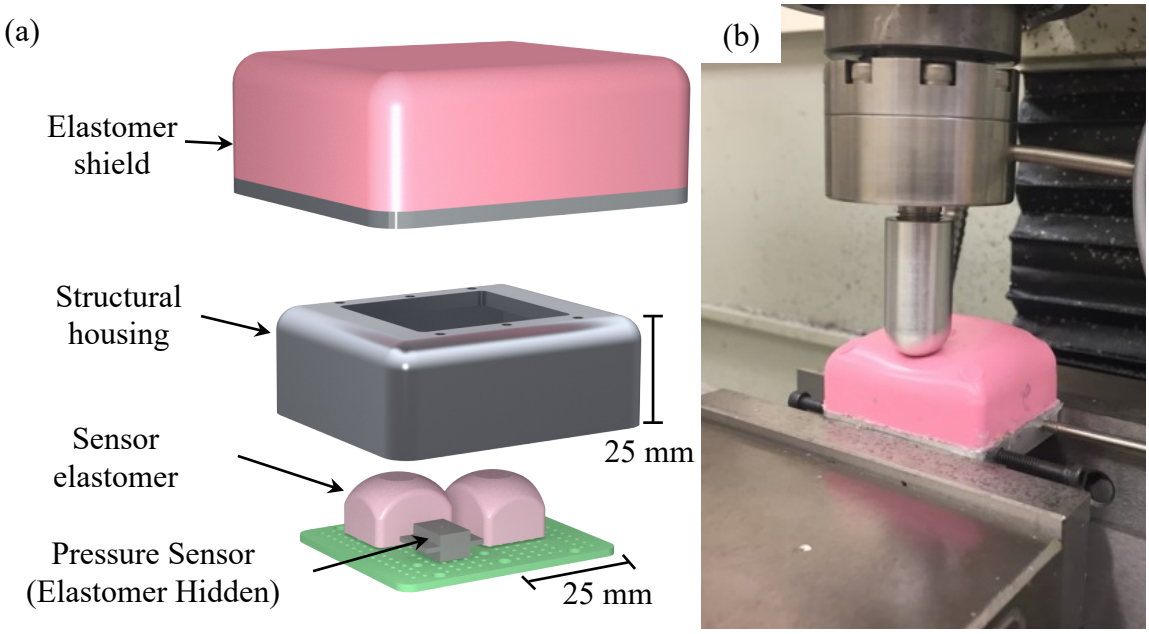

Figure 3.17: (a) Schematic of a force sensor array composed of three sensors, which was used in experiments such as (b) an indentation experiment using the CNC test rig.

The first step to understanding the responsiveness of the system is to calibrate

using a known grid of test points around the array of sensors. The same load cell and indenter setup of Figure 3.3 was used to calibrate the three-sensor array. The author selected a grid of 25 points uniformly distributed around the sensor array for the calibration process and measured $\tilde{P}$ versus force on each sensor in the array during indentation at a particular location. As an example, Figure 3.18(a) shows the measured normalized pressure versus time during indentations at the two locations denoted "A" and "B" as shown in Figure 3.18(b).

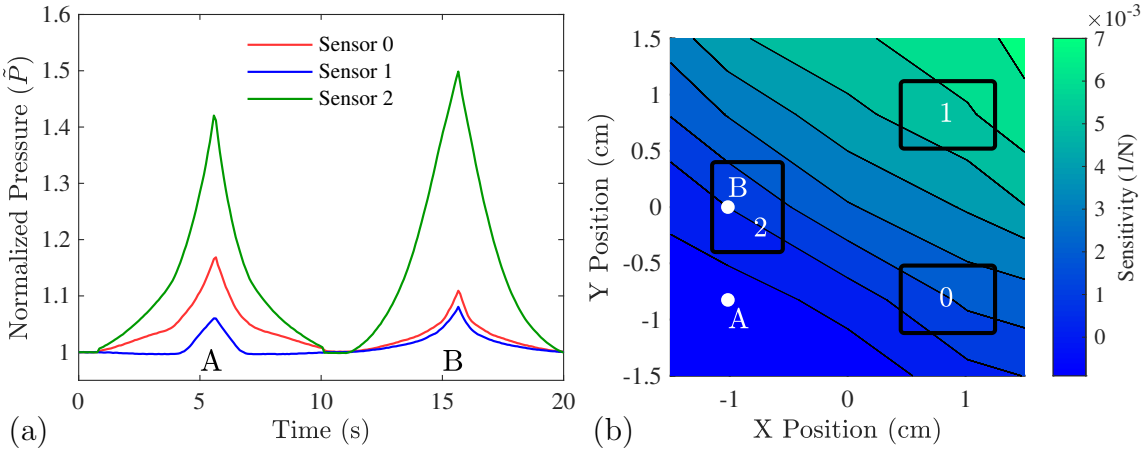

Figure 3.18: (a) Normalized pressure versus force for the three array sensors at two locations denoted by A and B. (b) Sensor sensitivity map for Sensor 1. The location of all three sensors (Sensor 0, 1, and 2) are highlighted by the black rectangles.

With normalized pressure versus force known at each grid point, it is possible to create a pressure-force sensitivity contour of each sensor in the array that is a function of location. This sensitivity contour is shown in Figure 3.18(b) for Sensor 1. For clarity, the figure highlights the physical location of all three sensors. It is observable from this plot that, as the location of applied force moves toward a particular sensor (Sensor 1 in this case), the particular sensor becomes more sensitive to the applied force. Figure 3.18(b) also demonstrates that forces applied far away from a particular sensor do not produce a significant response for that particular sensor. This behavior shows that the force plate in this design is allowed to unevenly distribute forces by pivoting about the three sensors.

The force plate applies a small amount of preload to each sensor in this specific design. As such, the pressure sensitivity might be negative if the applied load causes a sensor's measured force to decrease. This behavior is visible in Figure 3.18(a) and (b). When applying loads near the bottom left corner, the load on Sensor 1 decreases as the plate pivots about the other sensors.

The calibration data is now used to determine both the magnitude and application location of a force by training of a least squares estimator (LSE). First, define a general second order map of the normalized pressure measured by each sensor, $\tilde{P}$, to the force applied, F, and the point load equivalent location of the applied force denoted by (x, y). The estimate of these variables is denoted by $(\hat{x}, \hat{y})$ and $\hat{F}$. This general second order mapping is given by

$$\begin{Bmatrix} \tilde{P}_{0_k} \\ \tilde{P}_{1_k} \\ \tilde{P}_{2_k} \end{Bmatrix} = \left\{ \tilde{P}_k \right\} = h\left(x_k, x_k^2, y_k, y_k^2, F_k\right) \tag{3.3}$$

with the state variable estimates, $\hat{z}_k$, given by

$$\left\{ \hat{z}_k \right\} = \begin{Bmatrix} \hat{x}_k \\ \hat{y}_k \\ \hat{F}_k \end{Bmatrix}. \tag{3.4}$$

A second order map was chosen because of the high correlation between the experimental data and model fit that was not achieved with a first order model. In general, the first order model has a correlation coefficient between 0.91 and 0.96 for the three sensors' experimental data. However, a second order fit matches the data to the model with correlation coefficients of 0.99 or higher for each sensor.

Applied force, pressure ratio, and time data across all 25 grid points were used to compute the second order fit, $h(..)$ in (3.3), of pressure ratio versus force and

location. With a fixed, constant localization mapping, the remainder of the least-squares estimate problem follows. First, assume a starting location, $\hat{z}_0$ and linearize $h(..)$ about that estimate through

$$\left[H_k\right] = \left[\frac{d}{d\hat{z}}\left(h\left(\hat{z}_k\right)\right)\right]. \tag{3.5}$$

With a linearized mapping between the force estimate and measured pressure ratios, use a discrete Lyapunov estimation scheme at each time step to update estimates of location and force magnitude. Equations (3.6) through (3.8) outline this scheme that uses an optimal correction gain, K, and a state estimate covariance matrix, P, at each time step in order to minimize estimate error with respect to measurements. The x and y estimates' standard deviation values directly result from the diagonal elements of the covariance matrix are denoted as $\hat{\sigma}_x$ and $\hat{\sigma}_y$, respectively. These values are the estimator's confidence in the obtained solutions. Note that this method requires an initialization uncertainty matrix for the position and force estimates, P_0. For this implementation, the maximum force expected and the maximum x and y dimensions of the array populate the diagonal elements of this matrix. The rest of the matrix is filled with zeros (i.e. no cross correlation of uncertainty).

$$K_k = P_{k-1}H_k^T\left(H_kP_{k-1}H_k^T + R_k\right)^{-1} \tag{3.6}$$

$$\left\{\hat{z}_k\right\} = \left\{\hat{z}_{k-1}\right\} + K_k\left(\vec{\tilde{P}}_k - h(\left\{\hat{z}_{k-1}\right\})\right) \tag{3.7}$$

$$P_k = \left(I - K_kH_k\right)P_{k-1} \tag{3.8}$$

Figure 3.19 shows results of the LSE running for the experimental case of a 6.35 mm indenter applying a force at (-1.1, 1.0) cm relative to the center of the sensor array in Figure 3.18(b) at an indentation rate of 0.02 m/s. As these figures show, the least-squares estimator is able to converge an estimate of the 2D force location,

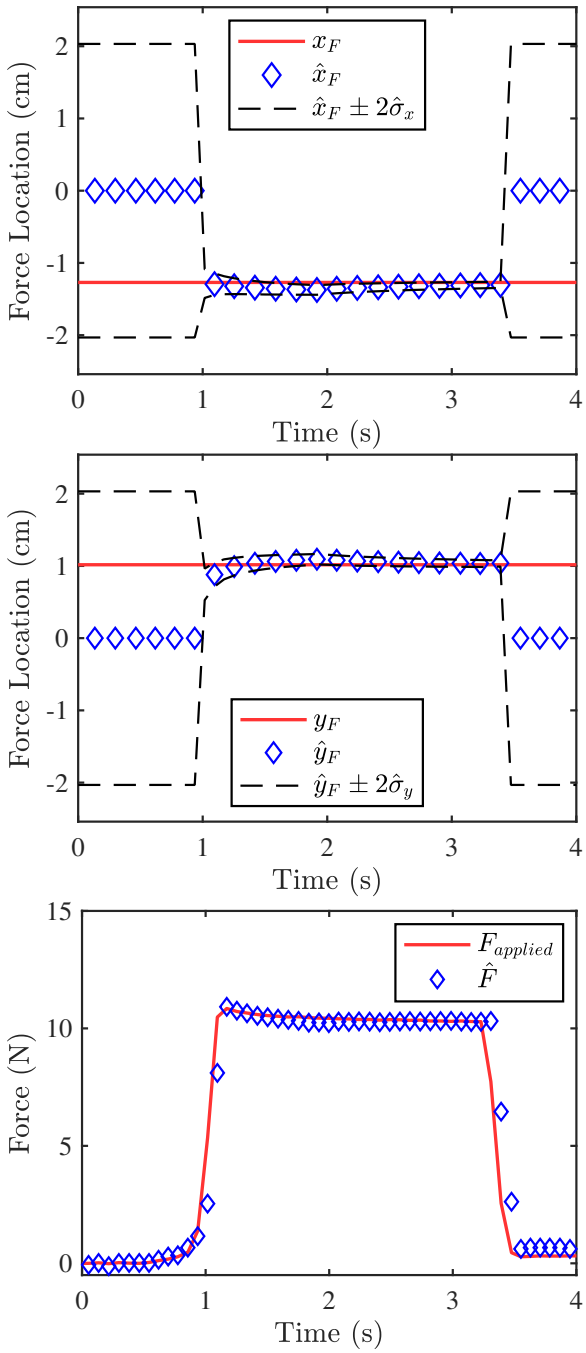

Figure 3.19: Force location and magnitude estimation results of a sensor array. (a) Shows estimated $\hat{x}_F$ with the filter's uncertainty, $\hat{\sigma}_x$, and actual horizontal X location, x_F. (b) Shows estimated $\hat{y}_F$ with the filter's uncertainty, $\hat{\sigma}_y$, and actual vertical Y location, y_F. (c) Shows the estimated force, $\hat{F}$, and applied force F_{applied}.

$(\hat{x}_F, \hat{y}_F)$, and the magnitude of the applied force $\hat{F}$, within 5%. Location estimates take approximately six time steps to converge, while the force estimate lags only one

time step behind the applied value.

This result successfully demonstrates force localization and magnitude estimation using an array of newly developed force sensors. These sensors will be integrated with the cable-driven, four-bar linkage RLG on a commercial aircraft in Chapter 6. Several topics of research are left for future work, though. First, the sensor array's sensitivity once wrapped in an elastomer shield was not characterized. This may have significant impact on the design of individual sensors and the elastomer shield geometry in future designs. Furthermore, the sensor array's hysteresis and frequency response of the shielded configuration was not tested. The author expects these properties to vary dependent on the elastomer shield material and rigid mounting points. Again, these topics should be analyzed in the future as the sensor's use on RLG matures.

CHAPTER 4
DISCRETE, REAL-TIME, SENSOR-FUSED RLG CONTROL

The control and integrated health-monitoring algorithms developed in this dissertation have general applications for RLG. This chapter introduces them at a high level for the cable-driven, four-bar linkage mechanism designed in Chapter 2. Later integration and experimental use on a commercial rotorcraft will be discussed in Chapters 6 and 7, respectively. This chapter introduces a force-feedback controller first based on RLG controller research reviewed in Chapter 1. It is designed to be a baseline for comparison with a new controller. Next, an aircraft roll- and force-fused feedback controller is detailed as a contribution of this work. This controller has one critical component never before implemented on previous RLG systems: a sensor and compute hardware status monitoring architecture. Some basic examples of the controllers implemented on cable-driven, four-bar linkage RLG are presented to align the reader with real-world implementations of both systems.

4.1 Baseline RLG Control: Parking Brake Controller

The most prevalent type of controller for RLG to date is ground contact feedback control, also referred to as parking brake control (PBC). Control of this manner is referred to as a parking brake controller because it follows three fundamental stages similar to parking and applying a parking brake. This section constructs a PBC for a four-bar RLG mechanism that is used as a comparison to a new, sensor-fused RLG controller. There are some minor variations on PBCs based on the type of sensors used (infrared, resistive film, etc.), but this section focuses on PBC with force feedback.

Figure 4.1 defines the three stages of PBC as 1) descent/approach with gear active,

2) actuate legs to minimize force or contact on the leg in contact, and 3) lock legs and system in place. Four feedback channels provide inputs to this controller through the

Figure 4.1: Force feedback control stages on the RLG 200 kg scale experimental prototype test-bed introduced for crashworthiness drop tests in Chapter 2.

three landing stages. The four feedback channels are two forces, one from each foot, and two leg-angle measurements, one from each leg.

The first stage, descent, represents the approach and landing initialization, when the RLG PBC activates and force measurements begin. Throughout the descent, force sensors in each foot pass their estimated state back to the main RLG compute avionics, and the controller awaits receipt of a minimum threshold force before actuating the legs. The second stage is the critical phase for force feedback control. The controller uses all four feedback channels as inputs to two control loops. Figure 4.2 shows a schematic of the PBC control loops that make use of foot-force feedback and leg-angle feedback. Force estimates on each foot, $\hat{F}_{L/R}$, feed an outer proportional-derivative (PD) control loop while leg-angle estimates relative to the fuselage of each four-bar linkage, $\hat{\theta}_{L/R}$, feed the inner PD loop. As soon as a user-defined threshold force is passed on one foot, the PBC actuates the legs using commands from a PD control algorithm. The controller computes the force error as

$$e_{F_k} = F_d - \hat{F}_{L/R_k}. \tag{4.1}$$

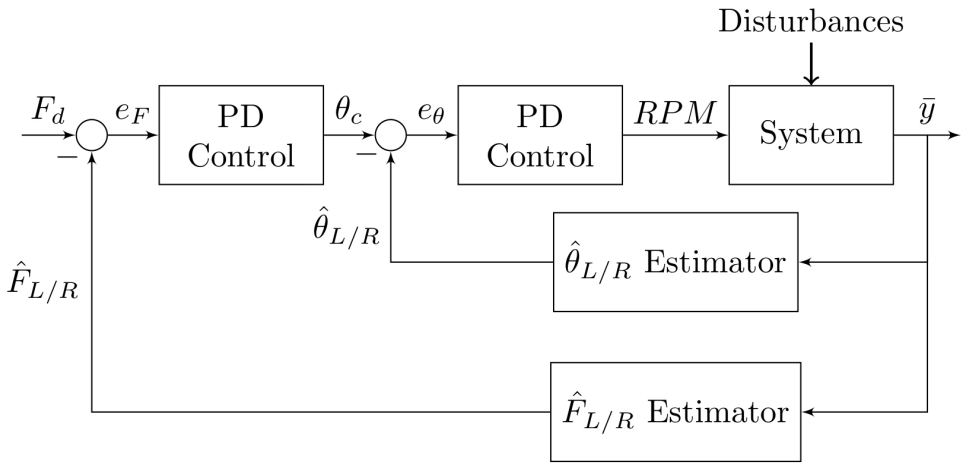

Figure 4.2: S-100 RLG PBC controller block diagram

Using this force error, the equation

$$\delta\theta_k = K_P e_{F_k} + K_D \left(\alpha_F \dot{e}_{F_k} + (1-\alpha_F)\, \dot{e}_{F_{k-1}}\right) \tag{4.2}$$

generates the desired change in leg angle, $\delta\theta_k$. This equation makes use of a discrete, low-pass filter with filter parameter, α, to attenuate noise from the incoming signals. Finally, the leg-angle command is computed by

$$\theta_{c_k} = \hat{\theta}_{L/R_k} \pm \delta\theta_k. \tag{4.3}$$

These equations apply to the left or right side of the RLG depending on which foot makes contact first. The motor speed is then controlled through another PD controller that computes desired RPM based on leg-angle error.

Analogous to the force feedback PD controller, the leg-angle control loop accepts leg-angle error values for the left or right side dependent on the foot in contact. The leg-angle error is computed by

$$e_{\theta_k} = \theta_{c_k} - \hat{\theta}_{L/R_k} \approx \delta\theta_k. \tag{4.4}$$

The commanded RPM follows from:

$$RPM = RPM_0 + K_P e_{\theta_k} + K_D \left(\alpha_\theta \dot{e}_{\theta_k} + (1 - \alpha_\theta) \dot{e}_{\theta_{k-1}} \right) \tag{4.5}$$

Similar to the force feedback loop, there is a low-pass filter on the derivative component due to the discrete implementation. Generally, the error in leg-angle is approximately equal to $\delta\theta_k$. There are a select number of operational situations where there is not a direct relation. One example is when one leg's angle encoders malfunction or sustain damage. Control is possible and safe because the controller may use secondary leg-angle estimates. This is enabled by the continuous cable design, as described in Chapter 2. Also, Equation (4.5) includes a non-zero bias term that represents the minimum RPM in any direction to overcome the static friction of the drive cable. Once both legs make contact, stage three commences with some type of brake locking the drivetrain into position so the legs remain stationary, similar to the function of a parking brake.

This controller was implemented and tested on the cable-driven, four-bar RLG testbed with full-scale legs sized for a 200 kg rotorcraft. This testbed was first presented in Chapter 2. An example landing is provided to the reader to translate how the concept applies to a real system. Figures 4.3(a) through (f) illustrates experimental data from landings on the left and right legs on 30 cm (≈12 in) platforms. The sensors used to gather measurements and generate the data will be further described in Chapter 6, where all systems are integrated into a commercial, unmanned rotorcraft. This experiment is provided as a physical example of how the control operates in a laboratory setting. Figures 4.3(a) and (b) show the differential angle between the left and right leg measured angles θ_L and θ_R. As a reminder, the differential angle, θ_D, is computed through

$$\theta_D = \frac{\theta_L - \theta_R}{2}, \tag{4.6}$$

and it is a useful quantity to plot the data from both leg measurements at once. The

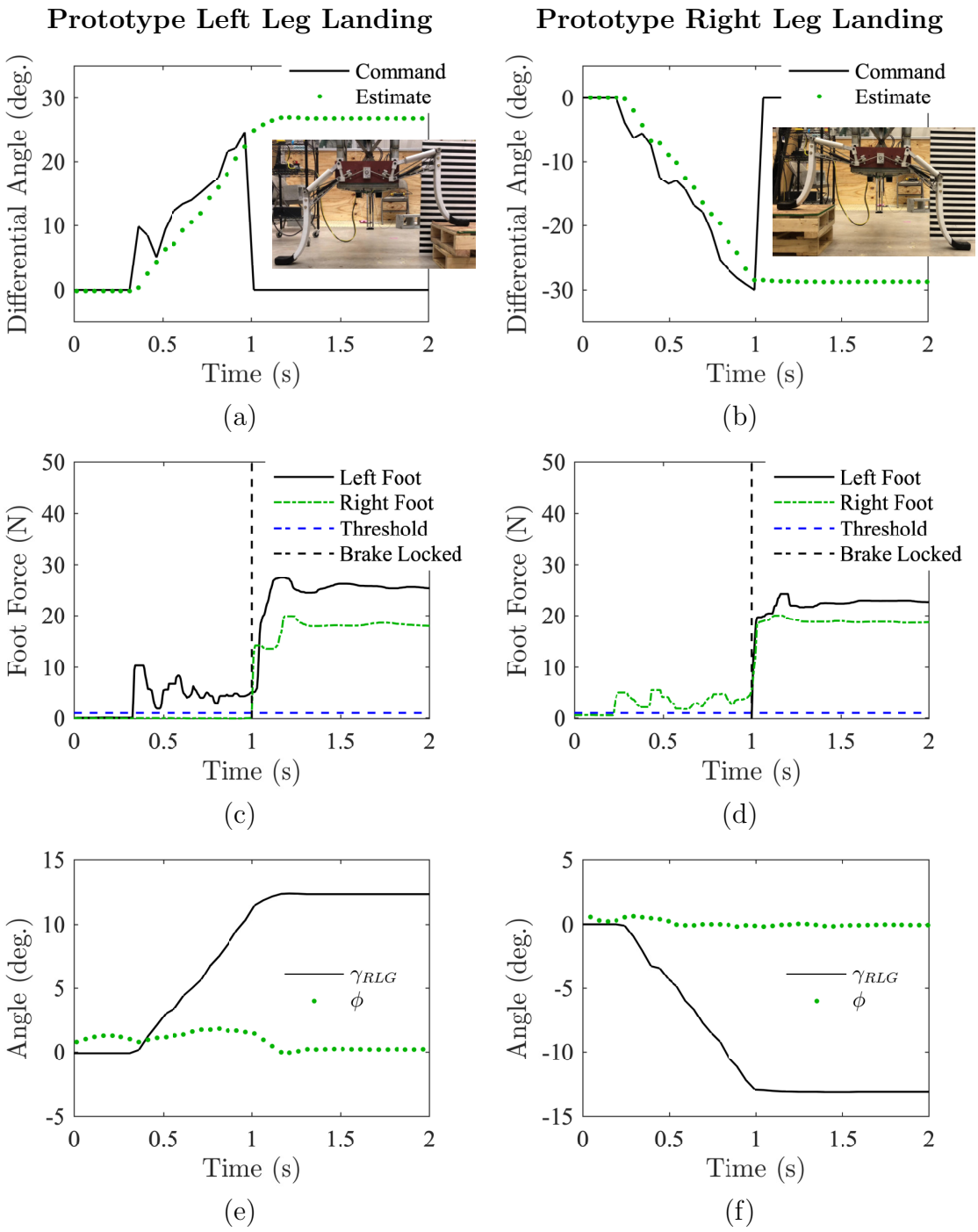

Figure 4.3: Right and left leg landing experimental data of a 30.48 cm (12 in), 0.381 m/s (15 in/s) platform landing showing (a) and (b) differential angle estimates and commands from the PBC, (c) and (d) force feedback, and (e) through (f) RLG absorbed ground angle (γ_{RLG}), estimated ground angle ($\hat{\gamma}$), and roll feedback (ϕ).

PBC controller drives the angle commands given the force measurements shown in

Figures 4.3(c) and (d). The experimental data contains a lag between the commands and state estimate. This is expected due to the short time period of the dynamics, <1 s, and the ramp-up time of the drivetrain motor. These landings confirmed that the force-feedback control behaves as an underdamped system when the foot force converges toward the desired force (≈5 N). When the force on both feet passes the threshold (≈1 N), PBC activates the brake and locks the legs into their final position. Figures 4.3(e) and (f) provide experimental data of the ground angle absorbed by the RLG based on the current leg angles, γ_{RLG}, and roll measurements, ϕ. For both landings, the absorbed ground angle tracks the estimated total ground angle by the time the brake engages, leaving the frame within 0.5° of roll for both landings. This example shows the basic operation of PBC under an ideal test condition (constant, slow descent), but fundamental limitations of the controller exist under a substantial number of other operating conditions.

4.1.1 Limitations of Parking Brake Controllers

PBC variants all have similar limitations. As alluded in the relevant background of Chapter 1, there are fundamental assumptions that drive the limitations. Multiple relevant works assumed that the landing surface is static, and the aircraft descends with constant descent rate within some nominal bounds that the RLG is capable of matching. Anytime these assumptions are not valid and only contact feedback is employed, there is poor observability of necessary states to safely operate the rotorcraft within roll angle requirements. The active landing gear cannot observe the descent rate and match changes in descent speed with the legs to minimize orientation perturbations when **only** contact feedback is available. In this case, the only option is for the legs to move as fast as possible until the system detects a loss of contact. This results in bouncing and potentially dangerous perturbations in roll and pitch angles. This phenomenon is exacerbated if the aircraft lands on a dynamic surface, where

the aircraft and surface have variable, relative speed and orientation perturbations are inevitable. Additionally, a system with only contact feedback does not reliably detect when a landing occurs. The aircraft may bounce and the controller incorrectly identify a "complete" landing. Even with debounce algorithms, the gear should not be moved during a bounce since there is no way to observe how such a leg movement will change aircraft orientation. As apparent with the limitations listed here, feedback of the aircraft orientation would be beneficial. The next section outlines a new, aircraft-orientation and force-feedback controller created to remove the limitations of contact feedback controllers.

4.2 Robust Roll-Angle and Foot-Force Fused Control

This section introduces a new RLG controller with fused roll- and foot-force feedback control loops. Roll fusion is considered because the experimental system will only have differential leg motion, which will align with the aircraft's roll axis. Roll measurements alone do not provide enough system observability to be the sole feedback channel, though. This is due to the uncertainty of whether roll perturbations from landing are caused by landing gear contact, wind, or other external driving forces. Furthermore, the foot-contact force required to induce a roll perturbation inherently pushes the aircraft toward the operational boundary. For these reasons, the roll measurements are fused with foot-force feedback channels. Thus, the avionics may determine with certainty if the aircraft roll perturbations are a result of contact or other external forces. Then it will combine the two types of observable states into one control signal. The methodology is extensible to roll, pitch, and foot-force fused control dependent on a RLG's DoF. In addition to the new controller, sensor health monitors and a human-machine interface are detailed as modules to improve the robustness and usability.

Roll- and force-feedback control follows three operational stages illustrated in

Figure 4.4. The first stage has the aircraft descend with no contact on either foot.

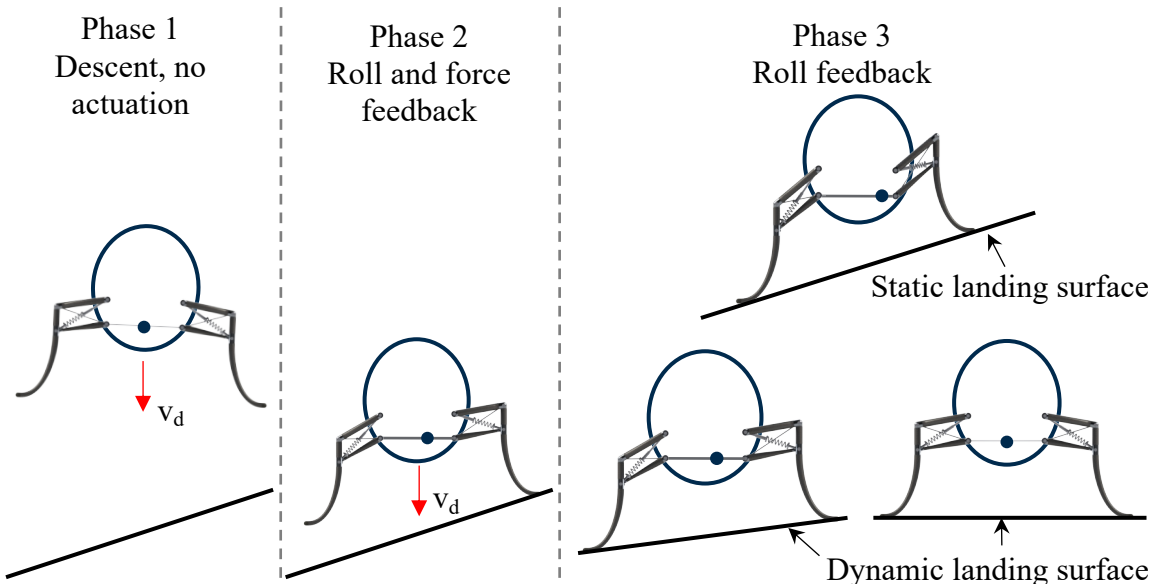

Figure 4.4: Diagram illustrating three phases of control using RLG with available roll and force feedback.

Regardless of the roll angle during the descent phase, the legs do not actuate. Once one leg makes contact with the landing surface, the second phase initiates. Control begins and incorporates both roll and force feedback to minimize dispersion in inertial roll angle until both legs make contact. The force sensor measurement saturates on both legs after landing, thus the final phase uses only roll angle feedback. Nominally, this last phase ends when the aircraft reaches a minimal roll angle within an acceptable deadband, ϕ_{DB}, regardless of the landing surface. The included roll feedback enables swift detection of whether or not the landing surface is dynamic.

Figure 4.5 shows the high-level block diagram of the combined roll and force feedback controller used in this dissertation. The leg-angle estimator and foot force feedback estimators may take on any form, as long as they provide an estimate and a health status flag to the outer loop PD controller. Flight software retrieves the roll estimate used for loop closure from an attitude and heading reference system (AHRS). RLG control starts with a conditional PD controller that uses desired and estimated foot forces in addition to the desired and estimated roll angles as inputs.

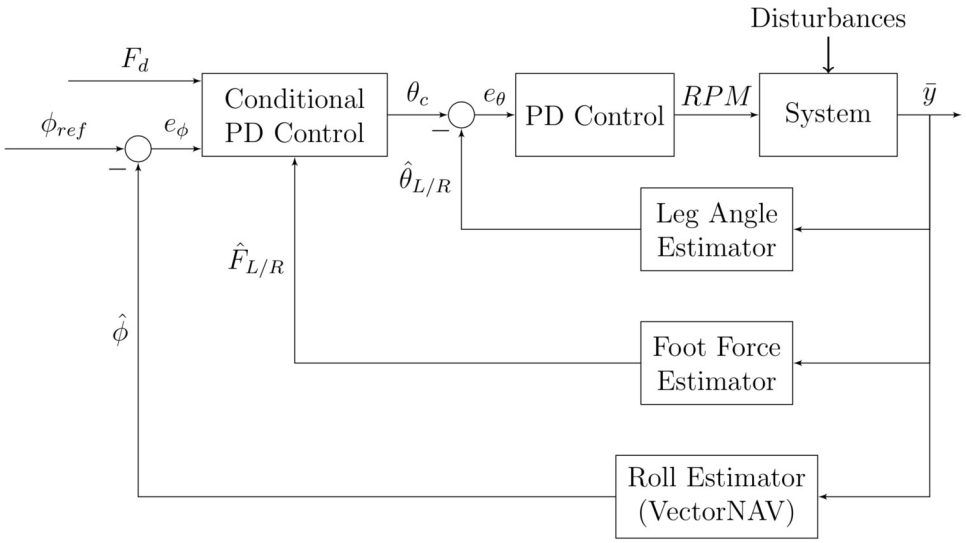

Figure 4.5: Roll- and force-fused RLG control algorithm block diagram.

The procedure follows as outlined in Algorithm 1.

Algorithm 1 generally mimics the procedures of the flight software, but it does not include specific logic of health monitor checks, output value clamps, nor the additional sanity checks on control outputs that exist in the flight software. This conditional PD algorithm is meant to be interrupt driven upon initial contact on either foot, so asynchronous inputs do not impede performance. The derivative control equations implement a first-order, low-pass filter on the control to limit noise from the incoming signals [95]. Each channel of control (roll and foot force) has a unique low-pass filter parameter, α_i, which is chosen based on the frequency characteristics of each input channel. Notable from this algorithm is that the controller uses force feedback control until the aircraft exceeds an allowable deadband along the roll axis. For this reason, it is advantageous to minimize the deadband of the system. Methods to minimize roll deadband include high-dynamic-accuracy roll measurements and/or actuation methods that can run continuously with little or no regard for power consumption. Note that the leg-angle control does not have a feed-forward term but the motor control does. This feed-forward term, RPM_0, is the required minimum RPM to

Algorithm 1 RLG conditional PD control

Control interrupt driven by $\hat{F}_{R/L} > F_d$ begins loop
repeat
  if $\hat{F}_L > F_d$ & $\hat{F}_R < F_d$ **then**
    $e_{F_k} = F_d - \hat{F}_{L_k}$
  else if $\hat{F}_R > F_d$ & $\hat{F}_L < F_d$ **then**
    $e_{F_k} = \hat{F}_{R_k} - F_d$
  else $\{\hat{F}_R > F_d$ & $\hat{F}_L > F_d\}$
    $e_{F_k} = 0$
  end if

  CHECK $\hat{F}_L$ and $\hat{F}_R$ FOR BOUNCE

  if $|\hat{\phi}| > \phi_{DB}$ **then**
    $e_{\phi_k} = \phi_d - \hat{\phi}$
  else $\{|\hat{\phi}| < \phi_{DB}\}$
    $e_{\phi_k} = 0$
  end if

  $\delta\theta_{k_F} = K_{P_F} e_{F_k} + K_{D_\phi} \left(\alpha_F \dot{e}_{F_k} + (1 - \alpha_F)\, \dot{e}_{F_{k-1}}\right)$
  $\delta\theta_{k_\phi} = K_{P_\phi} e_{\phi_k} + K_{D_\phi} \left(\alpha_\phi \dot{e}_{\phi_k} + (1 - \alpha_\phi)\, \dot{e}_{\phi_{k-1}}\right)$
  $\delta\theta_k = \delta\theta_{k_\phi} + \delta\theta_{k_F}$
  $\theta_{c_k} = \hat{\theta}_{L_k} + \delta\theta_k$
Ensure: $\theta_{c_k} < \theta_{max}$ & $\theta_{c_k} > \theta_{min}$

  $e_{\theta_k} = \theta_{c_k} - \hat{\theta}_{L_k} \approx \delta\theta_k$.
  $RPM_k = RPM_0 + K_{P_\theta} e_{\theta_k} + K_{D_\theta} \left(\alpha_\theta \dot{e}_{\theta_k} + (1 - \alpha_\theta)\, \dot{e}_{\theta_{k-1}}\right)$
Ensure: $|RPM_k| < RPM_{max}$
until $|\hat{\phi}| < \phi_{DB}$ & $\hat{\theta}_{L/R_k} \approx \theta_0$

overcome the static friction of the system. This algorithm succinctly fuses the roll angle feedback, and with a minor change to the $\delta\theta_{k_\phi}$ equation it also can fuse roll rate, p, feedback. This minor change takes on the form

$$\delta\theta_{k_\phi} = K_P e_{\phi_k} + K_D\,(p)\,. \tag{4.7}$$

Use of this alternate computation depends on the quality of roll rate feedback from an AHRS.

In a similar manner to the PBC, a single example of how this controllers operation is provided here. This is meant to align the reader with how the controller operates on a real system. Testing of this controller for this data point follows the same procedure implemented on the PBC for a flat landing block. The allowable roll deadband, ϕ_{DB}, for the experiment was 0.5°. The presented landing was on a 23 cm obstacle rather than the 30 cm obstacle from Section 4.1. Figures 4.6(a)-(d) illustrate data obtained during the representative experiment. There is an increase in roll that is

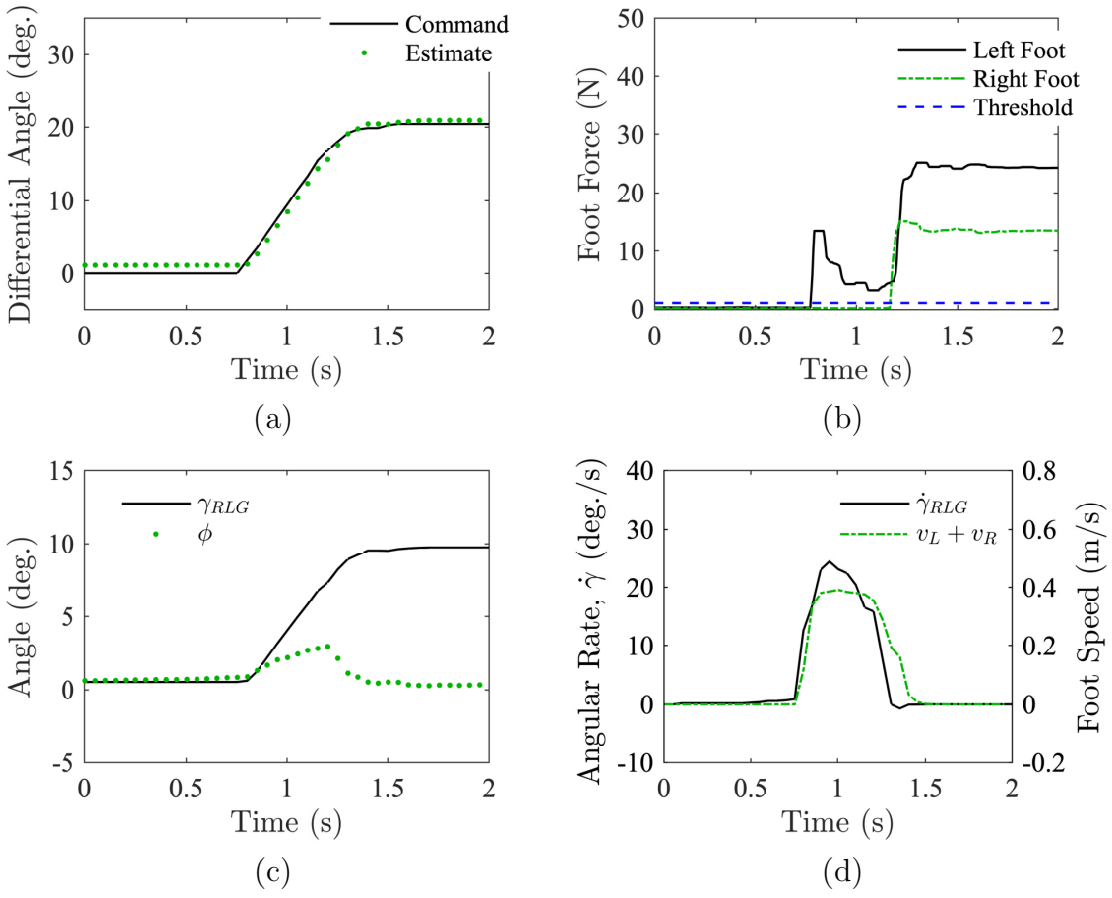

Figure 4.6: (a) Shows multi-sensor fusion control differential angle response. (b) Shows foot force response. (c) Illustrates RLG absorbed ground angle, (γ_{RLG}), estimated ground angle ($\hat{\gamma}$), and roll feedback (ϕ). (d) Shows ground angle absorption rate ($\dot{\gamma}_{RLG}$) and RLG combined left and right foot vertical displacement rate (v_L+v_R).

acceptable until the roll crossses the allowable threshold of 0.5° (Figure 4.6(c)). Once this threshold is crossed, the RLG roll feedback control reacts to minimize the roll

down to $\pm 0.5^\circ$ (Figure 4.6(a)-(b)). In this case, the RLG absorbed up to 10° of slope using the sensor-fused control with roll as the primary feedback channel. Note how in this case the controller does not lock the brake. The controller is experimentally implemented at this stage to leave the brake open even if $|\phi| < \phi_{DB}$ and $\hat{\theta}_{L/R} \approx \theta_0$ in case of continued landing surface motion. This is purely for the development cycle, and it is not a usable feature for operation.

4.2.1 Status Monitoring and Fault Detection

A critical component of this thesis is the tightly integrated status monitoring and fault detection. This contribution enabled the experimental integration and testing of the cable-driven, four-bar linkage RLG, force sensors, and the sensor-fused control on a commercial UAV. The status monitoring and fault detection logic is included within the foot-force and leg-angle estimators of Figure 4.5. This architecture is easily extendable to the AHRS estimation routine as well, if it is done by the RLG computing architecture. Figure 4.7 illustrates the logic generalized across the sensor measurement and state estimation subsystems, and it flows from the top down. One or more measurements are input to the monitor where self-reporting status indicators are monitored for each sensor. Most modern digital sensors have onboard state machines that output self-reported operation status along with any measurements. Additionally, the monitor checks whether the values measured are within acceptable ranges. This is particularly important for measurements of multiple, redundant sensors, where all sensor measurements may be compared against one another. If any sensor fails to pass the status and measurement checks, fault detection logic initiates. Anytime redundant sensors exist, the fault detection logic checks whether a redundant sensor is operational. If a redundant sensor or sensors continue to operate within expected bounds, then only a warning flag is set and reported. This alerts the control logic and users of a loss of sensor data. Error flags are set and reported to

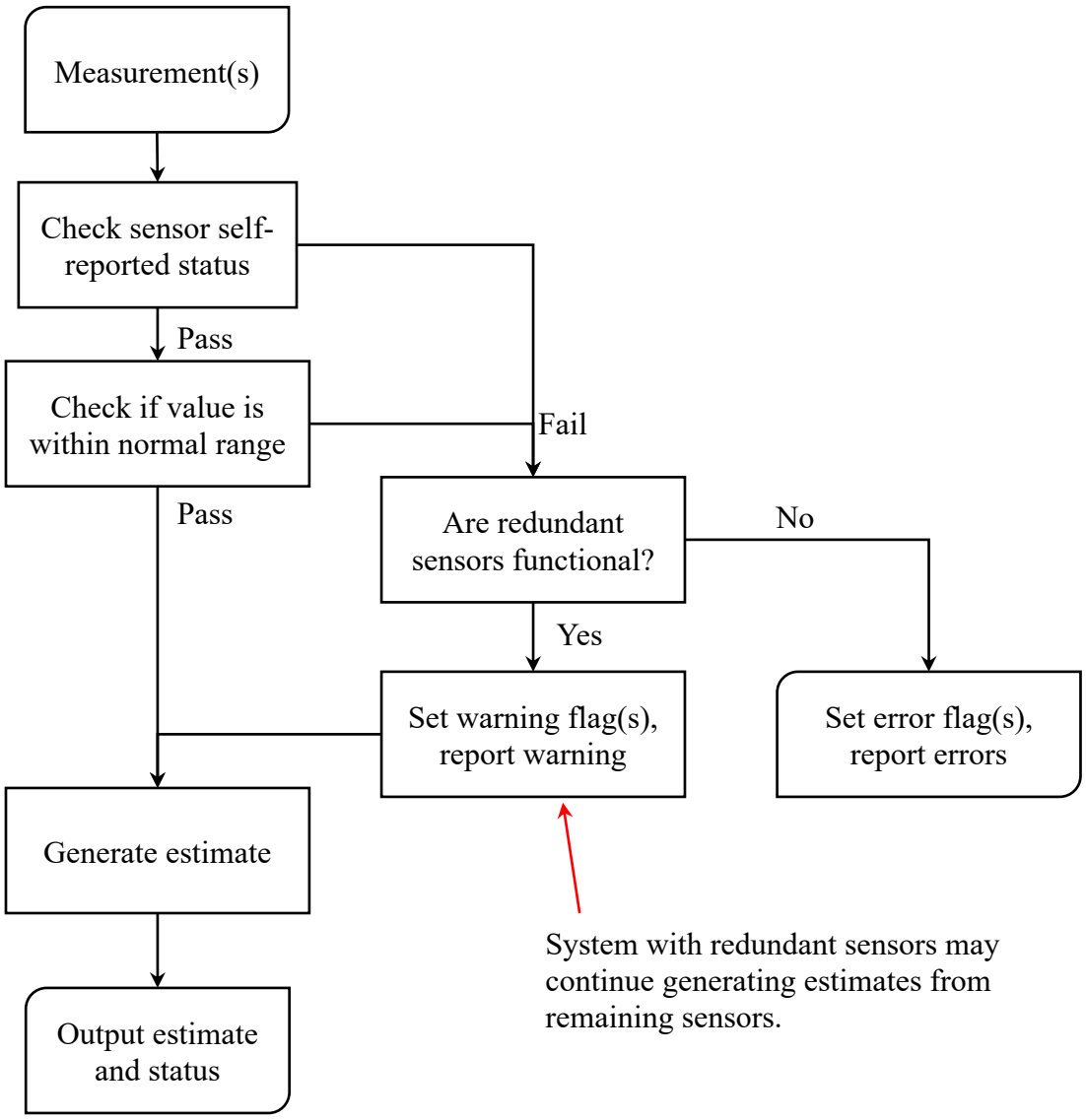

Figure 4.7: Generalized integrated sensor health monitor tree for fault tolerance.

the software anytime multiple sensors fail their health checks and they are meant to be redundant to one another. No measurement output is reported once an error flag is raised because feedback control stops immediately.

The status monitoring and fault detection system also includes a real-time memory health monitor. The entirety of this health monitor focuses on embedded system firmware and hardware. Therefore, the exact implementation is specific to the hardware platform. A generalized form of this monitor is depicted in Figure 4.8. Memory

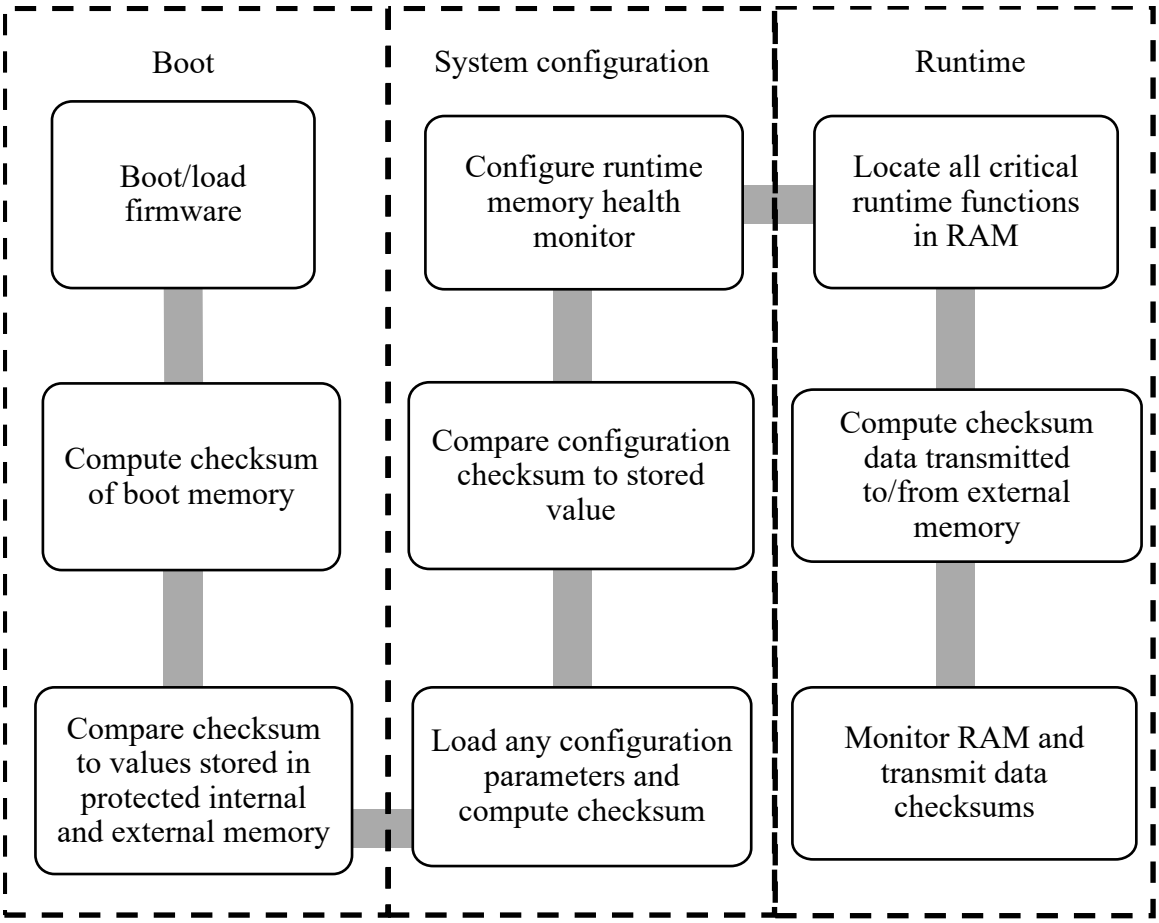

Figure 4.8: Embedded system memory monitor with specific checksum computations and consistency checks during boot, system configuration, and runtime.

status and health monitoring begins once an embedded system's firmware boots. At boot, the system loads the desired program from memory (usually FLASH memory). The memory health monitor computes and compares a cyclic redundant checksum (CRC) of the boot memory to a pre-computed checksum of the boot memory located elsewhere in the micro-processor's non-volatile memory and from an external source, such as an SD card. The author recommends a partitioned CRC-32 method since the program is typically booted from partition frames on an embedded system [96]. CRC-32 methods aid in the determination of whether a memory source has corruption, but it cannot determine the cause of or fix corruption. This process assumes the program boots from internal non-volatile memory. Once the program boots and passes, system

configuration begins. The program is allowed to initialize any tasks and configuration parameters (such as control gains), then the health monitor computes a checksum of all configuration parameters and compares them to a pre-computed value in a similar manner as the boot memory checksum confirmation.

Similar to the boot memory check, a CRC checksum helps determine if any configuration parameters are incorrect at the bit level during system configuration. Finally, a cyclic runtime health monitor is configured and started. This real-time checksum comparison tool is generalized to aid in the verification of data to/from external sensors, radios, and memory devices. Most consumer-off-the-shelf (COTS) sensors, radios, and memory devices support checksum verification during data transfer, but it is not guaranteed that all components will. An error flag is set anytime an error is found in a checksum during repeated attempts at data transfer. If the error occurs during boot or configuration, the RLG controller will not operate because the system cannot be certain that the loaded software and configuration parameters are correct. Errors during runtime require multiple failures before an error flag is set, dependent on the likelihood for one-off data transfer errors. Data transfer errors are dependent on the communication protocol used (such as SPI and CAN) and noise in the environment.

4.2.2 Comparison to PBC

Sensor-fused control and robust software presented here offers four differences compared to the parking brake class of controllers from previous works. Table 4.1 summarizes these differences. First, the new controller adds fuselage orientation (and angular rates if desired) into the feedback control loop. This single addition removes the observability and controllability constraints of the PBC. It does so by incorporating observable states so the aircraft orientation is controllable on dynamic landing surfaces and during high descent rate dynamic landings with any amount of

Table 4.1: Summary of the differences between parking brake RLG controllers and the contributed sensor-fused RLG control.

PBC	Roll and Force Fused Control
1. Simple baseline design with contact feedback	1. Contact and fuselage orientation feedback
2. Poor controllability for dynamic landing surfaces	2. Controllable aircraft orientation on dynamic surfaces
3. Poor controllability for landings with bounces	3. Control is uninterrupted by bounces
4. Basic (if any) robust software design	4. Status and memory fault detection

bouncing. Finally, the status monitoring and fault detection additions enable robust, fault-tolerant operation.

CHAPTER 5
DYNAMIC SIMULATION TOOLS

Simulation tools are vital to the design and performance expectations of aerospace systems because experimental aircraft carry a high cost and risk to personnel and property. This chapter elucidates the simulation tools implemented during the design and creation of RLG technologies for the remainder of this dissertation. Figure 5.1 shows the high-level steps used to simulate rotorcraft with RLG. Important factors include landing platform/surface dynamics and continuous-time, rigid-body dynamics simulation. Within rigid-body dynamics simulation, modular and user-defined subsystem models are necessary to study the effectiveness of RLG technologies.

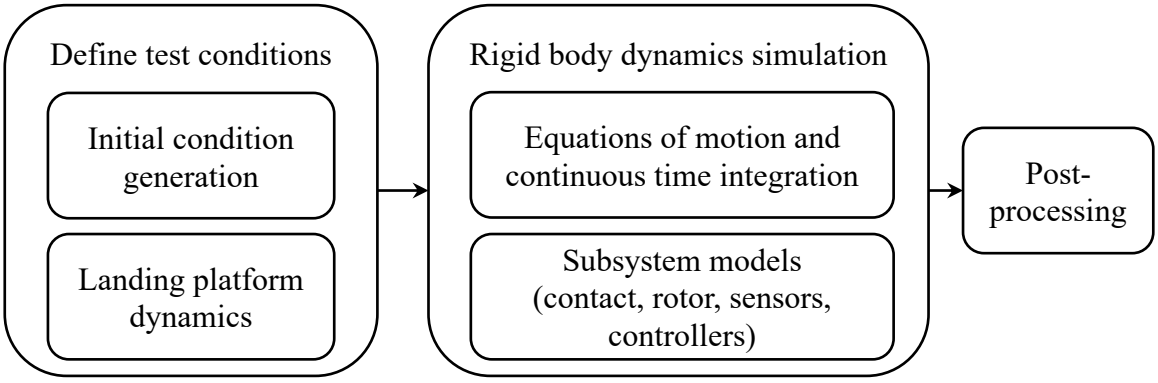

Figure 5.1: High-level procedure used to simulate new RLG technologies for rotorcraft.

This chapter is outlined as follows: First, a set of models for ground contact, rotor thrust, sensor measurements, and direct current (DC) motors are presented as modules for dynamic simulators to enhance the accuracy of results. Next, a set of landing platform motion simulation programs are described as aids to study rotorcraft landings on static or dynamic surfaces. Two rigid-body simulation tools are then detailed in the last two sections of the chapter. The first rigid-body dynamics simulator is

a four DoF model of a rotorcraft with cable-driven, four-bar linkage RLG restricted to planar motion. The equations for this tool are derived using Lagrange analytic mechanics. This tool is a fast-processing, low-fidelity design tool for controllers and sensor state estimation algorithms. The final tool is a multibody dynamics simulation environment with a pedigree of accurately simulating real system dynamics using constraint stabilization.

5.1 Subsystem Models

Rigid-body dynamic simulation tools will be introduced in Sections 5.3 and 5.4. They share a number of subsystem models that may be included or neglected during the force and moment calculations or controller design in a modular manner. Subsystem models include a method to generate ground contact forces using a physics-based model, a first-order rotor thrust model, a gaussian white noise model with bias for sensor measurements, and a DC motor performance prediction model.

5.1.1 Ground Contact

Ground contact is modeled as a standard linear solid (SLS) with friction. SLS models mimic ideal viscoelastic behavior with a single relaxation time of a material [97, 98]. The physical structure of the contact model, as depicted in Figure 5.2, requires the normal force time derivative at any given time to be computed. This normal force derivative is calculated as

$$\dot{F} = -\left[\frac{2k_v + k}{c}\right] F + \frac{k\ k_v}{c}\delta + k_v\dot{\delta} \tag{5.1}$$

for each point that is in contact. At each time step of the simulation, the displacement into the ground surface, δ, and the velocity of the displacement, $\dot{\delta}$, are computed and input into Equation (5.1) based on the relative motion between the ground and

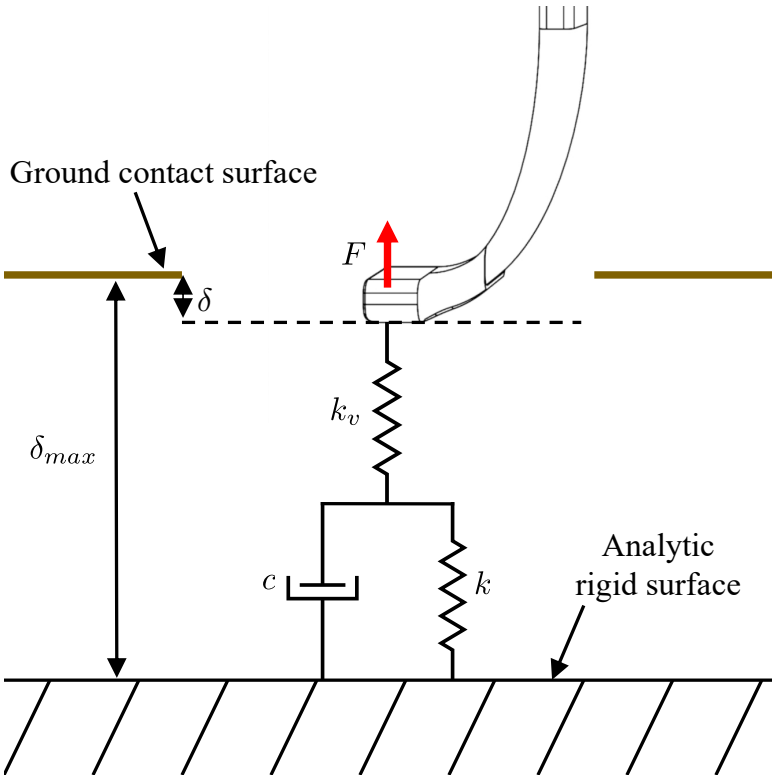

Figure 5.2: Diagram of the SLS ground contact model shown with a force normal to the plane of contact for the case of a static landing surface.

contact point. A coefficient of friction, μ, is multiplied by the normal force computation for tangential sliding force. While not a perfect assumption of contact, it is a suitable and fast model of contact for RLG contact and feedback control. Values for the spring and damper parameters will be presented in Chapter 6 when tuned for simulations of a commercial UAV.

5.1.2 Rotor Thrust Model

A first-order rotor thrust model is pertinent to this work because of the transient period of load reduction when a pilot reduces rotor collective during a landing. This transient period of load reduction puts the rotorcraft at risk of dynamic rollover on a landing surface because the rotor thrust may act as a destabilizing torque about the contact point. The model assumes that the rotor collective and cyclic react as first-order models on the commanded inputs. Prior work by Kim and Costello [75]

detailed this rotor model in the context of a pilot control model. With uncertainty in how pilot control inputs are mapped or filtered, the pilot model was neglected here, and a nominal rotor time constant of 0.75 s was chosen. This is meant to provide an ideal time delay between pilot commands and rotor thrust response. Variations on this time constant for understanding dynamic rollover of an example rotorcraft will be presented in Chapter 6. The complete rotor model then follows as

$$\tau_T \dot{T} + T = T_c, \tag{5.2}$$

$$\tau_\eta \dot{\eta}_{long} + \eta_{long} = \eta_{long_c}, \tag{5.3}$$

$$\tau_\eta \dot{\eta}_{lat} + \eta_{lat} = \eta_{long_c}, \tag{5.4}$$

where T is the rotor thrust, η_{long} is the thrust angle along the rotorcraft longitudinal plane, and η_{lat} is the thrust angle along the rotorcraft lateral plane. The angles η_{long} and η_{lat} stem from cyclic input to the rotor, but they are not actively controlled within this work's simulations.

5.1.3 Sensor Model

Sensor noise simulated within this work is modeled as a stochastic process; specifically, gaussian white noise [99]. The type of white noise requires a user or manufacturer defined mean, $\bar{v}$, and variance, σ_v^2, of each sensor. Random numbers are generated from the Gaussian probability density function defined as

$$f_v(v) = \frac{1}{\sigma\sqrt{2\pi}} e^{\left[-(v-\bar{v})^2/\left(2\sigma_v^2\right)\right]}. \tag{5.5}$$

Modern software language libraries include random number generators given a probability density function and any required parameters: in this case, $\bar{v}$ and σ_v^2. The discrete sensor measurement, y_k, is then sampled from the model at a predefined

measurement rate as

$$y_k = x_k + v_k, \tag{5.6}$$

where x_k is the state and v_k is the sensor's Gaussian white noise at the simulation's k'th iteration.

5.1.4 Direct Current Motor Model

DC motors have a generalized performance boundary that tracks a linear reduction in speed as the load torque increases, as illustrated in Figure 5.3. Any speed and torque combination under the curve may be achieved from pulse-width-modulating (PWM) the voltage applied across the motor windings. This generates the achievable performance region shaded red in the figure. The speed-torque performance boundary

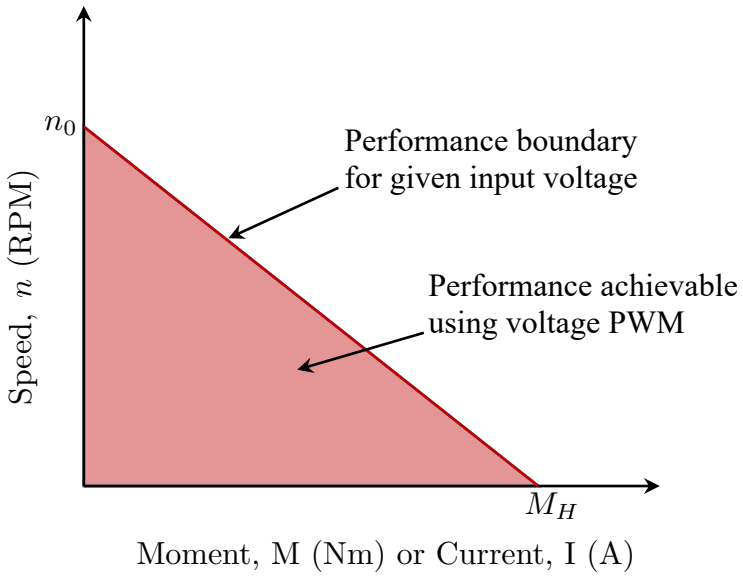

Figure 5.3: Generalized DC motor speed-torque performance curve.

is defined by the linear relationship

$$n_M = k_n \, V_M - \frac{\Delta n}{\Delta M} \, M, \tag{5.7}$$

where n_M is the maximum speed given a load torque, k_n is the motor's speed constant, V_M is the applied DC voltage, and M is the load torque. The free-spinning speed of the motor, n_0, is defined as

$$n_0 = k_n \, V_M, \tag{5.8}$$

and the stall torque, the lowest torque for which the motor cannot spin, is defined as M_H. Given a constant input DC voltage (no voltage dropouts caused by current changes), Equation 5.7 is reconfigured as

$$n_M = k_n \, V_M - \frac{n_0}{M_H} \, M. \tag{5.9}$$

Using a motor's specification, the performance boundary may be generated for an applied DC voltage. This dissertation assumes that the motor driver in use conducts speed control using PWM to reach speed and torque values beneath the performance boundary. This extends validity across brushless and brushed DC motors.

Transient dynamics of acceleration are as pertinent to the modeling of DC motors for RLG drivetrains as the speed-torque relationship. These dynamics determine the response bandwidth of the drivetrain, which bounds the landing speeds allowable for the system. The angular acceleration of a motor under a given load is

$$\alpha_{max} = \frac{M}{J_R + J_L}, \tag{5.10}$$

where α is the angular acceleration, M is the load torque, J_R is the moment of inertia of the motor, and J_L is the mass moment of inertia of the load. Components that make up the load inertia include any gearhead mounted to the motor in addition to the inertia of the winch or spool in the case of cable-driven, four-bar linkage RLG. All of these load inertias are simple to calculate or retrieve from commercial manufacturers.

The final aspect of DC motor modeling pertinent to RLG drivetrain design is the

thermal limitations of the motor windings. Some amount of power flowing through the motor is inevitably lost to heat. As the windings in the motor expand and deform from heating, they are less effective at generating the magnetic fields to drive the rotor. One method to model the limitations of a motor is to track motor overload [100]. Motor overload, K, is defined as

$$K = I_M/I_N\sqrt{\frac{T_{max} - 25°\text{C}}{T_{max} - T_A}\frac{R_{th1}}{R_{th1} + R_{th2}}}, \tag{5.11}$$

where I_N is the nominal current (the current corresponding to load torque for continuous use), T_{max} is the maximum winding temperature of the motor, R_{th1} is the winding thermal resistance, R_{th2} is the motor housing's thermal resistance. Each constant is generally provided by a motor manufacturer. If K is less than 1, then T_{max} is not reached during short-term operation. If K is greater or equal to 1, then T_{max} can be met in short-term operation. In this scenario, the allowable time for the motor to operate at a given current is given by

$$t_{on} = \tau_w \; ln\left[\frac{K^2}{K^2 - 1}\right], \tag{5.12}$$

where τ_w is the winding thermal time constant. The time the motor spends in an overload conditions is tracked by the subsystem model. Whenever the motor spends too much time in an overload condition, the maximum current is scaled by

$$I_{max} = KI_N\sqrt{\frac{T_{max} - T_S}{T_{max} - 25°\text{C}}\frac{R_{th1} + R_{th2}}{R_{th1}}}, \text{ where} \tag{5.13}$$

$$T_S = T_{max}\left[1 - e^{-\frac{t_{on}}{\tau_w}}\right]. \tag{5.14}$$

In (5.14), t_{on} is the amount of time speed in an overload condition where the windings and stator approach T_{max}. Figure 5.4 illustrates how this model integrates with other simulation tools in this dissertation. Another program sends the current motor speed,

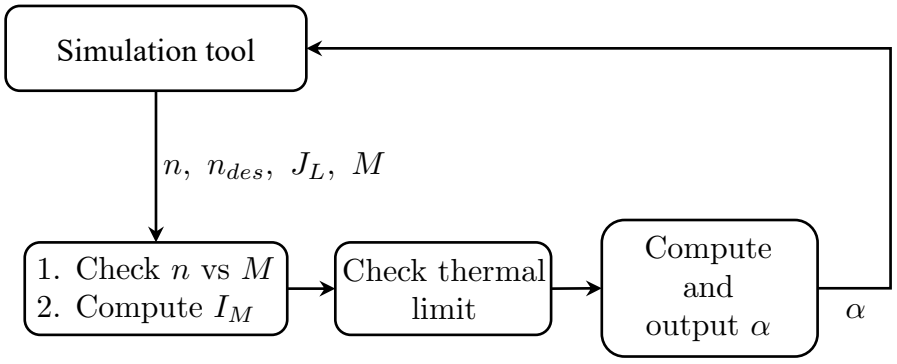

Figure 5.4: Diagram of how the motor model integrates with existing simulation tools as a module.

the desired speed (assuming a speed controlled system), the load inertia, and the load torque. Each step of the DC motor model is designed so that the output, α, is an accurate acceleration of the motor, given the loading conditions. This model assumes the simulation tool will integrate α to motor speed and position along with any rigid-body states.

5.2 Landing Platform Motion Generation Program

Three types of landing surfaces were simulated and experimented with in this work. The first is a static surface. This is the most basic landing surface for RLG to interact with, and it has been extensively simulated and tested. The remainder of this section describes sinusoidal and maritime ship deck platform simulation programs, and it explains how their motion is generated for later simulation and experiments.

5.2.1 Sinusoidal Platform Dynamics

All platforms that undergo sinusoidal motion in this work do so aligned with the roll axis of an aircraft. Roll sinusoidal motion is described by

$$\phi = A\ sin\left(2\pi f(t + t_0)\right), \tag{5.15}$$

where A is the desired sine wave amplitude, f is the frequency, t is the current simulation/experiment time, and t_0 is the time shift required to start with a desired roll angle. This assumes the oscillation always occurs around a 0° center point (i.e. no bias). In the simulation tool, a user defines the desired amplitude, A, initial roll angle, ϕ_0, and the maximum angular rate desired, $\dot{\phi}_r$. The tool determines t_0 as the first time where the sinusoid is the desired roll angle from the amplitude and initial roll angle inputs. Then, the frequency is computed as

$$f = \frac{\dot{\phi}_r}{(2\pi A)}. \tag{5.16}$$

A sine wave is generated for the simulation using the resultant frequency, f, and time shift, t_0, and output to the desired rigid body dynamics tool. Examples of this will be presented in Chapter 7.

5.2.2 Ship Deck Dynamics

A ship deck simulation tool provides realistic landing deck with six DoF motion, given the vessel's geometry, mass properties, and Sea State parameters. This simulation tool is crucial to understanding the benefits of a roll-fused RLG controller for rotorcraft operating on maritime ship decks. The ship motion simulation consists of two parts: the Ship Motion Program (SMP) [101] and the Simulation Time History (STH) [102]. Given a ship with specified dimensions and hull characteristics, the SMP generates six DoF response transfer functions. STH program uses the transfer functions from the SMP to predict the ship motion from to ocean waves. This ship motion simulation then generates deck motion as a function of user-input Sea State parameters.

The origin of the ship is located at the intersection of the ship's forward perpendicular, centerline, and baseline. This point is easily identifiable and does not vary with changes in ship draft or trim. The direction of the x, y, and z coordinates

from the ship's origin are depicted in Figure 5.5. Inputs to the simulation are the

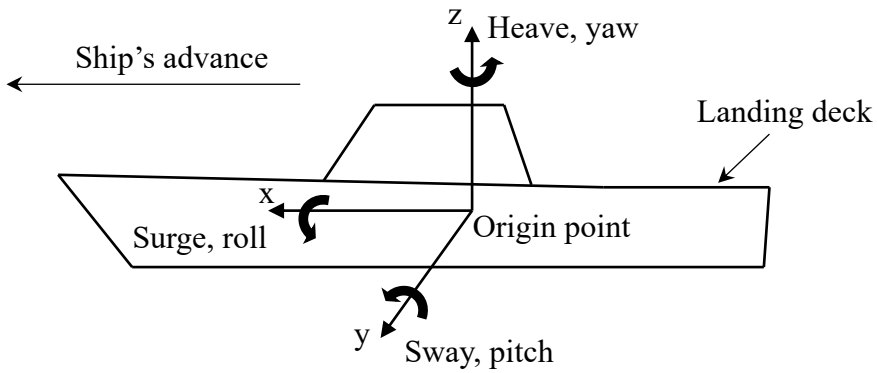

Figure 5.5: SMP, STH simulation tool CG location and motion definitions.

hull characteristics (ship length, draft, and trim). The particular ship configuration used to generate data in this dissertation is a Arleigh-Burke class naval destroyer as illustrated in Figure 5.6(a). It is ≈154 m in length with a draft of 7 m and trim set to 0 m. With this data, SMP generates the ship's six DoF response transfer functions for regular waves. It also provides absolute and relative six DoF information (surge, sway, heave, roll, pitch and yaw) of the ship at the origin and other desired points on the ship. The STH provides realistic, random wave time histories of six DoF ship responses using the regular wave response transfer functions obtained from the SMP. Random waves are simulated using a two-parameter Bretschneider wave spectral model to define the frequency content of the random sea waves [104]. The two parameters used are the significant wave height and the modal (peak-to-peak) wave period. Strip theory is used to obtain the response for a ship advancing at constant forward speed with arbitrary heading in regular sinusoidal waves. The Access Time History Computer Program (ACTH) then uses ship origin responses from the STH to generate response time histories at other locations on the ship. The inputs to the STH are the transfer functions for a particular ship generated by the SMP, Sea State (significant wave height, mean wave frequency), and the steaming condition (ship heading relative to predominant wave direction, ship speed). The outputs from

(a)

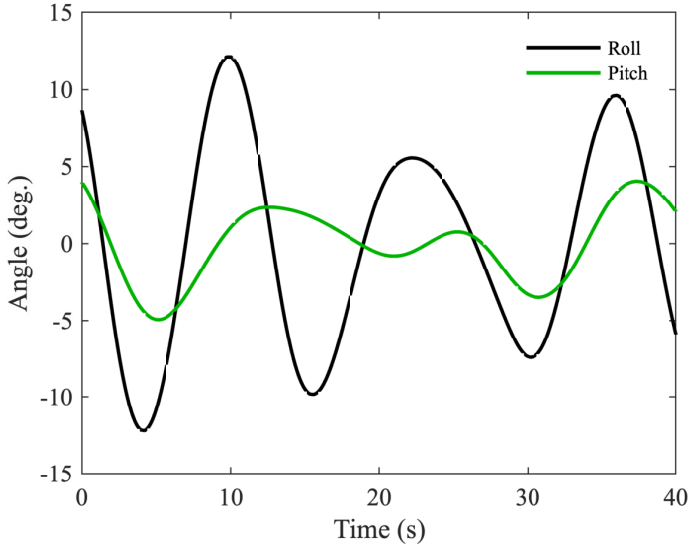

(b)

Figure 5.6: (a) Arleigh-Burke class navel vessel [103] and (b) its roll and pitch motion from a Sea State 6 simulation.

the STH are six DoF time histories for motion of the helicopter landing surface of the ship.

Nominal ranges of wave height and wave modal period are correlated to standard Sea State (SS) codes. Table 5.1 lists the SS parameters from SS 3, SS5, and SS 6. These values were retrieved from the nominal conditions listed by Bales [105] as

measured in the North Pacific. Simulations in this dissertation use the largest wave height and average wave modal period for a given SS code. An example of roll and

Table 5.1: Sea State parameters used for simulations and ground tests

Sea State	Wave Height (m)	Modal Period (s)
3	0.50 - 1.25	5.20-15.5 (7.50 mean)
5	2.50 - 4.00	7.20-16.4 (9.70 mean)
6	4.00 - 6.00	9.30-16.5 (13.8 mean)

pitch data using Sea State 6 wave conditions with STH is shown in Figure 5.6(b).

5.3 Lagrange Four DoF Simulation

A Lagrange analytic mechanics simulation tool was developed in Matlab to aid in rapid sensor, actuator, and controller selection of design iterations. This method requires unconstrained coordinates to develop unconstrained equations of motion. The unconstrained equations of motion for the RLG system designed in Chapter 2 restricted to planar motion yields four DoF. Three DoF ($y,\ z,\ \phi$) stem from planar motion of a rigid fuselage, and the final DoF, β, is the cable spool's rotation angle which changes the cable's center point. It should be noted that standard aerospace nomenclature is used including the use of right-handed North (I) - East (J) - Down (K) (NED) reference frame orientation for the fuselage and bodies modeled in all dynamic simulations of this work. Figure 5.7 diagrams this reduced DoF dynamic system and the unconstrained states. The mechanical design of the RLG presented in Chapter 2 uses the spool's rotation angle, β, to determine the cable's center point. This motion drives a single DoF of the legs relative to the fuselage.

The Lagrange equations of motion derivation follows the generalized, unconstrained procedure presented by Meirovitch [106]. The equations of motion were

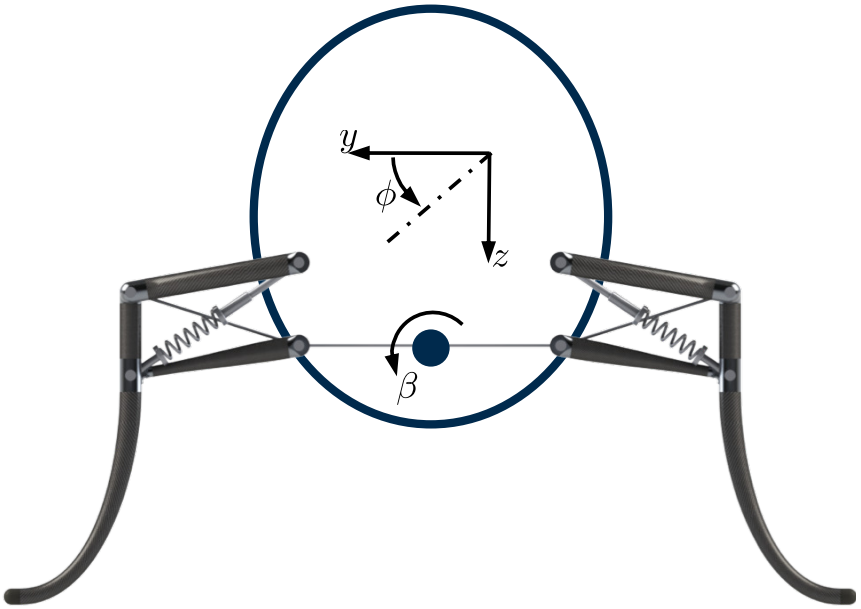

Figure 5.7: Diagram of the four DoF model states ($y,\ z,\ \phi,\ \beta$).

derived from

$$\frac{d}{dt}\left(\frac{\partial T}{\partial \dot{q}_i}\right) - \frac{\partial T}{\partial q_i} + \frac{\partial V}{\partial \dot{q}_i} = Q_i,\ q_i \rightarrow \{y, z, \phi, \beta\}. \tag{5.17}$$

In (5.17), T is the system's kinetic energy, V is the system's potential energy, Q_i are the generalized forces acting upon the system's bodies, and q_i are the unconstrained states. Each leg mass model uses the landing gear inertial mass properties to make the simulation as accurate as possible. The kinetic energy term is formulated with each component body's kinetic energy as

$$T = T_{ac} + T_{c_l} + T_{c_r} + T_{c_l} + T_{f_l} + T_{f_r} + T_{l_l} + T_{l_r}.$$

In this equation, the subscript ac denotes the aircraft, while c is a crank, f is a follower, and l is a leg. The subscripts l and r simply denote the left- or right-hand side of the aircraft (from the pilot's seat). The kinetic energy term for the aircraft is

derived as

$$T_{ac} = \frac{1}{2}\left[I_{ac}\right]\left(\vec{\omega}_{ac}\cdot\vec{\omega}_{ac}\right) + \frac{1}{2}m_{ac}\left(\vec{v}_{ac}\cdot\vec{v}_{ac}\right);$$
$$\rightarrow \vec{\omega}_{ac/I} = \left\{\dot{\phi} \quad 0 \quad 0\right\}^T, \quad \vec{v}_{ac} = \left\{0 \quad \dot{y} \quad \dot{z}\right\}^T.$$

These terms include the rotation and translation kinetic energy of the rotorcraft fuselage modeled as a rigid body. The remaining bodies are skipped for brevity, but the process for each body is conducted as follows

$$T_{l_r} = \frac{1}{2}\left[I_{l_r}\right]\left(\vec{\omega}_{l_r}\cdot\vec{\omega}_{l_r}\right) + \frac{1}{2}m_{l_r}\left(\vec{v}_{l_r}\cdot\vec{v}_{l_r}\right)$$
$$\rightarrow \vec{\omega}_{l_r/I} = \vec{\omega}_{ac/I} + \vec{\omega}_{c_r/ac} + \vec{\omega}_{l_r/c_r}$$
$$\rightarrow \vec{v}_{l_{r,cg}} = \vec{v}_{c_{r,cg}} + \vec{\omega}_{c_r/I}\times\vec{r}_{c_{r,cg}\rightarrow l_{r,joint}} + \vec{\omega}_{l_r/I}\times\vec{r}_{l_{r,joint}\rightarrow l_{r,cg}},$$

where this is the derivation for the *right leg*. Note the use of the vector derivative transport theorem formulated as the two points fixed on a rigid body equation to derive the right leg's CG velocity. This type of derivation is necessary for each body in the system using the unconstrained coordinates, q_i.

The system's potential energy, V, is broken down by each body to form the total. This is written as

$$V = V_{ac} + V_{c_l} + V_{c_r} + V_{c_l} + V_{f_l} + V_{f_r} + V_{l_l} + V_{l_r}.$$

Each component's potential energy is found to follow the same general form, written

as

$$V_{ac} = gm_{ac}z$$

$$...$$

$$V_{l_r} = gm_{l_r}z_{l_r}.$$

The last component required is the generalized force term, Q_i. Three generalized force vectors are considered in this simulation. They are the foot contact force on the left foot, right foot, and the thrust of the rotor. They are each written in the inertial frame as

$$\begin{aligned}
\vec{F}_{toe_l} &= \begin{Bmatrix} 0 & F_{\mathrm{t,l}} & -F_{\mathrm{n,l}} \end{Bmatrix}^T \\
\vec{F}_{toe_r} &= \begin{Bmatrix} 0 & F_{\mathrm{t,r}} & -F_{\mathrm{n,r}} \end{Bmatrix}^T \\
\vec{F}_{injection} &= \begin{Bmatrix} 0 & -F_{T_t} & -F_{T_n} \end{Bmatrix}^T .
\end{aligned}$$

Note that these vectors *include* the rotation required to transfer contact and rotor thrust forces into the inertial frame. These forces are generalized for the Lagrange equation as

$$\vec{Q}_i = \vec{F}_{toe_l} \cdot \frac{d\vec{v}_{toe_l}}{dq_i} + \vec{F}_{toe_r} \cdot \frac{d\vec{v}_{toe_r}}{dq_i} + \vec{F}_{injection} \cdot \frac{d\vec{v}_{ac}}{dq_i}. \tag{5.18}$$

Equation (5.18) shows that the left and right foot contact point velocities must be computed through kinematic relations in order to compute these generalized forces. The aircraft velocity and leg rotation rates from the generalized coordinates may be used to compute each contact point's velocity. This completes the components required to compute the Lagrange equations of motion for the system. The equations of motion were generated using Mathematica tools. Then, these equations were

reoriented into the form

$$[A]\,\vec{x} = \vec{b},$$

for which MATLAB has a fast-solve solution method. The solution to this equation is updated as appropriate for continuous time integration using a fourth-order, Runge-Kutta integrator. It is important to note that this methodology does not provide any forces or moments on the joints, nor on the cable. An estimate of the cable force was approximated from the kinematic and static loads analysis methodology of Chapter 2. This method provided an estimate of the spool torque to be input in thermal modeling and torque/acceleration limits of the motor model. All other subsystem models operate normally, albeit limited to the planar motion and contact, for this tool.

5.4 Multibody Dynamics Tool

This work implements an improved multibody dynamics simulation environment similar to those used by Leylek et al. [107], Gross and Costello [108], and Kim and Costello [75]. This dissertation implements improvements from the subsystem models into the original Fortran code. The tool starts with a general form of multibody dynamic equations of motion

$$\dot{\bar{X}} = \bar{F}\left(\bar{X}\right) + [G]\,\bar{U}. \tag{5.19}$$

$\bar{X}$ is the state vector containing states from any body, $\bar{F}$ is a vector containing the Newton-Euler rigid body equations of motion for a six DoF rigid body in this relation. The general form of the Newton-Euler rigid-body equations of motion of rigid body

i using quaternion notation is

$$\dot{\bar{X}}_i = \begin{Bmatrix} \dot{x}_i \\ \dot{y}_i \\ \dot{z}_i \\ \dot{q}_{0_i} \\ \dot{q}_{1_i} \\ \dot{q}_{2_i} \\ \dot{q}_{3_i} \\ \dot{u}_i \\ \dot{v}_i \\ \dot{w}_i \\ \dot{p}_i \\ \dot{q}_i \\ \dot{r}_i \end{Bmatrix} \text{ and } \bar{F}_i\left(\bar{X}_i\right) = \begin{bmatrix} [T_{IB_i}] \begin{Bmatrix} u_i \\ v_i \\ w_i \end{Bmatrix} \\ \hdashline \frac{1}{2} \begin{bmatrix} 0 & -p_i & -q_i & -r_i \\ p_i & 0 & r_i & -q_i \\ q_i & -r_i & 0_i & p_i \\ r_i & q_i & -p_i & 0 \end{bmatrix} \begin{Bmatrix} q_{0_i} \\ q_{1_i} \\ q_{2_i} \\ q_{3_i} \end{Bmatrix} \\ \hdashline \left[M_i^{-1}\right] \begin{Bmatrix} F_{B_{i,x}} \\ F_{B_{i,y}} \\ F_{B_{i,z}} \end{Bmatrix} - \begin{Bmatrix} p \\ q \\ r \end{Bmatrix} \times \begin{Bmatrix} u \\ v \\ w \end{Bmatrix} \\ \hdashline [I_{B_i}]^{-1} \left[\begin{Bmatrix} M_{B_{i,x}} \\ M_{B_{i,y}} \\ M_{B_{i,z}} \end{Bmatrix} - \vec{\omega}_{B_i/I} \times \left([I_{B_i}] \ \vec{\omega}_{B_i/I} \right) \right] \end{bmatrix}, \tag{5.20}$$

where $x_i,\ y_i,\ z_i$ are the inertial coordinates of the body; $q_{0_i},\ q_{1_i},\ q_{2_i},\ q_{3_i}$ are the quaternion values used to transform the inertial frame coordinates to body frame coordinates; $u_i,\ v_i,\ w_i$ are the velocity components in the body frame; and $p_i,\ q_i,\ r_i$ are rotation rates of the body in the body frame. $[M_i]^{-1}$ and $[I_{B_i}]^{-1}$ are the inverses of the mass and mass moment of inertia matrices for each body. External forces and moments that act on the body are encompassed by $F_{B_x},\ F_{B_y},\ F_{B_z}$ and $M_{B_x},\ M_{B_y},\ M_{B_z}$ which denote the forces and moments in the body coordinates.

In Equation 5.19, $\bar{U}$ is a vector of constraint forces and moments that are mapped through the linear operator $[G]$ appropriately to each body. The form factor of this equation is an opportunity to apply a control algorithm to compute $\bar{U}$ with feedback linearization. In order to compute $\bar{U}$ with feedback linearization, the constraints must be characterized. The set of translation and rotation constraints for each body's

interactions at joints may be defined for the given dynamic system then reconfigured into error equations such that

$$\bar{E}(\bar{X}) = \bar{0}, \tag{5.21}$$

where $\bar{E}$ contains the constraint error equations which the controller will track and minimize. Table 5.2 lists the table of joint types, their number of constraints, and the DoF for each joint included within the simulation tool that are relevant to this dissertation. The desired constraint stabilization controller is derived from the first and

Table 5.2: Types of joints, their constraints, and DoF relevant to this work

Joint type	Constraints	DoF
Rigid	3 position, 3 rotation	None
Pin/Hinge	3 position, 2 rotation	One axis of rotation
Two Axis Hinge	3 position, 1 rotation	Two axes of rotation
Gimbal	3 position	Three axes of rotation

second derivatives of this constraint error equation vector. Taking the first derivative of Equation (5.21) yields

$$\dot{\bar{E}}(\bar{X}) = \left(\frac{\partial \bar{E}}{\partial \bar{X}}\right)\left(\bar{F}\left(\bar{X}\right) + [G]\,\bar{U}\right). \tag{5.22}$$

Computation of the constraint error derivatives must be done with care. A detailed approach to the derivation of $\dot{\bar{E}}$ and any special care that must be taken is available in [109]. The second derivative of $\bar{E}$ follows as

$$\ddot{\bar{E}}(\bar{X}) = \tilde{F}\left(\bar{X}\right) + \left[\tilde{G}\right]\bar{U}, \text{ where} \tag{5.23}$$

$$\tilde{F} = \frac{\partial \dot{\bar{E}}(\bar{X})}{\partial \bar{X}}\bar{F}, \tag{5.24}$$

$$\left[\tilde{G}\right] = \frac{\partial \dot{\bar{E}}(\bar{X})}{\partial \bar{X}}[G]. \tag{5.25}$$

Feedback linearization is then applied to the dynamics of the constraint equation to compute the reaction forces and moments in $\bar{U}$. The desired constraint error acceleration, Equation (5.23), is a second order system with no force input

$$\ddot{\bar{E}} + 2\zeta\omega_n\dot{\bar{E}} + \omega_n^2\bar{E} = 0. \tag{5.26}$$

Replace $\ddot{\bar{E}}$ in Equation (5.23) with Equation (5.26) and rearrange to generate $\bar{U}$ at any time step of simulation as

$$\bar{U} = -\left[\tilde{G}\right]^{-1}\left(\tilde{F} + 2\zeta\omega_n\dot{\bar{E}}(\bar{X}) + \omega_n^2\bar{E}(\bar{X})\right). \tag{5.27}$$

Proper selection of the damping ratio, ζ, and the natural frequency, ω_n, provide a stable constraint stabilization controller. The optimal values of ζ and ω_n depend on the simulation time step and system dynamics or vibration frequencies of the system, but a wide range of values maintain stable constraint errors.

Elastic joints

The constraint stabilization technique previously defined has a numerical pitfall. During the computation of reaction forces and moments, the system may increase the forces instantaneously through the chain of bodies. This is often due to an external impulse or step force. The cause is the exact solution procedure to satisfy all constraints in one time step. Elastic, translational joints offer flexibility between bodies to mimic compliant joints and bodies. This type of joint is an optional feature of the mutlibody dynamics tool so that large impulse forces propagate throughout the chain of bodies in a more realistic manner.

Instead of rigid connection points, elastic joints implement SLS elastic elements. This is the same model used for ground contact in Section 5.1 that has a single characteristic relaxation time. Relative velocity and distance between the bodies

are computed at a simulation time step and input into a relation similar to Equation (5.1). The rate of change in force between the two bodies is computed, added to the simulation's state vector, and integrated at the next iteration. The end result is a joint with tunable impact load damping, transient response, and joint flexibility. During a design and development process, joint flexibility can be determined from impact data or FEA. Both impact data and FEA were used to tune joint flexibility during the iterative design workflow of Chapter 2 and for additional simulations of the cable-driven, four-bar linkage RLG that will be presented in Chapter 6.

Basic constraint generation example

This section illustrates a brief example of constraint generation between two rigid bodies. Say that two rigid, cylindrical bars are attached together using hinge joint (see Figure 5.8). The two points, one for each body, that are connected at the joint

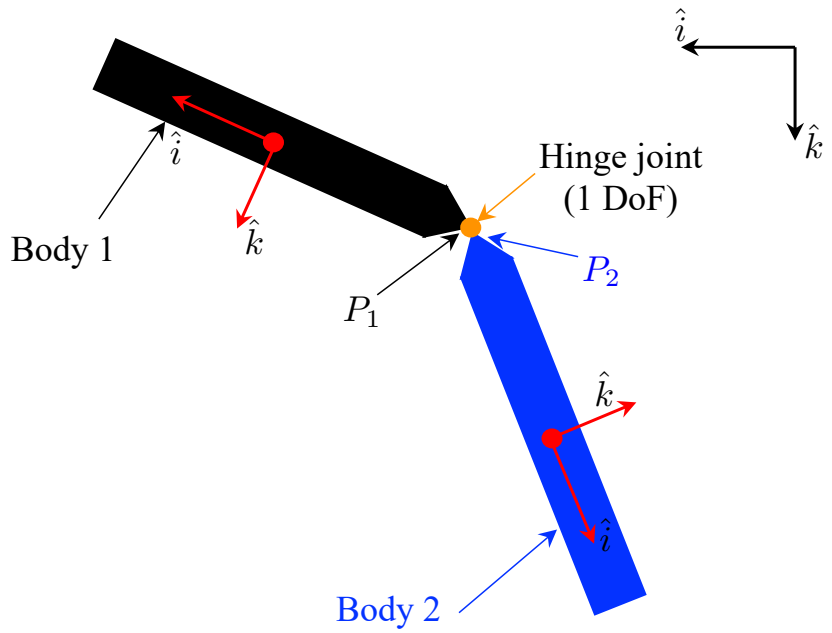

Figure 5.8: Example of a hinge joint with one DoF.

are P_1 and P_2. Note that each body has their own body coordinates relative to the inertial coordinates. The hinge joint provides one DoF, along the $\hat{j}$ axis of the

connected bodies. Otherwise, the bodies are constrained such that they may not rotate about any other axis relative to the joint. This yields five constraint error equations that may be written as

$$\begin{Bmatrix} e_1 \\ e_2 \\ e_3 \end{Bmatrix} = \vec{r}_{P_1} - \vec{r}_{P_2} \rightarrow \begin{Bmatrix} 0 \\ 0 \\ 0 \end{Bmatrix} \tag{5.28}$$

$$e_4 = \hat{j}_1 \cdot \hat{k}_2 \rightarrow 0 \tag{5.29}$$

$$e_5 = \hat{j}_1 \cdot \hat{i}_2 \rightarrow 0. \tag{5.30}$$

Consider Body 1 as the "parent, P" and Body 2 as the "child, C" in Figure 5.8, then the constraint error equations may be converted to a generalized form

$$\begin{Bmatrix} e_1 \\ e_2 \\ e_3 \end{Bmatrix} = \vec{E}_T = \vec{r}_{O \rightarrow P_J} - \vec{r}_{O \rightarrow C_J} \tag{5.31}$$

$$\begin{bmatrix} e_4 & 0 \\ 0 & e_5 \end{bmatrix} = diag(\vec{E}_R) = \Gamma_P \cdot \left([T_{P,C}] \, \Gamma_C^T \right), \text{where} \tag{5.32}$$

$$\Gamma_P = \begin{bmatrix} 0 & 1 & 0 \\ 0 & 1 & 0 \end{bmatrix}, \Gamma_C = \begin{bmatrix} 0 & 0 & 1 \\ 1 & 0 & 0 \end{bmatrix}. \tag{5.33}$$

This completes the generation of constraints and their associated error equations of this basic example. As mentioned, the derivatives must be taken with care and the generalized method to do so may be found in [109].

Subsystems and Time Integration

A fourth-order, Runge-Kutta (RK4) integrator is used to propagate continuous time states from one time step to the next. As first noted by Gross et al. [110], the compu-

tation of $\bar{U}$ is estimated once per full iteration of the RK4 (rather than four times) to improve computation time while maintaining low constraint errors. Subsystem models are included in this simulation tool in a manner compliant with Figure 5.9. The user defines which subsystems must be included in the computation of $\bar{F}(\bar{X})$ or in the user-defined sensor models and control algorithms. The user does this by setting flags in simulation input files. While this figure calls out three models specifically, any of the subsystem models from Section 5.1 may be turned on or off prior to the start of a simulation.

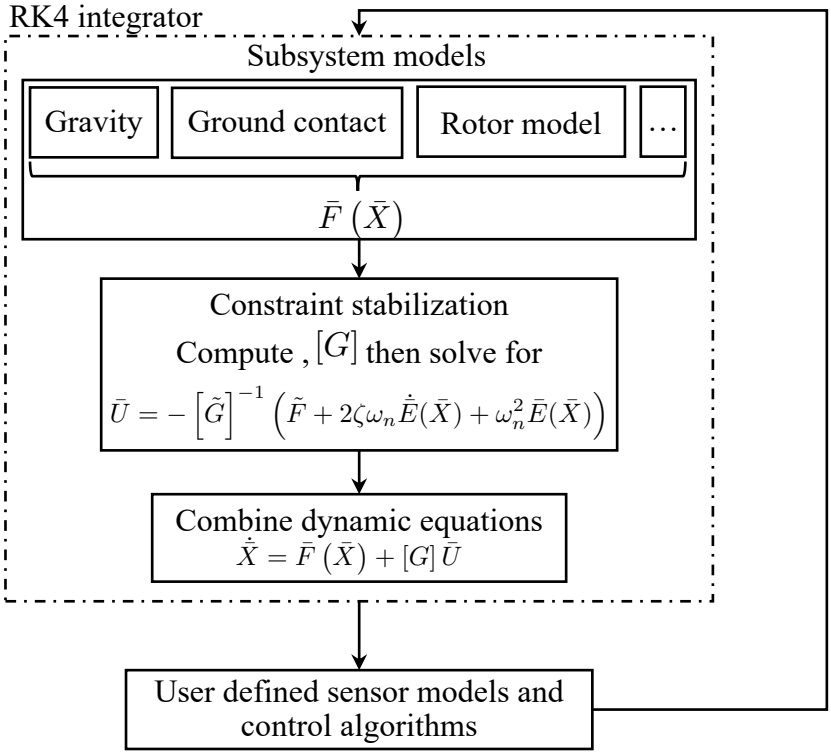

Figure 5.9: Diagram illustrating where subsystem models, user-defined sensor models, and control algorithms are incorporated into the multibody dynamics computation loop.

This chapter presented a four DoF simulation tool and a constraint stabilized multibody dynamics simulation tool. Both of these tools have enhanced, real-world accuracy enabled by incorporating subsystem physics models including ground contact; DC motor dynamics and thermal limits; first-order rotor dynamics; stochastic

sensor measurements; and dynamic platform motion. Simulation results of the cable-driven, four-bar RLG on a commercial rotorcraft will be presented in Chapter 6. These simulations will include a dynamic rollover study of the rotorcraft with locked, rigid gear; controllability studies using a COTS motor and gearbox; and a brief analysis of the motor selection methodology. Additional simulations generated through the multibody dynamics tool will be presented in Chapter 7. Those simulations include parallel comparisons to experimental system results. In that chapter, the simulations also show RLG responsiveness and usability beyond the limits of an experimental testbed.

CHAPTER 6
DESIGN AND INTEGRATION WITH THE S-100 ROTORCRAFT

6.1 The S-100 Airframe

The technologies and design tools developed in this work may be generalized across sizes of aircraft, but their implementation for the remainder of this dissertation is on the Schiebel S-100 Camcopter. The S-100 is a commercial rotorcraft platform (see Figure 6.1) with rigid, composite landing gear. It has a maximum takeoff weight

Figure 6.1: S-100 Camcopter render from Schiebel's website [111].

of 200 kg (440 lb) and a 3.4 m (11.2 ft) rotor diameter. The S-100 is primarily fielded in maritime surveillance operations, so the aircraft regularly operates on ship decks designed for manned helicopters. Its larger size (compared to the Rotor Buzz and multi-rotors from Chapter 1), unmanned semi-autonomous operation, and interactions with dynamic landing surfaces make it the ideal candidate for novel RLG technology implementation.

There are a few notable details of the S-100 landing gear configuration for RLG integration. First, the aircraft has a three-point contact plane from the tripod legs.

Two legs are located forward of the CG and one at the tail. The nominal stance has the front legs make contact with the landing surface before the tail strut, so the aircraft's neutral position on a landing surface has positive roll angle. There is also a small payload bay located above the camera pod in Figure 6.1. This payload bay provides an ideal location to house some electronics and drivetrain components of a tightly integrated RLG system.

6.2 Hardware and Software Integration

The cable-driven, four-bar mechanism design as outlined in Chapter 2 was tightly integrated into the S-100 airframe. Figure 6.2 illustrates this gear integrated in the fuselage. A white, matte paint was added to the gear to reduce the heating and lower risk of composite layers delaminating during field experiments. Sensors were added to the design at the crank-leg joints and within each foot, while the avionics and drivetrain were integrated into the payload bay.

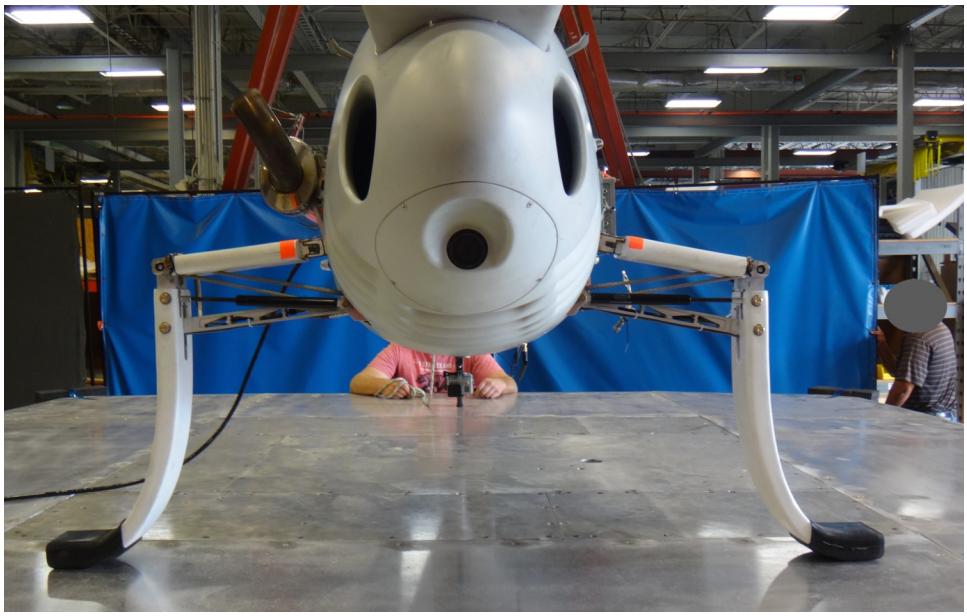

Figure 6.2: Front view of the S-100 with crashworthy, cable-driven, four-bar linkage RLG. This image is subject to Boeing Copyright, 2018. Distribution A: Approved for Public Release. Distribution Unlimited.

Figure 6.3(a) shows CAD models of the cable-driven, four-bar mechanisms, spool, drivetrain, sensor assemblies, and the RLG avionics enclosure. Each of these subsystems interconnect with mechanical joints and/or electric connections. The cable (shown in blue) begins at one shock absorber and routes through one four-bar linkage mechanism. It then routes through the spool and the second four-bar linkage mechanism, where it terminates at the second shock absorber. On each four-bar mechanism crank-leg joint are the leg-angle sensors. These provide feedback of the leg angles relative to the fuselage. Finally, each four-bar mechanism has a force sensor array located at the bottom of the leg.

Figure 6.3(b) is a high-level illustration of how the various RLG electronic components integrated into the S-100. The avionics enclosure is an aluminum enclosure that houses the RLG compute core. The RLG compute core contains all of the input and output channels for the various sensors and drivetrain components. This enclosure also houses a VectorNAV VN-100 AHRS, brushless DC (BLDC) motor driver, as well as power regulation and circuit protection components. The S-100 has a direct interface to the compute core through two general purpose input channels. These are meant for emergency mode activation. The two emergency modes activated by these inputs will be described with more detail in Section 6.2.3. Four subsystems interact with the main RLG avionics system: leg-angle encoders, foot-force sensors, RF communications, and the drivetrain. Section 6.2.1 details the force sensor and leg angle encoder subsystems and any state estimation associated with data from each subsystem. Section 6.2.2 provides a brief overview of the hot-swappable drivetrain structure and the type of drivetrain used. Finally, Section 6.2.3 presents a human-system interface that makes use of the 900 MHz radio.

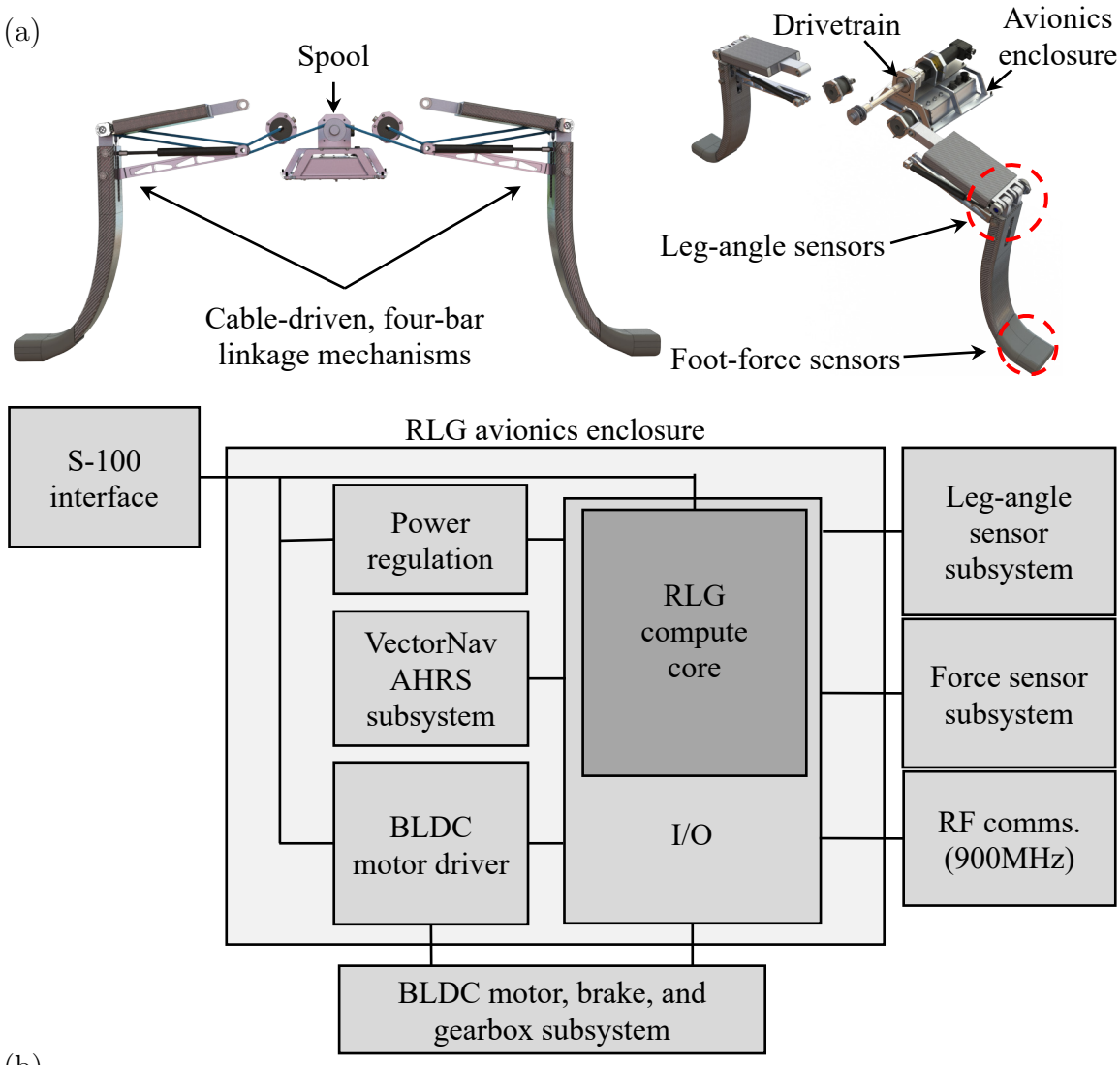

Figure 6.3: (a) Shows CAD model renders of the S-100 RLG system components. (b) Shows a high-level overview of the S-100 hardware integration.

6.2.1 Sensing

There are two state estimators running on the RLG compute core that provide accurate measurements and health status of the sensor subsystems. The first one considered is the foot-force estimator, which receives inputs from the force sensor subsystem of Figure 6.3. Four custom force sensors, designed at the end of Chapter 3, are arranged in an array for redundancy. The array configuration also provides a large coverage area of force measurements. Figure 6.4(a) presents the sensors in an array

as well as the data acquisition and state estimation board custom designed for the S-100 RLG. Exploded views of this hardware as installed into each RLG leg are illustrated in Figure 6.4(b). There is a force plate that is bolted on one end to the leg and free on the other end. The design aids the transfer of angled and point forces across the entire array of force sensors. A urethane-fiberglass composite cover was developed to protect the entire assembly and maximize the friction coefficient between the ground and leg. This leg assembly was not tested for its frequency or hysteretic response prior to ground and flight tests on the aircraft. Some frequency response data of the combined sensor, force plate, and composite cover will be presented from flight tests in Chapter 7. Similar to the recommendations in Chapter 3, future designs and integrations into rotorcraft should characterize the sensor assembly's hysteretic and frequency response.

Chapter 3 showed how sensor array sensitivity may be mapped to a second-order function and used as the measurement model for a recursive, least-squares estimator. The S-100 implementation does not treat the measurement model of the sensors in this manner. Rather, force on each foot is computed through the equation

$$\hat{F}_{L/R} = C_{F_{\tilde{P}}} \left(\tilde{P}_{L/R} - 1 \right). \tag{6.1}$$

This equation incorporates the sensor-array's linear relationship between force and normalized pressure, $\tilde{P}$, denoted as $C_{F_{\tilde{P}}}$. Nominally, the uncertainty of the force estimate is within 0.15 N (0.033 lb) based upon each individual pressure sensor's accuracy. Normalized pressure input to the force equation is computed using the following least-squares estimation [99] equation

$$\tilde{P}_{L/R} = \left(\sum_{i=1}^{4} \frac{1}{\sigma_{i_{L/R}}^2} \right)^{-1} \left(\sum_{i=1}^{4} \frac{P_{i_{L/R}}}{P_{i_0} \sigma_{i_{L/R}}^2} \right). \tag{6.2}$$

Flight software uses this equation to generate each foot's normalized pressure, $\tilde{P}$,

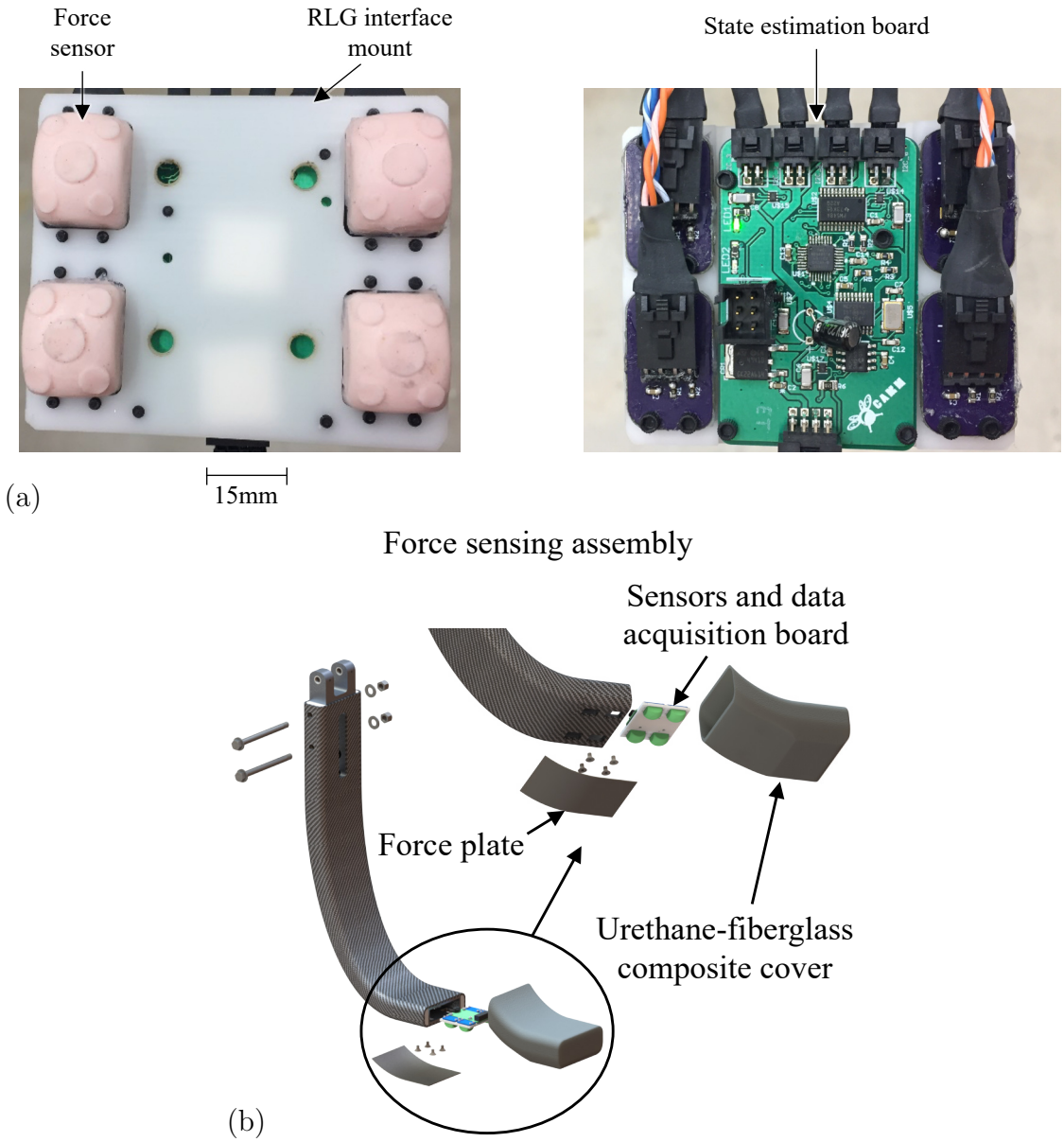

Figure 6.4: (a) Shows the S-100 RLG force sensors and data acquisition and state estimation board. (b) Shows an exploded CAD model of how the force sensor assembly installed into the S-100 RLG.

based on assumed measurement noise standard deviation, σ_i, for each individual pressure sensor. There are multiple operational scenarios when a sensor's health deteriorates. Anytime one or two sensors have a failure, a warning status flag is set by the health monitor algorithm (refer to Figure 4.7). In this case, the health monitor detects errors and understands there are redundant sensors, so it increases σ_i until

the damaged sensors have a negligible impact on the total estimate. If more than two sensors have a failure, then the error flags are reported, transmitted over the 900 MHz communication radio, and the RLG stops feedback control.

The leg-angle estimates follow a similar process to the force estimates, and integrated angle encoders provide the raw measurements to the estimator. Figure 6.5 displays a CAD rendering of the cable-driven, four-bar linkage RLG with the force sensor locations, as well as the angle encoder mount locations. As shown in the figure, there were two different angle sensors on each half of the RLG assembly. The CUI AMT203 is a digital encoder configured to output at 100 Hz with an accuracy of 0.2°, while the Honeywell 640ES series sensor is an analog encoder that was configured to have an accuracy of 0.5°. The analog sensor's output is read at 500 Hz with a moving average filter that computes an input value for the leg-angle estimator every 100 Hz. Safety of the aircraft is paramount to the system level design, and the redundancy of digital and analog encoders on each half-assembly provide triple redundancy. This measurement system is triple redundant because the orientation of one leg determines the orientation of the other leg through kinematics: a unique feature of this cable-driven RLG design. A least-squares estimation problem for the left and right leg fuselage-relative angles then follows as

$$\hat{\theta}_{L/R} = \left(\frac{1}{\sigma_D^2} + \frac{1}{\sigma_A^2} \right)^{-1} \left(\frac{\theta_{D_{L/R}}}{\sigma_D^2} + \frac{\theta_{A_{L/R}}}{\sigma_A^2} \right). \tag{6.3}$$

The standard deviation parameters, σ_D or σ_A, provide an assessment of each sensor's accuracy. The sensor health monitor will increase σ_D or σ_A to 360° for damaged or unresponsive sensors, similar to the process used on the force sensors.

The final sensor included for use in this dissertation is an AHRS. Rather than design a custom AHRS, a high quality off-the-shelf system is integrated within the RLG avionics enclosure. The VectorNav VN-100 is an industrial-grade inertial measure-

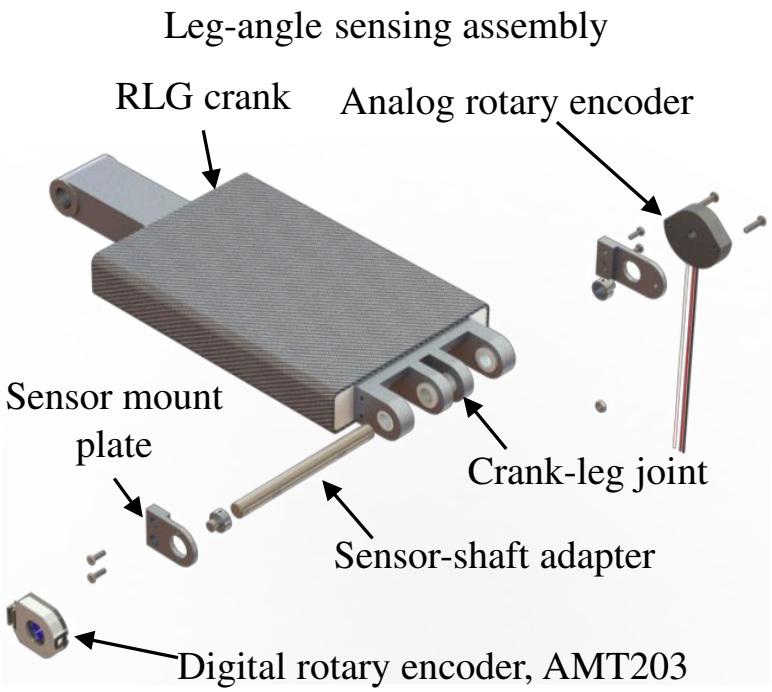

Figure 6.5: Exploded view of S-100 RLG sensor assemblies.

ment unit (IMU) and basic AHRS. It has automatic hard-iron calibration, floating point precision measurements, and industrial grade sensor encapsulation – making it an ideal off-the-shelf candidate for RLG integration. For the context of this chapter, it suffices that the sensor provides accurate roll measurements within the specifications in [112], which states the static and dynamic roll measurement accuracies are 0.5° and 1.0°, respectively. Furthermore, the sensor was aligned in the avionics enclosure such that the sensor axes matched the aircraft's coordinate system, and no additional layers of state estimation were added on top of the VN-100's estimation algorithms.

6.2.2 Drivetrain Integration

Figure 6.6 illustrates the drivetrain integration system and avionics enclosure which fit into the S-100 payload compartment. The RLG spool is driven by an adapter shaft (see Figure 6.3) that slides onto the gearbox output shaft and runs the distance between the spool and payload bay. The drivetrain, interface structure, and avionics

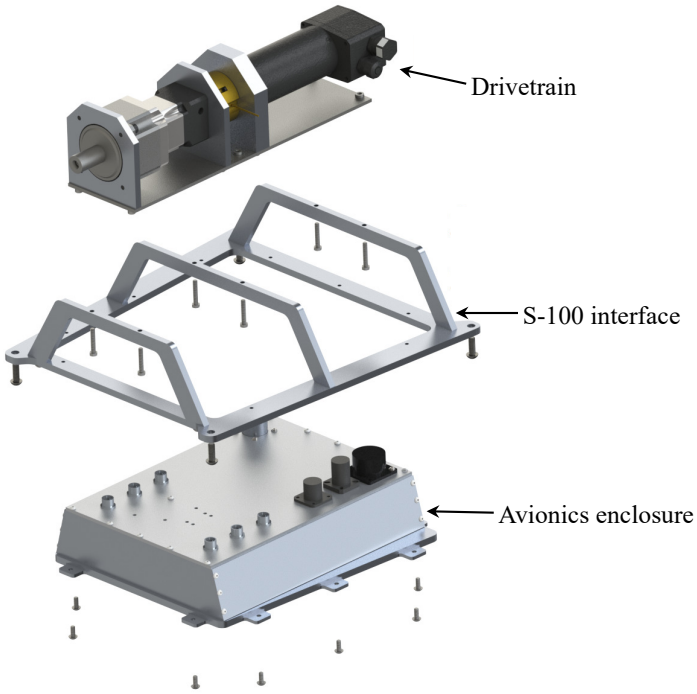

Figure 6.6: CAD model render of the drivetrain and avionics assembly of the S-100 RLG system.

are hot-swappable, hence the modular structure. This was done with the intent to change the drivetrain assembly for various motor and gearbox combinations. In practice, this was not done because the final drivetrain assembly is sufficient for landings on static and dynamic surface landings. The final drivetrain chosen though iterative design simulations is a Maxon EC45 136210 motor paired with an Apex dynamics 60:1 gearbox. A summary of the motor contenders will be presented later in this chapter.

6.2.3 Human-System Interaction

Given the number health and status monitors in the software, a human readable graphic user interface (GUI) was constructed around the available data. Figure 6.7 presents the main tab of the user interface. This GUI communicates mode and control gain settings from a user over the 900 MHz communication radio in Figure 6.3. The

Figure 6.7: Main RLG feedback and control tab of the GUI.

raw feedback data from each sensor is displayed on the right side for a user to monitor the data, and calibration buttons are provided to set the zero point of each sensor. On the left side are buttons for the user to select the operational mode of the gear. Locked and Free modes are user-selected operation modes where the brake remains locked or unlocked with no feedback control. Slope mode is for PBC feedback control landings (see Section 4.1). Motion Table mode engages the sensor-fused control (see Section 4.2). Motion Check and RTN are two modes for checking the functionality of sensors and the drivetrain prior to flight/ground tests. Note that each status monitor on the left is illuminated with a light green background. This color and illumination is designed for a user to quickly determine if any status or health monitors have warning or error flags set. Warning and error flags illuminate the status monitors with yellow and red backgrounds, respectively.

Figure 6.8 illustrates an example of when the RLG health monitors detect a prob-

lem and set a warning flag. The right leg's digital encoder was purposefully disconnected in this scenario. Since this is a redundant sensor, the health monitor only flags a warning and sends the warning flag to the GUI. If multiple sensors fail, the GUI illuminates the status monitor section red and the RLG automatically goes to Locked Mode. This is in compliance with the health and status monitor design of Chapter 4. Similar to this safety protocol, one emergency input activated by a pilot from the S-100 interface would activate the Locked Mode. The secondary emergency protocol input activated the RTN mode, which provided redundancy if the RLG avionics lost 900 MHz wireless communication.

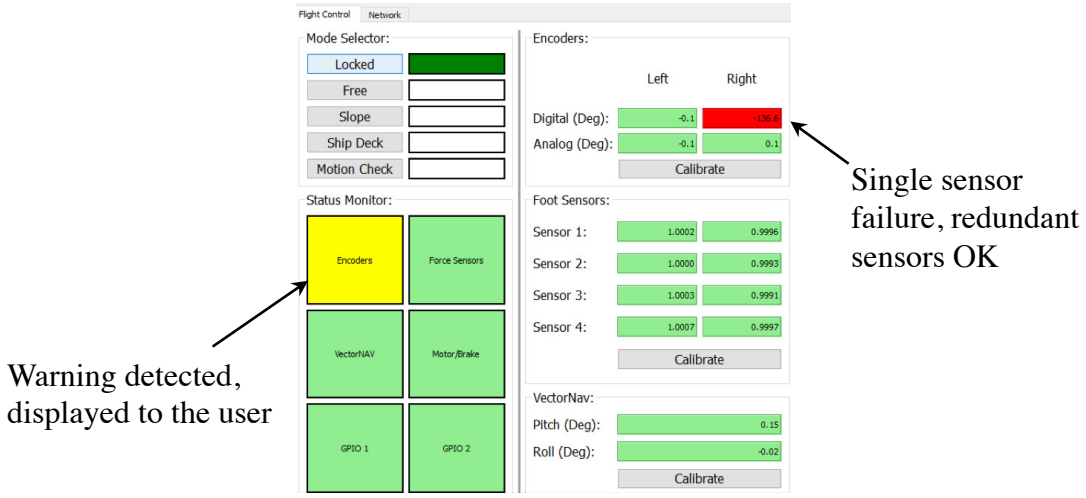

Figure 6.8: Main RLG feedback and control tab of the GUI with a sensor failure that results in a health monitor warning flag.

6.2.4 Weight

The last consideration of the integration presented in this dissertation is the system's weight. The total empty mass of the S-100 with RLG is ≈122 kg. The rotorcraft has an empty weight of 110 kg, so the RLG and drivetrain hardware represents a dry mass increase of 12 kg. This represents ≈24% of the payload weight. This is a

substantial reduction in payload penalty while being crashworthy up to 5 m/s [38] when compared to the >50% payload weight penalty of the previous designs [19, 20].

6.3 Design Simulations Summary

This section presents a summary of key simulation results that were completed to bound control expectations, tune controllers, and select the RLG drivetrain specifically for the S-100 application. This section also presents multibody simulations to understand the dynamic rollover implications of the design if the legs are locked in their neutral position. These are meant as introductory results to align the reader with expected performance for Chapter 7, which is dedicated to more detailed simulation and experiment results.

6.3.1 Lagrange 4 DoF Model

The simplified four DoF model was implemented such that Monte Carlo trade studies with hundreds of simulations across a large design space were simple. The design space encompassed various motors, gearboxes, and landing conditions such as descent rate, slope angle, and ground stiffness at the maximum expected takeoff mass of 167 kg. Mass moment of inertia properties are considered controlled, unclassified information. As such, they are not given in this dissertation. Landings from 0-15° with descent rates ranging from 0.1-0.5 m/s were considered. Each simulation had a fixed controller update rate of 100 Hz. The primary output from this design space search provided statistical results on the tuned controller feedback performance on sloped surfaces with compatible motor and gearbox combinations.

Figure 6.9(a) presents aircraft roll angle, ϕ, versus time data for landings at 0.5 m/s on 5°, 10°, and 15° slopes with the three stages of PBC landing pointed out for the 15° landing. These data were obtained through 200 stochastic simulations with the PBC active and minor variations to the landing surface coefficient of restitution

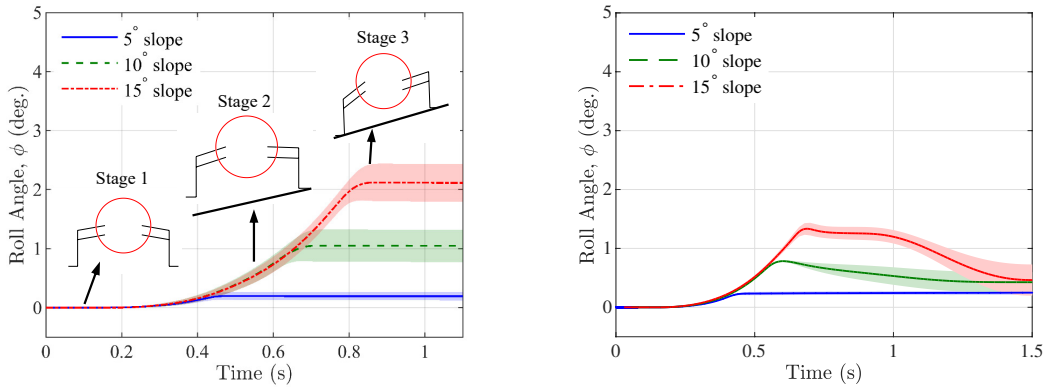

(a) Parking brake control (b) Sensor-fused control

Figure 6.9: Results from 200 simulations of the cable-driven, four-bar linkage RLG using a four DoF model with landings on 5°, 10°, and 15° slopes. (a) Shows the results of a traditional PBC. (b) Shows results of the sensor-fused feedback control. The three stages of PBC landing are pointed out on the 15° landing.

(ground contact model stiffness and damping ratios) and sensor noise. Perturbations were chosen around the nominal ground contact values listed in Table 6.1, which translates to a coefficient of restitution of ≈0.03.

Table 6.1: SLS contact model nominal values.

Parameter	Value (units)
k	1206790 (N/m)
c	7545 (N-s/m)
k_v	120697 (N/m)
μ	0.75

The key constants and tuned controller gains for PBC and sensor-fused control for the remainder of this dissertation are listed in Table 6.2. Roll deadband, ϕ_{DB}, and threshold foot force, F_d, are not listed since they will vary throughout the remainder of this dissertation. The gains presented are set for the simulations and experimental systems in Chapter 7. These gains were determined using an iterative procedure of simulation and experimental test rig validation. First, rough control gains were set from the simulation tool. They were iterated upon on the experimental test rig

Table 6.2: Key constants and tuned control gains for the PBC baseline and the new sensor-fused control. Commas denote the gain scheduled values for when a rotorcraft is descending versus when the rotorcraft is on the ground.

Parameter	PBC (units)	Sensor-Fused Control (units)
θ_{max}	120 (deg.)	
θ_{min}	45 (deg.)	
K_{P_F}	1.0 (deg./N)	0.8 (deg./N)
K_{D_F}	0.05 (deg./(N-s))	0.05 (deg./(N-s))
α_F	0.107 (nd)	
K_{P_ϕ}	-	1.0 (deg./deg)
K_{D_ϕ}	-	1.0 (deg./(deg.-s))
α_ϕ	-	0.07 (nd)
K_{P_θ}	5000	5000, 500 (RPM/(deg))
K_{D_θ}	400	400, 80 (RPM/(deg.-s))
α_θ	0.09 (nd)	
RPM_0	2500 (RPM)	2500, 500 (RPM)

(refer back to Figure 4.1) until the RLG responded as an overdamped system. There was a ≈20% difference between the original proportional gains and the final gains on the experimental system, which was due to larger-than-anticipated rope friction. The simulation model gains and motor acceleration were updated to mimic those of the experimental system afterward.

Conditions for the presented simulations of Figure 6.9 include stochastic measurements of the sensors, uncertainty in the motor performance based on thermal properties of a Maxon 136210 45 mm diameter motor attached to a 60:1 gearbox, and zero rotor thrust. The maximum RPM of this motor is between 8700 RPM and 12000 RPM based on the DC voltage. In each of these simulations, the max RPM was assumed to be 8700 RPM for an applied voltage of 24 V. Lastly, the deadband roll angle was assumed to be ±0.1°. This value assumes a higher-quality AHRS

than the VectorNAV VN-100 is used on future RLG systems (i.e. this assumes ideal performance of the sensor-fused control for S-100 integration).

The shaded regions around each line represent one standard deviation of the simulated results. For a 15° slope at 0.5 m/s, the PBC is able to conform the legs such that the final aircraft roll is 2.1°±0.3°. Even with variations in motor performance and sensor measurements, the PBC maintains the aircraft well within nominal roll limits of ±5°. A non-zero steady state roll is inherent from the lack of roll feedback in the PBC, yet the PBC is able to bound the roll.

Figure 6.9(b) presents aircraft roll angle, ϕ, versus time data for landings at 0.5 m/s on 5°, 10°, and 15° slopes for the sensor-fused control. There are three observable differences between the PBC and the sensor-sensor-fusedfused control responses.

1. The peak of the sensor-fused control response is lower than the PBC. This is directly caused by the inclusion of roll feedback for leg commands during descent. Since roll feedback is considered, the controller can minimize the steady-state roll using this additional data channel. The PBC has a maximum roll angle of 2.1° for the 15° landing, while the sensor-fused control has a maximum roll angle of 1.32° for the 15° landing.

2. The standard deviation of the data is lower for the sensor-fused control than the PBC. Again, the addition of roll feedback provides a high-quality data channel to improve the transient control performance. This yields a more consistent response from the RLG to the landing surface. Specifically, the PBC has a maximum standard deviation of 0.3° for the 15° landing while the sensor-fused control has a maximum standard deviation of 0.25° for the 15° landing.

3. The steady state roll angle is lower on the sensor-fused control than the PBC for large ground slopes. Since the sensor-fused control is able to use roll feedback after both legs make contact, the fuselage can level down to ±0.1°, while the

PBC does not conduct any control after both legs make contact.

Multibody dynamics simulations expand on these results by providing full six DoF motion and forces and moments on the cable and drivetrain.

6.3.2 Multibody Model

There are 15 rigid bodies used for dynamic simulation and constraint stabilization for the S-100 model (see Figure 6.10). Most bodies are direct counterparts to their

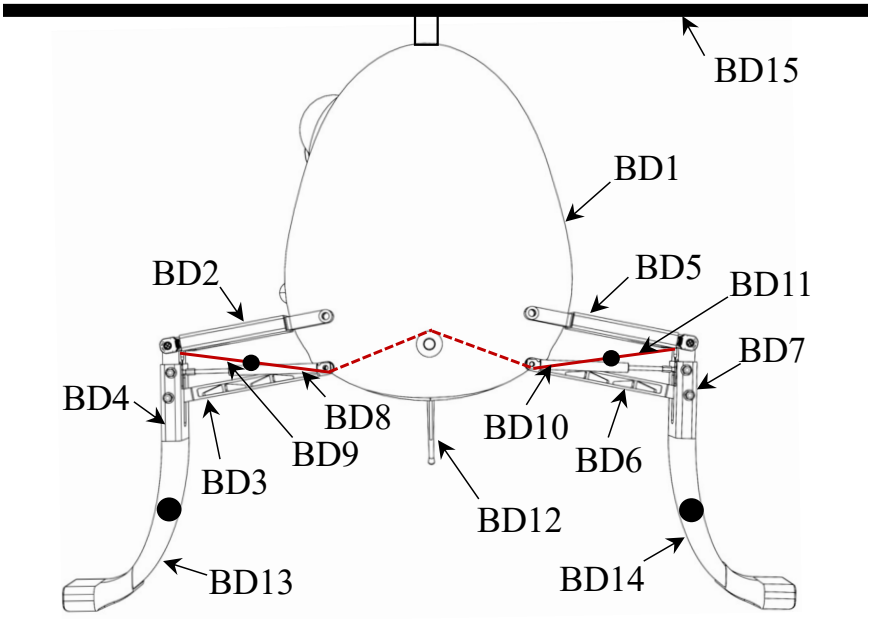

Figure 6.10: Diagram of the 15 connected bodies used to simulate the S-100 and RLG.

physical components, such as the fuselage, BD 1, and rotor, BD 15, but other physical parts are decomposed into multiple rigid bodies in order to introduce elastic behavior. For example, the cable is represented by two bodies, BD 8 and BD 9 on the right-leg assembly and BD 10 and 11 on the left-leg assembly (pilot's view). These bodies have variable length to mimic changes in rope length resultant from spool rotations. More important than the ability to vary geometry, these bodies are connected by an *elastic* joint, denoted by a black dot. The elasticity between BD 10 and 11 is along

the length of the cable; all other axes have fixed constraints. This captures some of the elastic behavior of the real cable. Joint stiffness, k, and damping, c, used in the simulation, which were derived from crashworthiness tests in Chapter 2, are listed in Table 6.3.

Table 6.3: Elastic joint stiffness and damping of the rope's elastic joint.

Parameter	Value (units)
k	4160000 (N/m)
c	28000 (N-s/m)

Similarly, the CFRP legs designed in Chapter 2 are represented by BD 4 and BD 13, as well as BD 6 and BD 14, with elastic joints in between. The spring stiffness and damping of each elastic joint (marked by black dots) were experimentally derived from drop tests of the full-scale system as summarized in Chapter 2 and published in [38, 76]. The rear leg of the aircraft, BD 12, also connects to the fuselage via an elastic joint, which is not shown in the figure. Joint elastic parameters for the rear leg were directly provided by the aircraft supplier, but they were not experimentally verified. This data is considered controlled, unclassified information, so it will not be provided here. Finally, BD 15 (rotor) rotates with the S-100's rotor nominal frequency, and all thrust model outputs are applied to this body's origin.

At this time, unsteady aerodynamics and ship wake are not modeled in these simulations. The simulations considered in this work assume the rotorcraft approach phase is complete, and the simulations initiate just prior to first contact of the gear during landing. Other works have studied aircraft (namely rotor) feedback [113, 114] and path planning [63] through the ship's wake field. Again, this work focuses on the *landing* problem when a rotorcraft enters a dangerous dynamic rollover scenario caused by aggressive roll and roll rate of a ship deck.

The author used the simulation tool to characterize roll dynamics of S-100 RLG in a rigid, locked configuration. A locked configuration is the dynamic rollover baseline

for comparison to the active gear. Table 6.4 lists the variables for the Monte Carlo. The variable μ_f is the friction with the landing surface, u is the aircraft's body relative

Table 6.4: List of Monte Carlo variables for locked S-100 RLG dynamic rollover characterization

Parameter	Nominal	Range Simulated
m	160 kg	[140, 180] kg
τ_T	0.75 s	[0.25, 1.25] s
μ_f	0.7	[0.25-0.75]
ϕ	-2°	[-3°, 0°]
θ_{AC}	0°	[-1°, 1°]
u	0 m/s	[-0.1, 0.1] m/s
w	0.5-0.6 m/s	[0, 1] m/s
γ	±5°	[-15°, 15°]

forward velocity, w is the aircraft's body relative downward velocity, and θ_{AC} is the aircraft's pitch angle. Each range of values considered is within the aircraft's expected landing envelope, and values simulated were generated using a uniform distribution. The simulations all initiate with one foot in contact on the ground surface, and the commanded thrust changes to the minimum value. This mimics how pilots land the S-100 (i.e. they initiate contact then lower collective to the minimum value). Figure 6.11 shows cumulative distributions of the fuselage's peak roll angle absolute value on eight landing surfaces, $\gamma = \pm 5, 7, 10, 15°$. The x-axis is limited to 20° to show the fine detail for each slope. Any portion of the cumulative distribution beyond 20° represents dynamic rollover. The results of the study show that the S-100 RLG configuration with the gear inactive, or locked, shows no risk with landings at $\gamma = \pm 5°$. The risk for dynamic rollover first appears at $\gamma = \pm 7°$. The simulations suggest that fewer than 5% of landings in the nominal landing envelope on a 7° slope result in dynamic rollover. By $\gamma = \pm 10°$, the risk increases with more than 40% of landings, in an otherwise nominal landing envelope, result in dynamic rollover, while

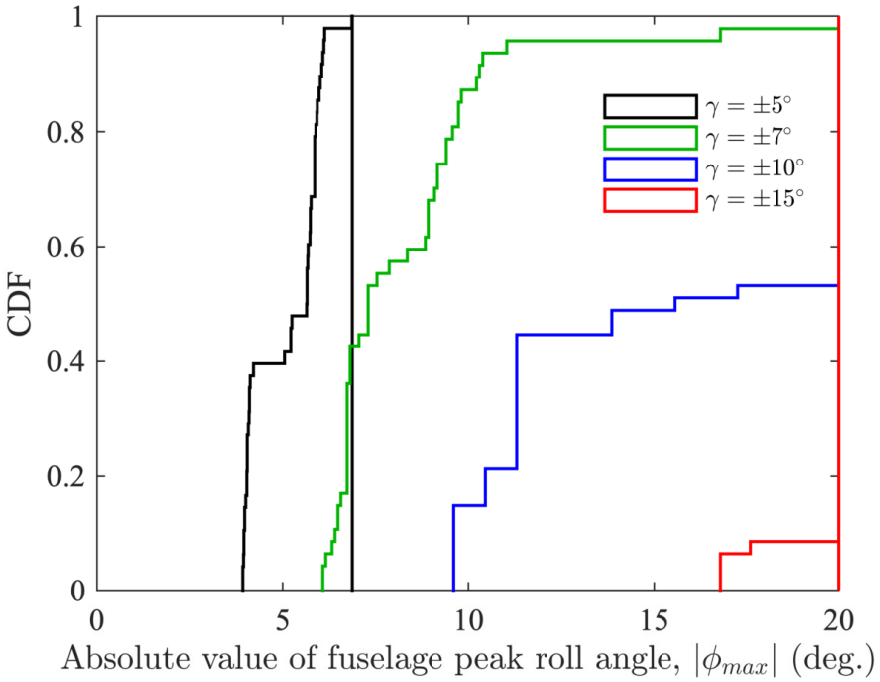

Figure 6.11: Peak roll angle cumulative distribution of Monte Carlo simulations of the locked S-100 RLG landing on static landing surfaces within nominal operation envelope.

$\gamma = \pm 15°$ results in more than 85% of landings with dynamic rollover. These results show that the S-100 will benefit from active gear on static surfaces at low as 7°. The author notes that these cumulative distribution plots will shift downward on dynamic platforms with similar γ because of the added interface dynamics between the aircraft and landing surface.

Figure 6.12 presents renderings and fuselage roll angle outputs of the multibody dynamics tool at each stage of a PBC landing on a 15° at a descent rate of 0.5 m/s. Ten simulations were run with stochastic sensor data to obtain the shaded region, which signifies uncertainty. The data is overlaid on the 15° slope roll data from the stochastic four DoF simulations. The roll angle bounce from this simulation stems from asymmetric stretching of the cable on the right leg momentarily at the elastic joint. This leads to the clear bounce in fuselage roll angle that settles back to a steady state value once the cable returns to its static loaded position. The roll performance

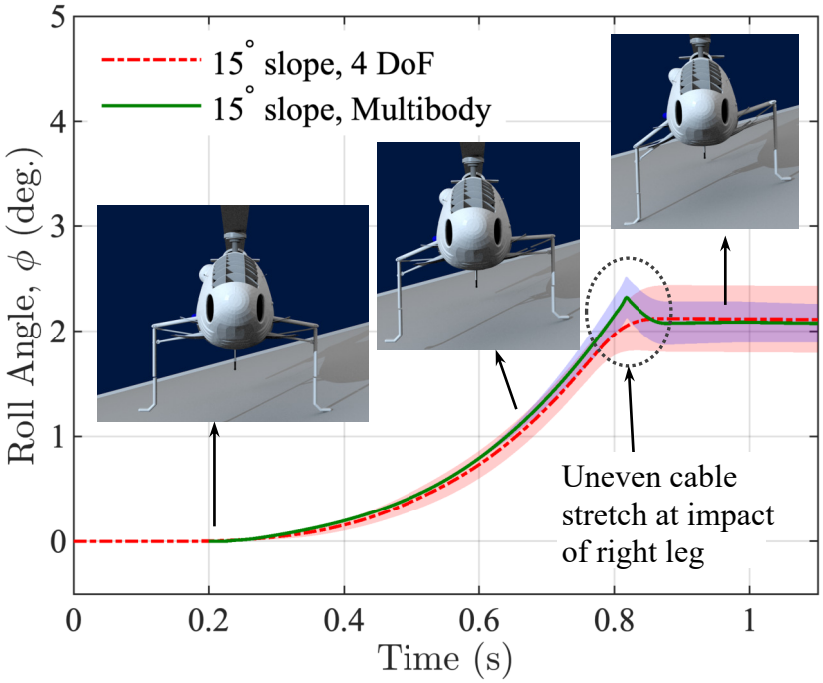

Figure 6.12: Roll angle results from four DoF and multibody stochastic simulations overlaid for a 15° sloped landing with renderings of the system at each stage of PBC.

obtained by the PBC in this tool confirms the results of the four DoF model with a peak roll angle near 2.2°, while landing on the highest slope of 15° and at the fastest considered landing speed.

Dynamic cable forces provided by the multibody simulation streamlined the actuator selection process and provided higher fidelity analysis of controller design. Simulated cable force was converted to a spool torque at each time step of the simulation. This torque was then input to the DC motor model. The speeds, torques, and their durations were compared to the motor's performance specification and thermal restrictions. Figures 6.13(a) and (b) show the speed-torque curve of the Maxon 136210 motor operated at 24 or 28 V with a 60:1 gearbox attached in two landing scenarios using the sensor-fused control. The S-100 uses a battery, so the usable voltage range is nominally within the specified range. Figure 6.13(a) shows a 0.5 m/s descent onto a 15° slope, while Figure 6.13(b) depicts data from a landing and leveling on a the

DDG-54 deck in Sea State 5. Vertical dashed lines illustrate operational time limits caused by the motor's thermal properties. Additionally, this plot presents torque and

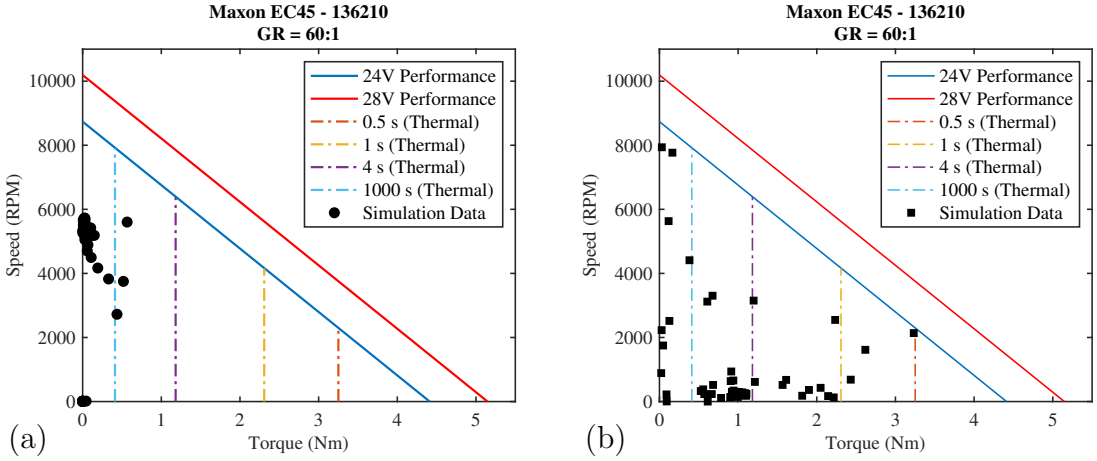

Figure 6.13: Example actuation simulation data overlaid with temporal motor performance data. (a) Shows the results for a 0.5 m/s landing on a static slope of 15° and (b) shows results for a landing on a ship deck in Sea State 5 conditions. Both simulations used sensor-fused RLG control.

speed simulation data when combined with a 60:1 gearbox as blue circles. Each point represents 0.01 s. This data indicate that the motor spends less than 0.04 s in the slow, high torque region that is thermally limited to 0.5 s. Since the remaining data are left of the 1 s thermal limitation mark, the motor gearbox combination is suitable for the simulated landing.

A number of inadequate motor and gearbox combinations were rapidly eliminated from consideration using this tool. All were tested and compared for a subset of the aircraft's landing conditions: 1) a 0.5 m/s landing on a sloped surface up to 15°, 2) a 1.0 m/s landing on a sloped surface up to 15°, and 3) leveling a fuselage on a dynamic platform in Sea State 5 conditions. Only motors with 24 V ratings were considered, while gearboxes with ratios above 100:1 were not considered because of their higher backlash and additional stages (volume restriction). Table 6.5 summarizes other motors that were considered and why they did not meet the criteria for use on the S-100 system. The final design converged on the Maxon motor and gearbox illustrated

in Figure 6.6 and analyzed in Figure 6.13.

Table 6.5: Summary of the motors tested in simulation and the reason why they were not used.

Motor	Result
Maxon EC40 - 393023	Large gearbox required (>100:1 gearing)
Allied Motion EMI75	Diameter too large for S-100 integration
Anaheim Automation BLY6534	Max speed was too low for 0.5 m/s-1m/s landings

This chapter showed the integration of each enabling technology into the S-100 commercial rotorcraft. Monte Carlo simulations showed that the rigid-gear configuration has at least a 5% chance of dynamic rollover. With the PBC and sensor-fused control, the aircraft does not reach a steady-state roll angle greater than 3° based on stochastic simulations of landings on static surfaces. The next chapter elucidates combined experimental and simulation results from this tightly integrated system on the S-100.

CHAPTER 7
SIMULATION AND EXPERIMENT RESULTS

This chapter presents simulation and experimental results of the enabling technologies integrated on the S-100 commercial rotorcraft. First, the experiment setup for ground tests is described. Then, a sample of key results is provided from the experiments on static and dynamic landing platforms. Simulation results of similar conditions are provided to show congruence between simulations and the experimental system. Next, results from flight test experiments are presented and key dynamic and sensor measurement phenomena elucidated. Since the ground and flight experiments could not cover the entire operational range of potential landing scenarios, extended simulation results are provided to conclude the chapter. Results from this chapter have been presented by León [115] and are undergoing peer review for publication [116, 117] at this time.

7.1 Experimental Setup

Ground experiments of the integrated system were performed at Boeing's Mesa, AZ facility using custom wood-pallet landing obstacles, and a Sarnicola Simulation Systems hexad series six DoF hydraulic motion table. Figure 7.1 illustrates the integrated S-100 RLG on the motion table. Red arrows call out the shore power cable, which was connected during RLG ground operation, and a crane connection point. The crane is capable of lowering the system at a constant 0.18 m/s. During a crane-controlled descent, the fuselage orientation is approximately level. Landing pallets were used as obstacles with variable heights of 3, 6, 9, and 12 in (8-31 cm), which represents slopes from 3.5-14°. Sloped surfaces up to 15° were generated using the dynamic motion table.

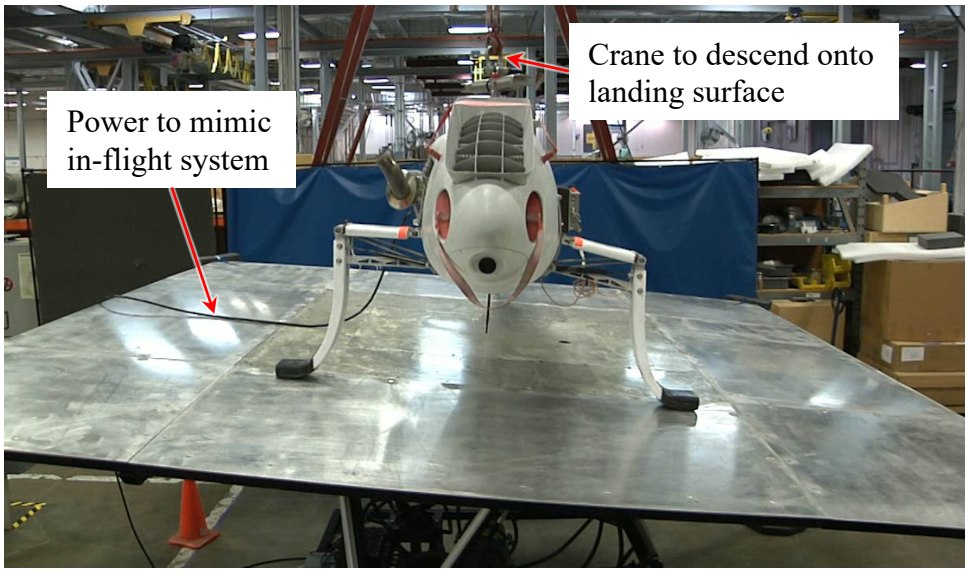

Figure 7.1: S-100 RLG on the Sarnicola motion table for experimental tests of roll-fused RLG control. Images subject to Boeing Copyright 2018. Distribution A: Approved for Public Release. Distribution Unlimited.

The Sarnicola motion table can maintain angular rates in excess of 30°/s, but it has hard limits at ±14 in (36 cm) of heave (vertical) motion [118]. This limitation meant experiments could not fully mimic ship deck surge-sway-heave conditions, but experiments were conducted up to the acceptable limits of the table. Operation of the table was limited to 10°/s in roll, pitch, and yaw rate. Additionally, the table's operation was constrained to SS 5 conditions with limits to surge, sway, and heave at 10% of maximum values output from STH and SMP (see Chapter 5). The experimental setup does not mimic the full range of landing speeds, and it does not include dynamic interactions from spinning rotor blades. Therefore, this ground test experimental setup will perform better than in flight. Experiments are used to verify realism of the simulation tools so that the entire landing envelope may be explored with the simulation tools further.

7.2 Ground Tests

Ground tests of the integrated system were split up between static and dynamic landing surfaces. The first set of experiments on static surfaces were used to verify general functionality of the cable-driven, four-bar mechanism, drivetrain, and force-sensor feedback using PBC. Dynamic platform tests then followed with experiments using sinusoidal and SS platform motion with the RLG sensor-fused control turned on.

7.2.1 Static Ground Tests

Static platform landings were completed in a build-up fashion from the smallest obstacle (≈3.5°) to the tallest obstacle (≈14°), then from steady state 5° to 15° roll angles of the motion table. The top image of Figure 7.2 depicts a front view of the S-100 with RLG on a Sarnicola motion platform at Boeing's Mesa facility. The center and bottom images in Figure 7.2 exhibit the integrated S-100 RLG after it was lowered onto a 12 in platform and a -15° slope, respectively. The motion table provided repeatable and constant sloped surfaces for tests up to 15°. It also provided a stable base to stack platforms for tests analogous to those on the experimental prototype.

Figures 7.3(a) to (h) present the experimental data obtained and post-processed for two right-leg landings. The left column shows a right-leg landing on a platform at 20 in/s (0.5 m/s), while the right column shows a right-leg landing on a 15° sloped platform at 7 in/s (0.18 m/s). The landing speed for the first landing is the maximum that the system is rated for by design, so the force feedback is substantially higher during the feedback control period of 0.43 s – refer to Figures 7.3(c) and (d). Since the landing was still within specification, the system was able to achieve a steady state roll angle of -0.746° with nearly zero roll angle as shown in Figure 7.3(e). The maximum vertical foot speed achieved was -27 in/s (0.68 m/s) (Figure 7.3(g)) when the legs

Figure 7.2: Front views of the S-100 with integrated RLG after descending onto a motion platform in a level configuration, a 12 in platform, and a -15° slope on a motion table. Images subject to Boeing Copyright 2018. Distribution A: Approved for Public Release. Distribution Unlimited.

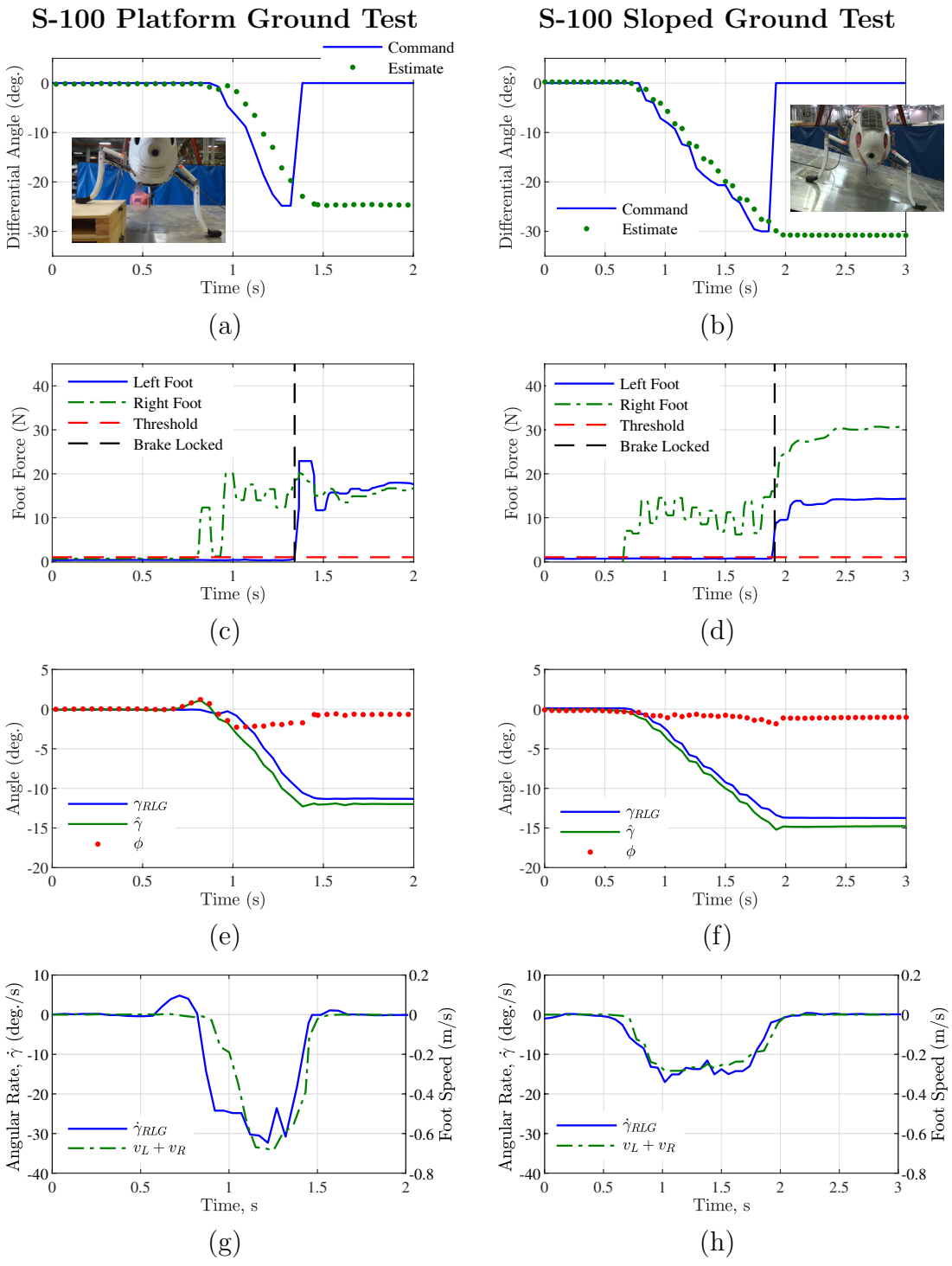

Figure 7.3: S-100 RLG integration experimental data of right leg landings on 9 in obstacle and a 15° slope. (a) and (b) Present differential angle estimates and commands. (c) and (d) Show force feedback from a sensor array. (e) and (f) Show estimated RLG absorbed ground angle, γ_{RLG}, and aircraft roll, ϕ. (g) and (h) Illustrate RLG ground angle absorption rate, $\dot{\gamma}_{RLG}$, and total vertical foot velocity, $v_L + v_R$.

were catching up to the descent rate, which corresponded to a $\dot{\gamma}_{RLG}$ of -32.9°/s.

The slow descent rate landing onto the 15° sloped motion table resulted in an oscillatory force-feedback-control response, see Figure 7.3(b) and (d), around the desired setpoint rather than convergence. This behavior was not seen during simulation studies because simulations were not conducted at lower than realistic aircraft weights and descent rates, which were both present during this test. The aircraft was empty of fuel, and the crane's descent rate limit prevented the author from testing realistic descent rates, placing the PBC in an unrealistic operating scenario. Nevertheless, the system is able to conform to the landing surface with a steady state roll of -1° (Figure 7.3(f)). The presented experiments illustrate the integrated S-100 RLG performs within expectations from Chapter 6 simulations and test facility capabilities.

7.2.2 Sinusoidal Platform Experiments

Sinusoidal landing experiments with roll amplitude of ±10° and peak roll rates between 3 and 5°/s were conducted with the sensor-fused control of Section 4.2. These experiments began with the S-100 on the table, then the table was activated. With the aircraft on the table, the force feedback portion of control is effectively turned off from the start. Numerous experiments were conducted prior to the examples presented in this section to converge on a smooth and fast response of the RLG. Figure 7.4 shows still images of the experiment in (a), still images of the simulations in (b), and experimental data in (c) and (d) of a motion table commanded ±10°, 3°/s peak roll rate sinusoid as an example of these tests. The images in Figure 7.4(a) through (b) illustrate the RLG and fuselage undergoing roll-feedback control and maintaining the fuselage within or at the bounds of ϕ_{DB} for the experiment and simulation, respectively. As expected from simulations and kinematic relations, the feedback controller and drivetrain are consistently able to absorb roll dynamics of the landing platform. Experiments were run for less than 30 s to prevent any motor overheating issues.

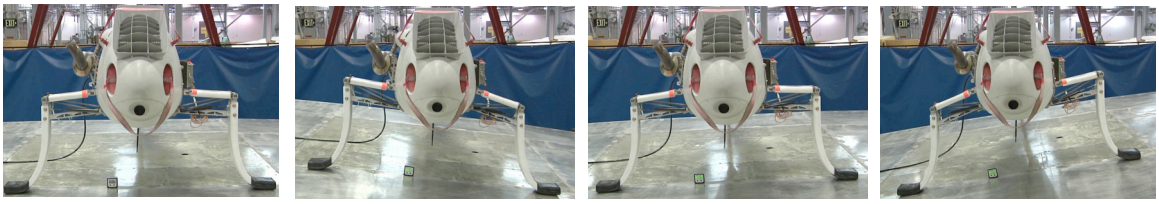

(a)

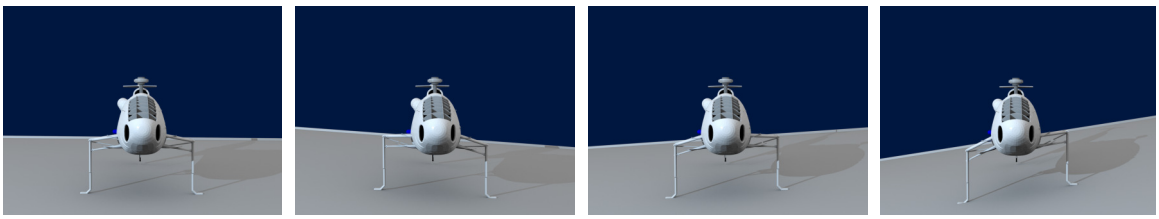

(b)

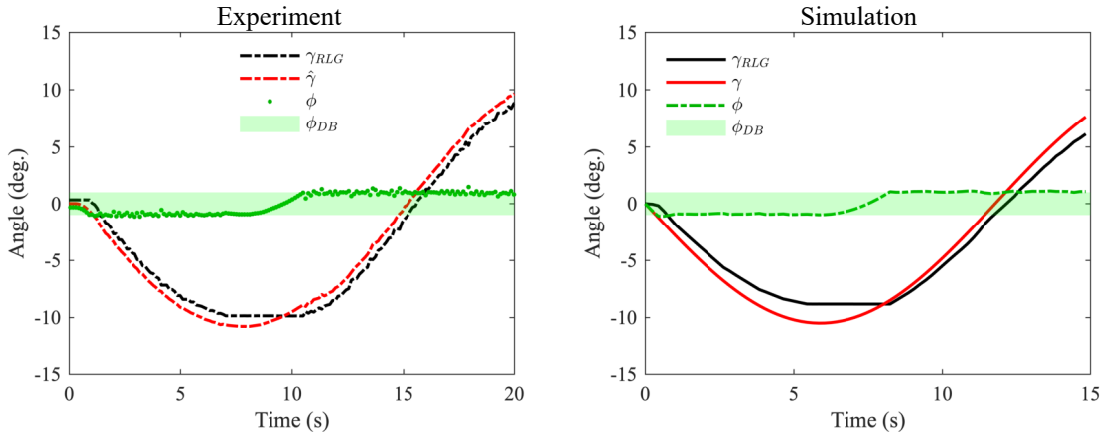

(c) (d)

Figure 7.4: (a) S-100 RLG response to a $\pm 10^{\circ}$ sinusoid using roll sensor-fused control with peak roll rates of $\pm 3^{\circ}/s$ where the aircraft starts the experiment on the table, (b) still images of a simulation under the same conditions, and (c) through (d) S-100 images are Boeing Copyright 2018: Approved for public release.

The plot in Figure 7.4(c) shows fuselage, RLG, and estimated table angle data from this experiment. Roll-controlled RLG maintains the fuselage roll angle (green data points) within or at the ϕ_{DB} (green-shaded region) boundary for the entirety of the table's dynamic motion (red-dashed line). Note that ϕ_{DB} was set to $\pm 1^\circ$ because of the VN-100's dynamic roll estimate accuracy (Section 6.2.1). Figure 7.4(d) shows the simulated response of the S-100 subjected to similar landing conditions. The motion table had a peak roll rate of 3.5°/s, while the simulation was ideal at 3.0°/s. The author computed the peak angular rate of the RLG by using measurements from all angular encoders and computing a moving-average filtered, discrete derivate of the measurements. During this experiment, the RLG achieved angular rates between 4.5-4.8°/s. Figure 7.4(c) shows the table reached peaks of $\pm 11^\circ$ based on the onboard computed estimate of ground angle, $\hat{\gamma}$, rather than the commanded $\pm 10^\circ$. This was accounted for in the matching simulation. Regardless of the motion platform's performance, the roll-feedback controller operated nominally for the entire sinusoid experiment. Furthermore, the simulation tool accurately represented the response of the experimental system.

The author conducted additional experiments wherein the aircraft was lowered onto the platform to close the roll- and force-feedback loops. Figures 7.5(a) shows data from all RLG sensors during one of these experiments where the table had a commanded 5°/s roll rate maximum sinusoid and amplitude of $\pm 10^\circ$. The aircraft descended onto the table at 0.18 m/s. For reference, the table only achieved $\approx \pm 8^\circ$ and peak angular rates of 4.5°/s, which the author accounted for in the comparable simulation. Visible in Figure 7.5(a) is the bump in ϕ and γ_{RLG} when the landing gear first make contact and begin to conform on the surface. Figure 7.5(b) presents comparable simulation results. While the aircraft does not undergo landing in the simulation at the same time as the experiment, the motion dynamics from 3 s onward match within 0.5°. The RLG prototype conformed onto the table undergoing roll

rates up to 5°/s and on slopes up to 11°. The simulations most comparable to the experiments show similar responses of the aircraft and gear, aiding the simulation's validation. This result verifies the simulation tool's ability to mimic the real-world system on mobile landing surfaces with sinusoidal motion. Furthermore, this example set of sinusoid responses of the S-100 and integrated RLG shows the ability of the prototype system to operate with force feedback and roll feedback closed-loop control of the gear from initial contact through the full landing sequence.

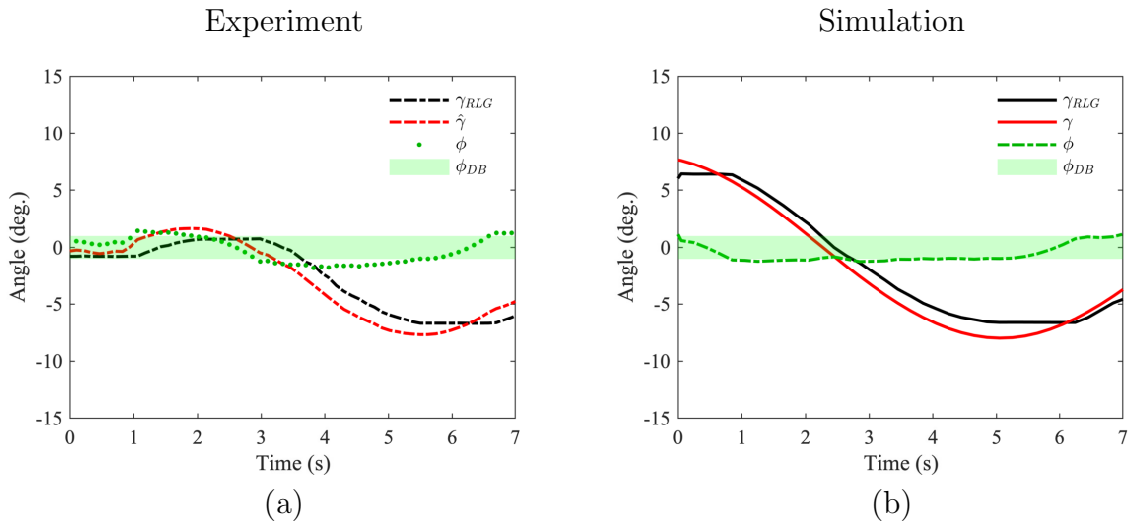

Figure 7.5: (a) Shows experimental system roll and ground angle estimates where the S-100 and RLG were lowered at 0.18 m/s onto a platform undergoing a ±10° sinusoid with maximum angular rate of 5°/s. (b) Presents roll and ground angle output from a simulation with similar platform dynamics.

7.2.3 Sea State Dynamic Platform Experiments

The final set of ground experiments conducted on the S-100 were SS 3 and SS 5 platform landings. Experiments began in a similar fashion to the sinusoidal experiments, with the the aircraft on the platform when the experiment began. The author chose to present two of these experiments in this work, one SS 3 landing and one SS 5 landing. Both of these experiments used the maximum allowable surge-sway-heave for the table, up to 10% of the value output from STH and SMP as described in

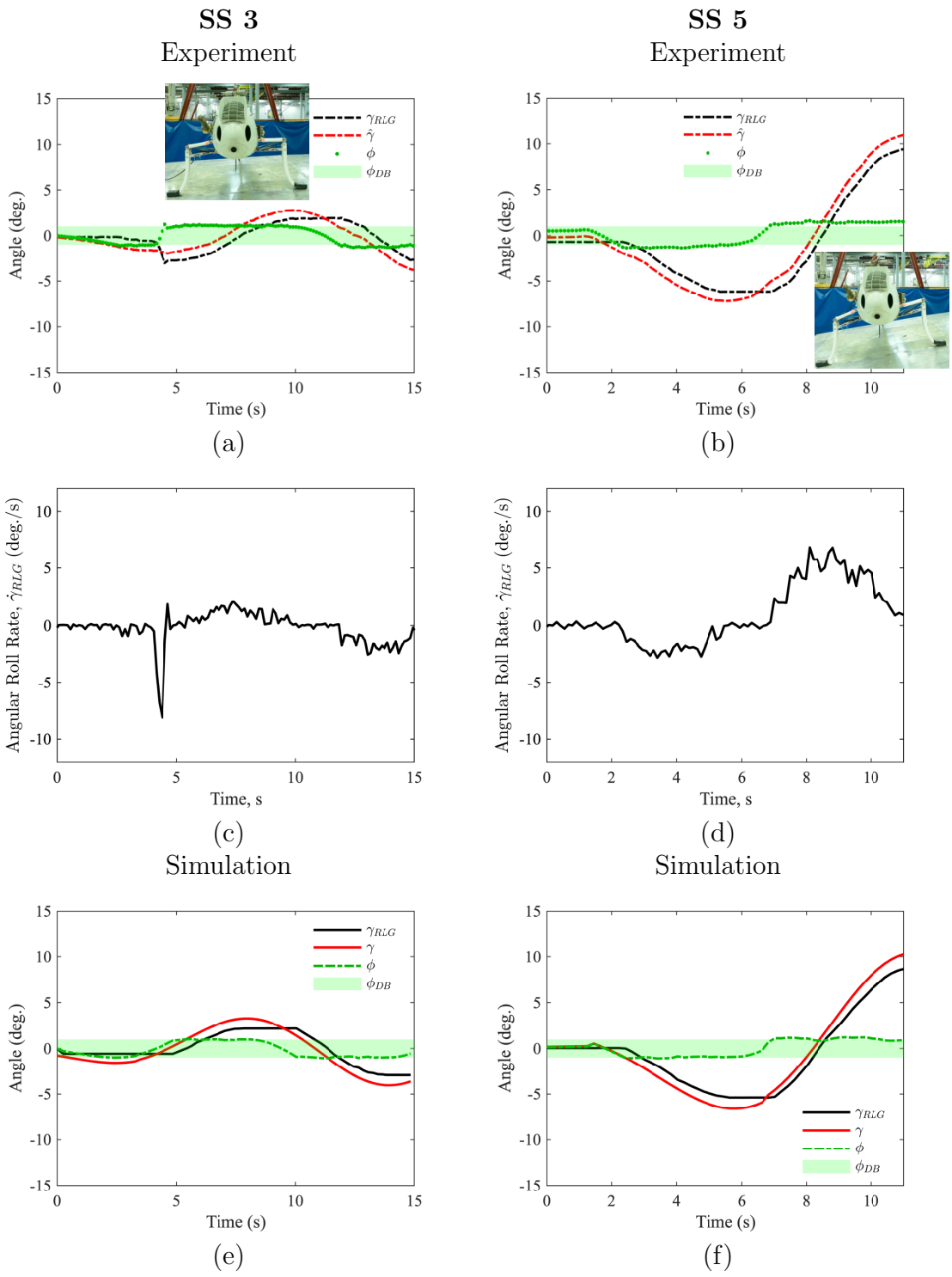

Figure 7.6: Angle measurements and RLG angular rate estimates of the S-100 roll with the aircraft initialized on a motion table undergoing a SS 3 (a) and (c) and SS 5 experiments in (b) and (d). Comparable simulations for SS 3 and 5 are depicted in (e) and (f), respectively. S-100 images are subject to Boeing Copyright 2018: Approved for public release.

Section 5.2. Figures 7.6(a) and (b) depict the angle measurements, and (c) through (d) present the angular rates of the gear for these two experiments. The SS 3 data in (a) and (c) show mild waves where RLG is not required for safe aircraft operation due to the low roll angles associated with the platform. This is in stark contrast to results from the SS 5 experiment. The particular SS 5 test chosen begins with mild waves, and within 10 s, the waves begin to increase such that the ship deck peaks near $\pm 10^{\circ}$ and angular rates at and above $5^{\circ}/s$. The operational range of the gear is apparent from these two vastly different experiments. For both systems, the gear maintains the experimental platform within 0.5° of the ϕ_{DB} bounds. Comparable simulations were executed to validate the simulation design further. Figures 7.6(e) and (f) illustrate the roll angle dynamics of the simulated systems undergoing the same motion table dynamics as the experimental system. The simulations closely match the response of the experimental system with one minor difference. The SS 3 experimental system over-corrected the roll angle of the fuselage, resulting in a minor difference in roll angle response between the real and simulated systems (see Figure 7.6(c) for the spike in $\dot{\gamma}_{RLG}$). The set of experiments conducted with the aircraft initialized on the motion table showed enough success to conduct experiments with the S-100 descending onto the platform while in motion.

Figures 7.7(a) through (d) show results from two SS 5 experimental landings, while (e) and (f) depict simulation results with similar conditions as the experiments. Both of the landings descended onto the platform at 0.18 m/s, and operators initiated descent at random times during the platform's dynamic motion. Therefore, the dynamics seen in the experiments look significantly different. Additionally, these specific dynamic motion programs were limited to 5% of the maximum surge, sway, and heave outputs from SMP and STH. This was done for operator and aircraft safety.

Data provided in plots (a), (c), and (e) present the landing response when the gear makes first contact while the table increases roll angle up to a peak near 10° (i.e.

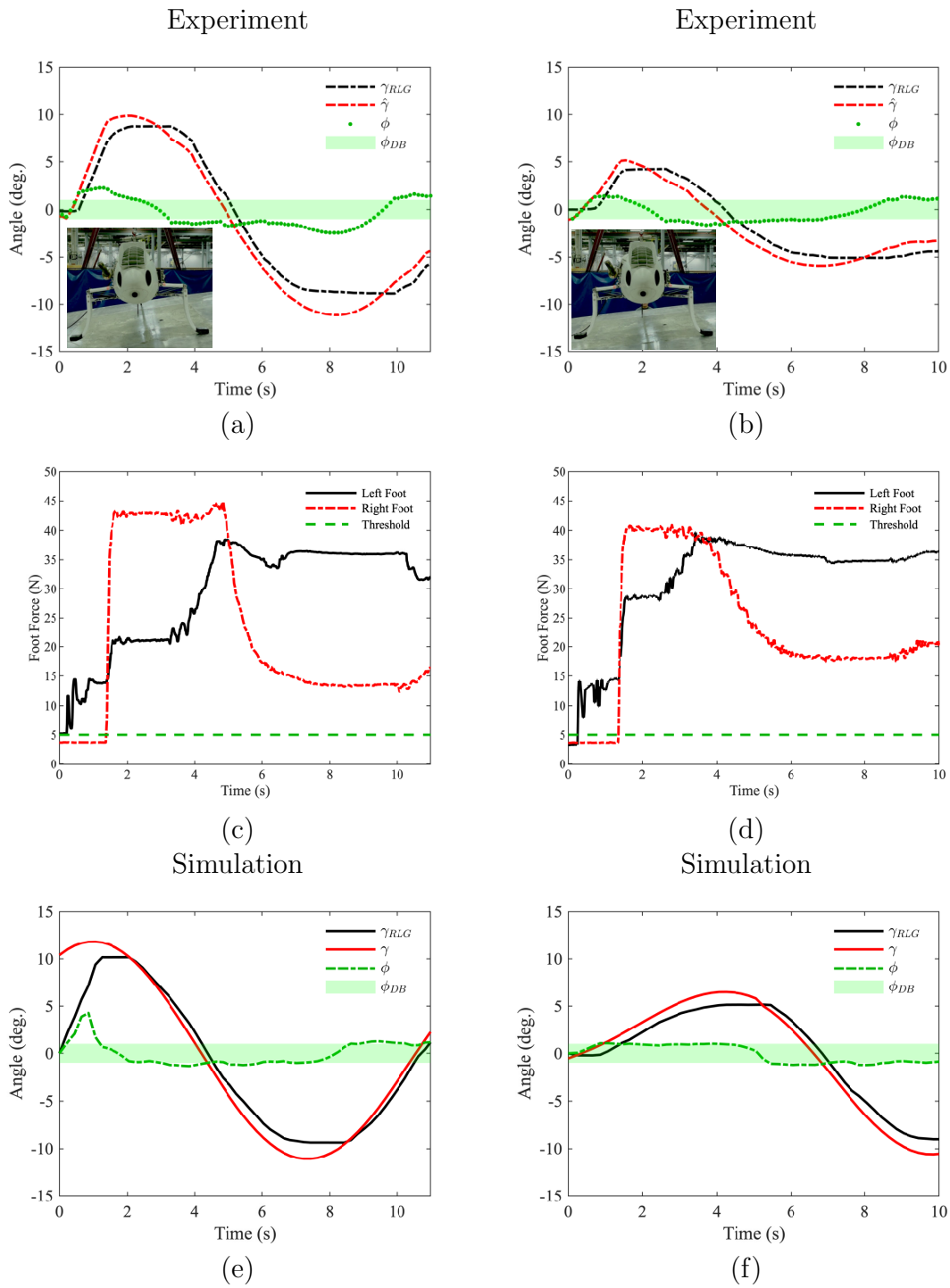

Figure 7.7: (a) and (b) Show angle measurements and computed estimates. (c) and (d) Present foot-force measurements. (e) and (f) Show simulated aircraft and gear response of the S-100 RLG with the aircraft initialized above the Sarnicola motion table and lowered onto the table while it undergoes two, different SS 5 dynamic motion programs.

positive roll rate). First contact is established, and the impact force of the aircraft combined with the table's heave pushed the force sensor measurement beyond the minimum threshold required for force-feedback control. Roll- and force-fused control maintains the aircraft at the boundary of ϕ_{DB} until the RLG achieves full contact. RLG roll- and force-fused control tracked angular rates of ≈9.5°/s to match the combined dynamics of the platform and aircraft. The gear makes full contact with both legs and matches the deck motion within 2 s from first contact. For the next 10 s, the RLG maintains the aircraft within 1.5° of ϕ_{DB}. The larges deviation in roll occurs at 8 s, at which time the cable friction under the aircraft's weight causes significant differential torque on the drivetrain's spool. The torque was large, and the motor entered a thermal overload condition by $t = 8$ s (see Figure 7.7(a). Simulation of this landing showed similar behavior during contact with the table, where the fuselage moves beyond ϕ_{DB} before rapid RLG motion starts (see Figure 7.7(e)). For the majority of the test, the simulation and experiment match one another except for the peak in roll on the experimental system noted at 8 s. While the simulation includes a motor thermal model for degradation of control, it assumes the motor is in free space with air at 25°C. Since the experimental drivetrain is enclosed in the fuselage, and operated for long periods of time before this experiment, these assumptions cannot mimic the torque (heating) limitation of motor speed at 8 s. The thermal model is accurate for short bursts of operation less than 4 s, as verified from the multiple experiments in this section.

The data in the plots of (b), (d), and (f) present a mild portion of SS 5 conditions. The largest angle magnitude achieved by the motion table during this landing was -6°, and the RLG never moved at angular rates above 6°/s to track the deck's motion. A simulation chosen for comparison has the same contact timing, but a different roll response from the simulated platform. Even with this minor difference, the simulation and experimental systems have matching responses to contact and platform motion

in the first 4-5 s. The gear never exceeded $|\phi_{DB} + 0.5°|$ for either the simulation or experiment. These results further verify the simulation as a valid tool for the S-100 RLG system.

In both landing scenarios, the contact force varies depending on contact angle with the deck. The amount of force variation is an unexpected experimental research finding of the, and it warrants future study of force-feedback control after full contact on both feet. Both landing scenarios presented in this work support the notion that the experimental prototype has the sensor measurements and drivetrain response to land on a deck in SS 5 conditions. These experimental results show, at a limited level, that the experimental prototype S-100 RLG meets the design performance expectations. Experiments and simulations of the same or similar landing conditions match well, validating the technologies and simulation tools used to design them.

7.3 Flight Experiments and Results

This section presents a set of flight tests and results as a study on the real-world environment performance of the crashworthy, cable-driven, four-bar linkage RLG and force sensor technologies. sensor-fused control was not permitted for use during flight tests. This is because the PBC has a strong pedigree of flight tests, and the S-100 RLG avionics did not have access to calibrated AHRS data while the rotor was active. Additionally, the impact of roll-pitch inertial coupling induced by the rotor is analyzed with simulations.

7.3.1 Flight Test Operations

Operations during flight tests added safety limitations to the system in order to limit risk to the rotorcraft. Prior to flight testing, tethered ground experiments were performed with full rotor power to test vibration of the landing gear and any possible ground resonance issues. The gear showed no signs of instability through the primary

vibrational modes of the rotorcraft's drivetrain. With respect to landing surfaces, the same ground tested platforms were used during flight testing to limit risk to the aircraft. Finally, the RLG system has an outside air temperature operational limit of ≈110°F (43°C) during experimental flight testing.

The RLG integrated S-100 flight tests were conducted in Florence, Arizona (AZ) at the National Guard Range. The aircraft mass for these operations was between 150-159 kg dependent on fuel remaining at the time of attempted landings. The aircraft was operated using a four-step procedure. First, the pilot took off and RLG locked in the neutral position. Second, the pilot flew a loiter pattern to maintain a cool engine, then approaches the landing zone. Third, the pilot attempted a landing on the designated platform. Finally, ground crew observed RLG and aircraft landing dynamics, and operators recorded aircraft steady-state roll angle. This procedure, in addition to demonstrated landings, proved the RLG's ability to withstand aerodynamic loads from forward flight. Figure 7.8 depicts the rotorcraft at the primary landing/takeoff site. The landing site presented in this image has a natural slope

Figure 7.8: S-100 Camcopter front view with cable-driven, four-bar linkage RLG at the test facility in Florence, AZ.

range from -1.5° to -2.5° aligned with the direction of landing for each case considered here. Additionally, ground tests had the aircraft within ±1° during the descent, but the rotorcraft approaches with a state roll angle between -1.5° and -2.5°.

7.3.2 Results and Discussion

The first set of results considered here are the 6 in landing platforms. Figure 7.9 shows three images of the S-100 integrated RLG landing on the 6 in platform with the left leg. In Figure 7.9, the rotorcraft is nearly level once landed, with performance

Figure 7.9: S-100 with RLG landing on a 6 in platform in Florence, AZ.

metrics confirming this observation.

Figures 7.10(a) through (h) show the experimental data and performance metrics for the left and right leg flight test landings on 6 in platforms. As with previous data, the roll data used for this plot came from the VN-100 AHRS system onboard the

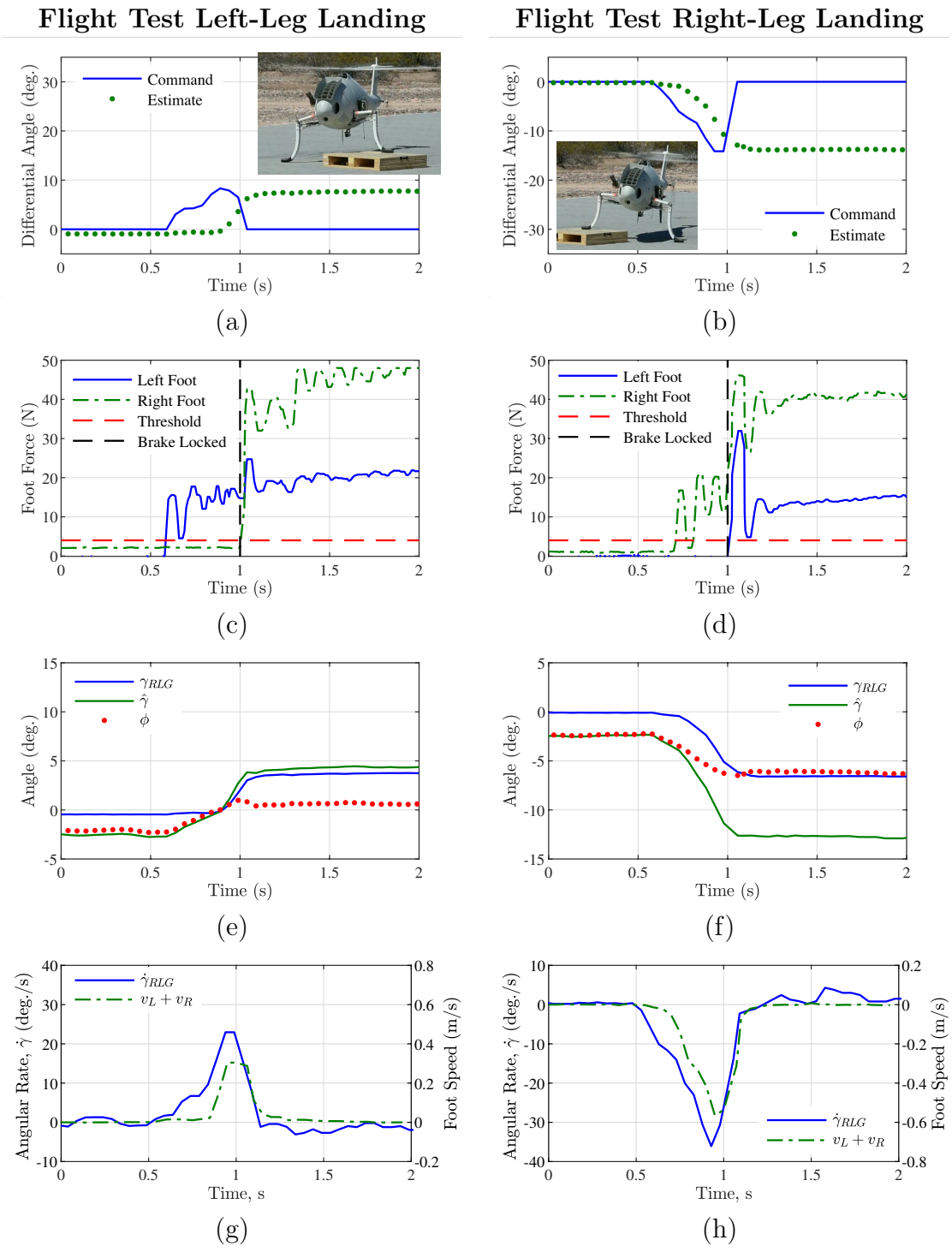

Figure 7.10: Left- and right-leg flight test landings on 6 in platform showing (a) and (b) differential angle estimates and commands; (c) and (d) force feedback from a sensor array; (e) and (f) estimated RLG absorbed ground angle, γ_{RLG}, and aircraft roll, ϕ; and (g) and (h) RLG ground angle absorption rate, $\dot{\gamma}_{RLG}$, and total vertical foot velocity, $v_L + v_R$.

RLG avionics, rather than from S-100 data systems. Both landings had a maximum, measured aircraft descent rate of 23.6 in/s (0.59 m/s). Figures 7.10(a) through (d) illustrate that both landings occurred in a short period of time, with the right leg landing taking 0.291 s from first contact to the brake lock command, while the left leg took 0.421 s. This allowed the left leg 0.13 s more to conform over the right leg, and this disparity impacted the steady state roll angle. As shown in Figure 7.10(e), the aircraft approached at -2.01° and ended with a final roll of 0.46°. Figure 7.10(f) indicates the aircraft approached at -1.45° and ended with a final roll of -4.62°. The author notes that the best possible steady-state roll is the helicopter's in-flight roll angle because the PBC operates only with foot-force feedback. The transient performance metrics, such as vertical foot speed, $v_L + v_r$ in Figures 7.10(g) and (h), as well as sensor feedback, were similar between the left and right legs given the landing periods, so there was no clear explanation for the apparent asymmetry.

This asymmetry trend continued with the 9 in landing case. Figures 7.11(a) and (b) show the steady state landing configurations and roll/ground angle data for the 9 in left- and right-leg landings. As clearly depicted in Figures 7.11(b) and (d), the right-leg landing yielded a significant roll angle even with the legs operating normally. The landing times for the right and left legs were 0.38 s versus 0.46 s, respectively. This asymmetry in left/right landing performance was not seen anytime during the ground tests at Boeing's facility or during regression tests in Florence.

The RLG was deemed to have functioned properly during these landings as experimentally evidenced by post-flight ground tests performed on site with a crane. Steady state roll measurements from these ground tests were analogous to previous experiments, and the simulated expectations yielded symmetric nominal angles within ±2.4° across all of the left- and right-leg tests using the crane. Those results confirmed that the asymmetry was not caused by a RLG sensor or controller error.

Flight experiments were repeated with contact on the right leg to better under-

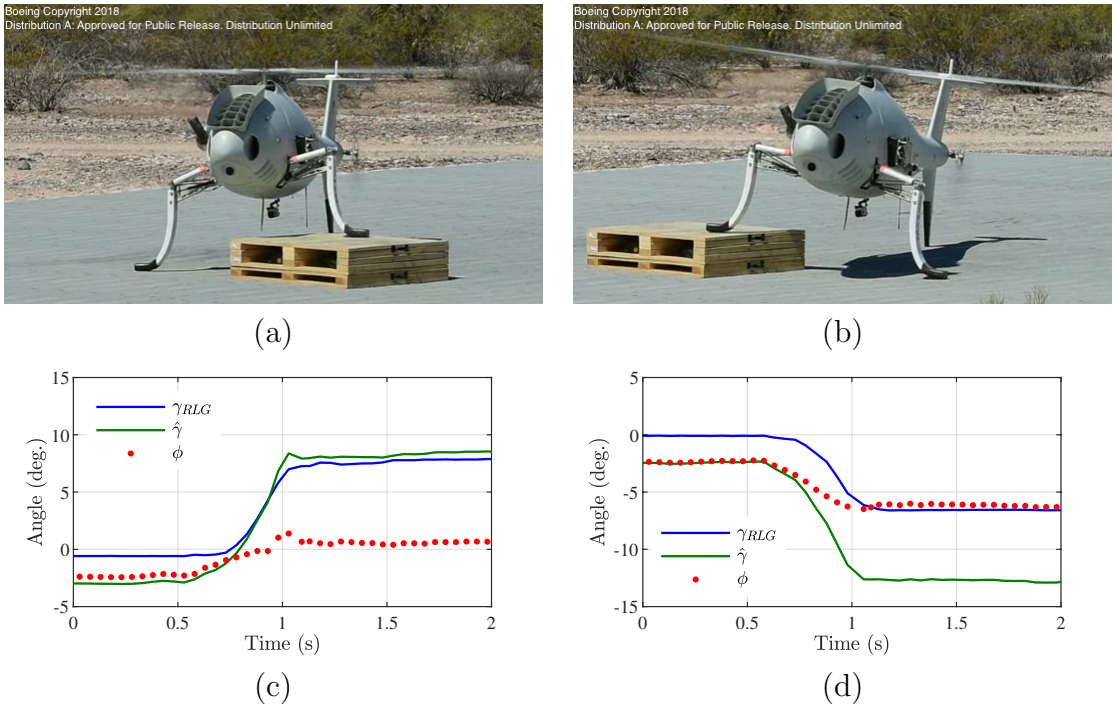

Figure 7.11: Left and right leg flight test landings on 9 in platforms. (a) and (b) Show steady state landing configuration of the S-100, while (c) and (d) present RLG measured ground angle, γ_{RLG}, and fuselage roll, ϕ.

stand the asymmetry. These landings had the approach angle rotated 180° in order to improve the total ground angle conditions and observe if the ground angle conditions caused the asymmetry. Even for these landings, a steady state roll angle of -4.9° on the 9 in landing block was at the bounds of acceptable operation. Further analysis of the experimental data verified the asymmetry, revealing the difference of landing times between the left and right side. While this is partially due to the difference in ground angle, another feasible contributing factor is rotor induced cross-coupling between pitch and roll rates.

Rotor induced pitch-roll cross-coupling

Rotor induced pitch-roll cross-coupling was not previously analyzed in the four DoF and multibody simulations. The author proposes that this dynamic interaction, also known as a rotor-induced gyroscopic moment [119, 120], contributed to the steady

state roll asymmetry seen during flight tests. The author also proposes that this dynamic interaction is pronounced because of the landing obstacle used for flight tests paired with the unique, three-legged geometry of the S-100. Landing on a naturally sloped surface has a minimal height difference between the contact points of the front and rear legs. That provides balanced support along the aircraft's longitudinal axis during descent and prevents significant pitch rates. The use of landing blocks created a convenient and artificial surface for contacting one leg during experiements, but it generated a large vertical displacement for the S-100's rear leg to travel before it arrested pitch rotation. Before the rear leg of this three-legged design made contact with the ground during a rotor-on landing, the aircraft pitched and the rotor inertial cross-coupling initiated. This coupling may be modeled as follows.

A Newton-Euler dynamic model derivation for a body with rotating mass [121], yields the angular momentum of the rotor's rotating mass as

$$\vec{h}_{GM} = [I_R]\,\bar{\Omega}_R. \tag{7.1}$$

Taking an inertial frame time derivative of this term yields the coupling cross product

$$\frac{d}{dt}^{I}(\bar{h}_{GM}) = \begin{Bmatrix} p \\ q \\ r \end{Bmatrix} \times \begin{Bmatrix} 0 \\ 0 \\ I_{zz_R}\Omega_R \end{Bmatrix}. \tag{7.2}$$

Computation, rearrangement, and inclusion of the sign of Ω_R yields the gyroscopic moment

$$\vec{M}_{GM} = \begin{Bmatrix} -I_{zz_R}\Omega_R q \\ I_{zz_R}\Omega_R p \\ 0 \end{Bmatrix} \tag{7.3}$$

caused by the rotor given a pitch and roll rate. The gyroscopic moment has a com-

ponent that changes pitch rate dependent on roll rate, and vice versa. Given a pitch rate perturbation caused by the RLG leg(s) contact the ground forward of the CG, the rotorcraft will begin an oscillatory transfer of angular momentum from the rotor blade to the pitch and roll rates of the fuselage.

The results of this dynamic interaction are important to understanding the observed flight experiment asymmetry, so the author conducted dynamic simulations of the phenomenon with experimentally measured pitch rates. Figure 7.12 shows the moving average smoothed (a) pitch angle and (b) pitch rate measured by the RLG AHRS before, during, and after the landing depicted in Figure 7.11(d). There is a

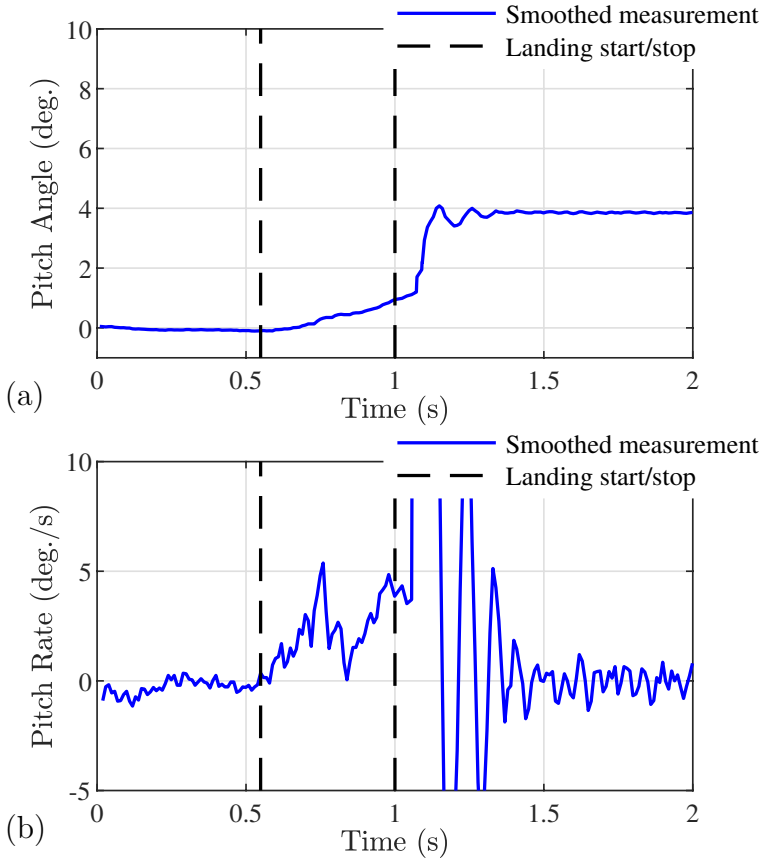

Figure 7.12: Moving average filtered (a) pitch and (b) pitch rate data for a right-leg landing on a 9 in platform during flight tests of the S-100 RLG with denotions for the landing period as measured by the system's force sensors.

clear period of rotorcraft pitching during the landing phase, marked by black-dashed

lines. The maximum pitch rate measured by the RLG AHRS was 5.38°/s. Again, this value was smoothed using a moving average filter, so the actual peak is above 5.5°/s. Either the rotorcraft or the natural coupling dynamics clearly attempted to correct this pitch rate throughout the landing; visible in the dip of pitch rate before another spike just before the brake engaged. Nevertheless, there was a non-zero pitch rate during the entire landing, so cross-coupling to roll rate was possible.

This phenomena was simulated in the multibody dynamics environment *after flight tests* to improve the modeling techniques and tools for future RLG. This model improvement adds the rotor as a *rotating mass* with an artificially injected thrust force, but no detailed aerodynamic forces are considered. The rotor blades are modeled as a thin plates by incorporating public data on the S-100 [111]. Due to its proprietary design, exact inertial properties of the rotor are not provided.

An exploratory multibody simulation designed to gauge the impact of rotor inertial coupling was executed prior to a simulated S-100 RLG landing. This representative simulation initialized the S-100 in free space with a constant rotor speed and an initial, non-zero pitch rate. The non-zero pitch rate is representative of the real system and is necessary to initiate a roll rate. Figure 7.13 illustrates the simulated pitch-rate, roll-rate, and roll-angle responses of the S-100 fuselage with approximate rotor mass properties and rotor speed. This does not inlcudde any main or tail rotor control inputs. The pitch rate, denoted by q, initial condition for this case was 5.5°/s while all other initial conditions are zero. As roll rate, p, increases, the inertial coupling moment decreases the pitch rate and the oscillation begins, eventually producing a roll angle oscillation with a -1.93° amplitude at 1.75 Hz. The roll angle difference between the left and right leg landings was ≈1.2°, so the amplitude of the coupling is comparable to the difference seen from flight test landings. The peak of the roll rate response varies between ±10°/s, double that of the pitch rate. The time scale for these dynamics are similar to the landing times (≈0.4 s for landing vs ≈0.6 s for a complete

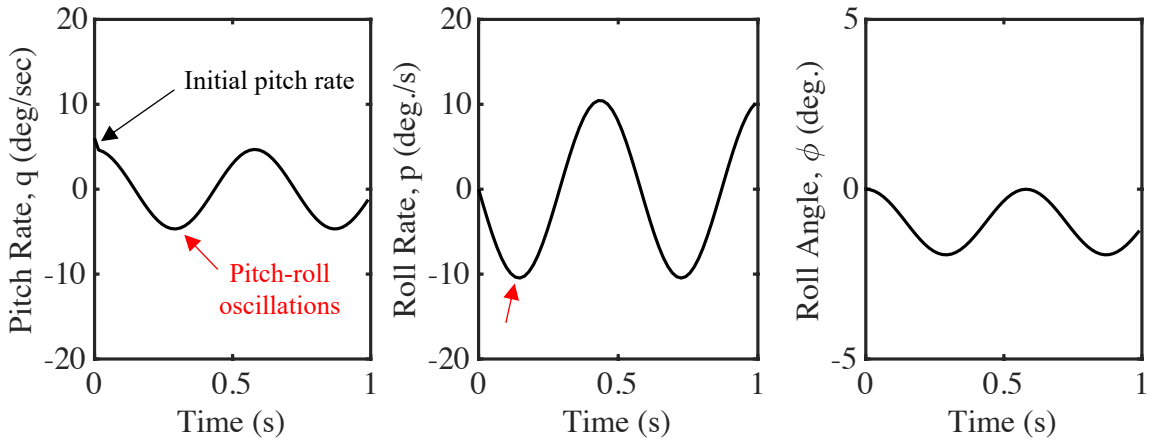

Figure 7.13: Pitch rate, q, roll rate, p, and roll angle, ϕ, results of an updated multibody dynamics simulation with included rotor inertial coupling and a pitch rate initial condition of 5.5°/s in free space.

roll angle oscillation). Without the rotating mass of the rotor blade in the simulation, these results are **not** present. This elucidates that the rotor-induced, pitch-roll rate coupling has the roll amplitude and time scale within the range experienced during flight experiments.

Replica simulations of the flight test with and without inertial-coupling were conducted next. Roll, roll rate, and pitch rate measured by the VN-100 AHRS from flight tests were noted, and they were used as initial conditions to match the flight conditions as closely as possible in the multibody simulator. Figure 7.14 shows simulated roll data with the rotor neglected (black), rotor included (red), as well as the experimentally measured roll data (blue) of the right leg landing on a 9 in platform. In order to mimic landings but minimize simulation time, the simulations were run for 1 s after initial contact. All three legs made contact during the 1 s window, and the simulated rotorcraft with rotating mass rotor blades ended with the same steady state pitch angle as the experimental aircraft (≈6°). There are minor differences in the total landing time between the simulation and experimental data. The simulations tend to complete the landing faster (≈0.05 s), which contributes to the minor

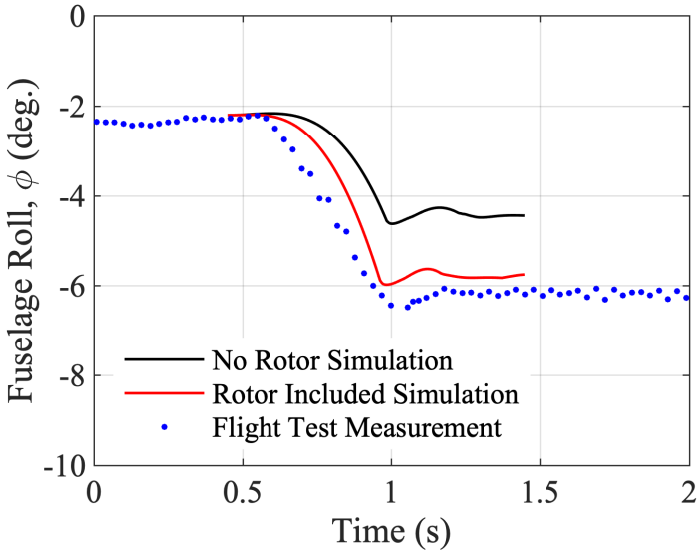

Figure 7.14: Multibody dynamics simulated roll response without the rotor rotating mass, with the rotating mass included, and measurements from the flight test experiment on a 9 in landing block.

differences in ground contact dynamics and descent rate control of the rotor. The black and red lines show the difference in fuselage steady state roll solely caused by the rotating mass inertial coupling. The simulation with included rotor inertial coupling underestimates the experimental steady state roll by only 0.2° while the simulation *without* rotor inertial coupling underestimates the steady state roll by ≈2°. The differences between experimental and simulation data for the inertial cross-coupled result are attributed to inexact landing speed dynamics, ground contact parameters, and uncertainty in the rotor mass moment of inertia.

Previously shown results present evidence that the inertial cross-coupling exists for the S-100 at a magnitude and time horizon consistent with the asymmetry observed during flight tests purely using publicly available estimates of the inertial and constant rotor angular velocity. The following results present inertial cross-coupling, roll-angle amplitude and oscillation frequency when the rotor mass moment of inertia is treated as variable. This study was conducted using the multibody dynamics tool to yield greater understanding of how the coupling varies based on relative mass

properties, not rotor speed (since rotor speed is assumed constant). Figure 7.15 shows the compiled results of roll-angle oscillation and roll-angle amplitude for varied rotor mass moment of inertia normalized by the S-100's roll axis mass moment of inertia, I_{xx}. The estimated range of mass properties for the S-100 during flight tests is marked

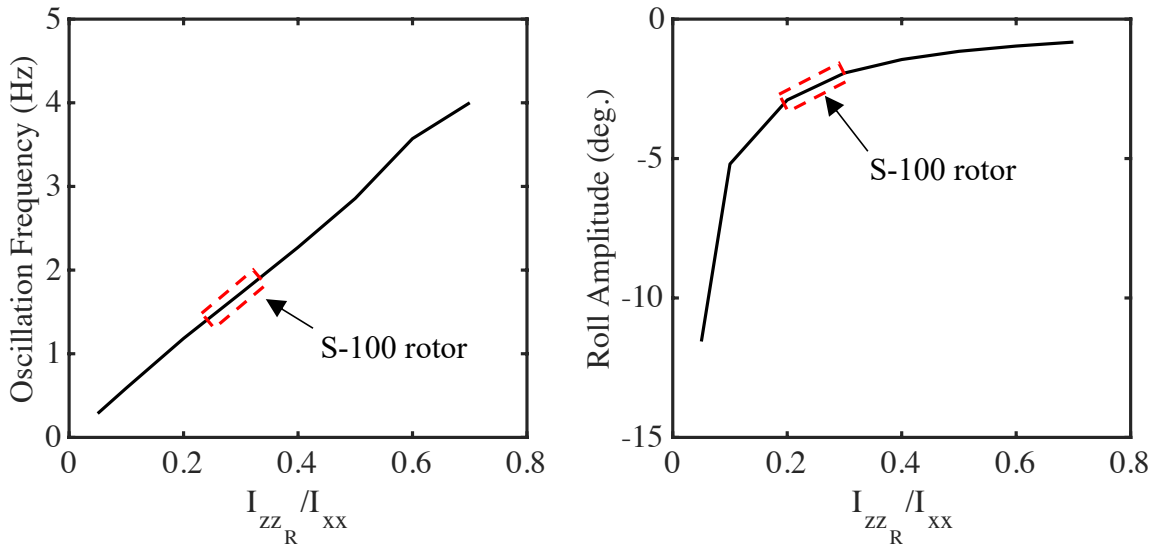

Figure 7.15: Roll angle oscillation frequency and amplitude from rotor-blade inertial coupling based on normalized rotor mass moment of inertia for a constant rotor speed and initial pitch rate of 5.5°/s in free space.

by a red-dashed box in order to provide a reference for the reader. The oscillation frequency increases in a linear manner as inertia ratio increases, while the roll sinusoid amplitude decreases in an asymptotic manner as the ratio increases. The S-100 rotor falls within the frequency range between 1-2 Hz and roll amplitudes between 1.5 and 3°. This result supports that using a PBC logic on an S-100 with dynamic landing gear will have inherent roll asymmetry in the 1.5-3° range depending on inertial properties and the time required to complete a landing.

It is not possible without additional experimental data to determine with certainty that inertial cross-coupling was the sole source of the asymmetry observed during the S-100 RLG landings. More experimental data would be necessary to discount other factors such as degraded motor performance due to high temperatures. Nevertheless,

it is clear from multibody simulations that inertial cross-coupling is a non-negligible component of the system dynamics for the three-legged S-100 RLG design. This is not, however, a necessary component of the system design for some rotorcraft systems that balance the center of gravity around skid gear under the main fuselage section, such as the UH-60. As a result of this finding, the S-100 RLG along with other three-contact point rotorcraft RLG would be guaranteed to benefit from the sensor-fused control during flight operations to mitigate roll angle errors effectively. A secondary option for future developments is to compensate for the inertial cross-coupling. One example of compensation may be directly integrated into the controller, where the contact feedback is more reactive to right-leg force response. Another example is to approach the landing site and and align the aircraft such that the left leg always makes contact first. By aligning the aircraft with the landing surface so the left leg makes contact first, the aircraft uses the cross-coupling to its advantage to bound steady state roll errors.

Force sensor array frequency response

The S-100 has significant vibrations from the drivetrain during operation, so data from force sensors was post-processed from flight and landing portions of operation. The desire of this analysis is to inform future RLG sensor filter and estimation techniques using the novel force sensors from Chapter 3. Sections of data up to 4 s long were used from multiple landings and free flight segments of operation to generate an average frequency response of force from both legs. Figures 7.16(a) and (b) show the frequency spectrum response of the left and right foot-force estimates during those phases of operation. These results are shown as a noise factor, normalized by F_{ref} (5 N). There are local peaks at ≈1, 37, and 43 Hz during free flight of the S-100 for both the left- and right-leg sensor array assemblies, with the right leg maintaining lower attenuation compared to the left foot. This could be caused by slight differences in the

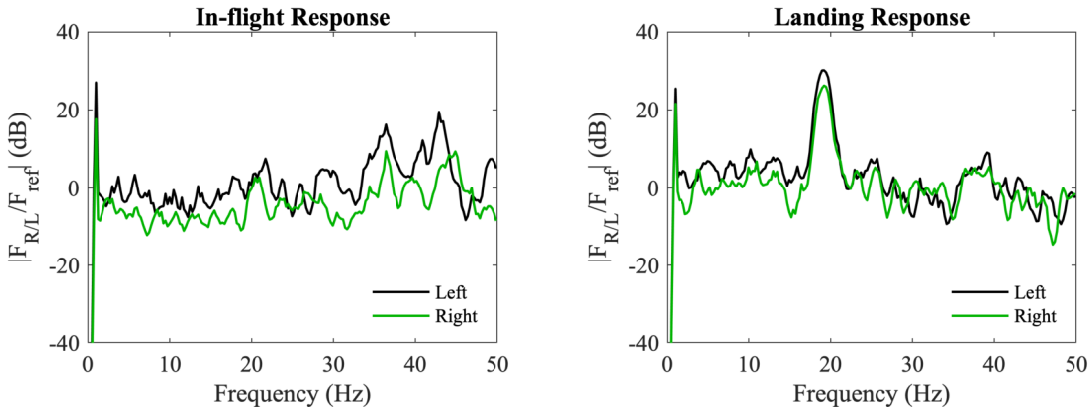

Figure 7.16: Frequency spectrum magnitude of force measurements when referenced to contact force threshold, F_{ref}, during (a) free-flight operation and (b) landing operation of the S-100.

elastomer-fiberglass cover and force plate installation between the two leg assemblies (i.e. freedom of the force sensor subsystem assembly to vibrate). This phenomena occurred across all free-flight segments of operation during the flight test opportunity. It should be noted that the range of 36-43 Hz contains a multiple of the primary rotor frequency.

A vastly different frequency response of the sensor arrays is observable during landing events. There are two local peaks for the sensor response in this case: ≈1 and 19 Hz. The first peak is consistent with free-flight frequency response, but the largest peak occurs at 19 Hz. This observed frequency response peak occurs near the sensor's primary frequency, signifying that the rotor's vibration propagates through the fuselage to the sensor array and elastomer cover assembly anytime there is contact with the ground. Another difference is the similar nature of left versus right foot gain. Both the left and right foot have similar noise profiles, which is different from the in-flight characteristics. This suggests that the left leg assembly has more freedom to vibrate. This freedom is limited as soon as the leg makes contact during landing. The large gain at this resonant frequency, when normalized by F_{ref}, suggests the largest peak-to-peak forces measured during landing match the sensor's natural frequency.

Improved force sensing filters and estimation techniques (implementation of a notch filter, for example) may be developed as a part of future RLG work because of this vital experimental data.

7.4 Extended Simulation Results

Additional simulations were conducted on static and dynamic landing platforms for three RLG operational cases: no feedback control (legs locked), force-feedback controlled, and roll- and force-feedback control. No feedback control was simulated as a part of this section to show a direct comparison between the locked and active landing gear configuration responses with respect to dynamic rollover. This *does not* represent the dynamic rollover scenario for the nominal static gear of the S-100. Force feedback control scenarios were simulated to compare a controller used for previous flight tests [115]. The roll- and force-feedback controller is *not* expected to significantly enhance performance during the short time horizon from initial contact to contact on all legs because of the fundamental acceleration (power) limits of the drivetrain as noted in Section 6.3.2. Nevertheless, this roll- and force-fused controller is expected to prevent dynamic rollover by pushing the rotorcraft's roll angle toward an ideal deadband of $\phi_{DB} = \pm 0.1^\circ$ once full contact is achieved. This deadband was chosen to simulate high-quality AHRS that are integrated into commercial rotorcraft, not the VN-100 used on the experimental platform.

The last consideration for these simulations is the landing velocity. Each simulation presented here considers the case wherein the aircraft starts at $\approx$0 m/s descent, but collective command drops at first contact to the mininum value, similar to how pilots fly this aircraft [115]. At full contact, the aircraft descent rates are typically within a range of 0.55-0.6 m/s; the upper end of the RLG's performance specification. Any additional vertical velocity from the platform will push the RLG up to its operating velocity boundary and beyond. Therefore, the landing simulations presented

here represent the performance boundary for the S-100 RLG, they do not include a full range of performance estimates.

7.4.1 Static Landings

The first landing cases simulated were on static surfaces with the aircraft descending with a roll angle of -2°, the nominal approach roll angle of the aircraft. Figure 7.17(a) illustrates the roll angle results for a 15° even slope landing without any feedback control (green line), force feedback controlled RLG (blue line), and roll- and force-feedback controlled RLG (black-dashed line). Four shaded regions are shown in (a) to distinguish risk of dynamic rollover for the given roll angle. These regions were analytically observed as low risk (orange, 5-10% chance) and high risk (red, >40% chance) for dynamic rollover in Chapter 6. As previously noted, the author has no knowledge of the aircraft's dynamic rollover risk with the OEM rigid landing gear installed, so this data is a baseline comparison of the active RLG system to the RLG without any active control (i.e. locked in the neutral position). The maximum descent speed achieved during this landing for the roll- and force-feedback controlled RLG is 0.56 m/s, so it is expected for the locked RLG to diverge and experience dynamic rollover during the short landing period. Since this descent rate is within the performance specification of the gear's drivetrain, the system compensates and maintains a roll angle throughout the landing with no risk of dynamic rollover. Figures 7.17(b) through (d) give physical pictures of the simulation data shown in Figure 7.17(a). These images and the simulation outputs clearly show that any feedback control of RLG is beneficial to prevent dynamic rollover on extreme slopes. The benefit of including roll feedback is clearer for landings where the aircraft's inertial cross-coupling impacts roll rate.

Figure 7.18(a) presents the roll data for a -10° roll angle sloped surface. In this scenario, the pitch-roll rate inertial cross-coupling exacerbates the roll rate increase

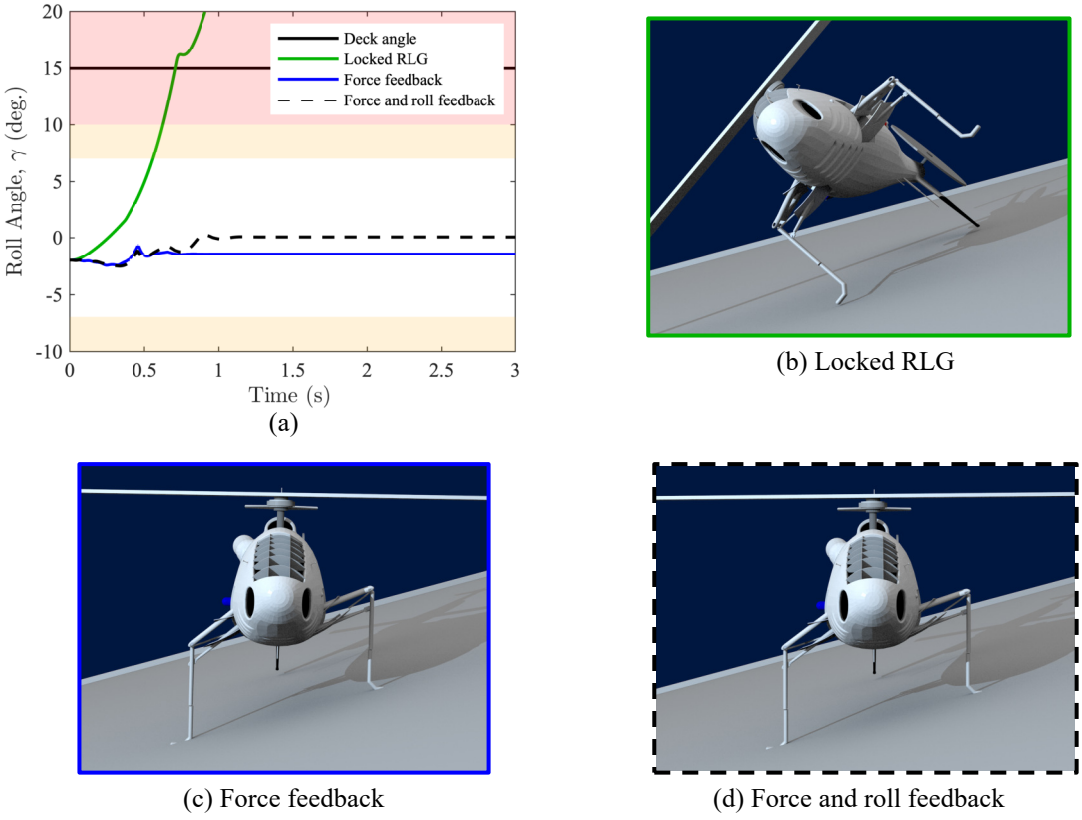

(a)

(b) Locked RLG

(c) Force feedback

(d) Force and roll feedback

Figure 7.17: Static surface landing simulation of a 15° slope without active RLG, with force-feedback control, and roll- and force-feedback control with shaded regions for low risk (orange) and high risk (red) of dynamic rollover.

during landing, which the roll-feedback control mitigates. The simulation with force feedback control leaves the aircraft above 5° of roll. This is consistent with the findings during flight test experiments of the force feedback controller in Section 7.3. The roll- and force-feedback controller is not able to completely mitigate roll angle increase prior to full contact of the legs. This is due to the physical power and speed constraints of the RLG. The added feedback channel (roll) allows the gear to return the aircraft to a safe operating region rapidly after full contact is made. A custom, high-power and faster drivetrain would be able to mitigate this issue. Nevertheless, the roll- and force-feedback fused control is especially important for limiting the dynamic rollover risk during subsequent takeoff when collective is increased and thrust begins to push the aircraft to roll about contact points. With the fused control system, the aircraft

is able to takeoff from a fuselage-level orientation, unlike the other configurations.

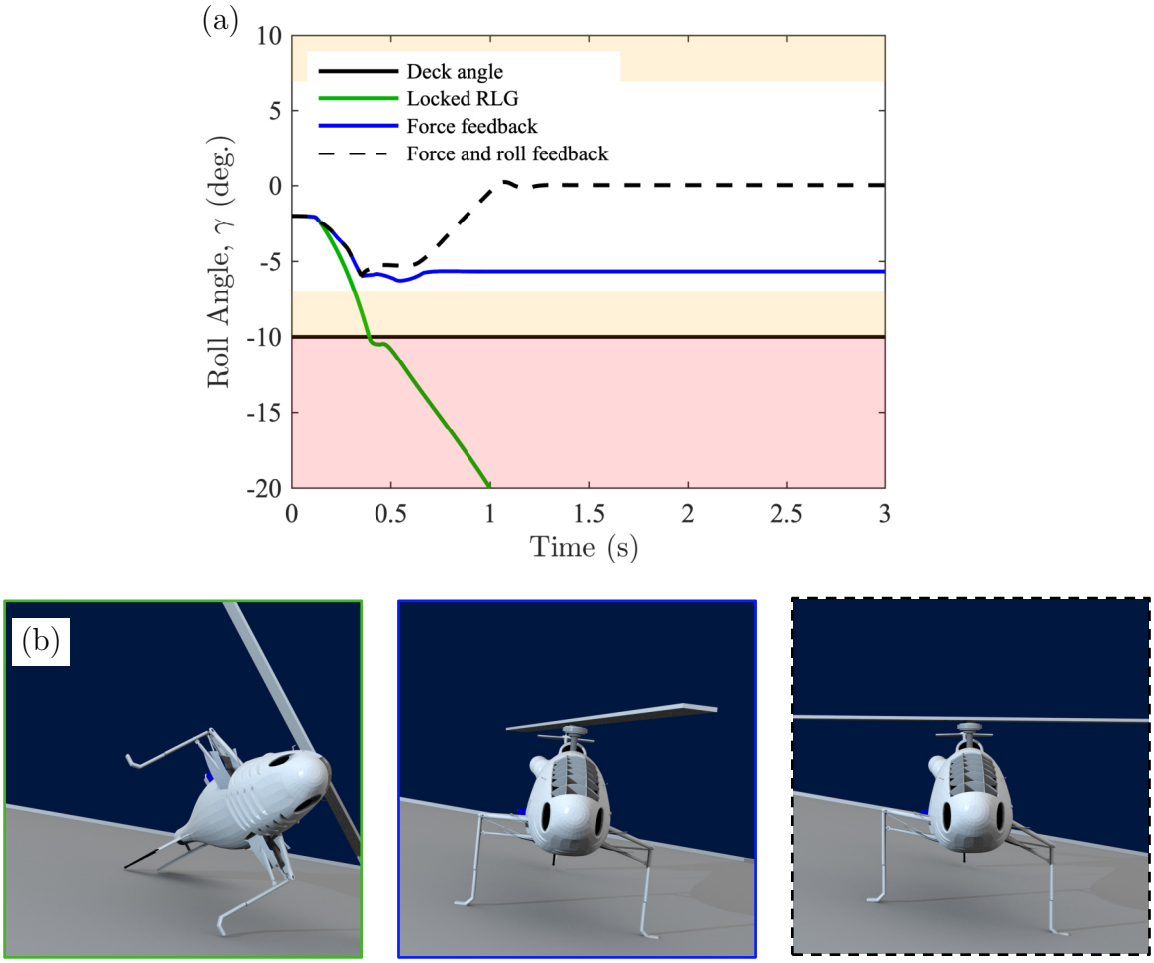

Figure 7.18: (a) Roll angle data from a static surface landing simulation of a -10° slope without active RLG, with force-feedback control, and roll- and force-feedback control with shaded regions for low risk (orange) and high risk (red) for dynamic rollover and (b) images of each simulation to illustrate the data at t = 1.25 s.

A series of static-slope simulations were conducted using uniform distributions of the nominal S-100 landing conditions as defined in Table 6.4. As a reminder, these variables include the aircraft mass, rotor time constant, ground contact friction, aircraft orientation, and aircraft body frame velocities. The distribution of variables was tested across the locked, PBC (force-feedback control), and roll- and force-fused RLG control configurations. Figure 7.19 shows the regions of steady state roll angle as a function of the ground slope, γ. Visible in this plot are the regions where the

S-100 may enter a dynamic rollover condition when the ground slope is less than -7° or greater than 7°. Prior to the dynamic rollover regions for the locked RLG configuration, the aircraft's steady state roll angle mimics the ground slope.

In contrast, the PBC has no regions of dynamic rollover. This supports that force feedback alone is enough to keep the aircraft from dynamic rollover in nominal conditions. However, the PBC struggles with the negative ground slopes due to the inertial cross-coupling detailed in Section 7.3.2. For the negative ground slopes, the aircraft has dangerous steady-state roll angles that would not be acceptable for normal operation due to the risk of dynamic rollover from ground obstacles and wind.

Finally, the sensor-fused controller shows consistent response for all of the ground slopes. This is primarily due to the third phase of landing, where the system includes roll feedback and continues control for a longer period than the PBC. This is the only configuration where the response is not only predictable, but consistent regardless of landing conditions.

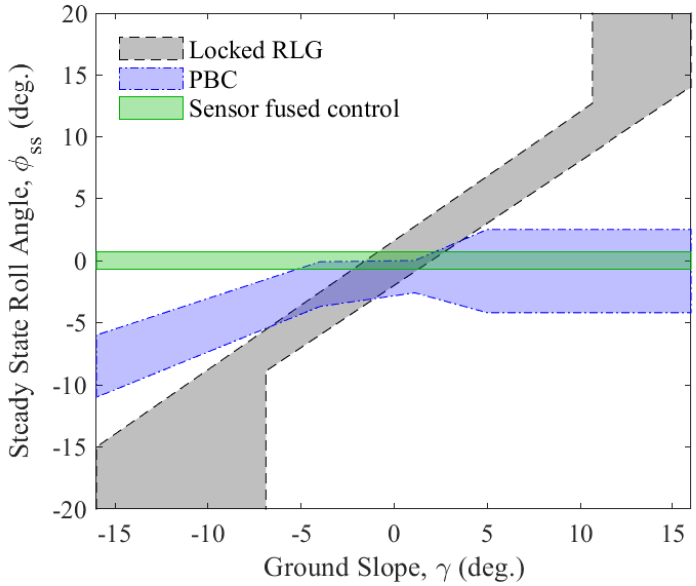

Figure 7.19: Comparison of steady-state roll angle for locked, PBC (force-feedback control), and sensor-fused controllers landing on static landing surfaces with slope γ.

7.4.2 Roll Sinusoid Platform Landings

Simulations were conducted landing the S-100 on a moving platform with *only* sinusoidal roll motion. The sine waves used to generate the deck motion have amplitudes from $\pm 15^\circ$ and frequencies that correspond to waves with maximum angular rates of 3-8°/s respectively. Sinusoid waves of these amplitudes and frequencies are within the SS 6 simulated ship deck response as shown in Figure 5.6(b). The primary benefit of simulations with only roll sinusoidal is the lack of surge, sway, and heave motion which adds to the dynamic interaction. These simulations are designed to be compared to SS platform simulations to determine the impact of angular versus translation motion on the systems performance.

Figure 7.20(a) shows the roll angle data for the three operation modes landing on a platform undergoing sinusoidal motion. The platform's sinusoid had a peak roll rate of $\pm 5^\circ$/s and initialized at -10°. Figure 7.20(b) illustrates each operation mode's orientation at t = 1.0 s, when the locked RLG is recovering from a bounce. The aircraft for each simulation has a peak descent speed of 0.61 m/s, near the bound of design specification for the RLG and well above the experimental tests conducted in Section 7.2.2. Simulation with locked RLG does not yield rollover, but it has a significant and dangerous bounce. The author notes that the aircraft does not enter dynamic rollover because the platform was moving toward $\gamma = 0^\circ$. Both RLG controllers prevent this large roll angle bounce and keep the aircraft outside the low-risk for dynamic rollover region. Again, the roll- and force-feedback controlled system quickly (<0.5 s) returns the aircraft to a level position even as the deck continues to move. The force-feedback controller does not have any sensor feedback to track the deck motion, so the aircraft has a constant roll offset as it rides along with the deck. This puts the aircraft in an unusual orientation for recovery or take off at a later time. All of these issues are dealt with by the roll- and force-feedback controlled gear since it converges toward and maintains the allowable ϕ_{DB}.

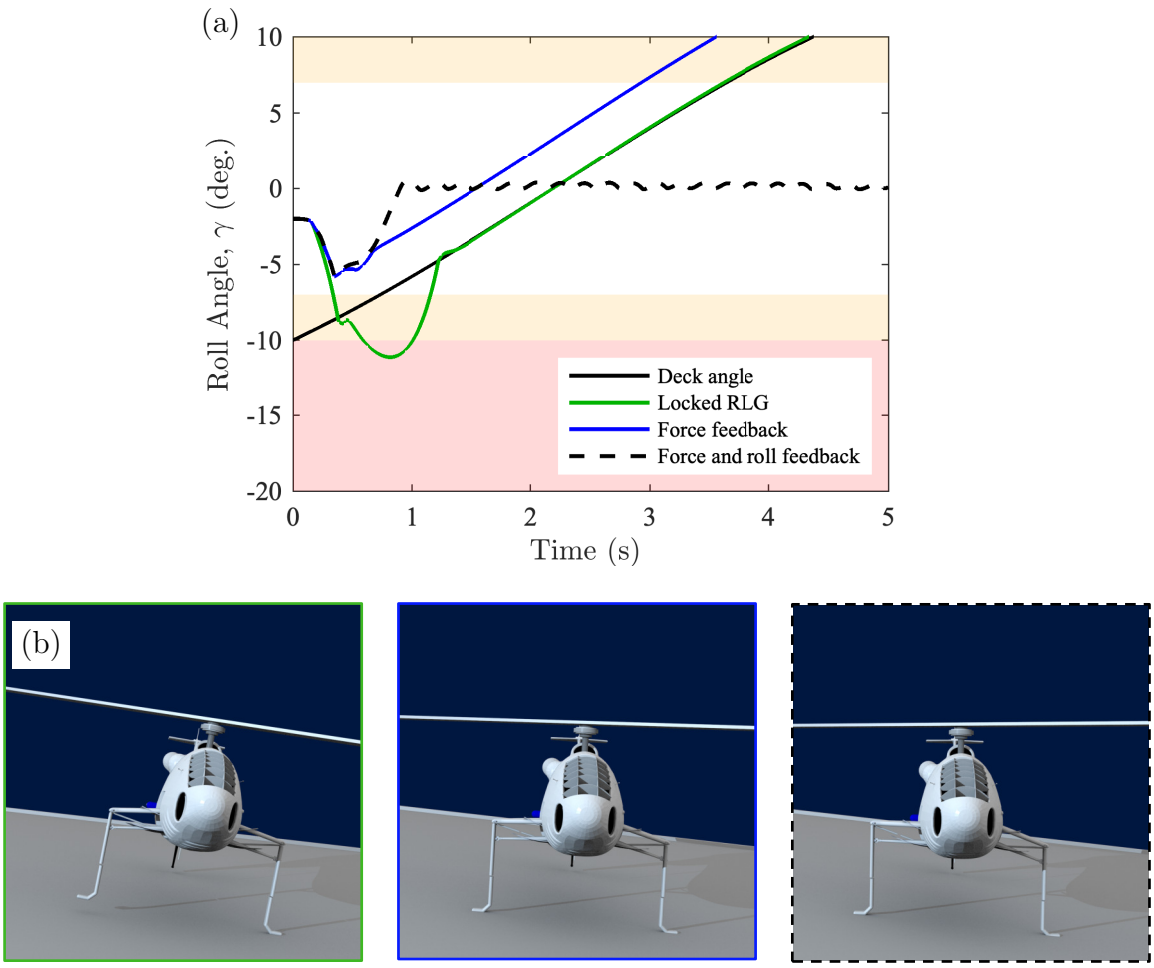

Figure 7.20: (a) Roll angle simulation data landing on a moving platform sinusoid initial condition of -10° for locked, force-feedback controlled, and roll- and force-feedback controlled RLG. (b) Shows renders of the system for each simulation at t = 1.0 s.

Similar behavior is observed from a landing where the platform's initial condition is 10° with positive angular rate. Figure 7.21(a) shows the roll feedback of the simulations for each operating mode. The author notes that the aircraft has a significant bounce, but it does not enter dynamic rollover in these ideal conditions (no wind modeled). In the locked RLG case, there is a ≈1° bias between the aircraft roll and the deck roll angle, which is due to semi-permanent stretch of the cable on one side of the RLG assembly. This semi-permanent asymmetry is caused by the large impact force on the right leg.

Some oscillations are visible on the force feedback controlled and roll- and forced-feedback controlled RLG simulations. The oscillations are caused by momentary loss of contact. Figure 7.21(b) further elucidates the roll- and forced-feedback controlled RLG simulation. The force-feedback control portions of both controllers are not perfectly tuned across a wide range of landing speeds; therefore, the gear can momentarily lose contact. Any momentary loss of contact results in a deceleration of the gear until contact is regained. This prevents the gear from impacting the surface with significant force, further destabilizing roll angle. In this case, the gear loses contact four times during the landing sequence (see Figure 7.21(b)). Regardless of this contact bouncing, the RLG is fast enough to bound the roll angle within a safe operating region during the transient period before full contact is established around 0.4 s. There is then a transient period where the torque on the spool from both cables is too high to achieve significant $\dot{\gamma}_{RLG}$. By 0.6 s, the torque stabilizes to a point where the drivetrain can drive the legs at a rate of $\approx 7.7^\circ$/s until the roll is within ϕ_{DB}. These sinusoid platform simulations show the roll- and force-feedback controlled RLG's ability to bound the roll angle to a safe operating region. The roll- and force-feedback control maintain the roll angle near the desired deadband even with significant pitch-roll inertial cross-coupling caused by the rotor blade and landing gear geometry.

7.4.3 SS Platform Landings

The final set of simulations conducted were on dynamic platforms simulated SS 5 and SS 6 conditions. These two conditions were chosen since they represent a combined 37% probability of occurrence in the northern hemisphere [105], and the dynamics of the ship decks at these SS pose a risk to pilots and aircraft.

Figure 7.22 depicts the fuselage roll angle output of a 4 s simulation where the aircraft initiates contact on the landing surface while at 10° roll. This particular

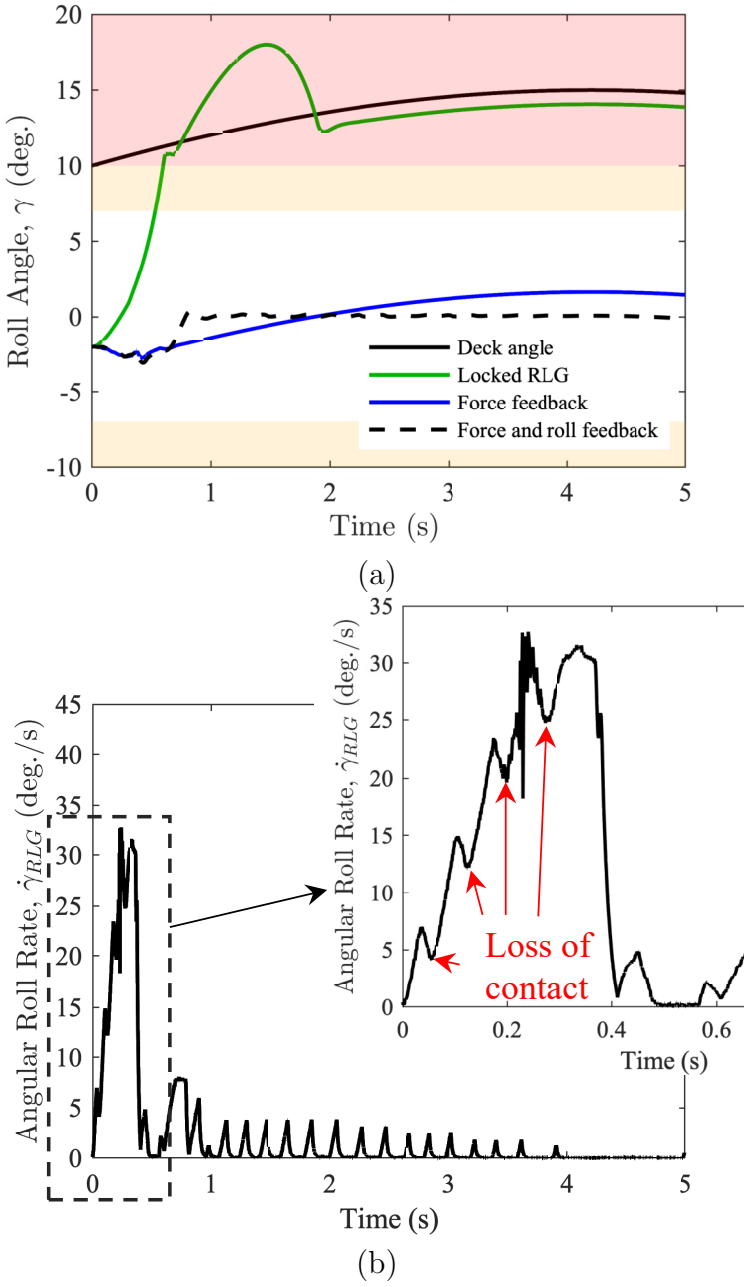

Figure 7.21: Sinusoidal moving plaftorm landing simulation with momentary loss of foot contact. (a) Shows roll angle outputs of a deck sinusoid with initial condition of 10° for locked, force-feedback controlled, and roll- and force-feedback controlled RLG. (b) Shows $\dot{\gamma}_{RLG}$ for the roll- and force-feedback controlled system with callouts for loss of contact during descent.

case leads to dynamic rollover of the locked RLG system. There is rolling motion of the fuselage for the active controlled systems as well, but no dynamic rollover or

dangerous bouncing behavior. The significant rolling of the fuselage of the actively controlled simulations is because the combined impact velocity between the helicopter and deck is 1.3 m/s. This is almost two times the maximum speed of the RLG, so they are unable to absorb all of the roll angle. The roll- and force-feedback RLG returns the fuselage to a safe operating condition within 1 s of initial contact even though the combine system dynamics are well outside of the nominal operating specification.

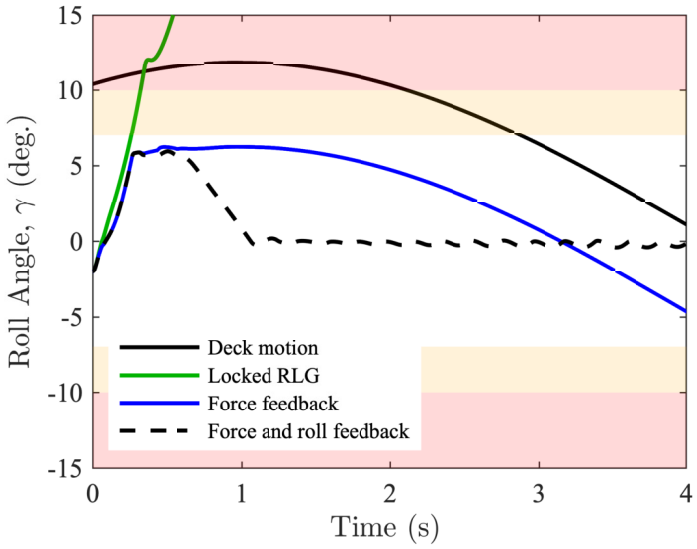

Figure 7.22: Roll angle outputs from a S-100 landing on a SS 5 simulated dynamic platform.

More detail of the drivetrain's response to this aggressive landing is illustrated in Figure 7.23. It is clear the system is accelerating as quickly as possible to keep up with the combined deck and aircraft dynamics until contact is made on all legs. The torque is too high to continue accelerating at the same magnitude, so it slows down. Once the drivetrain slows and the torque stabilizes across the spool, the RLG system begins to drive toward ϕ_{DB} at t = 0.7 s. Noise in the data between the time of full contact and the time of return to level is due to dynamics of the cable, ground, and elastic joints during the impact.

Similar responses result from SS 6 simulated landings. Figure 7.24(a) depicts the roll response to a SS 6 landing when contact begins with the deck near -7° and

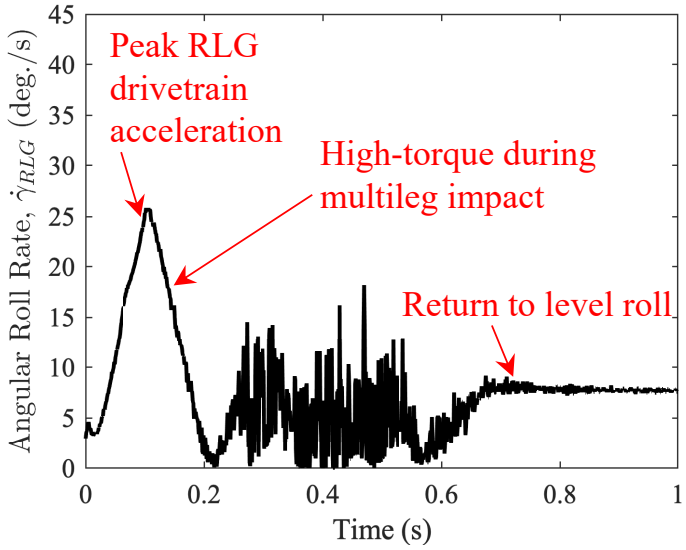

Figure 7.23: RLG ground angle absorption rate, $\dot{\gamma}_{RLG}$, outputs from a S-100 landing over the 1 s landing window on a SS 5 simulated dynamic platform using the fused roll- and force-feedback controller.

1.28 m/s relative vertical velocity, while Figure 7.24(b) shows the response to a SS 6 landing with contact initiated at 10° and relative velocity between the deck and aircraft at 0.98 m/s. In Figure 7.24(a), the difference between the roll angles of the three systems is small because of the large, relative velocity and inertial cross-coupling effect on roll rate. This represents an aggressive landing outside the normal bounds for the RLG. Active RLG systems of these simulations have a minor bounce but do not enter dynamic rollover. The gear's ability to push against the slope prevents the aircraft from a dangerous bounce and rollover. The locked RLG enters dynamic rollover in the low-risk region because of the higher-than-nominal landing velocity relative to the nominal value (see Table 6.4). This ability to combat dynamic rollover is more pronounced for the roll- and force-feedback system, which pushes the aircraft into the safe operating region well before the deck reaches a safe roll angle.

Each simulation presented shows that the force feedback controller is, at minimum, sufficient for preventing roll instability, but the danger with such a controller is clear in Figure 7.24(b). The gear using force feedback absorbs significant ground angle

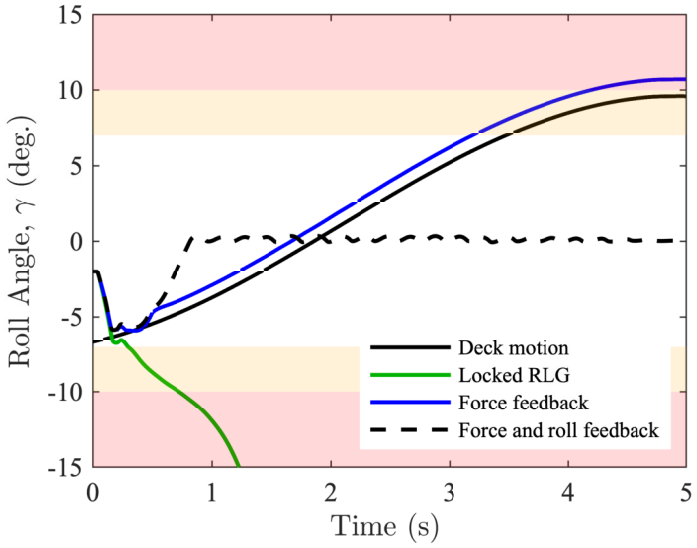

(a)

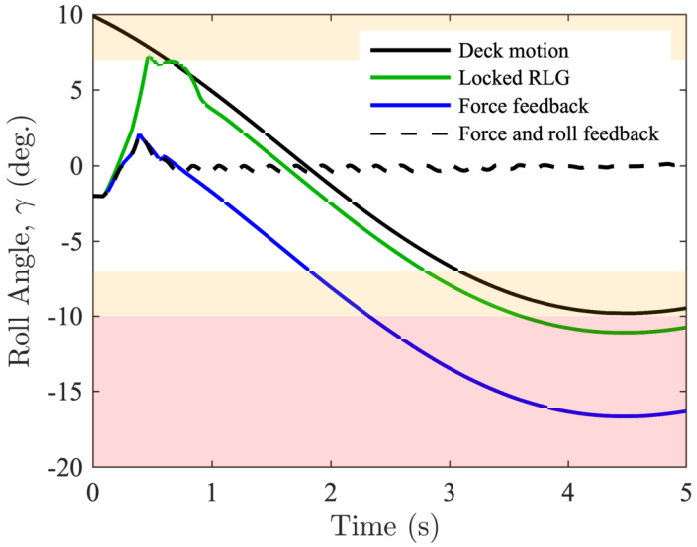

(b)

Figure 7.24: Roll angle outputs from two simulated S-100 landings on ship decks in SS 6 conditions.

(≈8°), which in turn puts the aircraft at a significant inertial roll angle of 17° by the end of the simulation at t = 5 s. At this roll angle, the aircraft is in danger of rollover if any collective is applied to the rotor. This is an example of a case where force feedback RLG is worse than a rigid-gear configuration, showing the need for continued feedback after landing. The roll- and force-fused-feedback controlled RLG

eliminates this issue by maintaining the aircraft roll near level.

CHAPTER 8

CONCLUSIONS

This dissertation spanned multidisciplinary developments of advanced RLG technologies. The disciplines considered are best summarized by Figure 8.1. This figure illustrates the high-level topics only. The specific technologies developed from this

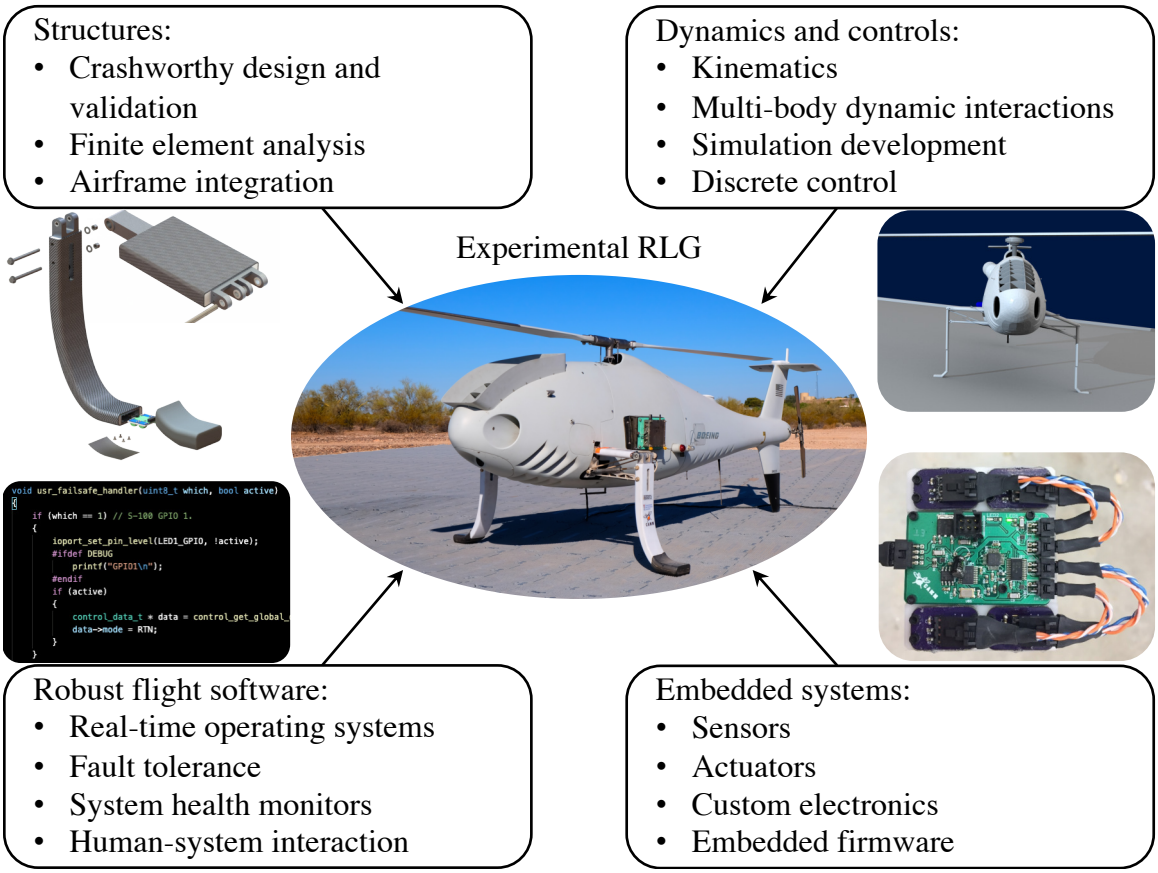

Figure 8.1: Multidisciplinary approach to the development of technologies that will enable autonomous landings using RLG.

dissertation are 1) crashworthy, cable-driven, four-bar linkage RLG structure, 2) a robust and high-sensitivity force sensor comprised of an elastomer-encapsulated pressure sensor with an engineerd air cavity, and 3) roll- and force-fused-feedback RLG control with robust sensor health monitoring and fault detection.

Chapter 2 presented the four-bar linkage mechanism as a suitable replacement to multi-jointed, DoF legs. A thorough actuation and kinematic analysis showed that a cable-driven design is the most suitable configuration for RLG use. A rapid simulation and experiment framework was proven to meet crashworthiness standards with impacts up to 5 m/s at 5° pitch and roll of the fuselage. Not only is this novel structure crashworthy, its design enables fuselage-housed actuators and reduces the number of actuators required per controllable DoF. Only one actuator is needed for symmetric or differential motion of a leg pair. This substantially reduces the overall RLG weight and aids the real-world viability of such systems.

Chapter 3 detailed the invention of a novel force sensor that can sustain large deformations from low applied force. This was enabled using a silicone elastomer-encapsulated pressure sensorwith an engineered air cavity designed using finite element methods. The sensor has a tunable, linear sensitivity until saturation. Experiments validated the analytic model within 5% for each of the considered geometric and material property variables. Its unique design is excellent for RLG because the sensor deforms into a protective structural housing during hard landings that other force sensors cannot mimic. Additional applications of the sensor as a single unit and as an array of sensors were presented to show usability in other areas of robotics and articulating manipulator research.

The third contribution, an aircraft-orientation- and foot-force-fused controller, was presented in Chapter 4. It has sufficient observable and controllable states for safe landings on static or dynamic surfaces. A nonlinear inner-outer loop PD control was derived with first-order filters on discrete measurements. The controller has unique features compared to other RLG systems, including integrated health and fault detection protocols. These features were included with the new controller, making it a robust, advanced RLG control system. Using each of the three technologies developed, a simulation-aided design commenced.

In Chapter 5, improved simulation and computed-aided design tools enabled the seamless design and integration of each contribution into a commercial helicopter (Chapter 6). Simulations revealed that the sensor-fused RLG controller yields nominal improvements to performance on static landing surfaces and substantial improvements for landings on dynamic surfaces. Furthermore, through extensive simulations, the new roll- and foot-force-feedback control was shown to be viable on slopes up to 15° and on ship decks in SS 6 conditions. Meanwhile, force-feedback control left the rotorcraft in a dangerous orientation.

This dissertation extended theoretical designs beyond the lab space into the real world with ground and flight tests of the technologies. These tests were presented in Chapter 7. Ground tests made use of a state-of-the-art dynamic motion table and customizable height obstacles. Experimental ground tests showed the roll- and foot-force-fused control, foot-force sensors, and cable-driven, four-bar gear function as designed on a representative ship deck in conditions up to SS 5. The new gear, force sensors, and robust control algorithms were all tested in the desert during the summertime to illustrate functionality in a relevant environment. Both the force sensors and cable-driven landing gear were tested in flight with landings on slopes up to 15° at descent rates near 0.5 m/s.

8.1 Future Work

This multidisciplinary dissertation generated and tested technologies that will enable autonomous landing with RLG in the future. They do so by providing a redundant, autonomous operational system that operates independent of the visual environment conditions and landing surface dynamics; as proven by the integration and experiments with the S-100 aircraft. Now, the author proposes four research topic areas and tasks based on the findings of this dissertation. Descriptions of each in no particular order may be found below:

8.1.1 Autonomous Landings with RLG

The purpose of this dissertation was to overcome technology roadblocks that inhibit autonomous landings of aircraft with RLG. The most important follow-on research is the development and integration of remaining technologies for autonomous landing. The first step to this process is the integration of this dissertation's sensors and RLG controller with aircraft flight controllers. There are many uncertainties of how the RLG may integrate into aircraft in the future and what benefits that will achieve from a controls and robust software perspective. The author proposes future work to study aircraft integration techniques to maintain robust operation during hard landings, and also enhance the controllability of the system.

The next step to this process will be the development and experimentation of guidance and navigation algorithms meant for autonomous landing with RLG. The previous step looks at the requirements and engineering challenges with direct integration, from the ground up, with an aircraft's flight control systems. Within the next 5 years the author believes a completely autonomous unmanned aircraft with RLG will exist. This belief is based on the multiple emerging markets and early adopters from Chapter 1. Many of the core technologies and design tools of this dissertation will make this concept a reality. The last major hurdle to overcome for completely autonomous landings will be guidance and navigation algorithms. The author suggests a research task to review existing algorithms, their limitations (if any), and create a method to guide the autonomous aircraft toward a moving target and use combined aircraft flight controls with RLG controls to safely land. This research task will also guide research into the sensors and state estimation processes required to navigate local to the landing target. Such sensors may include but is not limited to cameras, lasers, and ultra-wide band radios.

8.1.2 Landings on Complex, Unprepared Terrains

To date, RLG systems have been developed and flight tested on well prepared surfaces. Rotorcraft with RLG will need to land on a variety of complex, unprepared surfaces. In order to accomplish this, there are three research challenges which must be overcome. First, researchers will need to identify a range of obstructions or terrain complexities that the current RLG technologies cannot handle. For example, the S-100 RLG design assumes the aircraft will not land with a tall obstruction under the fuselage. The fuselage may impact the obstruction before any force is measured by the foot-force sensors. Second, suitable sensors and control algorithms must be researched to overcome current technology shortfalls for the most complex terrains. LiDAR and landing zone detection algorithms are one example of each. The measurements from LiDAR are useful to detect complex obstructions or features of the terrain, while the landing zone determination algorithms will guide the aircraft away from dangerous positions. Another example is an array of force sensors on the fuselage. An array of sensors along the fuselage generate contact feedback that ensures no portion of the fuselage touches an obstacle before a leg does. Finally, researchers will need to integrate each new technology with RLG and complete tests one unprepared landing sites.

8.1.3 Improvements to the Low-Force, Large-Deformation Force Sensor

Chapters 3 and 6 showed an extensive development cycle and rotorcraft integration of the elastomer-encapsulated force sensor, respectively. This dissertation was not able to completely characterize the sensor's hysteretic and frequency response characteristics when bundled as an array with an elastomer cover. Specifically, there will be changes to the overall force measurement responsiveness because of this implementation. Therefore, additional experimentation may be done in the future on the sensor array with an elastomer cover. Additionally, the author recommends fur-

ther frequency domain experiments of the single-sensor unit using elastomer's other than silicone. These experiments will inform future use cases and implementation constraints.

8.1.4 Airframe Diversification

The majority of experimental RLG developments from the literature and this dissertation focus on rotorcraft, due to their risk of dynamic rollover and widespread use. Many other vertical take-off and landing (VTOL) platforms are emerging for missions of surveillance, cargo delivery, and personnel delivery. For this reason, the author proposes a mechanical design and structural analysis study of the cable-driven, four-bar RLG on additional aircraft platforms. VTOL aircraft are not limited to rotorcraft, so the opportunities for RLG to improve safety on general rotary wing aircraft should be explored in the future. This may be done through a mechanical design study of how a cable-driven, four-bar mechanism integrates with multirotor aircraft (such as quadcopters) and fixed wing VTOL aircraft (such as a tail sitter).

8.1.5 Scaling RLG Concepts and Enabling Technologies

A majority of future research into active landing gear should focus on scaling down to 10 kg aircraft and scaling up to 500+ kg aircraft since there is ample research at the $\approx$ 100 kg sized rotorcraft. With regards to scaling down the technologies, future research should consider volume-optimized sensors and actuators. Small-scale RLG designs would also see benefits from grasping or locking mechanisms that large scale aircraft would not. Such grasping mechanisms may enable perch and observe style missions for small scale aircraft (<20 kg), but there is uncertainty with regards to usability and the weight penalty of such technologies. For example, surveillance aircraft for fire fighters observing forest fires would greatly benefit from the ability to land on trees or boulders using a grasping RLG, which fixed-gear UAVs cannot

accomplish today. However, the weight of such a system may be prohibitive.

Scaling up RLG as a technology requires research in different technology areas. Large-scale aircraft will not trade significant range or payload capacity for RLG; therefore, tools for structural weight optimization must be developed. All previous experimental RLG systems used electric actuation, which is not reasonable for large-scale systems because of their power-to-weight ratio. The author recommends a trade study of the various types of actuation suitable for large scale aircraft. Examples of these include pneumatic, hydraulic, and electrohydraulic actuators. With each actuation type, the controllability and aircraft integration considerations will change.

Usability is important to scaling up RLG as a technology. Most rotorcraft with skid or wheeled gear conduct missions that require roll-on landings, which current RLG technologies inhibit. Future research on wheeled RLG concepts on 500+ kg rotorcraft would expand the mission capabilities of rotorcraft with integrated RLG. Finally, marinisation of the cable-driven, four-bar linkage mechanism design is crucial for real-world usability. Considerations for marinisation include the wear and tear on the drive cable, implementation of non-corrosive metal alloys, and protection of the structural carbon-fiber from saltwater exposure. While this is not a research heavy task, it is critical to wide-spread implementation of this novel RLG design on large rotorcraft.

APPENDIX A
CRASHWORTHINESS DESIGN ITERATIONS OF A CABLE-DRIVEN, FOUR-BAR LINKAGE RLG

This appendix outlines the first three design and drop-test iterations of a cable-driven, four-bar linkage RLG design that converged on a crashworhty design.

A.1 First Design & Testing Iteration

The first iteration serves to introduce a basic design concept. As shown in Figure A.1(a), there is a basic four-bar link mechanism composed of a CFRP leg, CFRP crank, and aluminum follower. With respect to the actuation of this mechanism, there are three important design choices which will carry through every design:

1. First, the elastic element that drives the system upwards is in the form of a gas spring positioned parallel to the cable. It connects the lower-inner and upper-outer joints of the four-bar mechanism (see red arrow in Figure A.1(a)). This configuration has some unique benefits. First, it simplifies the mechanical design as all of the cable routing and gas spring attachments occur at the same joints. Second, and more importantly, it provides a fail-safe mechanism for the landing gear in the event of a cable failure.

   The system is designed such that in the event of a cable failure, the legs will move to a fully retracted position where the gas spring is fully extended; however, they will still be able to carry load with the gas spring carrying the tensile load that the cable is no longer withstanding. In this appendix, there will be some drop test results in which the cable incurred damage, but the test frame did not impact the ground as the legs retracted to the fail-safe position where the gas

spring becomes load bearing.

2. Second, the cable which drives the mechanism routes through the follower-fuselage joint of the four-bar mechanism (as described in Chapter 2); however, it does not terminate at the crank-leg joint. Rather, the cable loops around that joint and then returns to the follower-fuselage joint of the four-bar mechanism, where it is routed into the body of the vehicle and terminates, see Figures A.1(a) to (c). This gains some additional mechanical advantage by effectively increasing the amount of cable movement required to achieve the differential leg movement. This also allows for the third design choice.

3. Third, the cable terminates on a shock absorber which takes the form of a simple rubber compression spring. In the drop test rig, this was achieved by routing the cable through a 90° re-direct towards the rear of the drop test frame where the cable then terminates on a rubber shock absorber, see Figure A.1(d).

Figure A.1(a) shows the CAD of the detailed mechanical design for the first iteration that incorporates the three key design concepts described above. Figures A.1(b) through (d) show photographs of the manufactured system mounted on the drop test rig, where (d) shows details of how the cable is routed towards the rear of the drop test rig and terminated on a rubber shock absorber. For this first design, the detailed finite element analysis for sizing of all the components was not done. Rather, as a proof of concept, as many COTS component were utilized as possible for the manufacturing of the crank, leg, and follower. For example, the crank is mainly formed from COTS square aluminum extrusion. As such, and as will be shown during drop testing, this concept was not expected to meet impact speed and orientation requirements. One important design choice for this particular iteration was that the cable was not routed about the crank/leg joint, but rather through a pin placed about one inch below, see Figure A.1(c). Finally, note that the end of the cable is simply

terminated on an eye bolt threaded onto a solid aluminum block, see Figure A.1(d).

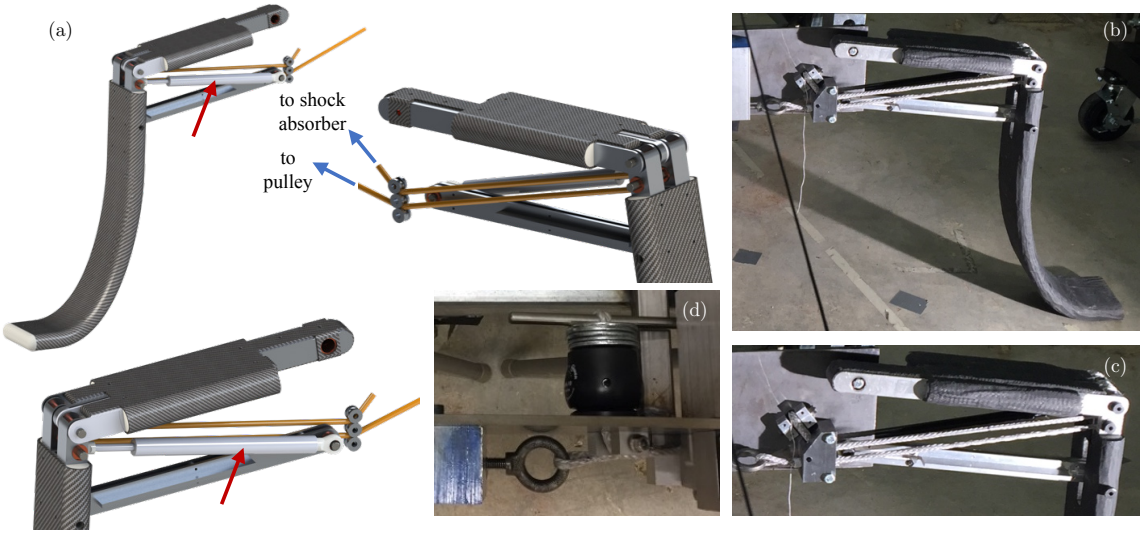

Figure A.1: First design iteration with three basic design concepts: i) gas spring in parallel to the cable; ii) cable system terminating in the interior of the drop test frame; and iii) cable terminating on a shock-absorbing, rubber compression spring.

Drop test results and observations for the first iteration:

- The first drop test was performed at a weight of 180 lb (82 kg) and a drop height of 24 in (0.61 m). This equates to an impact velocity of roughly 3.5 m/s and an impact energy of roughly 490 J. The results are shown in Figure A.2, and the drop was successful with no visible damage being incurred.

- The second drop test was performed at a weight of 360 lb (163 kg) and a drop height of 24 in (0.61 m). This equates to an impact velocity of roughly 3.5 m/s and an impact energy of roughly 980 J. This weight was chosen as it mimics the same impact energy which would be experienced with a full velocity 5 m/s impact of a system with a weight of 180 lb (82 kg), thus enabling a test of the correct energy range at a lower impact velocity. The results are shown in Figure A.3, and show failure of the RLG during impact. Figures A.3(a) and (b) show the system being loaded to its maximum deflection at which stage the pin at the leg where the cable loops over begins to fail. This is highlighted in

Figure A.3(c). Following this, the pin shears the leg metal hard point entirely and the leg loses all structural integrity as shown in Figure A.3(d).

This failure is a result of the fact that the cable routes about a pin which is below the crank/leg joint. As such, the leg loads from the cable place the leg under a large bending/shear load which ultimately leads to failure. In the next design iterations, this is addressed by making sure the cable loads act at the crank/leg pin. This greatly improves the structural integrity of the leg component.

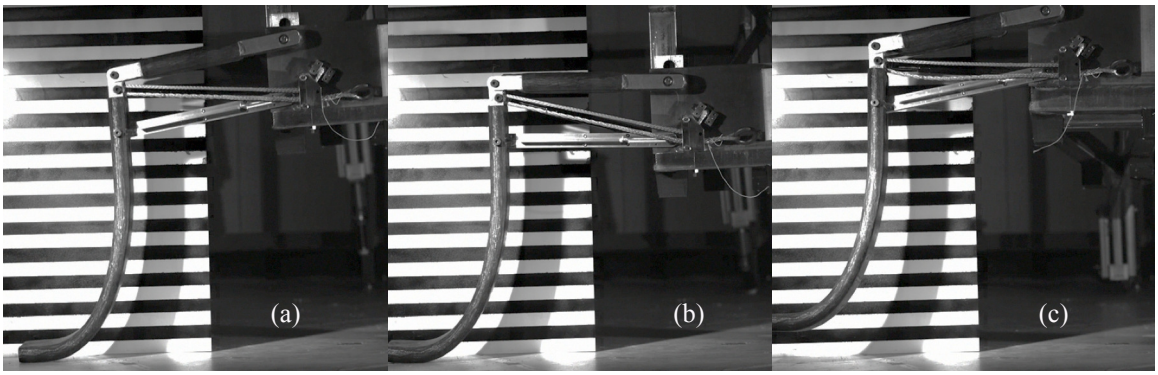

Figure A.2: First design iteration drop test at 24 in (0.61 m) and 180 lb (82 kg) ($\approx$ impact velocity of 3.5 m/s and impact energy of 490 J). (a) Shows the moment of first contact. (b) Shows the point of maximum loading. (c) Shows the transient frame after spring back.

A.2 Second Design & Testing Iteration

The second design iteration, shown in Figure A.4, uses all custom machined CNC metal hard points and was no longer restricted to using COTS metal extrusions. The major re-designs from the previous iteration are as follows:

- The cable is now routed through the crank/leg pin, thus reducing the bending loads induced in the leg due to the tensile loads carried by the cable (see red arrow in Figure A.4(a)).

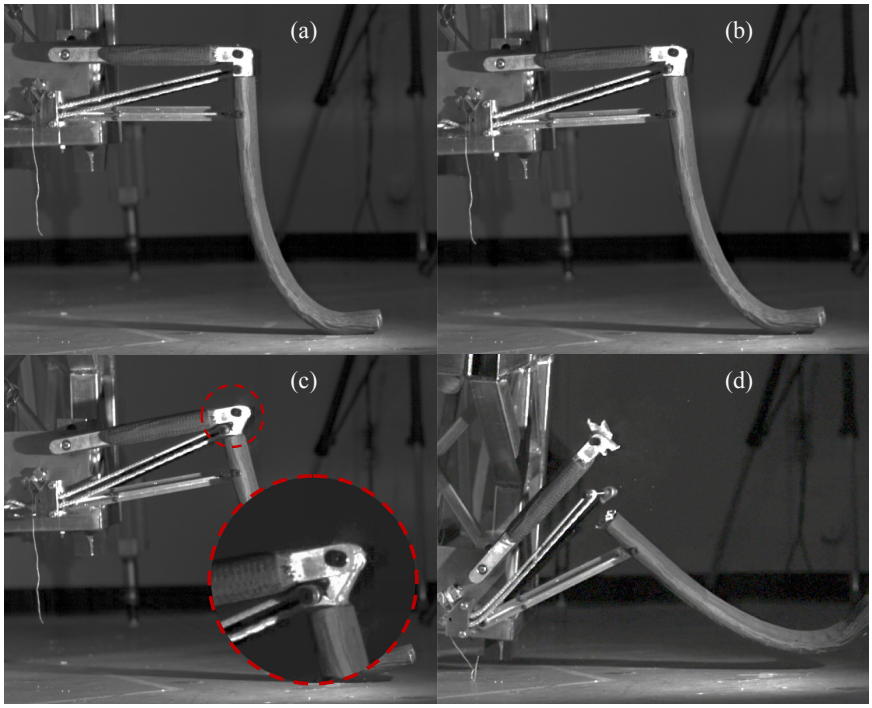

Figure A.3: First design iteration drop test at 24 in (0.61 m) and 360 lb (163 kg) ($\approx$ impact velocity of 3.5 m/s and impact energy of 980 J). (a) and (b) Show loading to maximum deflection. (c) Shows the onset of failure at the leg pin supporting the cable loads, this ultimately leads to failure of the leg component in (d).

- A new structure was developed for attaching the four-bar mechanism to the drop test rig shown in green in Figure A.4(a) and also in the detailed photograph in Figure A.4(c). This structure provides both mechanical support for the four-bar link mechanism — by adding clevises to both the crank and follower attachment joints — as well as provides the structure for routing the two ends of the cable.

- The crank was redesigned such that it is symmetric about its attachment arm. Refer to the blue arrow in Figure A.4(a) and compare to the design shown in Figure A.1(a).

- In addition to the modifications visible in Figure A.4, the metal hard points in the crank and leg were increased in strength by custom machining aluminum hard points rather than using COTS aluminum extrusion.

Drop test results and observations for the second iteration:

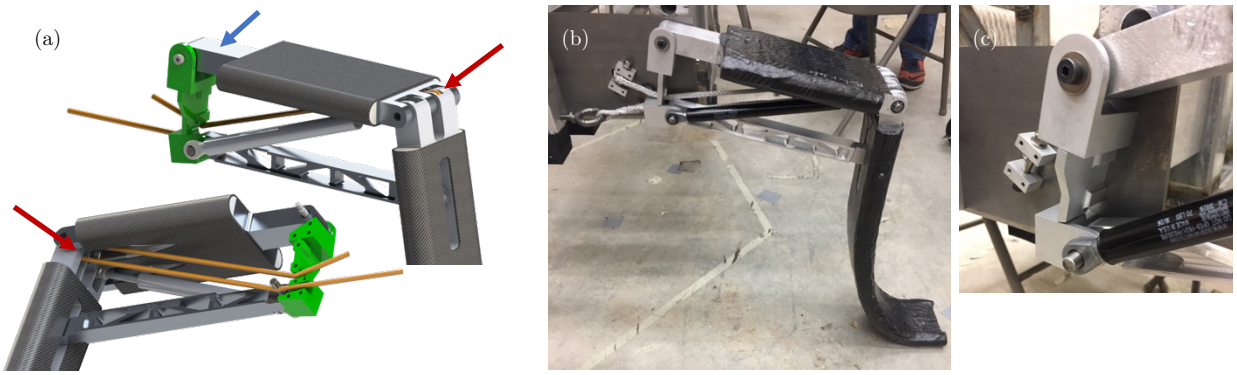

Figure A.4: Second design iteration. Red arrows highlight routing of the cable about the crank/leg interface. Blue arrow highlights the symmetric crank design about its attachment arm.

- The first drop test was performed at a weight of 200 lb (100 kg) and a drop height of 50 in (1.27 m). This equates to an impact velocity of roughly 5 m/s, and an impact energy of roughly 1250 J. This is about half the impact energy that is the ultimate target, but it is at the full impact velocity. The results are shown in Figure A.5, and the drop was successful with no visible damage being incurred.

- The second drop test was performed at a weight of 440 lb (200 kg) and a drop height of 50 in (1.27 m). This equates to an impact velocity of roughly 5 m/s, and at the target impact energy of 2500 J.

  Figure A.6 shows the results of the drop test. As the leg is loaded from (a) to (b), the system experiences a cable failure, the onset of which is visible in Figure A.6(b). At this point, the leg moves to the fully-retracted, fail-safe position where the gas spring carries tensile loads, this occurs between Figures A.6(b) and (c). However, as highlighted in Figure A.6(c), the load carried by the gas spring causes failure of the clevis holding the follower to the drop test rig. Following this failure, as shown in Figure A.6(d), the follower fails and the four-bar mechanism becomes disconnected from the drop test rig at the follower connection point.

It is clear in this drop test that the cable failed prematurely. Post-mortem inspection showed that manufacturing defects (burrs) on the crank had likely contributed to the premature failure of the cable by essentially cutting (or damaging) the cable as it slides past the slot on the crank at the crank/leg pin.

With the failure of the cable being so premature, not enough energy was dissipated through cable failure and hence the loads transferred to the follower clevis were larger than designed for. The follower clevis was sized based on multibody dynamic simulations of the system in a configuration without the cable but with an impact velocity of 1 m/s (rather than the 5 m/s used to size the structure in its normal configuration).

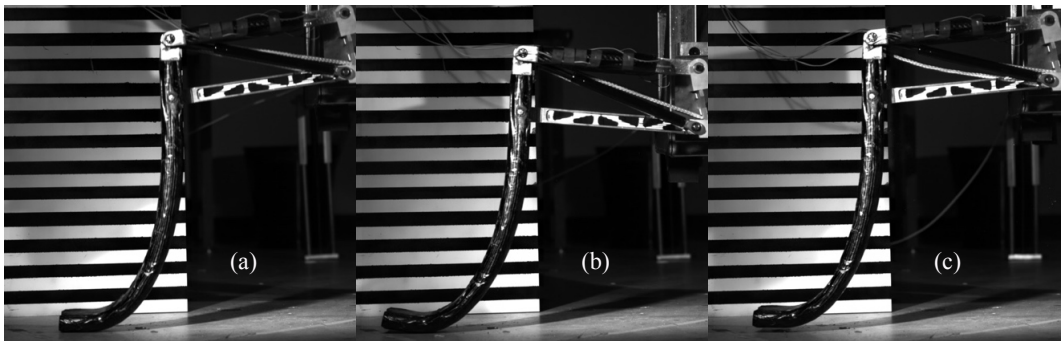

Figure A.5: Second design iteration drop test at 50 in (1.27 m) and 220 lb (100 kg) ($\approx$ impact velocity of 5 m/s and impact energy of 1250 J). (a) Shows the moment of first contact. (b) Shows the point of maximum loading. (c) Shows the transient frame after spring back.

A.3 Third Design & Testing Iteration

The third design iteration, shown in Figure A.7, maintains many of the design features of the previous iteration with some minor changes to improve strength. The re-designs from the previous iteration are as follows:

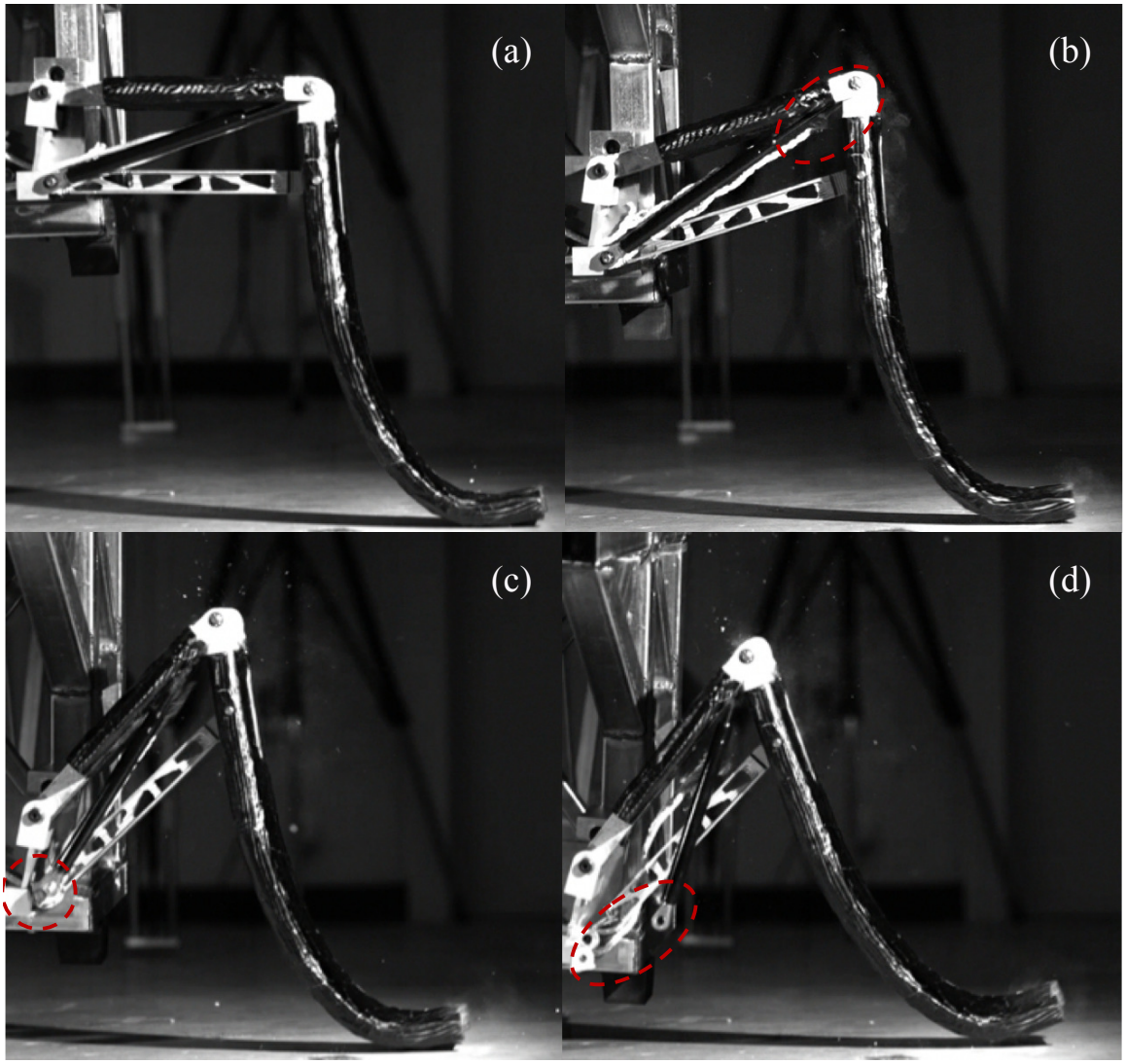

Figure A.6: Second design iteration drop test at 50 in (1.27 m) and 440 lb (200 kg) ($\approx$ impact velocity of 5 m/s and impact energy of 1250 J). (a) Shows the moment moment of first contact. (b) Shows the point of maximum loading where failure of the cable begins at the crank/leg joint. (c) Shows the leg moving to the fully retracted position and subsequent failure of the follower clevis holding the gas spring as it begins to take load. (d) Shows final failure of the follower clevis and of the follower itself leading to failure of the four-bar mechanism.

- The cable is now routed through a slot on the center of the crank/leg interface pin, see blue arrow in Figure A.7(a) and contrast with red arrow in Figure A.4(a). This is primarily done to reduce the torque induced in the crank arm due the loads on the cable.

- To accommodate this placement of the cable while maintaining suitable structural integrity at the crank/leg interface, the gas spring is now connected on a new pin located on the leg below the crank/leg pin (see red arrow in Figure A.7). If the gas spring were to carry significant loads this attachment location, it would introduce structural integrity problems. This was the case with the first design shown in Sect. A.1 . However, the gas spring only carries load in the event of a cable failure, and in which case the loads are significantly lower and the system is sized appropriately.

- As shown by the green part in the CAD model in Figure A.7(a), the structure supporting the four-bar mechanism to the drop test rig was slightly modified for improved strength. It also increases the radii across which the cable routes.

- Finally, as shown in Figure A.7(d), the cable now terminates on a moving spool. The spool is held in place by the same drive system that would be used in actuating the system. (In earlier iterations, as shown in Figure A.1, the cable was simply terminated on an eye-bolt attached to an aluminum block). This enables testing for any potential structural integrity issues associated with the cable/spool termination and/or the spool itself.

Although from the previous iteration it was clear that cable failure was a possibility, this is meant as a beneficial failure mode as there is the redundancy of carrying load through the gas spring. As such, cable failure acts as a fuse preventing other structural failure modes which have no redundancy. In this design iteration, however, the purpose was to control the cable failure such that it would result in a graceful retraction of the legs to their fail-safe position.

Drop test results and observations for the third iteration:

- The drop test was performed at a weight of 440 lb (200 kg) and a drop height of 50 in (1.27 m). This equates to an impact velocity of roughly 5 m/s, and an

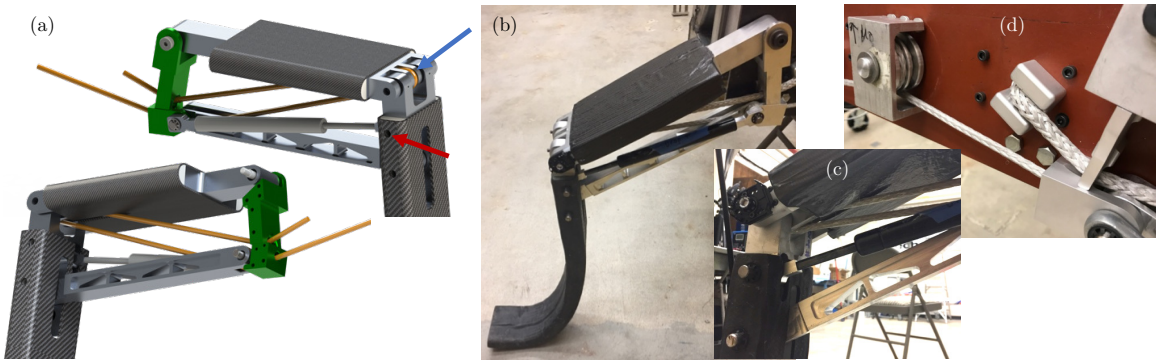

Figure A.7: Third design iteration. Blue arrow highlighting the cable routing now centered about the crank, red arrow highlighting the new location of the gas spring attachment pin, and the green part highlighting the new interface structure.

impact energy of roughly 2500 J which is the target drop weight and velocity. As shown in Figure A.8, the RLG incurred damage; however, the drop test *was successful* as the drop test frame did not impact the ground. The vehicle carrying the RLG would not have incurred any damage.

Figure A.8(a) shows the point of maximum deflection of the system before damage is incurred. Damage first occurs in the form of localized crumpling on the compression side of the CFRP legs as highlighted in Figure A.8(b). Although the legs crumple, they do not lose load carrying capability. Following this crumpling, there is damage of the cable at the spool resulting in a loss of tension on the cable, this first occurs on the right leg as shown in Figure A.8(c). The legs then move to the fully retracted fail-safe position as shown in Figure A.8(d) where the gas spring is carrying the remaining loads necessary to maintain the gear in position.

Although this is considered a successful drop test at the full weight and impact velocity requirements, there was one additional design modification. This final iteration and associated drop tests were described in Chapter 2.

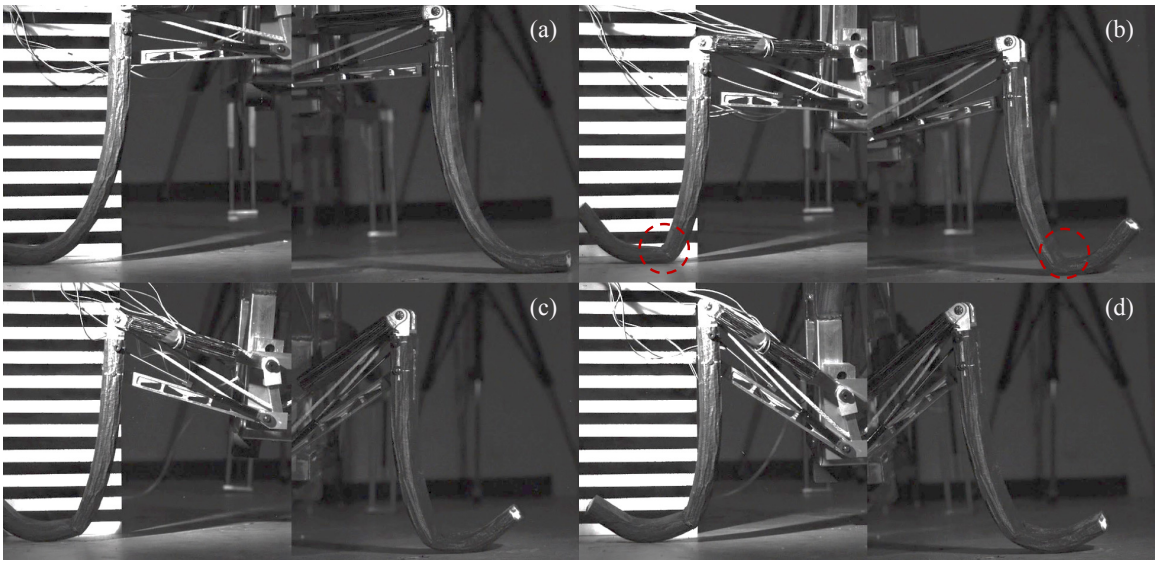

Figure A.8: Third design iteration drop test at 50 in (1.27 m) and 440 lb (200 kg) ($\approx$ impact velocity of 5 m/s and impact energy of 2500 J). Although damage was incurred by the RLG, this is considered a *successful* drop test.

REFERENCES

[1] "Helicopter flying handbook," in. Federal Aviation Administration: 2012, ch. 10: Advanced Landing Maneuvers, pp. 10.7–10.9.

[2] R. Fang and B. Finlay, "Aircraft ship operations," in. BM, Amsterdam: Advisory Group for Aerospace Research and Development (AGARD), Nov. 1992, ch. Determination of Limitations for Helicopter Ship-Borne Operations, pp. 18.1–19.14.

[3] R. A. Ibrahim and I. M. Grace, "Modeling of ship roll dynamics and its coupling with heave and pitch," *Mathematical Problems in Engineering*, p. 32, 2010. DOI: 10.1155/2010/934714.

[4] M. H. Raibert, "Legged robots," *Commun. ACM*, vol. 29, no. 6, pp. 499–514, Jun. 1986. DOI: 10.1145/5948.5950.

[5] M. Buehler, R. Playter, and M. Raibert, "Robots step outside," in *Int. Symp. Adaptive Motion of Animals and Machines (AMAM)*, Ilmenau, Germany, 2005, pp. 1–4.

[6] M. Ahmadi, H. Michalska, and M. Buehler, "Control and stability analysis of limit cycles in a hopping robot," *IEEE Transactions on Robotics*, vol. 23, no. 3, pp. 553–563, 2007. DOI: 10.1109/TRO.2007.898956.

[7] M. Raibert, K. Blankespoor, G. Nelson, and R. Playter, "Bigdog, the rough-terrain quadruped robot," *IFAC Proceedings Volumes*, vol. 41, no. 2, pp. 10822–10 825, 2008, 17th IFAC World Congress. DOI: 10.3182/20080706-5-KR-1001.01833.

[8] V. Manivannan, J. P. Langley, M. Costello, and M. Ruzzene, "Rotorcraft slope landings with articulated landing gear," in *AIAA Atmospheric Flight Mechanics (AFM) Conference*, Boston, MA, 2013, p. 5160. DOI: 10.2514/6.2013-5160.

[9] B. German, M. Daskilewicz, T. Hamilton, and M. Warren, "Cargo delivery by passenger evtol aircraft: A case study in the san francisco bay area," in *AIAA SciTech Forum*, Kissimmee, FL, Jan. 2018. DOI: 10.2514/6.2018-2006.

[10] O. Cornes, "Basic design limitations for urban electric vtol aircraft," in *VFS Forum 75*, Philadelphia, PA, May 2019.

[11] K. Stanzione, D. Schrage, and A. Sirirojvisuth, "Jaunt: Design, build, and test of an evtol aircraft for urban air mobility," in *VFS Forum 75*, Philadelphia, PA, May 2019.

[12] C. Al Haddad, E. Chaniotakis, A. Straubinger, K. Plötner, and C. Antoniou, "Factors affecting the adoption and use of urban air mobility," *Transportation Research Part A*, vol. 132, pp. 696–712, 2020. DOI: 10.1016/j.tra.2019.12.020.

[13] J Kiefer, M Ward, and M Costello, "Rotorcraft hard landing mitigation using robotic landing gear," *Journal of Dynamic Systems, Measurement, and Control*, vol. 138, no. 3, p. 031 003, 2016. DOI: 10.1115/1.4032286.

[14] M. Harden, "Army 20.1 small business innovation research (sbir) topic a20-006," *US DOD Army SBIR Office*, Jan. 2020.

[15] *Autonomous aerial cargo/utility system*, Aurora Flight Sciences, Mar. 2017. [Online]. Available: https://www.aurora.aero/wp-content/uploads/2017/03/AACUS-Brochure_X9a.pdf.

[16] S. Baker, D. Soccol, A. Postula, and M. V. Srinivasan, "Passive landing gear using coupled mechanical design," in *Proceeding of Australasian Conference on Robotics and Automation*, Sydney, Australia, 2013.

[17] M. Huang, H. Nie, M. Zhang, X. Wei, and S. Yue, "Design of mission adaptive landing gear for near space travel lander," *Journal of Vibroengineering*, vol. 18, no. 8, pp. 4949–4963, 2016. DOI: 10.21595/jve.2016.17078.

[18] J. Wachlin, "Computational improvements of a multibody dynamic simulation algorithm applied to a landing event simulation of a flexible legged europa lander," Georgia Institute of Technology, Aug. 2018.

[19] B. Stolz, T. Brödermann, E. Castiello, G. Engelberger, D. Erne, J. Gasser, E. Hayoz, S. Müller, L. Mühlebach, T. Löw, D. Scheuer, L. Vandeventer, M. Bjelonic, F. Günther, H. Kolvenbach, M. Höpflinger, and M. Hutter, "An adaptive landing gear for extending the operational range of helicopters," in *2018 IEEE/RSJ International Conference on Intelligent Robots and Systems (IROS 2018)*, Madrid, Spain, 2018. DOI: 10.3929/ethz-b-000291626.

[20] *Robotic landing gear could enable future helicopters to take off and land almost anywhere*, Defense Advanced Research Projects Agency, Sep. 2015. [Online]. Available: https://www.darpa.mil/news-events/2015-09-10.

[21] Y. Yamada and M. R. Cutkosky, "Tactile sensor with 3-axis force and vibration sensing functions and its application to detect rotational slip," in *Proceedings*

of the 1994 IEEE International Conference on Robotics and Automation, San Diego, California, 1994, pp. 3550–3557. DOI: 10.1109/ROBOT.1994.351572.

[22] N. M. White and J. D. Turner, "Thick-film sensors: Past, present and future," *Measurement Science and Technology*, vol. 8, no. 1, p. 1, 1997.

[23] B. Puers, W. Sansen, and S. Paszczynski, "Assessment of thick-film fabrication methods for force (pressure) sensors," *Sensors and Actuators*, vol. 12, no. 1, pp. 57 –76, 1987. DOI: 10.1016/0250-6874(87)87006-3.

[24] J. Shah, "Strain sensivity of thick-film resistors," *IEEE Transactions on Components, Hybrids, and Manufacturing Technology*, vol. 3, no. 4, pp. 554–564, Dec. 1980. DOI: 10.1109/TCHMT.1980.1135645.

[25] D. Whitney, "Force feedback control of manipulator fine motions," *Journal of Dynamic Systems, Measurement and Control, Transactions of the ASME*, vol. 99, no. 2, pp. 91–97, 1977.

[26] D Goger, H Alagi, and H Worn, "Tactile proximity sensors for robotic applications," in *2013 IEEE International Conference on Industrial Technology (ICIT)*, IEEE, 2013, pp. 978–983. DOI: 10.1109/ICIT.2013.6505804.

[27] L. D. Harmon, "Touch-sensing technology- a review," *Society of Manufacturing Engineers*, vol. 58, 1980.

[28] J. Tegin and J. Wikander, "Tactile sensing in intelligent robotic manipulation – a review," *Industrial Robot: An International Journal*, vol. 32, no. 1, pp. 64–70, 2005. DOI: 10.1108/01439910510573318.

[29] M. R. Cutkosky, R. D. Howe, and W. R. Provancher, "Force and tactile sensors," in *Springer Handbook of Robotics*, Berlin, Heidelberg: Springer, 2008, pp. 455–476.

[30] H. Khamis, S. J. Redmond, R. Tripodi, A. Linarts, J. Zavickis, M. Knite, and I. Birznieks, "Design principles for building a soft, compliant, high spatial resolution tactile sensor array," in *International Conference on Human Haptic Sensing and Touch Enabled Computer Applications*, Springer, vol. 9775, 2016, pp. 25–34. DOI: 10.1007/978-3-319-42324-1_3.

[31] S. Begej, "Planar and finger-shaped optical tactile sensors for robotic applications," *IEEE Journal on Robotics and Automation*, vol. 4, no. 5, pp. 472–484, Oct. 1988. DOI: 10.1109/56.20431.

[32] J. Park, S. J. Kim, Y. Na, and J. Kim, "Custom optoelectronic force sensor based ground reaction force (grf) measurement system for providing absolute

force," in *2016 13th International Conference on Ubiquitous Robots and Ambient Intelligence (URAI)*, Aug. 2016, pp. 75–77. DOI: 10.1109/URAI.2016.7734024.

[33] O. Al-Mai, M. Ahmadi, and J. Albert, "Design, development and calibration of a lightweight, compliant six-axis optical force/torque sensor," *IEEE Sensors Journal*, vol. 18, no. 17, pp. 7005–7014, Sep. 2018. DOI: 10.1109/JSEN.2018.2856098.

[34] S. Ando and H. Shinoda, "Ultrasonic emission tactile sensing," *IEEE Control Systems Magazine*, vol. 15, no. 1, pp. 61–69, Feb. 1995. DOI: 10.1109/37.341866.

[35] H. Lee, J. Chung, S. Chang, and E. Yoon, "Normal and shear force measurement using a flexible polymer tactile sensor with embedded multiple capacitors," *Journal of Microelectromechanical Systems*, vol. 17, no. 4, pp. 934–942, Aug. 2008. DOI: 10.1109/JMEMS.2008.921727.

[36] T. Agcayazi, M. McKnight, P. Sotory, H. Huang, T. Ghosh, and A. Bozkurt, "A scalable shear and normal force sensor for prosthetic sensing," in *2017 IEEE SENSORS*, Oct. 2017, pp. 1–3. DOI: 10.1109/ICSENS.2017.8233977.

[37] P. S. Girão, P. M. P. Ramos, O. Postolache, and J. M. D. Pereira, "Tactile sensors for robotic applications," *Measurement: Journal of the International Measurement Confederation*, vol. 46, no. 3, pp. 1257–1271, 2013. DOI: 10.1016/j.measurement.2012.11.015.

[38] C. V. Di Leo, B. Leon, J. Wachlin, M. Kurien, J. J. Rimoli, and M. Costello, "Cable-driven four-bar link robotic landing gear mechanism: Rapid design and survivability testing," in *2018 AIAA/ASCE/AHS/ASC Structures, Structural Dynamics, and Materials Conference*, Kissimmee, Florida: American Institute of Aeronautics and Astronautics, 2018. DOI: 10.2514/6.2018-0491.

[39] J. W. Dally, W. F. Riley, and K. G. McConnell, "Instrumentation for engineering measurements," in. Wiley New York, 1993.

[40] T. Liu, Y. Inoue, and K. Shibata, "A small and low-cost 3-d tactile sensor for a wearable force plate," *IEEE Sensors Journal*, vol. 9, no. 9, pp. 1103–1110, Sep. 2009. DOI: 10.1109/JSEN.2009.2026509.

[41] J. Dargahi and S. Najarian, "Advances in tactile sensors design/manufacturing and its impact on robotics applications–a review," *Industrial Robot: An International Journal*, vol. 32, no. 3, pp. 268–281, 2005. DOI: 10.1108/01439910-510593965.

[42] S. Kim, C. Kim, S. Park, and D. Y. Lee, "A 3-dof sensor to estimate the force applied to the tip of a surgical instrument," in *2017 18th International Conference on Advanced Robotics (ICAR)*, Hong Kong, China, Jul. 2017, pp. 143–148. DOI: 10.1109/ICAR.2017.8023509.

[43] A. Cranny, D. Cotton, P. Chappell, S. Beeby, and N. White, "Thick-film force and slip sensors for a prosthetic hand," *Sensors and Actuators A: Physical*, vol. 123-124, pp. 162 –171, 2005, Eurosensors XVIII 2004. DOI: 10.1016/j.sna.2005.02.015.

[44] E. Hwang, J. Seo, and Y. Kim, "A polymer-based flexible tactile sensor for both normal and shear load detections and its application for robotics," *Journal of Microelectromechanical Systems*, vol. 16, no. 3, pp. 556–563, Jun. 2007. DOI: 10.1109/JMEMS.2007.896716.

[45] R. Platt, C. Ihrke, L. Bridgewater, D. Linn, R. Diftler, M. Abdallah, S. Askew, and F. Permenter, "A miniature load cell suitable for mounting on the phalanges of human-sized robot fingers," in *2011 IEEE International Conference on Robotics and Automation*, Shanghai, China, 2011, pp. 5357–5362. DOI: 10.1109/ICRA.2011.5980169.

[46] A. R. R. Morales, "Highly sensitive wearable piezoelectric force sensor with quasi-static load testing," PhD thesis, The George Washington University, 2017.

[47] M. J. Dixon, "Development of a load-cell compensation system," *Experimental Mechanics*, vol. 31, no. 1, pp. 21–24, Oct. 1991. DOI: 10.1007/BF02325718.

[48] D. J. Le Pelley, P. J. Richards, and A. Berthier, "Development of a directional load cell to measure flying sail aerodynamic loads," in *The 5th High Performance Yacht Design Conference*, Auckland, New Zealand, 2015, pp. 66–75.

[49] S. K. Hnat, B. J. H. van Basten, and A. J. van den Bogert, "Compensation for inertial and gravity effects in a moving force platform," *Journal of biomechanics*, vol. 75, pp. 96–101, Jun. 2018. DOI: 10.1016/j.jbiomech.2018.05.009.

[50] Y. Liu, H. Han, T. Liu, J. Yi, Q. Li, and Y. Inoue, "A novel tactile sensor with electromagnetic induction and its application on stick-slip interaction detection," *Sensors*, vol. 16, no. 4, 2016. DOI: 10.3390/s16040430. [Online]. Available: http://www.mdpi.com/1424-8220/16/4/430.

[51] A. Ananthanarayanan, S. Foong, and S. Kim, "A compact two dof magneto-elastomeric force sensor for a running quadruped," in *2012 IEEE International Conference on Robotics and Automation (ICRA)*, Saint Paul, Minnesota, 2012, pp. 1398–1403. DOI: 10.1109/ICRA.2012.6225201.

[52] M. Y. Chuah and S. Kim, "Enabling force sensing during ground locomotion: A bio-inspired, multi-axis, composite force sensor using discrete pressure mapping," *IEEE Sensors Journal*, vol. 14, no. 5, pp. 1693–1703, May 2014. DOI: 10.1109/JSEN.2014.2299805.

[53] M. Zillich and W. Feiten, "A versatile tactile sensor system for covering large and curved surface areas," in *2012 IEEE/RSJ International Conference on Intelligent Robots and Systems*, Vilamoura, Portugal, Oct. 2012, pp. 20–24. DOI: 10.1109/IROS.2012.6385806.

[54] Y. Tenzer, L. P. Jentoft, and R. D. Howe, "The feel of mems barometers: Inexpensive and easily customized tactile array sensors," *IEEE Robotics Automation Magazine*, vol. 21, no. 3, pp. 89–95, Sep. 2014. DOI: 10.1109/MRA.2014.2310152.

[55] D. Maturana and S. Scherer, "3d convolutional neural networks for landing zone detection from lidar," in *2015 IEEE International Conference on Robotics and Automation (ICRA)*, Seattle, WA, USA, May 2015, pp. 3471–3478. DOI: 10.1109/ICRA.2015.7139679.

[56] J. C. Curlander and R. N. McDonough, *Synthetic aperture radar*. Wiley, New York, 1991, vol. 11.

[57] E. A. Reber and B. J. Bernard, "The sea of simulation: Improving naval shiphandling training and readiness through game-based learning," Naval Postgraduate School, 2012. [Online]. Available: http://www.dtic.mil/docs/citations/ADA561764.

[58] G. Xu, Y. Zhang, S. Ji, Y. Cheng, and Y. Tian, "Research on computer vision-based for uav autonomous landing on a ship," *Pattern Recognition Letters*, vol. 30, no. 6, pp. 600–605, 2009. DOI: 10.1016/j.patrec.2008.12.011.

[59] S Saripalli, J. Montgomery, and G. Sukhatme, "Visually guided landing of an unmanned aerial vehicle," *IEEE Transactions on Robotics and Automation*, vol. 19, no. 3, pp. 371–380, 2003. DOI: 10.1109/TRA.2003.810239.

[60] R. Polvara, S. Sharma, J. Wan, A. Manning, and R. Sutton, "Autonomous vehicular landings on the deck of an unmanned surface vehicle using deep reinforcement learning," *Robotica*, vol. 37, no. 11, pp. 1867–1882, 2019.

[61] M. Voskuijl, G. Padfield, D. Walker, B. Manimala, and A. Gubbels, "Simulation of automatic helicopter deck landings using nature inspired flight control," *The Aeronautical Journal*, vol. 114, no. 1151, pp. 25–34, 2010. DOI: 10.1017/S000192400000350X.

[62] L. A Sandino, M Bejar, and A Ollero, "On the applicability of linear control techniques for autonomous landing of helicopters on the deck of a ship," in *2011 IEEE International Conference on Mechatronics*, Istanbul, Turkey: IEEE, 2011, pp. 363–368. DOI: 10.1109/ICMECH.2011.5971312.

[63] "Autonomous control modes and optimized path guidance for shipboard landing in high sea states," Tech. Rep. AD1013549, 2016. [Online]. Available: http://www.dtic.mil/docs/citations/AD1013549.

[64] C. K. Tan, J. Wang, Y. C. Paw, and F. Liao, "Autonomous ship deck landing of a quadrotor using invariant ellipsoid method," *IEEE Transactions on Aerospace and Electronic Systems*, vol. 52, no. 2, pp. 891–903, 2016. DOI: 10.1109/TAES.2015.140850.

[65] M. Bloesch, M. Hutter, M. A. Hoepflinger, S. Leutenegger, C. Gehring, C. D. Remy, and R. Siegwart, "State estimation for legged robots-consistent fusion of leg kinematics and imu," *Robotics Science and Systems*, vol. 17, pp. 17–24, 2013. DOI: 10.15607/RSS.2012.VIII.003.

[66] S Nobili, M Camurri, V Barasuol, M Focchi, D Caldwell, C Semini, and M. Fallon, "Heterogeneous sensor fusion for accurate state estimation of dynamic legged robots," Robotics: Science and Systems Foundation, 2017. DOI: 10.15607/RSS.2017.XIII.007.

[67] J. Simanek, M. Reinstein, and V. Kubelka, "Evaluation of the ekf-based estimation architectures for data fusion in mobile robots," *IEEE/ASME Transactions on Mechatronics*, vol. 20, no. 2, pp. 985–990, Apr. 2015. DOI: 10.1109/TMECH.2014.2311416.

[68] L. Moreno, J. M. Armingol, S. Garrido, A. de la Escalera, and M. A. Salichs, "A genetic algorithm for mobile robot localization using ultrasonic sensors," *Journal of Intelligent and Robotic Systems*, vol. 34, no. 2, pp. 135–154, Jun. 2002. DOI: 10.1023/A:1015664517164.

[69] J. Ma, S. Susca, M. Bajracharya, L. Matthies, M. Malchano, and D. Wooden, "Robust multi-sensor, day/night 6-dof pose estimation for a dynamic legged vehicle in gps-denied environments," in *2012 IEEE International Conference on Robotics and Automation*, Saint Paul, MN, USA, May 2012, pp. 619–626. DOI: 10.1109/ICRA.2012.6225132.

[70] W. W. Chen, S. Wang, Y. Chen, C. Tsai, and P. Lin, "Sensor data fusion for body-pitch estimation in a quadruped robot," in *2016 International Conference on Advanced Robotics and Intelligent Systems (ARIS)*, Taipei, Taiwan, Aug. 2016, pp. 1–1. DOI: 10.1109/ARIS.2016.7886616.

[71] F. Edrisi, V. J. Majd, M. Attar, and N. Dini, "Modifying the attitude of quadruped robot body against disturbances via data fusion," in *2016 4th International Conference on Robotics and Mechatronics (ICROM)*, Tehran, Iran, Oct. 2016, pp. 55–60. DOI: 10.1109/ICRoM.2016.7886817.

[72] S. Nicosia and P. Tomei, "Robot control by using only joint position measurements," *IEEE Transactions on Automatic Control*, vol. 35, no. 9, pp. 1058–1061, Sep. 1990. DOI: 10.1109/9.58537.

[73] W. C. Myeong, K. Y. Jung, S. W. Jung, Y. H. Jung, and H. Myung, "Development of a drone-type wall-sticking and climbing robot," in *2015 12th International Conference on Ubiquitous Robots and Ambient Intelligence (URAI)*, Goyang, South Korea, 2015, pp. 386–389. DOI: 10.1109/URAI.2015.7358881.

[74] W. R. T. Roderick, M. R. Cutkosky, and D. Lentink, "Touchdown to take-off: At the interface of flight and surface locomotion," *Interface Focus*, vol. 7, no. 1, p. 20 160 094, 2017. DOI: 10.1098/rsfs.2016.0094.

[75] D. Kim and M. Costello, "Virtual model control of rotorcraft with articulated landing gear for shipboard landing," in *AIAA Guidance, Navigation, and Control Conference*, San Diego, CA, USA, 2016, 1863(15). DOI: doi.org/10.2514/6.2016-1863.

[76] C. V. Di Leo, B. León, J. Wachlin, M. Kurien, A. Krishnan, A. Krishnan, J. J. Rimoli, and M. Costello, "Design of a crashworthy cable-driven four-bar link robotic landing gear system," *Journal of Aircraft*, vol. 57, no. 2, pp. 1–21, 2020. DOI: 10.2514/1.C035386.

[77] *Stronger than steel*, Teufelberger Corporation, 2017. [Online]. Available: https://www.defender.com/pdf/STS_HSR.pdf.

[78] *Hsr-75, sts (stronger than steel) dyneema*, New England Ropes, 2020. [Online]. Available: https://www.neropes.com/products/grand-prix-racing/product/detail/hsr-75/.

[79] B. León, J. J. Rimoli, and C. V. Di Leo, "Elastomer encapsulated pressure sensor with engineered air cavity for force sensing," *IEEE Sensors Journal*, vol. 19, no. 16, pp. 6628–6643, 2019.

[80] *Abaqus/standard*, SIMULIA, 2019.

[81] L. R. G. Treloar, *The Physics of Rubber Elasticity*, 3rd ed. New York: Oxford University Press, 1975.

[82] *Mold max series condensation cure silicone rubber compounds*, Smooth-On, Apr. 2018. [Online]. Available: https://www.smooth-on.com/tb/files/Mold_Max_Series_TB.pdf.

[83] A. Mix and A. Giacomin, "Standardized polymer durometry," *Journal of Testing and Evaluation*, vol. 39, no. 4, pp. 696–705, 2011. DOI: 10.1520/JTE103205.

[84] H. Qi, K Joyce, and M. Boyce, "Durometer hardness and the stress-strain behavior of elastomeric materials," *Rubber chemistry and technology*, vol. 76, no. 2, pp. 419–435, 2003. DOI: 10.5254/1.3547752.

[85] G. O'hara, "Mechanical properties of silicone rubber in a closed volume," Army Armament Research and Development Center, Tech. Rep. ARLCB-TR-83045, 1983.

[86] *Trustability board mount pressure sensors.* Honeywell Sensing and Control, Nov. 2017. [Online]. Available: https://sensing.honeywell.com/honeywell-sensing-trustability-rsc-series-data-sheet-32321348-c-en.pdf.

[87] *Dual study mount load cell universal*, Transducer Techniques, LLC, 2018. [Online]. Available: https://www.transducertechniques.com/dsm-load-cell.aspx.

[88] *Device specifications: Ni 6356*, National Instruments, Jun. 2016. [Online]. Available: http://www.ni.com/pdf/manuals/374452c.pdf.

[89] C.-L. Choong, M.-B. Shim, B.-S. Lee, S. Jeon, D.-S. Ko, T.-H. Kang, J. Bae, S. H. Lee, K.-E. Byun, J. Im, Y. J. Jeong, C. E. Park, J.-J. Park, and U.-I. Chung, "Highly stretchable resistive pressure sensors using a conductive elastomeric composite on a micropyramid array," *Advanced Materials*, vol. 26, no. 21, pp. 3451–3458, 2014. DOI: 10.1002/adma.201305182.

[90] L. Helseth, "Optical force sensing principle based on transparent elastomer with a rough surface," *Sensors and Actuators A: Physical*, vol. 263, pp. 667–676, 2017. DOI: 10.1016/j.sna.2017.07.033.

[91] S. Polukoshko, A. Martinovs, and E. Zaicevs, "Influence of rubber ageing on damping capacity of rubber vibration absorber," *Vibroengineering Procedia*, vol. 19, pp. 103–109, 2018. DOI: 10.21595/vp.2018.20219.

[92] P. Henyš and M. Ackermann, "Natural frequencies of instron electropuls e3000 testing machine," in *Applied Mechanics Conference*, Pilsen, Czech Republic, Apr. 2012.

[93] V. Somashekar, S Harikrishnan, P. Aejaz Ahmed, and D Kamesh, "Vibration response prediction of the printed circuit boards using experimentally validated finite element model," *Procedia Engineering*, vol. 144, pp. 576–583, 2016. DOI: 10.1016/j.proeng.2016.05.044.

[94] M. Samridhi, S. Kumar, K. Dhariwal, P. Singh, and P. Alvi, "Stress and frequency analysis of silicon diaphragm of mems based piezoresistive pressure sensor," *International Journal of Modern Physics B*, vol. 33, no. 7, 2019. DOI: 10.1142/S0217979219500401.

[95] J. O. Smith, "Introduction to digital filters: With audio applications," in. W3K Publishing, 2008, ch. 1: The Simplest Low-Pass Filter, pp. 1–25.

[96] J. L. Calvignac, C. D. Jeffries, and F. J. Verplanken, *Cyclic redundancy check for partitioned frames*, Patent US6681364B1, US Patent office, Jan. 2004.

[97] Y. A. Rossikhin and M. V. Shitikova, "The analysis of the impact response of a thin plate via fractional derivative standard linear solid model," *Journal of Sound and Vibration*, vol. 330, no. 9, pp. 1985–2003, 2011. DOI: 10.1016/j.jsv.2010.11.010.

[98] G. Carbone and C. Putignano, "A novel methodology to predict sliding and rolling friction of viscoelastic materials: Theory and experiments," *Journal of the Mechanics and Physics of Solids*, vol. 61, no. 8, pp. 1822–1834, 2013. DOI: 10.1016/j.jmps.2013.03.005.

[99] D. Simon, "Optimal state estimation: Kalman, h infinity, and nonlinear approaches," in. New York, NY, USA: Wiley-Interscience, 2006, ch. 2, ISBN: 0471708585.

[100] J. Braun, *Formulae Handbook*. Maxon Academy, Sachseln, 2012, pp. 35–54.

[101] R. E. Conrad, "Smp95: Standard ship motion program user manual," Naval Surface Warfare Center Carderock, Tech. Rep. NSWCCD-50-TR–2010/047, 2005.

[102] W. G. Meyers, C. Benne, and T. Applebee, "Users manual for the simulation time history and access time history programs," Naval Surface Warfare Center: Carderock Division Ship Hydromechanics Department, Tech. Rep. SHD-1297-01, 1993.

[103] D. Barnes, *Uss curtis wilbur (ddg 54) crosses into 2016*, NAVY Live, Dec. 2015. [Online]. Available: https://navylive.dodlive.mil/2015/12/31/uss-curtis-wilbur-ddg-54-crosses-into-2016/.

[104] B. Kinsman, *Wind Waves. The Generation and Propagation on the Ocean Surface*. Prentice-Halle Incorporated, 1965, ISBN: 0486646521.

[105] S. Bales, "Designing ships to the natural environment," Association of Scientists and Engineers, Tech. Rep. ADA114147, 1982. DOI: 10.1111/j.1559-3584.1983.tb00574.x.

[106] L. Meirovitch, "Fundamentals of vibrations," in. Waveland Press, 2010, ch. 6: Elements of Analytical Dynamics, pp. 273–277, ISBN: 1577666917.

[107] E. Leylek, M. Ward, and M. Costello, "Flight dynamic simulation for multibody aircraft configurations," *Journal of Guidance, Control and Dynamics*, vol. 35, no. 6, pp. 1828–1842, 2012. DOI: 10.2514/1.55858.

[108] M. Gross, M. Costello, and F. Fresconi, "Impact point model predictive control of a spin-stabilized projectile with instability protection," in *AIAA Atmospheric Flight Mechanics (AFM) Conference*, Boston, MA, USA: American Institute of Aeronautics and Astronautics, Nov. 2013. DOI: 10.2514/6.2013-4509.

[109] M. Costello, C. Montalvo, and F. Fresconi, "Multiboom: A generic multibody flight mechanics simulation tool for smart projectiles," Army Research Laboratory, Aberdeen Proving Ground, Maryland, Tech. Rep. ARL-TR-6232, Oct. 2012.

[110] M. Gross, J. D. Rogers, and M. Costello, "Computational improvements to multibody projectile dynamics simulation," in *AIAA Modeling and Simulation Technologies Conference*, Atlanta, GA, USA, 2014, p. 2648. DOI: 10.2514/6.2014-2648.

[111] *Camcopter s-100 unmanned air system specifications*, Schiebel, Jan. 2019. [Online]. Available: https://schiebel.net/products/camcopter-s-100-system-2/.

[112] *Vectornav industrial series*, VectorNav Technologies, 2017. [Online]. Available: https://www.vectornav.com/docs/default-source/product-brochures/industrial-series-product-brochure-(12-0009).pdf.

[113] G Syms and S. J. Zan, "Analysis of rotor forces in a ship airwake," Tech. Rep., 1994. [Online]. Available: http://www.dtic.mil/docs/citations/ADA640406.

[114] M. Snyder, H. Kang, C. Brownell, and J. Burks, "Validation of ship air wake simulations and investigation of ship air wake impact on rotary wing aircraft," *Naval Engineers Journal*, vol. 125, no. 1, pp. 69–79, 2013.

[115] B. León, J. Rimoli, and C. V. D. Leo, "Ground and flight tests of a cable-driven four-bar linkage robotic landing gear for rotorcraft," in *Vertical Flight Society 75th Annual Forum & Technology Display*, Philadelphia, PA, USA, May 2019.

[116] B. León, J. J. Rimoli, and C. V. Di Leo, "Ground and flight tests of an unmanned rotorcraft with cable-driven robotic landing gear," *Journal of the American Helicopter Society*, 2020(Under peer review).

[117] ——, "Rotorcraft dynamic platform landings using robotic landing gear," *Journal of Dynamic Systems, Measurement, and Control*, 2020 (Under peer review).

[118] *Hexad*, Sarnicola Simulation Systems, 2007. [Online]. Available: `https://sarnicola.com/hexad3000h.html`.

[119] P. M. Rothhaar, P. C. Murphy, B. J. Bacon, I. M. Gregory, J. A. Grauer, R. C. Busan, and M. A. Croom, "Nasa langley distributed propulsion vtol tiltwing aircraft testing, modeling, simulation, control, and flight test development," in *14th AIAA Aviation Technology, Integration, and Operations Conference*, Atlanta, GA, USA, 2014, p. 2999. DOI: 10.2514/6.2014-2999.

[120] Z. J. Goraj and E. Cichocka, "Influence of weak and strong gyroscopic effects on light aircraft dynamics," *Aircraft Engineering and Aerospace Technology*, vol. 88, no. 5, pp. 613–622, 2016. DOI: 10.1108/AEAT-03-2015-0076.

[121] F. Kendoul, I. Fantoni, and R. Lozano, "Modeling and control of a small autonomous aircraft having two tilting rotors," *IEEE Transactions on Robotics*, vol. 22, no. 6, pp. 1297–1302, 2006. DOI: 10.1109/TRO.2006.882956.

VITA

Benjamin (Ben) León was born in Warner Robins, GA where he spent his formative years until college. He attended Georgia Tech's School of Aerospace Engineering, and he graduated with this Bachelor's of Science in Aerospace Engineering in 2015. During his undergrad, Ben held multiple internships at NASA Langley research center where he built continuous, flexible control surfaces for drag and noise reduction of wings and unmanned aircraft landing safety systems. He joined the Center for Advanced Machine Mobility at the start of his graduate career at Georgia Tech. There, he worked on advanced, articulated landing gear concepts for tail-sitter aircraft and novel force sensors for aerospace robotics applications. Ben completed his Master's of Science in Aerospace Engineering in 2017. He transferred to the Multiphysics Mechanics of Materials Lab, and he was the lead Research Assistant on the DARPA S-100 robotic landing gear demonstration program. In 2018, Ben began work in autonomous cargo airdrop, where he continues to design, build, and experimentally validate enabling technologies for autonomous payload delivery using parachutes.